

UNIVERSIDADE FEDERAL DE
SANTA CATARINA

TESE DE DOUTORADO

Analysis of SDSS spectra and GALEX
photometry with STARLIGHT: Stellar
populations and dust attenuation in local
galaxies

Autor:
Ariel Werle

Orientador:
Dr. Roberto Cid Fernandes

*Tese submetida ao programa de pós-graduação em física como
requisito para a obtenção do título de doutor em física.*



Departamento de Física
Florianópolis, June 4, 2019

Ficha de identificação da obra elaborada pelo autor,
através do Programa de Geração Automática da Biblioteca Universitária da UFSC.

Werle, Ariel

Analysis of SDSS spectra and GALEX photometry
with STARLIGHT: Stellar populations and dust
attenuation in local galaxies / Ariel Werle ;
orientador, Roberto Cid Fernandes, 2019.
193 p.

Tese (doutorado) - Universidade Federal de Santa
Catarina, Centro de Ciências Físicas e Matemáticas,
Programa de Pós-Graduação em Física, Florianópolis,
2019.

Inclui referências.

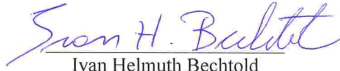
1. Física. 2. Galáxias. 3. Evolução de Galáxias.
4. Síntese Espectral de Galáxias. I. Cid Fernandes,
Roberto. II. Universidade Federal de Santa
Catarina. Programa de Pós-Graduação em Física. III.
Título.

Ariel Werle

**ANALYSIS OF SDSS SPECTRA AND GALEX PHOTOMETRY
WITH STARLIGHT: STELLAR POPULATIONS AND DUST
ATTENUATION IN LOCAL GALAXIES**

Esta Tese foi julgada adequada para a obtenção do título de
DOUTOR EM FÍSICA, na área de concentração Astrofísica e
aprovada em sua forma final pelo Programa de Pós-Graduação em
Física.

Florianópolis, 28 de fevereiro de 2019.




Ivan Helmuth Bechtold
(Coordenador do Programa)

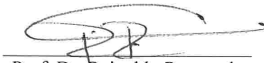
Banca Examinadora:



Prof. Dr. Roberto Cid Fernandes
Junior
(presidente - UFSC)




Prof. Dr. Antônio Nemer Kanaan
Neto
(membro titular - UFSC/FSC)



Prof. Dr. Reinaldo Ramos de
Carvalho
(membro externo - INPE)



Prof. Dr. Abílio Mateus Junior
(membro titular - UFSC/FSC)



Dr. Guilherme dos Santos Couto
(membro externo - Universidade de Antofagasta)

Resumo

O software de síntese espectral STARLIGHT é uma ferramenta que permite a extração de propriedades físicas de galáxias ajustando suas componentes estelares com uma combinação de espectros de populações estelares. Nesta tese, apresentamos uma nova versão do código que permite a combinação de dados espectroscópicos e fotométricos, permitindo melhores estimativas de propriedades de galáxias. O código é aplicado a dados do Sloan Digital Sky Survey (SDSS) e do Galaxy Evolution Explorer (GALEX) para uma análise simultânea de espectros ópticos e fotometria ultravioleta em uma amostra de 231643 galáxias usando modelos do estado da arte para populações estelares. Desenvolvemos um novo método para estimar a fotometria do GALEX em aberturas compatíveis com espectros do SDSS. Nosso método é confiável quando aplicado a amostras grandes e compatível com outro método encontrado na literatura. Em concordância com experiências anteriores baseadas em espectros integrados do CALIFA, nossos resultados mostram que a adição de dados ultravioleta leva a um aumento moderado nas frações de luz atribuídas a populações estelares de $\sim 10^7 - 10^8$ anos; também é possível identificar uma concomitante diminuição nas frações de luz das populações mais jovens e mais velhas. Quando analisamos estas tendências em um espaço de cor-magnitude, percebemos que as mudanças são mais dramáticas em galáxias da chamada nuvem azul ($NUV - r < 4$), especialmente para as menos brilhantes. Também observa-se um aumento na atenuação por poeira estimada para galáxias dominadas por populações estelares jovens. Investigamos a contribuição de diferentes populações estelares para a emissão em filtros do GALEX e do SDSS e como estas variam no espaço de cor-magnitude, mostrando que populações estelares jovens têm contribuições significativas para o ultravioleta em galáxias de cor $4 < NUV - r < 5$ (vale verde) e uma contribuição pequena na região menos brilhante da sequência vermelha inferior ($5 < NUV - r < 6$). Em galáxias com cores $NUV - r > 6$ (sequência vermelha superior) a emissão ultravioleta é dominada por populações velhas que contribuem mais para o FUV do que populações de idade intermediária. A contribuição de populações estelares para a luz ultravioleta é usada para evidenciar as diferenças entre galáxias aposentadas com e

sem linhas de emissão detectáveis. Em concordância com trabalhos anteriores, mostramos que o primeiro grupo apresenta um excesso em populações estelares de idade intermediária quando comparado com o segundo grupo, evidenciando que a ionização em galáxias aposentadas está conectada com diferentes históricos de formação. Por fim, comparamos os resultados obtidos com duas prescrições diferentes para os efeitos da poeira em uma sub-amostra composta apenas por galáxias espirais. Nosso conjunto de dados é mais bem representado pela lei de atenuação de galáxias *starburst*, apesar de os resultados assumindo a lei de extinção da Via-Láctea como modelo de atenuação melhoram conforme a profundidade óptica da poeira diminui, especialmente em galáxias cujos discos são vistos em alta inclinação, indicando que estas galáxias podem ser mais bem representadas com leis de atenuação de formas similares à curva de extinção da Via-Láctea, mas com características menos acentuadas. Verificamos que os modelos de populações estelares usados neste trabalho, que atribuem o *UV upturn* apenas a estrelas *post-AGB*, reproduzem a emissão *FUV* de galáxias com *UV upturn* em nossa amostra com margem de 0.25 magnitudes em 62% dos casos. Esse resultado indica que fontes adicionais de emissão são necessárias para explicar as magnitudes *FUV* de uma fração considerável destes objetos.

Palavras-chave: Galáxias, Evolução de Galáxias, Síntese Espectral de Galáxias

Resumo Expandido

Introdução

Síntese espectral ou síntese de populações estelares é um processo que permite a extração informações codificadas nas distribuições espectrais de energia de galáxias ajustando a estas uma combinação de espectros de populações estelares. Este processo permite a medida de uma série de propriedades físicas de galáxias; tais como massa, composição química das estrelas, histórias de formação estelar e de enriquecimento químico e dispersão de velocidade das estrelas. Informações como estas fornecem uma ponte entre observações e modelos de evolução de galáxias. O STARLIGHT (Cid Fernandes et al., 2005) é uma ferramenta de síntese espectral não paramétrica, isto é, que não impõe qualquer suposição sobre a forma funcional da história de formação estelar de uma galáxia. Esta implementação dá flexibilidade ao código, porém requer vínculos detalhados que só podem ser fornecidos por dados espectrais, o que impede a aplicação do código a dados de fotometria de banda larga. Este requisito impõe restrições à aplicabilidade do código, já que grandes bancos de dados de fotometria estão disponíveis do ultravioleta ao infravermelho médio, enquanto dados dados espectroscópicos estão disponíveis em grandes quantidades apenas no óptico. Com o objetivo de aproveitar a grande disponibilidade de dados fotométricos sem perder a capacidade de analisar as informações espectrais necessárias para um ajuste não paramétrico, o STARLIGHT foi recentemente atualizado para ajustar espectros e fotometria simultaneamente. Uma versão preliminar do novo código foi aplicada por López Fernández et al. (2016) a uma combinação de espectros integrados do CALIFA survey (*Calar Alto Legacy Integral Field Area Survey*; Sánchez et al. 2012) com a fotometria ultravioleta (UV) do GALEX (*GALaxy Evolution EXplorer*; Martin et al. 2005) obtida em duas bandas, *FUV* e *NUV*.

Objetivos

Do ponto de vista técnico, os objetivos deste trabalho são finalizar a atualização do STARLIGHT iniciada por López Fernández et al. (2016) e aplicar o novo código a dados do GALEX e do SDSS (*Sloan Digital Sky Survey*; York et al. 2000), viabilizando a análise de propriedades

de milhares de galáxias. A partir destes dados, pretendemos investigar a história de formação das galáxias do universo local, bem como os constituintes do seu meio interestelar. Como ponto de partida, vamos verificar como a inclusão de dados ultravioleta altera a estimativa da história de formação estelar em diferentes tipos de galáxias e como estas alterações impactam nosso entendimento de propriedades da população local de galáxias. Iremos analisar as formas das leis de atenuação das galáxias de nossa amostra, investigando a presença ou ausência de um pico na atenuação em $\sim 2175\text{\AA}$. Por fim, iremos verificar a capacidade de nossos modelos de populações estelares em reproduzir a emissão UV em galáxias elípticas.

Metodologia

Nossa metodologia consiste em três etapas: (i) Primeiramente, desenvolvemos um novo método para estimar a fotometria do GALEX em aberturas compatíveis com espectros do SDSS, visto que a PSF do GALEX ($4.6''$ em NUV e $5.4''$ em FUV) é maior do que a abertura em que espectros do SDSS são coletados ($1.5''$), requerendo uma estimativa indireta da fotometria de abertura no UV. Nosso método parte da diferença entre magnitudes totais e magnitudes na abertura espectroscópica nas bandas do SDSS, denominada $\Delta m_{1.5}$. Ajustamos uma reta à distribuição de $\Delta m_{1.5}$ com comprimento de onda e a extrapolamos até o ultravioleta. Isso nos dá uma estimativa da diferença de magnitude nas bandas do GALEX, que é então combinada com as magnitudes totais do GALEX para estimar magnitudes de NUV e FUV na abertura de $1.5''$. Testes mostram que nosso método é confiável quando aplicado a grandes amostras e compatível com um método independente desenvolvido por Battisti, Calzetti & Chary (2016). (ii) Finalizamos o desenvolvimento de uma nova versão do STARLIGHT para viabilizar a análise simultânea de espectros e fotometria. O código foi testado em dados do ultravioleta ao infravermelho próximo e possui um manual disponível. (iii) Aplicamos o novo código à combinação de espectros ópticos do SDSS e fotometria ultravioleta do GALEX, obtendo propriedades físicas para uma amostra de 231643 galáxias. Vale mencionar que nossa análise é feita usando modelos robustos de populações estelares que incluem objetos em fases complexas da evolução estelar como estrelas *Wolf-Rayet* e *post-AGB*.

Resultados e Discussão

Em concordância com os resultados de López Fernández et al. (2016), verificamos que a inclusão de dados ultravioleta leva a um aumento moderado nas frações de luz atribuídas a populações estelares de $\sim 10^7 - 10^8$ anos. Além disso, nossos resultados mostram diminuição nas frações de luz atribuídas às populações mais jovens e mais velhas da base, o que não é identificado por López Fernández et al. (2016), esta discrepância é devida a diferenças nos dados e modelos de populações estelares. Galáxias pobres em metais têm estimativas de metalicidade levemente maiores quando incluímos dados UV. Quando analisamos estas tendências em um espaço de cor-magnitude, percebemos que as mudanças são mais dramáticas em galáxias da chamada nuvem azul ($NUV - r < 4$), especialmente para as menos brilhantes. Em galáxias da sequência vermelha ($NUV - r > 5$) os dados ultravioleta previnem a detecção de falsos eventos de formação estelar. Ao analisar a relação de Meurer, Heckman & Calzetti (1999) entre a inclinação do espectro no ultravioleta (β) e a atenuação no ultravioleta distante (A_{FUV}), percebe-se a relação é reproduzida para galáxias dominadas por populações jovens, permitindo atribuir a dispersão na relação a uma diversidade de histórias de formação estelar. Ao comparar a relação $\beta \times A_{FUV}$ obtida apenas com dados do SDSS com a relação obtida da combinação do SDSS com o GALEX, é possível identificar que a inclusão de dados ultravioleta aumentam as estimativas de atenuação em galáxias dominadas por populações estelares jovens, apesar de esta tendência não ser identificada na média geral. Usando a natureza pancromática do nosso conjunto de dados, investigamos a contribuição de diferentes populações estelares para a emissão em filtros do GALEX e do SDSS e como estas variam no espaço de cor-magnitude, mostrando que populações estelares jovens têm contribuições significativas para o ultravioleta em galáxias de cor $4 < NUV - r < 5$ (vale verde) e uma contribuição pequena na região menos brilhante da sequência vermelha inferior ($5 < NUV - r < 6$). Em galáxias com cores $NUV - r > 6$ (sequência vermelha superior) a emissão ultravioleta é dominada por populações velhas que contribuem mais para a FUV do que populações de idade intermediária. A contribuição de populações estelares para a luz ultravioleta evidencia as diferenças entre galáxias aposentadas com e sem linhas de emissão detectáveis. Em concordância com o trabalho de Herpich et al. (2018), mostramos que o primeiro grupo apresenta um excesso em populações estelares de idade intermediária quando comparado com o segundo grupo,

evidenciando que a ionização em galáxias aposentadas está conectada com diferentes históricos de formação. Por fim, comparamos os resultados obtidos com duas prescrições diferentes para os efeitos da poeira: Um modelo assumindo a curva de atenuação de galáxias *starburst* obtida por Calzetti, Kinney & Storchi-Bergmann (1994) e Calzetti et al. (2000) e outro assumindo a curva de extinção da Via-Láctea (conforme parametrizada por Cardelli, Clayton & Mathis 1989) como modelo para atenuação. Esta comparação é feita em uma sub-amostra composta apenas por galáxias classificadas como espirais pelo projeto Galaxy Zoo. Nosso conjunto de dados é mais bem representado pela lei de atenuação de galáxias *starburst*, apesar de os resultados assumindo a lei de extinção da Via-Láctea como modelo de atenuação melhoram conforme a profundidade óptica da poeira diminui, especialmente em galáxias cujos discos são vistos em alta inclinação, indicando que estas galáxias podem ser mais bem representadas com leis de atenuação de formas similares à curva de extinção da Via-Láctea, mas com características menos acentuadas. Verificamos que os modelos de populações estelares usados neste trabalho, que atribuem o *UV upturn* apenas a estrelas *post-AGB*, reproduzem a emissão *FUV* de galáxias com *UV upturn* em nossa amostra com margem de 0.25 magnitudes em 62% dos casos. Esse resultado indica que fontes adicionais de emissão são necessárias para explicar as magnitudes *FUV* de uma fração considerável destes objetos.

Considerações Finais

Demonstramos neste trabalho que a inclusão de dados ultravioleta na síntese espectral de galáxias usando um método não paramétrico fornece informações importantes sobre populações estelares e poeira, além de abrir uma interessante janela para perguntas científicas que só podem ser respondidas com informações vindas do ultravioleta. Apesar de termos obtidos muitos resultados, ainda há muito o que investigar. Entre os projetos futuros que podem ser explorados estão a inclusão de uma lei de atenuação flexível (e.g Noll et al. 2009; Salim, Boquien & Lee 2018) que permita uma investigação mais detalhada da variação das curvas de atenuação de galáxias e da dispersão na relação $\beta \times A_{FUV}$. Outro aspecto importante e pouco explorado neste trabalho é a emissão ultravioleta em galáxias elípticas, que pode ser uma ferramenta poderosa para distinguir entre populações estelares velhas. Este trabalho também abre espaço para outras combinações de dados fotométricos e espectroscópicos. Um exemplo

é a combinação de dados espectroscópicos do MUSE (*Multi Unit Spectroscopic Explorer*) com fotometria em filtros azuis que incluem informações cruciais para análises de populações estelares.

Palavras-chave: Galáxias, Evolução de Galáxias, Síntese Espectral de Galáxias

Abstract

The STARLIGHT spectral synthesis code is a tool that extracts physical information of galaxies by fitting their stellar component using a combination of stellar population spectra. In this thesis, we present a new version of the code, which allows the combination of spectroscopic and photometric information to better constrain galaxy properties. The code is applied to data from the Sloan Digital Sky Survey (SDSS) and the Galaxy Evolution Explorer (GALEX) to simultaneously analyze optical spectra and ultraviolet photometry of 231643 galaxies using state-of-the-art stellar population models. A new method was developed to estimate GALEX photometry in the SDSS spectroscopic aperture. The method proves itself reliable when applied to large samples and is compatible to another method found in the literature. We find that, in agreement with previous experiments based on CALIFA data, the addition of UV constraints leads to a moderate increase on the fraction of $\sim 10^7 - 10^8$ yr populations; we also find a concomitant decrease of younger and older components. In color magnitude space, changes are most relevant for galaxies at the faint end of the blue cloud. We investigate the contribution of different stellar populations to the fraction of light in GALEX and SDSS bands across the UV-optical color-magnitude diagram, showing that young stellar populations contribute significantly to UV emission up to the green valley ($4 < NUV - r < 5$) and to a smaller extent in the faint end of the lower red sequence ($5 < NUV - r < 6$). In the upper red sequence, UV emission is dominated by old stellar populations that contribute more to FUV emission than intermediate age populations. As an example application, we use this λ dependence to highlight differences between retired galaxies with and without emission lines. In agreement with previous work, we find that the former show an excess of intermediate age populations when compared to the later. Testing the suitability of two different prescriptions for dust in a subsample of spiral galaxies, we find that our data-set is best fitted using the attenuation law of starburst galaxies. However, results assuming the Milky Way extinction curve as an attenuation model improve with decreasing τ_V , especially for galaxies viewed edge-on, indicating that highly inclined galaxies may exhibit attenuation curves with

shapes similar to the one of the Milky Way extinction curve, although with less prominent features. We find that the models used in this work, on which the UV upturn phenomenon is solely due to post-AGB stars, can reproduce *FUV* emission within 0.25 magnitudes in 62% of UV upturn galaxies in our sample. This indicates the need for additional UV sources to reproduce the *FUV* magnitudes of a significant portion of these objects.

Keywords: Galaxies, Galaxy Evolution, Spectral Synthesis of Galaxies

Agradecimentos

"Oh, I get by with a little help from my friends."

— The Beatles, With a Little Help From My Friends

Agradeço ao meu orientador, Cid, por ajudar este trabalho a emergir do caos dialético de nossas discussões, e também por ser uma constante fonte de inspiração. Também agradeço meu orientador anterior, Abilio, que me introduziu à área de astrofísica extragaláctica e provavelmente conduziu a parte mais difícil da minha formação: obrigado pela paciência. Incluo um agradecimento especial à professora Natalia, que providenciou um apoio pessoal, acadêmico e financeiro que foi crítico para este trabalho. Ademais, agradeço a todos os demais professores do grupo de astrofísica da UFSC, como se diz em inglês: "it takes a village". Agradeço também ao chefe de expediente do PPGFSC: Obrigado Antônio, por todas as vezes que você me explicou pacientemente coisas que eu poderia ter lido em algum lugar.

Faço um agradecimento especial aos membros da banca: Reinaldo Ramos de Carvalho, Guilherme Couto, Antônio Kanaan e Abilio Mateus. Muito obrigado pela apreciação crítica deste trabalho, que me ajudou a aumentar consideravelmente a qualidade do texto na versão final.

Agradeço especialmente aos meus pais, Ari e Iria, que me apoiaram durante todos os anos da minha formação. Estendo este agradecimento a minha irmã Isabel e a minha avó Adelita. Agradeço também a minha tia Aline e a meu tio Lorival, que nutriram meu interesse inicial pela ciência. Por fim, gostaria de agradecer a minha namorada, Bruna, por me acompanhar durante todo o período de doutorado e ouvir longos monólogos sobre este trabalho, sei que não deve ter sido fácil, amo você.

Agradeço também a todos os profissionais envolvidos no SDSS, no GALEX, no Galaxy Zoo, no NSA e em outros projetos que forneceram os dados necessários para a realização deste trabalho. Estendo este agradecimento a todos os voluntários que participaram do projeto Galaxy Zoo.

Contents

Resumo	v
Resumo Expandido	vii
Abstract	xiii
1 Introduction	1
1.1 Galaxies	2
1.1.1 Galaxy constituents and their signatures	2
1.1.2 Galaxy Morphology	3
1.1.3 A touch of cosmology	6
1.1.4 Galaxy evolution	7
1.2 Spectral synthesis of galaxies	9
1.2.1 Stellar population models	10
1.2.2 Spectral synthesis codes	15
1.3 Ultraviolet emission from galaxies	18
1.3.1 Stellar populations	18
1.3.2 Dust	20
1.3.3 The UV power-law index	22
1.4 This Work	23
2 Data, sample and the curse of aperture matching	25
2.1 Data sources and sample selection	25
2.1.1 The Sloan Digital Sky Survey	26
2.1.2 The Galaxy Evolution Explorer	27
2.1.3 Other data sources and value-added catalogs	27
2.1.4 GALEX+SDSS sample selection	28
2.2 Combining SDSS spectra and GALEX photometry	28
2.2.1 Investigating the difference between total and fiber magnitudes in the optical	29
2.2.2 Proposing a solution	32

2.2.3	Testing our method in a PSF-independent aperture	35
2.2.4	Comparison with another method found in the literature	37
2.2.5	Spectrophotometric correction of SDSS spectra	37
2.3	Final Sample	39
3	A new version of STARLIGHT	45
3.1	The original STARLIGHT	46
3.1.1	Method	46
3.1.2	Physical properties measured by STARLIGHT	48
3.2	Including photometry in STARLIGHT	49
3.2.1	Calculating magnitudes from model spectra	49
3.2.2	Combining photometric and spectroscopic figures of merit	51
3.2.3	Range fitting	52
3.3	Using STARLIGHT for simultaneous spectroscopic and photometric analysis	53
3.3.1	Basic example	55
3.3.2	An example of UV-NIR synthesis	58
3.3.3	Testing different χ^2 scaling methods	59
3.3.4	Range-fitting and upper or lower limits	63
4	Spectral synthesis of GALEX and SDSS data	67
4.1	STARLIGHT setup	68
4.1.1	Pre-processing data	68
4.1.2	Stellar population base	68
4.1.3	Dust attenuation model	70
4.1.4	Technical parameters	72
4.2	Spectral fits and UV magnitudes	72
4.3	Star Formation Histories	75
4.3.1	The overall trend	76
4.3.2	Star-formation histories in color-magnitude space	77
4.4	Global properties	79
4.5	Effects on dust attenuation	81
5	Applications of the GALEX+SDSS Synthesis	85
5.1	Wavelength-dependent star formation histories	86
5.1.1	Spectral algebra: Converting $\vec{x}(\lambda_0)$ to $\vec{x}(\lambda)$	86
5.1.2	Wavelength-dependent SFHs in the CMD	87
5.2	Liny and lineless retired galaxies	89

5.2.1	Wavelength-dependent SFHs in the WHAN diagram	89
5.2.2	Differences between liny and lineless retired galaxies	91
5.3	Comparing results for different attenuation laws	92
5.4	The UV upturn in early-type galaxies	97
6	Final remarks	103
6.1	Conclusions	103
6.2	Reveries about future work	105
A	SQL query used for sample selection	107
B	Article: Simultaneous analysis of SDSS spectra and GALEX photometry with STARLIGHT: method and early results	109
C	Manual of the Version of STARLIGHT Presented in this Thesis	127
	Bibliography	151

List of Figures

1.1	Examples of galaxies with different morphological types.	4
1.2	UV-Optical color magnitude diagram.	8
1.3	Examples of stellar spectra from the MILES library. . .	12
1.4	Examples of stellar isochrones from Marigo et al. (2017).	13
1.5	Examples of IMFs.	14
1.6	Examples of spectral fitting with STARLIGHT.	16
1.7	Examples of extinction laws and the Calzetti attenuation law for starburst galaxies.	21
2.1	Comparison between SDSS and GALEX false color images.	29
2.2	Relations of $\Delta m'_{1,5}$ with galaxy properties.	30
2.3	Box plots showing the distribution of $\Delta m_{1,5}$ in SDSS bands for galaxies with different fiber coverage factors.	32
2.4	Relation between $\Delta m'_{1,5}$ and $\Delta m_{1,5}$ in other SDSS bands.	33
2.5	Examples of linear fits used to predict $\hat{\Delta} m_{1,5}^{NUV}$ and $\hat{\Delta} m_{1,5}^{FUV}$	34
2.6	Illustration of the correspondence between $\Delta m_{1,5}$ in distant galaxies and Δm_6 for nearby ones.	36
2.7	Comparison between predicted and measured values of Δm_6^{NUV} and Δm_6^{FUV} for a test sample of 6105 galaxies from the NASA-Sloan Atlas.	36
2.8	Illustration of the method of Battisti, Calzetti & Chary (2016).	38
2.9	Comparison of UV magnitudes calculated by Battisti, Calzetti & Chary (2016) with UV magnitudes calculated using the method of this paper for an aperture of radius $2.25''$	39
2.10	Illustration of the spectrophotometric recalibration of SDSS spectra.	40

2.11	UV-Optical color-magnitude diagram for the general sample shown as a filled contour plot with marginal distributions.	41
2.12	UV-Optical color-magnitude diagram for the low- z sample shown as a filled contour plot with marginal distributions.	42
3.1	Illustration of STARLIGHT's fitting method.	47
3.2	Likelihood functions for different values of the range parameter R_Y	54
3.3	Example of simultaneous fitting of SDSS spectra up to 5000Å and r and z photometric fluxes	58
3.4	Simultaneous fit of optical spectra and UV+NIR photometry of NGC 0855	60
3.5	Simultaneous fit of optical spectra and UV+NIR photometry of NGC 0855 using different χ^2 scaling methods.	61
3.6	Simultaneous fit of optical spectra and UV+NIR photometry of NGC 0855 using different χ^2 scaling methods and quadruplicated errors.	62
3.7	Simultaneous fit of optical spectra and UV+NIR photometry of NGC 0855 using range fitting and upper/lower limits.	64
4.1	Optical spectra of base elements used in the synthesis.	70
4.2	UV spectra of base elements used in the synthesis.	71
4.3	Examples of STARLIGHT fits for three galaxies in our sample.	73
4.4	Histograms comparing differences between observed NUV and FUV magnitudes and the values predicted from optical spectra and fitted from GALEX photometry.	74
4.5	Average star formation histories calculated with and without photometric constraints.	76
4.6	Average star-formation histories calculated with and without photometric UV constraints across the $NUV - r$ vs. M_r color-magnitude diagram.	78
4.7	Comparison between galaxy properties derived with and without UV data.	80
4.8	Relation between far-UV dust attenuation A_{FUV} UV power-law slope β for fits with and without UV data for three ranges of light-weighted mean stellar age.	82

5.1	Average star formation histories expressed as cumulative light fractions $x(> t, \lambda)$ in wavelengths corresponding to SDSS and GALEX bands.	88
5.2	Wavelength dependent SFHs for galaxy classes defined in the WHAN diagram.	90
5.3	Wavelength dependent SFHs for liny and lineless retired galaxies at different mass ranges.	92
5.4	Histograms of χ_{UV} for the CAL attenuation and CCM extinction laws.	94
5.5	Median $\Delta\chi_{UV}$ plotted against dust optical depth τ_V in different bins of redshift.	95
5.6	Median $\Delta\chi_{UV}$ plotted against dust optical depth τ_V in different bins of redshift in four ranges of inclination b/a	96
5.7	Histograms of χ_{FUV} of UV upturn galaxies for fits performed with our standard base and for an optimized base.	98
5.8	Star-formation histories of UV upturn galaxies obtained with and without UV constraints.	99
5.9	FUV averaged stellar ages and metallicities plotted against $FUV - NUV$ color.	100

Chapter 1

Introduction

“The story so far: In the beginning the Universe was created. This has made a lot of people very angry and been widely regarded as a bad move.”
— Douglas Adams, *The Restaurant at the End of the Universe*

The study of galaxies is a relatively new subject in astronomy. In 1920, a historical debate between Harlow Shapley and Heber Curtis (see Hetherington 1970) was held to discuss whether the then called spiral nebulae were objects inside our own Milky Way (MW) or of extragalactic origin. It was only after the works of Leavitt & Pickering (1912), Hubble (1925) and others that these nebulae came to be widely recognized as other galaxies, or island universes, following the terminology of Immanuel Kant. Shortly after, Hubble (1926) provided the first galaxy classification scheme, dividing them in terms of morphology into ellipticals, lenticulars (which together are called early-type), barred or unbarred spirals (late-type) and irregulars¹.

In the almost 100 years that followed, extragalactic astrophysics (the study of galaxies other than our own) has grown into a vast body of knowledge. We now understand galaxies as collections of stars, gas and dust that are held together by the gravitational potential of a dark matter halo, each of these components with a science of its own. In this chapter, we will provide a broad introduction to extragalactic astrophysics in general (section 1.1) and then proceed to subjects more closely related to the present work (sections 1.2 and 1.3).

¹In Hubble’s 1936 book “The Realm of Nebulae” (Hubble, 1936), this classification was organized in a diagram now known as the Hubble tuning fork.

1.1 Galaxies

1.1.1 Galaxy constituents and their signatures

As mention above, the four building blocks of galaxies are stars, gas, dust and dark matter. The first three, which together are called "baryonic components", leave distinct spectral signatures that can be traced either with actual spectra or broadband measurements provided by photometry. The measurement of galaxy luminosity against wavelength obtained with either photometry, spectra or a combination of the two is called *spectral energy distribution* (SED). Stars leave their footprints in the spectral continuum and absorption lines. In general, young stars emit strongly in the ultraviolet (UV), while older ones are more relevant at the near-infrared (NIR). However, stellar emission can be quite diverse. Interacting binary stars, for instance, can produce photons as energetic as X-rays. Other extreme stellar objects such as planetary nebulae or horizontal branch stars also produce UV emission and high-energy photons that ionize the surrounding gas. Gas in molecular form is detected from its emission in radio wavelengths, while ionized gas produces emission lines that superpose the stellar continuum. Dust grains absorb and scatter photons, specially at short wavelengths. Radiation absorbed by dust is then re-emitted in the far infrared (FIR), where dust accounts for most of the emission.

In the case of dark matter, we have to rely on indirect measurements that trace the gravitational effect it has on baryons. One of the first scientists to recognize these effects was Fritz Zwicky (Zwicky, 1933), who found a discrepancy between the gravitational mass of galaxy clusters (obtained from the virial theorem) and the mass accounted for by visible matter². Latter studies by Vera Rubin (Rubin & Ford, 1970) and others also found evidence for dark matter in the rotation curves of spiral galaxies: rotation velocities at the edge of these galaxies suggest that they contain more mass than what the baryons can account for. Dark matter can also be measured by the gravitational lensing effect that galaxy clusters have on background galaxies, a technique that has been widely used in recent years (e.g Montes & Trujillo, 2019).

In regions of active star-formation, young stars are embedded in the clouds of gas and dust from which they are formed. Hence,

²We now know that part of the mass of clusters that is unaccounted for by galaxies is due to a hot intra-cluster gas detected in X-rays.

star-formation is detectable from the radio emission of the gas, UV emission from young stars, optical emission lines generated by the ionization of gas by young stars, and dust-reprocessed radiation emitted in the FIR. An updated overview of star-formation indicators can be found in Brown et al. (2017), a complete review on the subject is given by Kennicutt & Evans (2012). Star-formation regions are present at least to a small extent in most galaxies in the universe.

Massive galaxies host supermassive black holes at their centers. When material is being accreted onto these black holes, the central region of their host galaxy is called an active galactic nucleus (AGN). Recent reviews on the topic are given by Heckman & Best (2014) and Netzer (2015). AGN emit radiation across a wide range of wavelengths and produce strong emission lines in the optical, which sometimes exhibit a broad component due to the velocity dispersion of ionized material near the AGN. The region defined as AGN is restricted to the scale of a few parsecs, but these objects can lead to effects in much larger scales (e.g Silk & Rees, 1998). In the local universe, $\sim 1\%$ of galaxies are AGN hosts, although these objects were far more numerous in the past.

Some galaxies also exhibit low ionization nuclear emission-line regions (LINERs, Heckman 1980) that can be produced by weak AGN, hot low-mass evolved stars (HOLMES, Stasińska et al. 2008) or shocks.

1.1.2 Galaxy Morphology

As mentioned before, Hubble (1926) classified galaxies in four morphological types: Spiral, elliptical, lenticular and irregular. Examples of galaxies of different morphological types are shown in Figure 1.1. Although not physically motivated, this morphological classification scheme is a useful tool to study galaxy properties. Differences observed in galaxy morphology reflect differences in other properties and in the underlying physics that is relevant to describe these objects. In this section, we will review some of the key aspects of galaxies with different morphologies.

The stars in spiral galaxies are distributed over four components: bulges, disks and bars and halos. Bulges are mostly formed of old metal-poor stars, which give them a red color. The dynamical support of bulges relies strongly on velocity dispersion, although a relevant level of rotation is also observed (Kormendy & Illingworth, 1982). Disks in these galaxies are formed of spiral arms populated

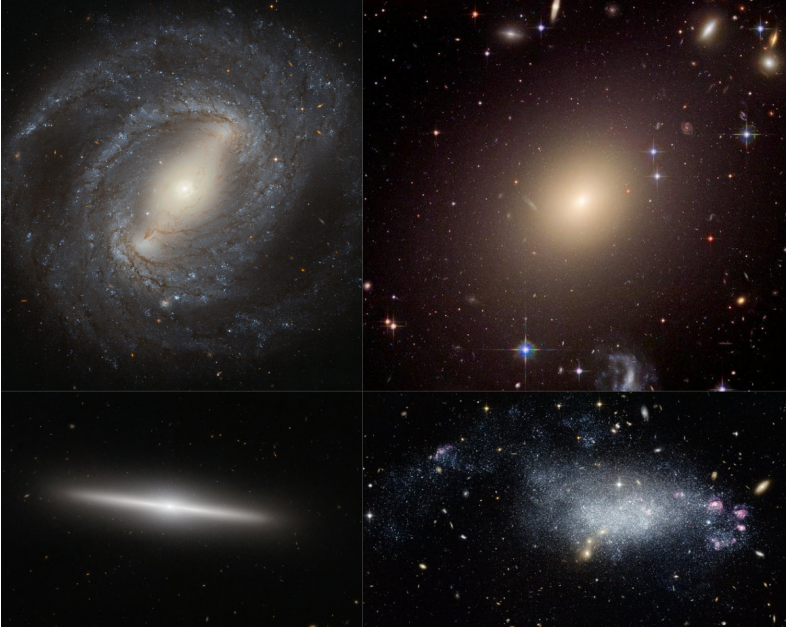


FIGURE 1.1: Examples of galaxies with different morphological types. At the top left is the spiral galaxy NGC 4394, the elliptical galaxy ESO 325-G004 at the center of the Abell S0740 cluster is shown in the top right, the lenticular galaxy IC 335 is shown in the bottom left and the irregular dwarf galaxy DDO 68 is shown in the bottom right. Images were obtained from the Hubble Space Telescope website <https://www.spacetelescope.org/images/>.

by young stars and conspicuous star-formation regions, they also harbor most of the gas and dust found in this type of galaxy. Bars are detected $\sim 50\%$ of spiral galaxies and have stellar populations similar to the ones in the disk. Halos are the home of a sparse population of old metal poor stars, some of which reside in globular star-clusters.

Elliptical galaxies appear more homogeneous in terms of color and stellar populations. These systems are formed of old, metal rich stars and exhibit little or no sign of ongoing star-formation. These galaxies are largely supported by velocity dispersion, but also exhibit

a rotational component (Bertola & Capaccioli, 1975; Illingworth, 1977; Binney, 1978). Elliptical galaxies can be classified into fast or slow rotators (Emsellem et al., 2007) according to the strength of their rotational component, a classification that is linked to different formation processes (Cappellari et al., 2011; Penoyre et al., 2017).

Differences in physical processes lead spiral and elliptical galaxies to follow different scaling relations. A fundamental relation for spirals is the Tully-Fisher relation (Tully & Fisher, 1977), that relates the rotation velocity at the edge of the disk of a spiral galaxy with its total luminosity. This relation is widely used as a distance indicator, as it allows the measurement of a distance-dependent quantity (luminosity) from a distance-independent one (rotational velocity). Its interesting to note that the Tully-Fisher relation connects galaxy rotation curves, which are determined mostly by dark matter, to luminosity, which reflects the stellar component of the galaxy. Another important relation for spirals is the Kennicutt-Schmidt law (Kennicutt, 1989; Kennicutt, 1998; Schmidt, 1959), that relates the molecular hydrogen gas surface density to the specific star-formation rate by a power-law of index ~ 1.4 . This law has been shown to be universal for a wide range of scales, from molecular clouds in the MW to entire galaxies (Krumholz, Dekel & McKee, 2012). The main scaling relations relevant for elliptical galaxies are the fundamental plane (Djorgovski & Davis, 1987), a three-dimensional relation between radius, velocity dispersion and mean surface brightness, and the Faber-Jackson relation (Faber & Jackson, 1976) between luminosity and velocity dispersion.

Another important distinction between spiral and elliptical galaxies is in their surface brightness profiles. Elliptical galaxies follow a Sérsic profile (Sérsic, 1963), characterized by a free parameter n . For the specific case of $n = 4$ the Sérsic profile is reduced to a de Vaucouleurs profile (de Vaucouleurs, 1948). Spiral galaxies follow a two-component model, with an exponentially declining component for the disk and a Sérsic profile for the bulge.

Lenticular galaxies are intermediate between spirals and ellipticals. These are red galaxies with old stellar populations and little or no ongoing star-formation. Lenticular galaxies are formed of bulges and disks, although their disks do not contain spiral arms.

Hubble's classification also includes irregular galaxies, which show neither spiral nor elliptical shapes. These systems are usually either dwarf galaxies or spiral and ellipticals that had their shapes distorted by interactions with other galaxies.

1.1.3 A touch of cosmology

The work of Slipher (1915) was the first study to detect that the spectral lines of spiral galaxies (then called "spiral nebulae") are systematically shifted to longer wavelengths, an effect now known as *redshift* and quantified as

$$z = \frac{\lambda_{\text{obs}} - \lambda_{\text{int}}}{\lambda_{\text{int}}}, \quad (1.1)$$

where λ_{obs} and λ_{int} are the observed and intrinsic line wavelengths. Slipher (1915) used this measurement to determine the recession velocities of the "nebulae", finding that most of them were moving away from us at large speeds. About a decade later, when the extragalactic nature of these nebulae was already established, Lemaître (1927) and Hubble (1929) used redshift data in combination with distance measurements from Hubble (1926) (obtained with the method of Leavitt & Pickering 1912) and found that the recession velocity of extragalactic nebulae correlated with their distance to us, showing that our universe is expanding.

Redshift serves a measurement of the relative expansion of the universe and is commonly used as an indicator of both distance and lookback time, i.e how long ago the detected photons were emitted. Different redshift ranges correspond to different epochs of the history of universe. This work is mainly focused in galaxies in the local universe, which are close enough so that their z corresponds to timescales shorter than the ones involved in galaxy evolution. The exact limits of the local universe are arbitrary, but a good reference point is $z < 0.1$, which gives a timescale of slightly over a billion years. Its interesting to note that the distance to an object at $z = 0.1$ assuming standard cosmological parameters is slightly larger than 1.286 billion light years, as the universe's expansion rate is faster than c .

In more recent years, large surveys measuring the redshift of galaxies were used to map the large scale structure of the universe (e.g Peacock et al., 2001). In parallel, simulations have been developed to reproduce and interpret these observations. Cosmological simulations assuming cold dark matter models including dark energy (Λ CDM) have been remarkably successful in reproducing the evolution of the large scale structure and its evolution over cosmic time (Springel et al., 2005). The current consensus is that structure formation is driven mainly by dark matter, having grown from small

initial density perturbations observed in the Cosmic Microwave Background (CMB). The gravitational potential of dark matter drives the clustering of baryons and in turn the formation of galaxies (Vogelsberger et al., 2014; Lacey et al., 2016).

1.1.4 Galaxy evolution

There is a clear bimodality in the population of galaxies in the local universe. We have already discussed the differences between spiral and elliptical galaxies, but morphology is only one of the aspects on which two distinct galaxy populations can be identified. Bimodal distributions are found in properties such as color, stellar mass, luminosity, star-formation rate and line emission. Studies of galaxy formation and evolution aim to explain the physical processes that shaped this bimodality.

An important tool to study the bimodality is the galaxy color-magnitude diagram (CMD, Baldry et al., 2004; Wyder et al., 2007), which divide galaxies in three classes: (i) The blue cloud, a sparse region in color-magnitude space populated by blue, actively star-forming, mostly spiral galaxies; (ii) the red sequence, a narrower region occupied by red, quiescent, elliptical galaxies and (iii) the green valley, an intermediate and less populated region between the blue cloud and the red sequence, the exact boundaries of the classes depend on the colors being used. It is understood that galaxies evolve from the blue cloud to the red sequence through the green valley after the quenching of their star-formation. There is also evidence that this process is relatively fast when compared to cosmological timescales, as evidenced by the small number of galaxies currently crossing the green valley. It can also be seen in Figure 1.2 that the brightest galaxies are in the red sequence, while the faintest are in the blue cloud³, this reflects the concept of downsizing: galaxies that are now more massive have assembled their stellar mass faster and early on, leading them to appear older (redder) at the present time. Another relevant diagram is the one connecting stellar mass and star-formation rate (SFR) (e.g Brinchmann et al., 2004), which can be broadly viewed as a physically driven version of the CMD. In this diagram, star-forming galaxies form a tight correlation called the star-formation main sequence (or star-formation sequence).

³This translates into an even larger difference in stellar mass, since the old stars that account for most of the emission in red sequence galaxies have mass to light ratios much larger than the ones from the young stars most common in the blue cloud.

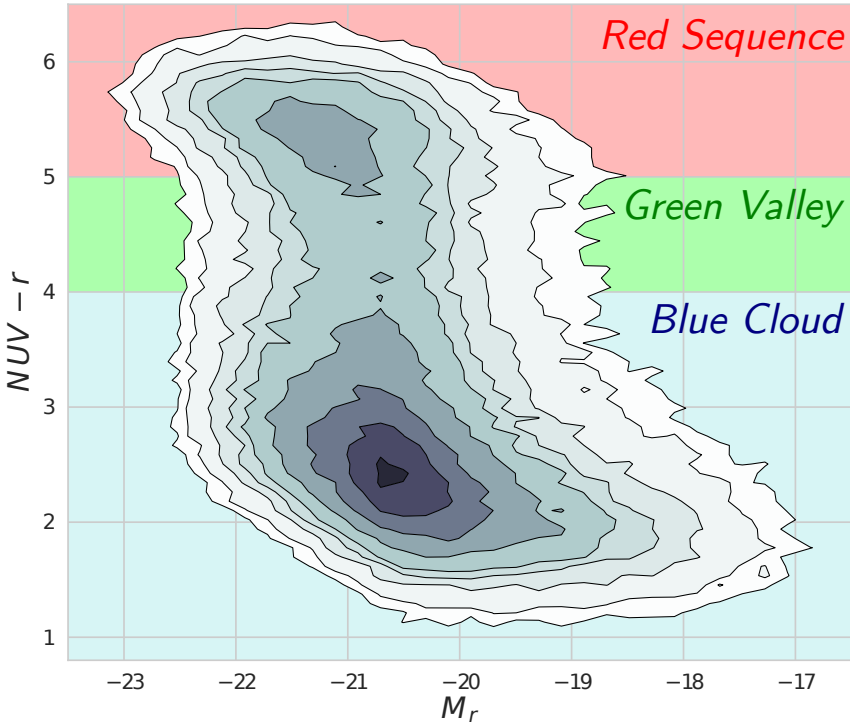


FIGURE 1.2: UV-Optical color magnitude diagram for a sample of 334997 local galaxies ($z < 0.1$). For this redshift range, we adopt the definitions of blue cloud ($NUV - r < 4$), green valley ($4 < NUV - r < 5$) and red sequence ($NUV - r > 5$) as indicated in the figure.

A color bimodality can be identified in color-color diagrams up to $z \sim 2.5$ (Williams et al., 2009), although the present structures of the color-magnitude diagram are only clearly visible since $z \sim 1.25$ (Cirasuolo et al., 2007). There is evidence that the red-sequence has doubled in mass since $z \sim 1.0$ (Bell et al., 2004). Complementary, Gonçalves et al. (2012) show that the mass flux density entering the red-sequence is larger at $z \sim 0.8$ than what was previously obtained by Martin et al. (2007) at $z \sim 0.2$, indicating that galaxy evolution was a more rapid process in the past. Multiple studies at a wide range of redshifts have found that the quenching of star-formation can be

triggered by a variety of processes that act on different timescales (Peng et al., 2010; Peng, Maiolino & Cochrane, 2015; Wild et al., 2016; Trussler et al., 2018; Wu et al., 2018; Rowlands et al., 2018).

Galaxy evolution is also known to depend on environment, quantified by the local galaxy density. In a study of 55 galaxy clusters, Dressler (1980) found an increase of elliptical and lenticular galaxies towards denser environments, with a corresponding decrease in the fraction of spirals. Using a large data-set from the Sloan Digital Sky Survey, Mateus et al. (2007) clearly shows that denser environments harbor more massive galaxies with older stellar content, evidencing that their star-formation was boosted at high redshifts. Effects related to environment such as ram pressure stripping, harassment and strangulation (see Trussler et al. 2018 and references therein) also contribute to the quenching of star-formation (e.g Peng et al. 2010).

Galaxy mergers also play a major role as drivers of galaxy evolution. Major mergers, when the galaxies involved have similar masses, can dissipate angular momentum and transform a pair of disk dominated galaxies into an elliptical (Toomre & Toomre, 1972; Negroponte & White, 1983), although it has recently been shown that the remnants of gas-rich major mergers can still be disk dominated (Hopkins et al., 2009). Minor mergers, when one of the galaxies is significantly more massive than the other, are less dramatic but far more common. These events are considered as important as major mergers for the mass assembly of elliptical galaxies, and can also account for some of the discrepancy between the sizes of elliptical galaxies at low and high redshift (Bluck et al., 2012). It has also been shown that mergers are efficient in cooling gas by dynamical friction, which in turn ignites star-formation activity (Negroponte & White, 1983; Barnes & Hernquist, 1991). Studies of the merger history of the universe (Conselice et al., 2003; Jogee et al., 2008; Lotz et al., 2008; Lotz et al., 2011) have shown that these events were more common in the past, reaching their peak at $z \sim 2.0$, around the same epoch of the peak of the cosmic star-formation history (see review by Madau & Dickinson 2014).

1.2 Spectral synthesis of galaxies

One of the most popular techniques to map galaxy observables into physical properties is *spectral synthesis*, which aims at extracting information encoded in galaxy spectra or broadband SEDs by matching

them to a combination of stellar population models. The technique is also referred to as *stellar population synthesis* (SPS), or simply *population synthesis*. Complete reviews on the topic are given in Walcher et al. (2011) and Conroy (2013), other works such as Cid Fernandes (2007) also provide insightful information.

Stellar population synthesis allows the measurement of a series of physical properties of galaxies, such as star-formation or chemical enrichment histories, stellar mass, chemical composition, velocity dispersion and age. The technique also provides a measurement of the stellar component of galaxy spectra, which can be subtracted from an observed spectrum to obtain residuals containing only information about the ionized gas. Dust attenuation is also modeled in the process, as it is key to obtaining the right stellar population estimates. Hence, one could say that spectral synthesis is a way of decoupling the three baryonic components of galaxies: stars, gas and dust.

All in all, spectral synthesis works as a reverse engineering of galaxy evolution: It seeks to understand the formation histories of galaxies by breaking them into their constituent parts.

1.2.1 Stellar population models

While early forms of spectral synthesis can be found in works as early as Morgan (1956), Wood (1966) and Faber (1972), that aim to reproduce a set of observables by means of a linear combination of simpler systems such as star clusters or individual stars (see also Bica & Alloin 1987), population synthesis as we know today was pioneered by Tinsley (1968). What sets this study apart from previous work is that it models galaxy spectra by following the time evolution of entire stellar systems. In modern SPS methods, this feature is implemented through libraries of stellar population spectra, the main astrophysical ingredient for spectral synthesis.

Stellar populations are ensembles of stars originated from the same birth cloud, thus with uniform age and initial chemical composition. Stellar populations can be simple (Simple stellar population, SSP) when all stars are born at the same time, or composite (Composite stellar population, CSP), when star-formation happens over an extended period of time according to a given star-formation history (SFH). To calculate the spectra of simple stellar populations, one has to consider a library of stellar spectra, a initial mass function (IMF) and a set of isochrones, each of which is a function of metallicity.

The IMF determines which fraction of stars are born with a given mass, while isochrones determine how these stars evolve over time in the color-magnitude diagram according to a set of stellar evolution models. These ingredients are generally combined according to

$$F_{\lambda}^{\text{SSP}}(t, Z) = \int F_{\lambda}^{\star}(T_{\text{eff}}, \log g | t, Z) \phi(M) dM, \quad (1.2)$$

where M is the initial stellar mass, $\phi(M)$ is the initial mass function, $F_{\lambda}^{\star}(T_{\text{eff}}, \log g | t, Z)$ is the spectrum F_{λ}^{\star} of a star with stellar parameters T_{eff} and $\log g$ given age t and metallicity Z . $F_{\lambda}^{\text{SSP}}(t, Z)$ is the spectrum of a simple stellar population at a given time according to the specified IMF and stellar evolution prescription. Each one of these components has its own caveats and involves particular design choices.

Libraries of stellar spectra can be observational, such as STELIB (Le Borgne et al., 2003) and MILES (Sánchez-Blázquez et al., 2006), or theoretical, like the Granada library (Martins et al., 2005). Observational libraries are limited to the stars found in the solar neighborhood, and are therefore naturally biased. Theoretical libraries, on the other hand, are subject to uncertainties in models of stellar atmospheres. Examples of stellar spectra from the MILES library for stars of different surface gravity $\log g$ and effective temperature $\log T_{\text{eff}}$ (stellar parameters) are shown in Figure 1.3.

Stellar isochrones reflect our understanding of stellar evolution, a field that despite its well deserved recognition as cornerstone of modern astrophysics still carries its share of uncertainties. Among others, one could cite the thermally pulsating asymptotic giant branch (TP-AGB) phase, stellar winds and UV emission from old stellar populations as parts of stellar evolution that are still subject to debate in the community. Different isochrones, constructed with different stellar evolution models, will give distinct results with respect to each of these issues. At NIR wavelengths, for instance, there has been a large debate on how much TP-AGB stars typically contribute to the spectra of galaxies and globular clusters (Maraston, 2005; Maraston et al., 2006; Kriek et al., 2010; Zibetti et al., 2013), leading some authors to state that NIR information may do more harm than good to galaxy stellar mass estimates (Taylor et al., 2011). The rising consensus seems to be that there is a limited contribution from these stars at NIR wavelengths, although the debate is ongoing. Other issues such as the contribution of binaries and rotation to the ionizing and UV fluxes of stellar populations are also sources of uncertainties

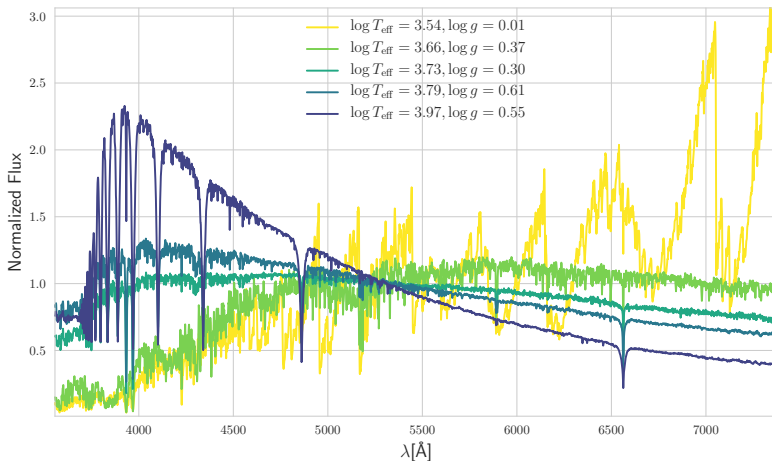


FIGURE 1.3: Examples of spectra from the MILES library for stars with different values of stellar parameters.

(Hernández-Pérez & Bruzual, 2013; Hernández-Pérez & Bruzual, 2014; Choi, Conroy & Byler, 2017) In Figure 1.4, we plot isochrones of the recent stellar evolution models by Marigo et al. (2017) for solar metallicity $Z_{\odot} = 0.0152$, isochrones are shown in both stellar parameter and color-magnitude spaces.

A topic that is subject to even more debate is the IMF, a long standing problem in astrophysics dating back to the work of Salpeter (1955) who first introduced the concept. Salpeter (1955) described the IMF as a power law, which was later shown to over-estimate the amount of low mass stars formed in birth clouds. Many alternative IMFs were introduced over the years, including multisegment power-laws (Kroupa, Tout & Gilmore, 1993; Kroupa, 2001) and log-normal formulations (Chabrier, 2003), although a full physical understanding of the IMF and its link to other observables in star-formation still hasn't been achieved. There is also evidence that the IMF is not be universal. For instance, Ferreras et al. (2013) found a correlation between the IMF slope and velocity dispersion in early-type galaxies, with an excess of low mass stars in the most massive galaxies. Cappellari et al. (2012) finds that the IMF in early-type galaxies varies as a function stellar mass-to-light ratio, leading to differences in stellar mass estimates of up to a factor of three. Other works such as La

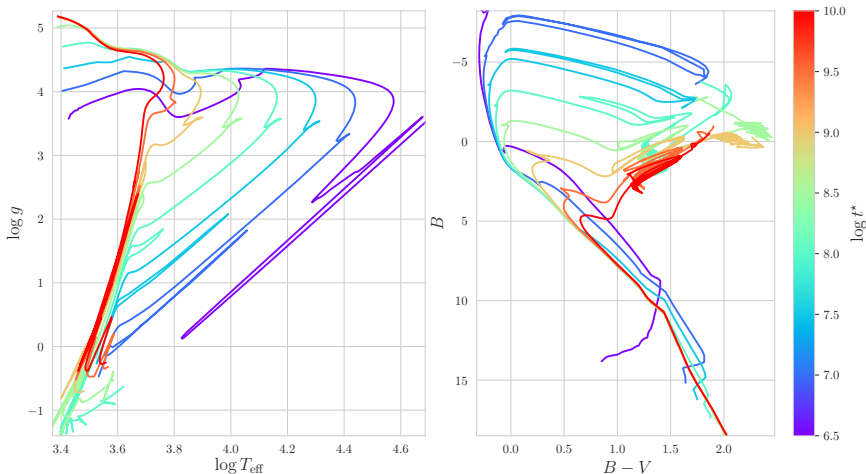


FIGURE 1.4: Examples of stellar isochrones from Marigo et al. (2017) for different ages and $Z_{\odot} = 0.0152$. Isochrones are shown in stellar parameter (left) and color-magnitude (right) spaces.

Barbera et al. (2013), Treu et al. (2010), Dokkum & Conroy (2012) and Conroy & Dokkum (2012) also find variations in the IMF. The IMFs from Salpeter (1955), Kroupa (2001) and Chabrier (2003) are plotted in Figure 1.5.

One of the most widely used set of stellar population models in the literature is the one from Bruzual & Charlot (2003) (BC03), based in the STELIB stellar library, with IMF from Chabrier (2003) or Salpeter (1955) and Padova 1994 (Alongi et al., 1993; Bressan et al., 1993) or Padova 2000 (Girardi et al., 2000) isochrones. The BC03 spectra cover the spectral range from 91\AA to $16\mu\text{m}$, with spectral resolution of 3\AA in the region from 3200\AA to 9500\AA and smaller resolution in other spectral regions. A base that has gained popularity in recent years is the one from Vazdekis et al. (2010) which is built from MILES stellar spectra and Padova 2000 isochrones. In recent years the Vazdekis et al. (2010) base has been expanded to include α -enhanced populations (Vazdekis et al., 2015) and a wider range of wavelengths, now covering the region between 1680\AA and $5\mu\text{m}$ (Vazdekis et al., 2016). Other set of models that deserves mentioning is the Granada+MILES base, used in Cid Fernandes et al. (2013) and Cid Fernandes et al. 2014. This base combines stellar spectra from

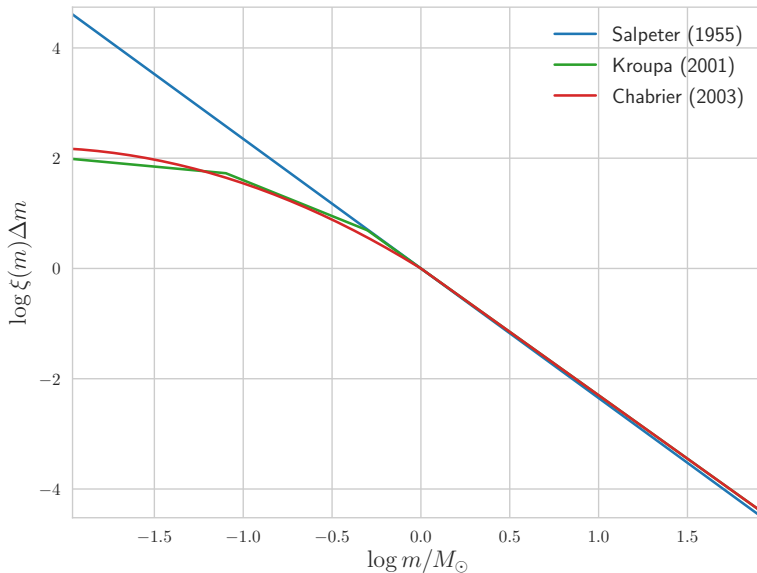


FIGURE 1.5: IMFs from Salpeter (1955) (blue), Kroupa (2001) (green) and Chabrier (2003) (red). The quantity $\xi(m)\Delta m$ represents the fraction of the total mass accounted for by stars with mass between m and $m + \Delta m$.

Vazdekis et al. 2010 with models for young stars from the Granada theoretical library.

An important recent development in the topic are the new SSP models from Charlot & Bruzual (in preparation, CB18 hereafter), which will be adopted in this work. The CB18 models represent considerable improvements upon BC03, the new models are based in PARSEC isochrones (Bressan et al., 2012) computed by Chen et al. (2015) for 16 metallicities from $Z = 0$ to $Z = 0.06$. These isochrones include state-of-the art models for massive stars in the Wolf-Rayet (WR) phase and are complemented by the work of Marigo et al. (2013) to follow the evolution of stars through the TP-AGB phase. CB18 models combine a wide range of stellar libraries, including MILES and IndoUS (Valdes et al., 2004) in the optical and NIR and a blend of theoretical libraries (Lanz & Hubeny, 2003a; Lanz & Hubeny, 2003b; Lanz & Hubeny, 2007; Leitherer et al., 2010; Martins et al.,

2005; Rodríguez-Merino et al., 2005; Rauch, 2003) and high resolution PoWR models (Sander, Hamann & Todt, 2012; Hamann, Gräfener & Liermann, 2006; Hainich et al., 2014; Hainich et al., 2015; Todt et al., 2015; Gräfener, Koesterke & Hamann, 2002; Hamann & Gräfener, 2003) in the UV. The effects of dust shells surrounding TP-AGB (Aringer et al., 2009; Rayner, Cushing & Vacca, 2009; Westera et al., 2002) is treated as in González-Lópezlira et al. (2010).

1.2.2 Spectral synthesis codes

Spectral synthesis methods serve a wide range of purposes and can follow many different implementations. This has led to the development of a variety of spectral synthesis codes.

Among the codes described in the literature are STECKMAP (*Stellar Content and Kinematics via Maximum A Posteriori likelihood*; Ocvirk et al. 2006), MOPED (*Multiple Optimized Parameter Estimation and Data compression*; Heavens, Jimenez & Lahav 2000; Panter, Heavens & Jimenez 2003) and its successor VESPA (*Versatile SPectral Analysis*; Tojeiro et al. 2007), ULySS (*University of Lyon Spectroscopic analysis Software*; Koleva et al. 2009), FIT3D (Sánchez et al., 2016), PPXF (*Penalized Pixel-Fitting method*; Cappellari 2017) and STARLIGHT (Cid Fernandes et al., 2005), on which this work is based upon. Each one of these codes implements SPS in its own way: STECKMAP fits a linear combination of simple stellar populations to the spectrum of a galaxy regularizing the process with penalization functions; VESPA uses an adaptive parametrization, that takes into the account the resolution of the star-formation history that can be inferred from the spectrum of a galaxy. ULySS fits spectra as a linear combination of non-linear components convolved with a polynomial continuum, PPXF uses a penalized maximum likelihood approach and stands out for its thorough implementation of stellar kinematics. Finally, the STARLIGHT spectral synthesis code fits spectra using a metropolis algorithm to find out the combination of base spectra that best fits the observed spectrum. Examples of spectral fitting with STARLIGHT are shown in Figure 1.6.

The codes presented above do what is called full spectral fitting, taking into account the full λ -by- λ information provided by galaxy spectra. A perhaps even larger family of codes is dedicated to measuring galaxy properties from their spectral energy distributions (SEDs), a low resolution measurement of spectral information provided by broadband photometry, these are called *SED fitting* or *SED*

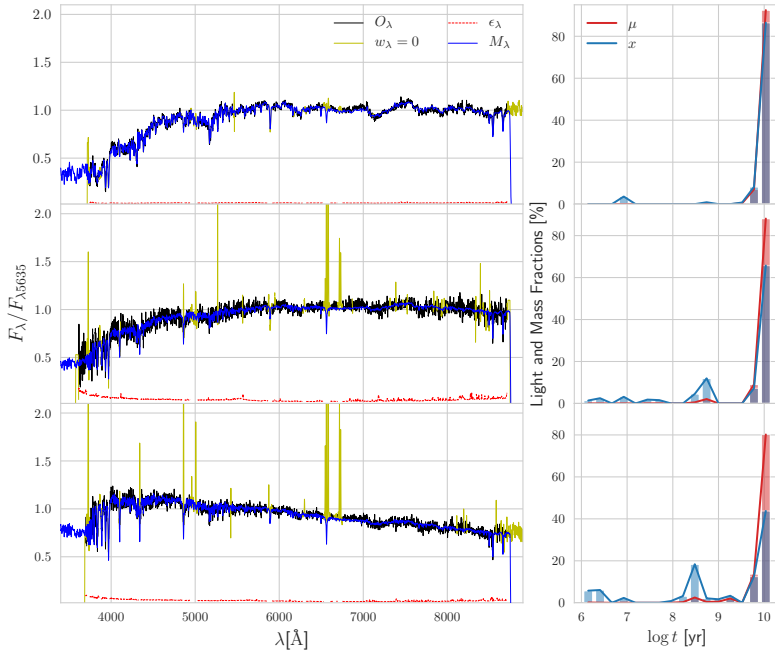


FIGURE 1.6: Examples of spectral fitting with STARLIGHT for three galaxies ordered from quiescent (top) to star-forming (bottom). Panels to the left show the spectral fits, panels on the right side show the recovered star-formation histories, portrayed by the contribution of different stellar populations to the stellar mass (μ) and optical luminosity (x) of each galaxy.

*synthesis codes*⁴. Among examples of SED fitting codes are MAGPHYS (da Cunha, Charlot & Elbaz, 2008), PROSPECTOR (Leja et al., 2017) and CIGALE (Noll et al., 2009; Boquien et al., 2018), that are able to fit photometric fluxes from the ultraviolet to the far infrared. Variations of this method are also used to calculate k-corrections and photometric redshifts (Blanton & Roweis, 2007; Brammer, van Dokkum & Coppi, 2008).

SPS methods can also be categorized into parametric (Chevallard

⁴A third category of spectral synthesis is based in spectral indices, although this technique is not explored in this work.

& Charlot, 2016; Carnall et al., 2018; Noll et al., 2009) and non parametric (or inverse) methods (Panter, Heavens & Jimenez, 2003; Cid Fernandes et al., 2005; Tojeiro et al., 2007; Ocvirk et al., 2006; Koleva et al., 2009; Cappellari, 2017), according to how the codes compute star-formation histories⁵. Parametric methods compare galaxy spectra or SEDs with a set of composite stellar population models built by combining simple stellar population spectra according to prescribed star-formation and chemical enrichment histories. In contrast, the latter retrieves stellar population information without any assumptions about the functional of the galaxy's SFH.

The main advantage of parametric models is that they require less detailed spectral information to constrain physical properties. This allows them to be applied to broadband photometry, while the application of non-parametric population synthesis is usually restricted to full spectral fitting. For the same reason, certain galaxy properties such as abundance patterns and the contribution of binary stars to the SED can currently only be investigated through parametric models. Nonparametric methods are also more exposed to degeneracies in pairs of properties such as mass and metallicity (Worthey et al., 1994) or age and dust attenuation, that may leave similar spectral signatures.

A particular asset of using broadband photometry to measure galaxy properties is that large photometric data-sets are publicly available across the entire electromagnetic spectrum, allowing for the analysis of panchromatic SEDs. Large databases of galaxy spectra, on the other hand, are only available in the optical region. Moreover, spectra usually don't cover the entire galaxy, leading to the so called "aperture effects" when comparing spectra to the galaxy's integrated emission.

In order to take advantage of the wealth of photometric data available today, as well as to achieve a more realistic modeling of galaxy properties, the STARLIGHT spectral synthesis code (Cid Fernandes et al., 2005) was updated to simultaneously account for spectral and photometric information. This combination enables the analysis of panchromatic data while maintaining the detailed spectral constraints necessary for a non-parametric fit. Extending the wavelength coverage also allow us to gather more information about the spectral footprints of different galaxy components, thus breaking degeneracies. This method was first applied by López Fernández

⁵PROSPECTOR is an example of a code that implements both parametric and non-parametric SFHs.

et al., 2016 to simultaneously fit integrated spectra from the CALIFA survey (Sánchez et al., 2012) and photometry from the Galaxy Evolution Explorer (GALEX, Martin et al. 2007). We note that while STARLIGHT is the first non-parametric code to include this feature, some parametric codes described in the literature also allow for the combination of spectra and photometry (e.g BEAGLE, Chevallard & Charlot 2016, and BAGPIPES, Carnall et al. 2018).

This update to the STARLIGHT code and its application to simultaneous analysis of optical spectra and UV photometry is the central point of this work. Other updates to STARLIGHT that are still under development are the inclusion of a Charlot & Fall (2000) model for dust attenuation and the fitting of far-infrared luminosities.

1.3 Ultraviolet emission from galaxies

The ultraviolet is a particularly interesting wavelength range, it encodes spectroscopic signatures of young stars, the most conspicuous features of dust attenuation curves, as well as the UV upturn in elliptical galaxies. In this section, we will review the main aspects that make ultraviolet information so important for stellar population synthesis.

1.3.1 Stellar populations

Providing better constraints on the estimates of young stellar populations was the original motivation that led to this thesis. STARLIGHT fits to optical spectra tend to produce SFHs that slightly overestimate the contribution of young stars, leading to a dramatic overshooting in the UV. This happens because young stellar populations are largely comprised of hot massive stars of spectral type O or early-type B, the so called OB stars. These systems contribute little to the optical but are dominant in the UV. This sensitivity of the UV to the emission of young stellar populations makes it key for galaxy evolution studies, as it allows for a clear separation of actively star-forming, quiescent and intermediate populations. To obtain a proper description of young stellar populations without making strong assumptions about the functional form of the SFH, one has to take UV data into account.

Despite being usually associated with young stars, the ultraviolet also encodes important information about the stellar populations of early-type galaxies. Some of these systems exhibit a phenomenon

called the *UV upturn*, a strong rise in emission towards the far-UV in galaxies with otherwise red spectra first identified by Code & Welch (1979) (see review by Yi 2008). This effect has been associated with stars at several locations of the HR diagram, the most likely candidates seem to be low mass, core helium burning stars in the horizontal branch (HB) and extreme horizontal branch (EHB) (e.g Yi, Demarque & Oemler, 1997) or post-AGB stars (central stars of planetary nebulae). Binary stars are also expected to play a role as progenitors of EHB stars (e.g Han, Podsiadlowski & Lynas-Gray, 2007; Hernández-Pérez & Bruzual, 2014). In the models used in this work, the source of the UV upturn is only the post-AGB stars. The UV upturn also has a known dependence on galaxy environment. Early works seemed to point to the conclusion that the effect was present in all bright elliptical. Further studies showed this not to be universal, although the effect remains more commonly detected in brightest cluster galaxies (e.g Yi et al., 2005; Yi et al., 2011).

The ultraviolet emission in early-type galaxies also provides clues on their formation and evolution (see Kaviraj et al. 2005 and references therein). The formation of early-types may follow a monolithic scenario (Larson, 1974), on which these galaxies form from a single burst of star-formation, or a hierarchical model where significant merging is required. Its important to note that these scenarios are not entirely mutually exclusive, as galaxies may result from an initially monolithic formation followed by subsequent merging events. The differences between these formation mechanisms are hard to constrain in the optical, but UV data allows the detection of small amounts of young stellar populations indicative of low levels of recent star-formation in these systems (e.g Yi et al., 2005; Jeong et al., 2009). Kaviraj et al. (2007) tested these formation scenarios, finding that the blue UV colors ($NUV - r < 5.5$) found in $\sim 30\%$ of their sample of early-type galaxies could not be explained solely by monolithic formation.

Other interesting issue regarding stellar populations in the ultraviolet is the effect of binary stars. Recent studies conducted by Hernández-Pérez & Bruzual (2013) and Eldridge & Stanway (2012) show that stellar population models that include the effect of binary stars are better in reproducing galaxy spectra in the UV.

1.3.2 Dust

Understanding the absorption and scattering of starlight by dust is key for calculating galaxy properties such as star-formation rate, stellar mass and mean stellar ages. Yet, many aspects of interstellar dust remain poorly understood, specially galaxies outside the local group.

The effects of dust in galaxy spectra are quantified by two basic quantities: (i) extinction, represents the scattering and absorption of photons out of the line of sight; (ii) attenuation is defined as the combination of absorption and scattering in and out of the line as well as the relative distribution of dust and stars, referred to as star-dust geometry. Both quantities are represented as the difference between intrinsic and obscured magnitudes, represented as A_λ when measured at a specific wavelength, or A_{band} when integrated over a photometric filter, say A_V for the V band. Extinction and attenuation curves (or laws), represented by $q(\lambda) = A_\lambda / A_V$, measure how these quantities vary with wavelength. Extinction curves are only measured for the MW and the Magellanic clouds, where individual stars can be resolved, thus allowing a comparison between stars of the same spectral type observed through different dust column densities. For galaxies with unresolved stellar populations, one can only measure attenuation curves, as the effects of the dust grains in these systems is heavily entangled with the star-dust geometry.

Extinction laws towards different Milky Way sight lines can be distinguished by the ratio of total to selective extinction $R_V \equiv A_V / (A_B - A_V)$ ⁶, which also represents the inverse slope of the curves. R_V varies roughly from 2 to 6 inside the MW, with an average value of 3.1 (Cardelli, Clayton & Mathis, 1989). The MW extinction curve shows a steep rise in A_λ towards the ultraviolet, attributed to a population of small dust grains that preferentially affect photons of short wavelengths. A more mysterious feature of the MW extinction curve is the UV bump, a peak in extinction around $\sim 2175 \pm 350$ Å first identified by Stecher (1965). It is not clear what dust grain population is associated with the bump, although models suggest polycyclic aromatic hydrocarbons (PAHs) or graphite-based compounds as the most likely suspects (see review by Draine 2003). The extinction law measured for the Large Magellanic Cloud (LMC) is quite similar to the one of the Milky Way, only with a slightly weaker

⁶The selective extinction ($A_B - A_V$) is also referred to as the color excess or reddening, and can be represented as $E(B - V)$.

bump. In the Small Magellanic Cloud (SMC), the extinction law is steeper and the bump is very weak or absent. The average extinction curves for the MW, LMC and the SMC bar taken from Gordon et al. (2003), as well as the Calzetti attenuation curve of starburst galaxies (which will be explained next) are plotted in Figure 1.7.

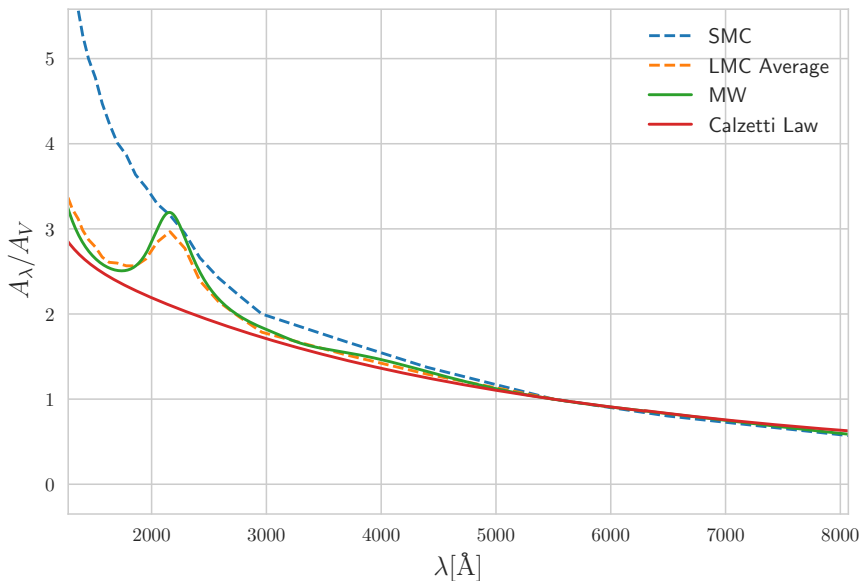


FIGURE 1.7: Examples of extinction laws and the Calzetti attenuation law for starburst galaxies.

A widely used method to measure attenuation laws is by comparing galaxy spectra to unattenuated templates. This method was developed by Kinney et al. (1994) and refined by Calzetti, Kinney & Storchi-Bergmann (1994) and Calzetti et al. (2000), who calculated templates by stacking the spectra of a sample of 39 starburst galaxies according to their nebular attenuation and derived an attenuation curve by dividing each template by the less reddened one. The derived attenuation curve, now known as the Calzetti law, shows no trace of a bump and has $R_V = 4.05$, which is shallower than the extinction curves of the MW and Magellanic clouds. The method of Calzetti, Kinney & Storchi-Bergmann (1994) and Calzetti et al. (2000) was recently extended by Battisti, Calzetti & Chary (2016) to a much larger sample of ~ 10000 local star-forming galaxies with SDSS

spectra and GALEX photometry, their results are compatible with the Calzetti curve for the majority of the sample. Battisti, Calzetti & Chary (2017) examined attenuation curves for galaxies viewed at different inclinations, finding a bump of 17%-26% the MW level for highly inclined galaxies (axial ratio $b/a < 0.42$). A similar method was used by Wild et al. (2011), who find curves with slopes that vary with galaxy inclination and stellar mass surface density.

Other popular way of measuring attenuation curves is by performing SED fitting with a flexible parametrization of the attenuation curve, a method pioneered by Noll et al. (2009) in the CIGALE code. There have been variations of this parametrization throughout the literature, but all of them include a power-law modification of the Calzetti curve to allow for different slopes and a Drude profile around 2175\AA to account for the bump. Kriek & Conroy (2013) used a similar method to a sample of galaxies at $z \sim 2$ to demonstrate a correlation between the strength of the UV bump and the slope of the attenuation curve. A different parametrization was developed by Conroy, Schiminovich & Blanton (2010), who used a version of the Cardelli, Clayton & Mathis (1989) law with a flexible bump strength, finding that the local population of galaxies is best described by a law of 30% of the MW bump strength.

Another aspect of dust attenuation that may affect the ultraviolet is the distribution of dust within galaxies: young stars, which are still embedded in their birth clouds, are subject to more attenuation than old stars. The proper modeling of this effect, however, requires extra constraints such as the $H\alpha/H\beta$ emission line ratio or FIR luminosity, which is why this analysis is not included in this work.

1.3.3 The UV power-law index

A vastly studied quantity in the ultraviolet spectra of galaxies is the UV power-law index, obtained by fitting a power law of shape

$$F_\lambda \propto \lambda^\beta \quad (1.3)$$

to the flux F_λ in the UV. This index was conceived by Calzetti, Kinney & Storchi-Bergmann (1994) as a probe for dust attenuation in starburst galaxies. A latter study by Meurer, Heckman & Calzetti (1999) (also for starburst galaxies) found a relation between β , far-UV attenuation A_{FUV} and the ratio of far-IR to far-UV luminosity (IRX). This relation has been widely used to determine A_{FUV} -corrected UV

luminosities, used as a star-formation rate indicator mainly at high redshift.

Subsequent studies of more diverse samples revealed significant scatter and a small offset in the Meurer, Heckman & Calzetti (1999) relation (e.g Kong et al., 2004; Seibert et al., 2005; Burgarella, Buat & Iglesias-Páramo, 2005) when extending it to normal star-forming galaxies. This scatter is attributed to a diversity of star-formation histories and attenuation laws (Boquien et al., 2012), but the extent of the contribution of each effect remains an open issue. Kong et al. (2004) investigates the problem in terms of the birth rate parameter (the ratio of present-to-past SFR) finding that star-formation history plays a role in driving the scatter and the offset in the relation. In a study of dust-poor star-forming galaxies, Grasha et al. (2013) also finds clear trends of β with age estimators. A recent study by Salim & Boquien (2019) argues that the scatter is entirely due to variations in the shape of attenuation curves.

1.4 This Work

From a technical perspective, the overall goal of this work is to perform the spectral synthesis of a combination of SDSS spectra and GALEX photometry. This depends on two specific tasks: (i) The development of a method to estimate GALEX photometry in an aperture compatible with SDSS spectroscopy, an issue that will be addressed in Chapter 2, and (ii) completing the development of a new version of STARLIGHT, which is presented in Chapter 3. Once these requirements are met, we perform the aforementioned combined analysis, which is presented in Chapter 4. In the same chapter, we discuss the effect of UV data on the estimates of physical properties of galaxies.

We then proceed to explore the applications of the GALEX+SDSS synthesis to astrophysical problems that cannot be tackled with optical-only analysis, such as the ones described in section 1.3. This analysis starts at the end of Chapter 4 and is completed in Chapter 5. The main conclusions of the work are summarized in Chapter 6.

This thesis is largely based upon the work published in Werle et al. (2019) (Appendix B). At some points, the text presented in the thesis will be very similar to the one in Werle et al. (2019), although most of the text was extended for a clearer and more complete presentation of the work.

Chapter 2

Data, sample and the curse of aperture matching

Up until the late 90's, large data-sets of astronomical data were scarce and rarely made publicly available. The landscape started to change in the beginning of the 2000's, when the Sloan Digital Sky Survey (SDSS; York et al. 2000; www.sdss.org) and other large data-sets such as the Two Micron All-Sky Survey (2MASS, Skrutskie et al. 2006) and the 2dF Galaxy Redshift Survey (2dFGRS; Folkes et al. 1999) brought vast amounts of standardized data to the astronomical community. Large surveys are now available across the whole electromagnetic spectrum, allowing panchromatic studies in a statistical scale, although combining data from different wavelength is often a non-trivial task.

In this chapter, we describe the main aspects of the data-sets used throughout the thesis, the main ones being the Sloan Digital Sky Survey and the Galaxy Evolution Explorer (GALEX; Martin et al. 2007). We also provide a description of the methodology developed to combine SDSS spectra and GALEX photometry.

2.1 Data sources and sample selection

In this section, we will describe the data-sets used throughout the thesis and how these were obtained.

2.1.1 The Sloan Digital Sky Survey

The Sloan Digital Sky Survey is comprised of a series of astronomical surveys obtained with a dedicated 2.5m telescope at the Apache Point Observatory, in the USA state of New Mexico. In this work, we will use data from the SDSS Legacy Survey, which combines a photometric and a spectroscopic survey.

SDSS photometry is measured in five bands: u , g , r , i and z ; with effective wavelengths $\lambda_{\text{eff}} = 3557, 4825, 6261, 7672$ and 9097 \AA , respectively. The photometry is nearly AB (Oke & Gunn, 1983), with only small zero-point corrections of 0.04 in the u band and 0.02 in the z band. A complete description of the SDSS photometric system is provided in Fukugita et al. (1996). SDSS measured photometry for objects with r band magnitudes brighter than 22, covering 7500 square degrees of the northern sky ($\sim 20\%$ of the whole sky).

For SDSS total galaxy magnitudes, we adopt the Petrosian system (Petrosian, 1976). These are measured in an aperture of $2R_p$, where R_p is the Petrosian radius given by

$$I(R_p) = \eta \left(\frac{\int_0^{R_p} I(r) 2\pi r dr}{\pi R_p^2} \right), \quad (2.1)$$

$I(r)$ is the galaxy's surface brightness profile, r is the distance to the center of the galaxy and η is a constant equal to 0.2 in SDSS. η aside, the Petrosian radius is the radius where the galaxy flux is equal to the mean flux within R_p .

SDSS spectra are collected through optical fibers of cross-section $1.5''$ in radius, which yields an aperture bias, as only a R_p -dependent portion of the observed galaxies is sampled by the fibers. The spectra cover the region between 3800 and 9200 in the rest-frame, with spectral resolution $R \equiv \lambda/\Delta\lambda \sim 1800$.

SDSS data is publicly available and distributed in data releases. The project is currently in its 13th data release, which includes a series of surveys with a variety of scientific purposes (see www.sdss.org/surveys). The data used in this work are compiled from the eight data release (DR8; Aihara et al. 2011). All of the publicly available data from SDSS can be accessed through SQL in skyserver.sdss.org/CasJobs.

2.1.2 The Galaxy Evolution Explorer

The Galaxy Evolution Explorer (GALEX; Martin et al. 2005) is a NASA space telescope launched in April 28, 2003. The telescope was dedicated to imaging in two UV bands: *NUV* (Near Ultraviolet; $\lambda_{\text{eff}} = 2267$) and *FUV* (Far Ultraviolet; $\lambda_{\text{eff}} = 1528$).

Before being deactivated in 2012, GALEX completed a series of surveys: The AIS (All Sky Imaging Survey), imaged the whole sky (41253 square degrees) up to a magnitude of 20.5; the MIS (Medium Imaging Survey) observed 1000 square degrees of the sky up to magnitude 23; the DIS (Deep Imaging Survey) observed 100 square degrees up to magnitude 25; additionally, the NGS (Nearby Galaxy Survey) observed nearby galaxies. GALEX was also available for observing proposals from the astronomical community, data from these observations are now available as the GIS (Guest Investigator Survey).

GALEX total galaxy magnitudes are obtained with the `MAG_AUTO` routine from Source Extractor (`SEXTRACTOR`; Bertin & Arnouts 1996). These magnitudes are measured in kron-like elliptical apertures which are slightly different from the ones in SDSS petrosian photometry. However, this difference is very small and will be neglected throughout this work.

GALEX data are available in the Mikulski Archive for Space Telescopes (MAST) and can be accessed through a SQL interface similar to the one of the SDSS in galex.stsci.edu/casjobs/. As in SDSS, GALEX data is also distributed in data releases; in this work, we will use data from the sixth data release, or GR6, which compiles data from all GALEX surveys, including the GIS.

2.1.3 Other data sources and value-added catalogs

GALEX and SDSS provide the bulk of the observational data required for our work. However, some of the data used in our analysis comes from value-added catalogs provided by third-party sources. For emission line measurements we use the catalog from Mateus et al. (2006), morphological classification is drawn from the Galaxy Zoo project (Lintott et al., 2008). To test our method to combine SDSS spectra and GALEX photometry, we use the astrometry-matched radial profiles available in the NASA-Sloan Atlas (NSA), which are based in the improved SDSS and GALEX photometry described in Blanton et al. (2011).

Absolute magnitudes are k-corrected to redshift 0 using the KCORRECT code (Blanton & Roweis, 2007) assuming standard Λ CDM cosmology with $\Omega_M = 0.3$, $\Omega_\Lambda = 0.7$ and $h = 0.7$. Albeit the core analysis of this work depends only on apparent magnitudes, these absolute magnitudes are used to build color-magnitude diagrams.

In chapter 3, we use data from the Brown et al. (2014) atlas of SEDs to provide an example of UV-NIR synthesis with STARLIGHT. This atlas includes aperture-matched data from several telescopes for 129 galaxies. Our use of the catalog, however, is restricted to the optical spectra (which are compiled from Moustakas & Robert C. Kennicutt 2006, Moustakas et al. 2010, Kennicutt 1992 and Gavazzi et al. 2004) along with UV and NIR photometry obtained from GALEX, SDSS (z band only) and 2MASS.

2.1.4 GALEX+SDSS sample selection

As aforementioned, the work presented in this thesis is based primarily on optical spectra from the eight data release of the SDSS (York et al., 2000; Aihara et al., 2011) and on UV photometry from GALEX GR6 (Martin et al., 2007).

Our initial sample contains 232372 galaxies from the SDSS main galaxy sample with photometry in both GALEX bands. The sample was selected from the GALEX CasJobs (<http://galex.stsci.edu/casjobs/>) by matching the UV object closest to each of the SDSS sources within a $0.3''$ search radius. We exclude duplicate spectra by setting `SciencePrimary=1` in SDSS's `SpecObjAll` table. The SQL query used for the sample selection is presented in Appendix A.

Some further cuts are applied in the sample to ensure consistency between SDSS spectra and GALEX photometry, these will be described in section 2.3.

2.2 Combining SDSS spectra and GALEX photometry

SDSS spectra are collected through optical fibers with a cross-section radius that corresponds to $1.5''$ of sky, which is smaller than the FWHM of the GALEX point spread function (PSF; $4.6''$ for *NUV* and $5.4''$ for *FUV*). The large PSF of the GALEX satellite, which is illustrated by Figure 2.1, comprises the main observational limitation to our analysis.

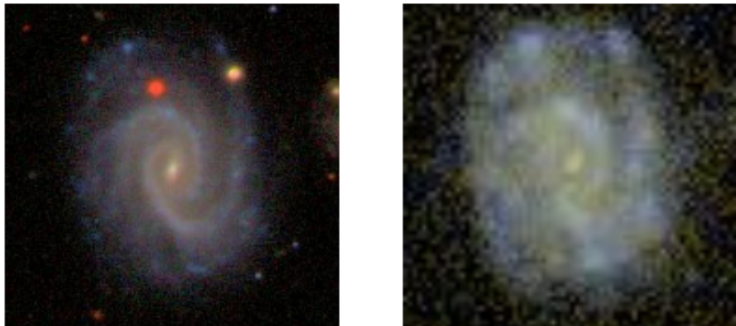


FIGURE 2.1: Comparison between SDSS (left) and GALEX (right) false color images.

In this section, we will present our strategy to circumvent this issue and estimate PSF-independent UV magnitudes consistent with SDSS spectra.

2.2.1 Investigating the difference between total and fiber magnitudes in the optical

Let's begin by studying the difference between total (m_{tot}) and fiber ($m_{1.5}$) magnitudes,

$$\Delta m_{1.5} \equiv m_{\text{tot}} - m_{1.5}, \quad (2.2)$$

in the SDSS $ugriz$ bands. This quantity reflects the ratio of the total flux to the flux in the spectroscopic fiber, being zero when the galaxy's total flux is contained in the $1.5''$ aperture and becoming more negative as the aperture flux decreases with respect to the total. $\Delta m_{1.5}$ can (and should) be thought of as a scale factor in logarithmic scale. If we are able to estimate $\Delta m_{1.5}$ in the UV we can use it to scale the total GALEX magnitudes down to the fiber radius, thus obtaining PSF-independent $1.5''$ magnitudes in the GALEX filters. This is precisely what we will do, but let's not get ahead of ourselves.

Right now, let's concentrate in understanding how $\Delta m_{1.5}$ in the optical varies with certain parameters. A good starting point is Figure 2.2, where the median $\Delta m_{1.5}$ in the r -band ($\Delta m_{1.5}^r$) is plotted against a series of galaxy properties. r_P and ρ_S indicate the Person and Spearman correlation coefficients, P -values are omitted from the Figure as they are close to zero for all correlations. Panels (a) and

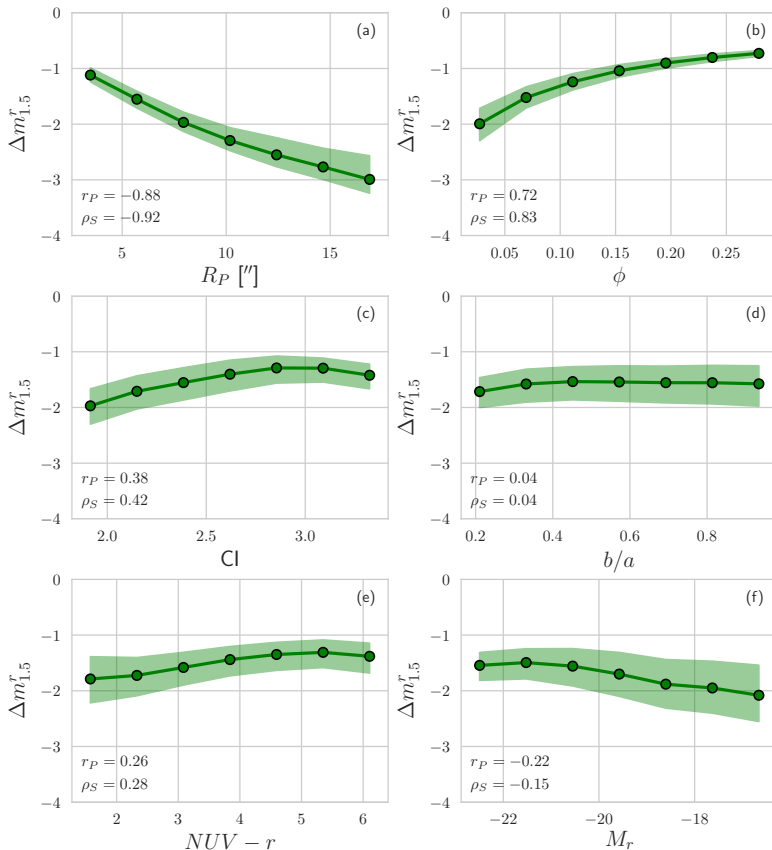


FIGURE 2.2: Median curves (green lines) showing relations of $\Delta m_{1.5}^r$ with galaxy properties. Green circles show the median value of $\Delta m_{1.5}^r$ in the center of each x bin. Variables in the x -axis are Petrosian radius (R_p) in panel(a), fiber coverage factor (ϕ) in panel (b), concentration index (CI) in panel (c), galaxy inclination (b/a) in panel (d), integrated $NUV - r$ color in panel (e) and r -band absolute magnitude in panel (f). r_P and ρ_S are the Person and Searman correlation coefficients.

(b) show the main variables that correlate with $\Delta m_{1.5}^r$: The Petrosian radius R_P , and the fraction of the area of the galaxy that is sampled

by the spectroscopic fiber, quantified by the fiber coverage factor

$$\phi = \left(\frac{R_f}{R_{90}} \right)^2, \quad (2.3)$$

where $R_f = 1.5''$ is the fiber radius and R_{90} is the radius containing 90% of the galaxy's Petrosian flux. Both of these correlations indicate the same thing: The size of the galaxy compared with the fiber aperture.

We also find a weak trend of $\Delta m_{1.5}$ with galaxy morphology. Which is shown in panel (c) of Figure 2.2, where $\Delta m_{1.5}$ is plotted against the concentration index, defined as the ratio between the 90% and the 50% light radii,

$$CI = \frac{R_{90}}{R_{50}}. \quad (2.4)$$

There is also no dependence in galaxy inclination (b/a), shown in panel (d). This is expected as b/a should neither affect the Petrosian nor the $1.5''$ photometry. Very weak trends are found in panels (e) and (d), that show integrated color and absolute magnitude, indicating that $\Delta m_{1.5}$ is not a strong function of galaxy type.

Complementing Figure 2.2, Figure 2.3 shows another important aspect of the problem: $\Delta m_{1.5}$ is larger in bluer filters, reflecting the difference in color between the central regions of galaxies (bulges) and their integrated light (bulges+disks). This trend generates a linear correlation between $\Delta m_{1.5}$ and the effective wavelengths of the filters, with a decreasing slope for larger coverage factors (lower panels in Figure 2.3), where the integrated and fiber colors become more similar. The Figure also shows that the distributions of $\Delta m_{1.5}$ are wider in the u -band, a statistical consequence of the larger observational errors at this band.

In Figure 2.4, we show the relations between $\Delta m_{1.5}^r$ and $\Delta m_{1.5}$ in other SDSS bands. These relations are almost linear and show little scatter, as evidenced by the correlation coefficients annotated in each panel. The tight correlation between $\Delta m_{1.5}$ on different SDSS filters indicates that the values of $\Delta m_{1.5}$ in one band can be used to estimate $\Delta m_{1.5}$ in other wavelengths. Moreover, it is interesting to note that the information contained in the relation of $\Delta m_{1.5}^r$ with R_P , ϕ and CI (Figure 2.2) is already included in the relations shown in Figure 2.4.

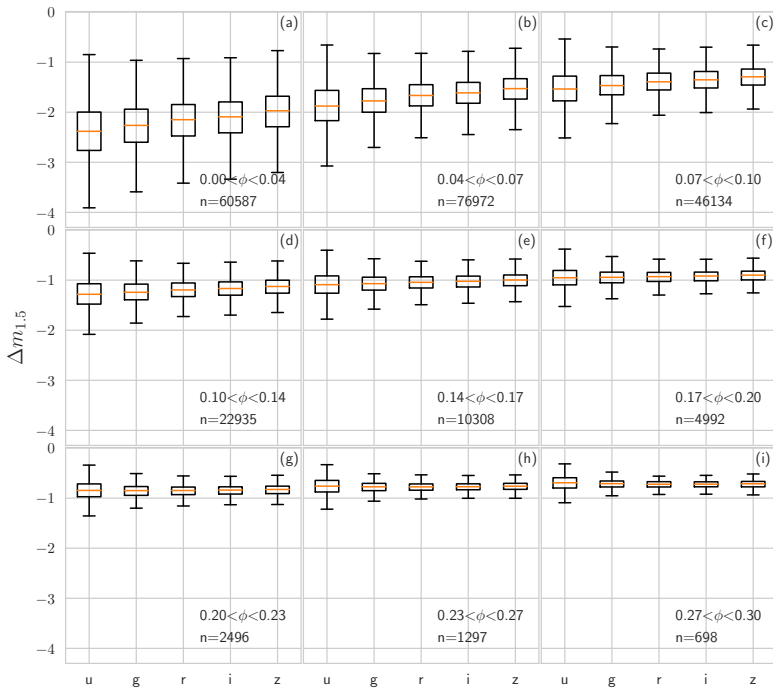


FIGURE 2.3: Box plots showing the distribution of $\Delta m_{1.5}$ in SDSS bands for galaxies with different fiber coverage factors. Boxes indicate the interquartile regions (IQR), medians are shown as orange lines and bars (or *whiskers*) extend from the quartiles to 1.5 times the width of the interquartile region.

2.2.2 Proposing a solution

Based in the information gathered in the previous section, we chose to estimate $\Delta m_{1.5}$ in the UV by exploring the relation between $\Delta m_{1.5}$ and the effective wavelengths of the filters shown by the box plots in Fig 2.3. The procedure is presented in Figure 2.5 for three example galaxies. We fit a straight line to the *ugriz* measurements in the $\Delta m_{1.5} \times \lambda$ plane and extrapolate it to the UV to obtain estimates of $\Delta m_{1.5}$ in the GALEX bands, $\hat{\Delta} m_{1.5}^{NUV}$ and $\hat{\Delta} m_{1.5}^{FUV}$, where the $\hat{\cdot}$ symbol was included to distinguish estimated and observed values. These

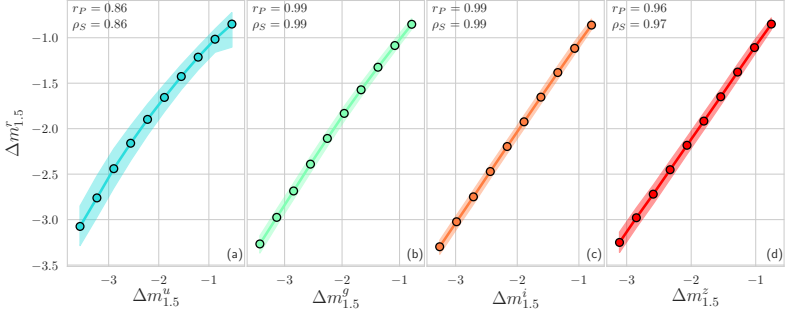


FIGURE 2.4: Relation between $\Delta m_{1.5}^r$ and $\Delta m_{1.5}$ in other SDSS bands. The medians in each bin are shown as circles, colored bands indicate the regions between 25% and 75% percentiles. Pearson and Spearman correlation coefficients are annotated in each panel.

lines were fitted using the BCES method (Akritas & Bershady, 1996), as implemented in python by Nemmen et al. (2012). In this context, the offset of the fitted line acts as a first order correction that is equal for all bands and accounts for the fraction of total light sampled by the spectroscopic fiber, while the slope accounts for the difference between central and integrated colors. Note that these corrections are estimated for each individual galaxy using its own *ugriz* data.

The UV magnitudes in the SDSS spectroscopic aperture will thus be estimated from

$$\begin{aligned} NUV_{1.5} &= NUV_{\text{tot}} - \hat{\Delta}m_{1.5}^{NUV} \\ FUV_{1.5} &= FUV_{\text{tot}} - \hat{\Delta}m_{1.5}^{FUV}. \end{aligned} \quad (2.5)$$

Uncertainties in $\hat{\Delta}m_{1.5}^{NUV}$ and $\hat{\Delta}m_{1.5}^{FUV}$ indicated as blue error bars in Figure 2.5 are derived from the $\pm 1\sigma$ prediction bands for the fitted lines. These are given by

$$\epsilon_{\hat{\Delta}m_{1.5}} = \hat{\Delta}m_{1.5} \pm t_{n-2} \sigma_{\Delta m_{1.5}} \sqrt{1 + \frac{1}{n} + \frac{(\hat{\lambda} - \bar{\lambda})^2}{(n-1)\sigma_{\Delta m_{1.5}}^2}}, \quad (2.6)$$

where n is the number of degrees of freedom and t_{n-2} is the value at

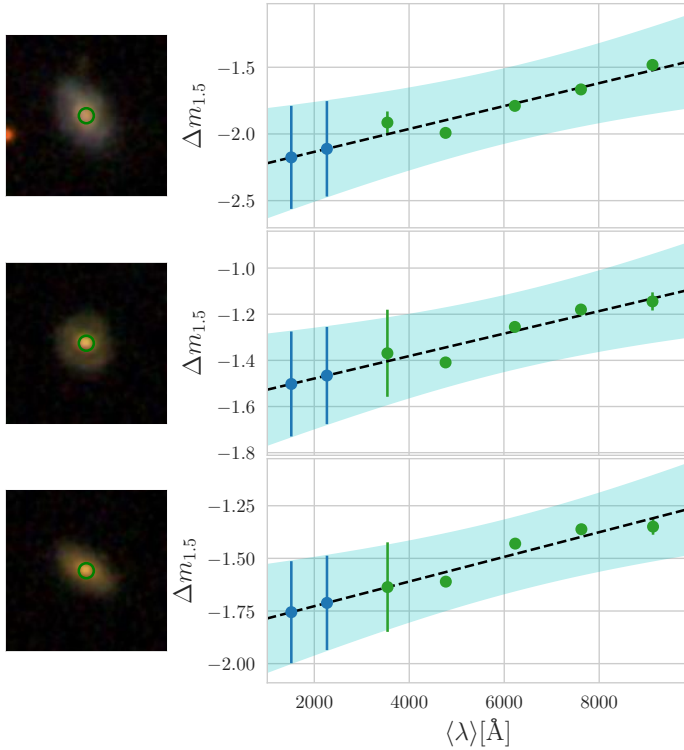


FIGURE 2.5: Examples of linear fits used to predict $\hat{\Delta}m_{1.5}^{NUV}$ and $\hat{\Delta}m_{1.5}^{FUV}$. Optical values of $\Delta m_{1.5}$ are plotted in green and the predicted values in blue. The best-fit linear relation is shown as a dashed line. The cyan band shows a $\pm 1\sigma$ prediction band, used to estimate the uncertainties in $\hat{\Delta}m_{1.5}^{NUV}$ and $\hat{\Delta}m_{1.5}^{FUV}$. The estimated error bars are plotted in blue. An image of the corresponding galaxy is shown to the left of each fit, with the region covered by the SDSS fiber indicated by a green circle.

1σ of the Student t distribution for $n - 2$ degrees of freedom. $\sigma_{\Delta m_{1.5}}$ is given by

$$\sigma_{\Delta m_{1.5}} = \sqrt{\frac{\sum_i (\Delta m_{1.5,i} - \widehat{\Delta m}_{1.5,i})^2}{n - 2}}, \quad (2.7)$$

σ_λ is calculated in the same way. These aperture matching uncertainties are added in quadrature to the errors in NUV_{tot} and FUV_{tot} to obtain the error in $NUV_{1.5}$ and $FUV_{1.5}$.

The median aperture corrections for the sample are -1.79 mag for NUV and -1.82 for FUV , while the median errors are 0.28 and 0.31 mag, respectively. We note, however, that since our method is completely unsupervised, it is expected to produce outliers, in particular for galaxies in close pairs or with odd morphological features. Indeed, in some cases the method returns unphysical values such as $\Delta m_{1.5} > 0$ (0.08% of the sample), as well as very high error estimates (larger than 1 mag in the FUV band for 0.07% of the sample). Ultimately, the reliability of our method depends on the linearity of the $\Delta m_{1.5} \times \langle \lambda \rangle$ relation. In cases where one or more bands deviate much from the linear trend the method is not reliable and will return high error estimates.

2.2.3 Testing our method in a PSF-independent aperture

In order to test the reliability of our method, we use the GALEX-SDSS astrometry-matched radial profiles available in the NASA-Sloan Atlas (NSA, Blanton et al., 2011) to calculate the differences between the total magnitudes and that in an aperture of $6''$ in radius (Δm_6), where the image degradation caused by the GALEX PSF can be neglected. The idea behind this test is that $\Delta m_{1.5}$ can be thought of as the log of the ratio between total flux and the flux in the fiber, which is a *relative* quantity. Therefore, by choosing a larger aperture we can use nearby galaxies (with large projected radii) to mimic the distribution of $\Delta m_{1.5}$ in the general sample, this equivalence is illustrated by Figure 2.6. With that in mind, we selected a test sample of 6105 galaxies with values of Δm_6 in the SDSS bands in the same range as the $\Delta m_{1.5}$ values for the general sample. Our method was then applied to estimate the values of Δm_6 for the test sample.

Results of this test are shown in the histograms of Figure 2.7, where we plot the distributions of $\widehat{\Delta m}_6^{NUV} - \Delta m_6^{NUV}$ and $\widehat{\Delta m}_6^{FUV} - \Delta m_6^{FUV}$. The distributions are centered near zero, with medians of 0.07 mag for NUV and -0.01 for FUV . However, both distributions

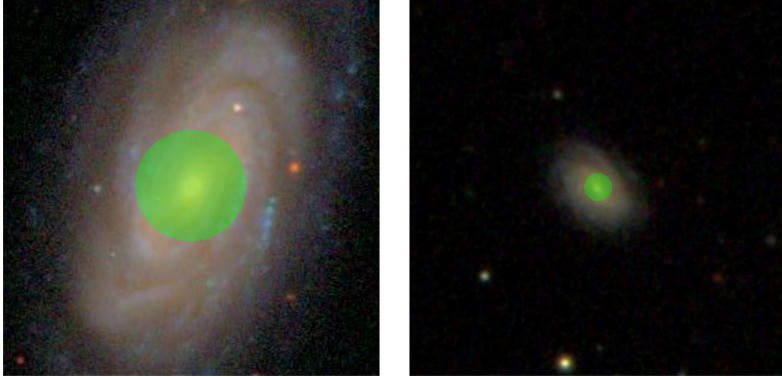


FIGURE 2.6: Illustration of the correspondence between $\Delta m_{1.5}$ in distant galaxies and Δm_6 for nearby ones. Regions in green indicate the regions with radius $1.5''$ and $6''$.

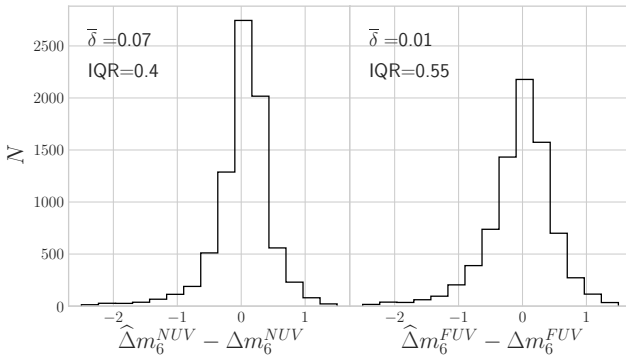


FIGURE 2.7: Comparison between predicted and measured values of Δm_6^{NUV} and Δm_6^{FUV} for a test sample of 6105 galaxies from the NASA-Sloan Atlas. Histograms show the differences between estimated and observed Δm_6 for *NUV* (left) and *FUV* (right) bands. Medians ($\bar{\delta}$) and interquartile regions (IQR) of the distributions are annotated in each panel.

are quite wide, with interquartile regions of 0.4 on *NUV* and 0.55 on *FUV*. These statistics confirm that our estimates are good for large samples, although results for individual sources may not be reliable.

Despite the wide distributions of $\widehat{\Delta m}_6^{NUV} - \Delta m_6^{NUV}$ and $\widehat{\Delta m}_6^{FUV} - \Delta m_6^{FUV}$, the predicted values are, on average, in very good agreement with the observed ones. This is sufficient for the purpose of this work, since our results will be averaged in relatively large samples.

2.2.4 Comparison with another method found in the literature

We also used the NSA to calculate Δm in an aperture of $2.25''$ in radius, which allows us to compare our aperture matching scheme to the one of Battisti, Calzetti & Chary (2016), that is calibrated in this aperture. This correction uses a convolution of the galaxy's Sérsic profile in the u band with the GALEX PSF to calculate scale factors that are applied to the GALEX $1.5''$ photometry, as illustrated in Figure 2.8. The premise of this method is that the u band Sérsic profile is a good tracer of the galaxy's radial profile in the GALEX bands. Indeed, the values of $\Delta m_{1.5}$ that we find in the UV are statistically similar to the ones in the u band, which agrees with this assumption.

The comparison between GALEX aperture magnitudes obtained with our method and the ones obtained by the method of Battisti, Calzetti & Chary (2016) is shown in Figure 2.9. Results from the two methods are linearly correlated, although the method described here produces systematically dimmer magnitudes. Over the whole sample, the median difference between the methods is 0.19 magnitudes on NUV and 0.18 on FUV , the interquartile regions (IQR) are of 0.35 magnitudes on NUV and 0.56 on FUV , with a larger scatter for dimmer sources, specially in the FUV band.

Considering that these two aperture matching schemes follow completely different routines and are even based on different data, the agreement between the predicted magnitudes is reassuring for both methods.

2.2.5 Spectrophotometric correction of SDSS spectra

From DR7 onward, SDSS spectra are calibrated to match the flux of a point source within one FWHM of the PSF, leading to fluxes for extended sources typically 25% smaller than their photometric counterparts. Due to this offset, calculating NUV and FUV fluxes compatible with fiber photometry does not directly imply compatibility with spectroscopic fluxes. We have thus rescaled the SDSS spectra to match the $1.5''$ photometry in the r band, as done in the

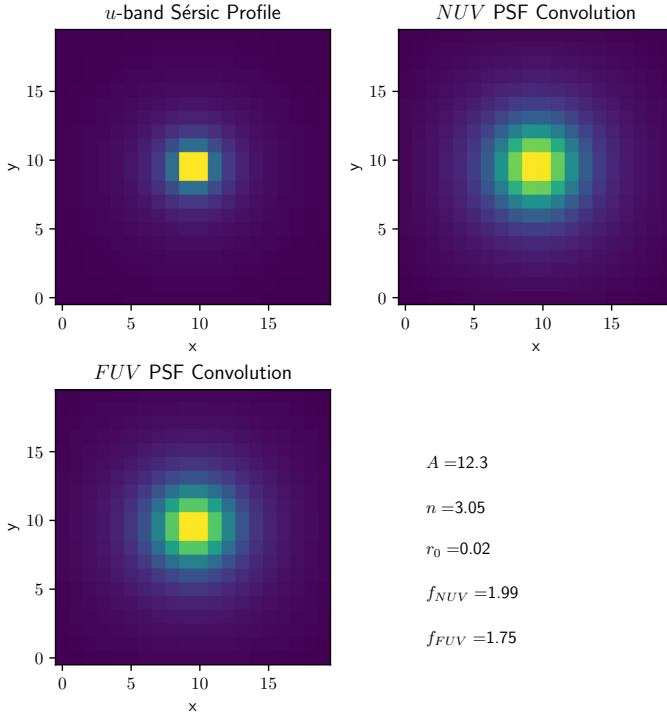


FIGURE 2.8: Illustration of the method of Battisti, Calzetti & Chary (2016). Upper left panel shows the *u* band Sérsic profile; upper right and lower left panels show the *u* band convolved with the *NUV* and *FUV* PSFs, respectively. Parameters of the Sérsic profile and *NUV* and *FUV* fluxes obtained with the method are annotated at the lower right part of the Figure.

MPA/JHU value added galaxy catalog (wwwmpa.mpa-garching.mpg.de/SDSS/DR7). Since the shape of the photometric SEDs is very similar to the shape of the spectra, this procedure ensures the compatibility of SDSS spectra with *ugriz* fiber photometry and, by extension, with the estimated $NUV_{1.5}$ and $FUV_{1.5}$ estimated fiber magnitudes.

This process is illustrated in Figure 2.10, where we show an SDSS spectrum before and after the spectrophotometric recalibration. Note

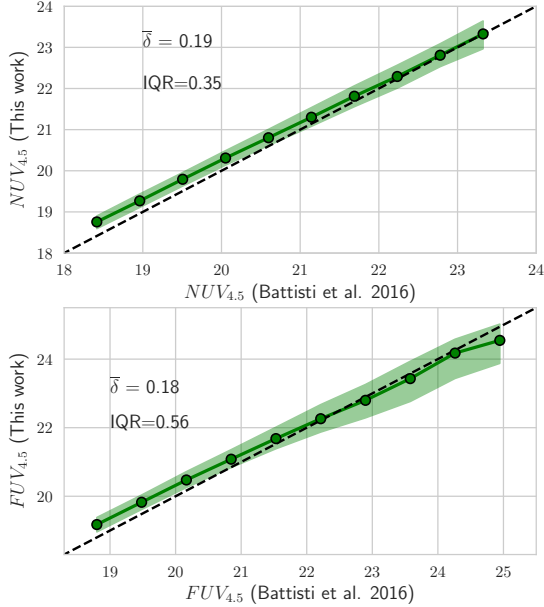


FIGURE 2.9: Comparison of UV magnitudes calculated by Battisti, Calzetti & Chary (2016) with UV magnitudes calculated using the method of this paper for an aperture of radius $2.25''$. Green lines show median curves with the region between 25 and 75% percentiles is shaded in green. Median $y - x$ ($\bar{\delta}$) values and interquartile regions (IQR) are annotated on each panel.

that, as mentioned above, matching the spectra to r -band photometry is sufficient to ensure compatibility with the other bands.

2.3 Final Sample

The selection of our general GALEX+SDSS sample was already presented in section 2.1.4. However, some additional quality control cuts were made before the data-set was used for scientific analysis.

To prevent outliers of the aperture matching procedure from affecting our scientific results, we remove from the sample galaxies with corrections larger than 0 or smaller than -4 magnitudes in one

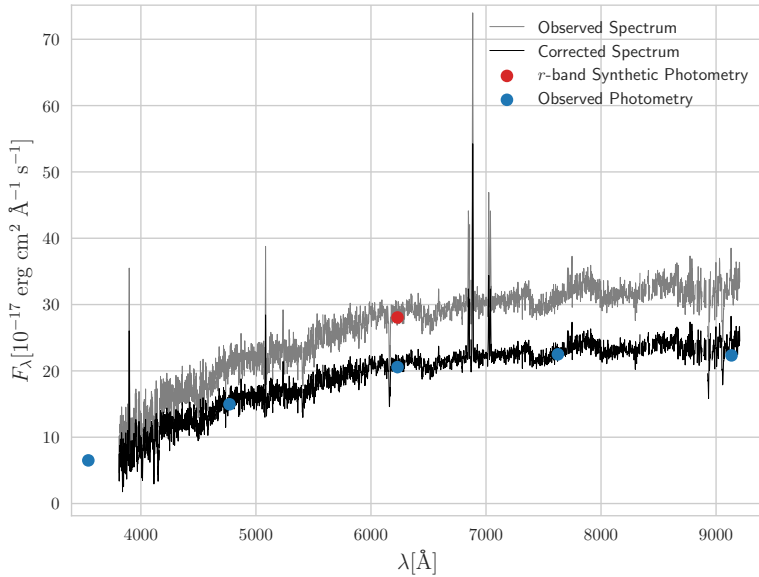


FIGURE 2.10: Illustration of the spectrophotometric recalibration of SDSS spectra. The original spectrum is shown in gray, with r band synthetic photometry marked in red. Blue points indicate $ugriz$ photometry. The corrected spectrum is plotted in black.

of the GALEX bands, discarding 3323 galaxies. For 162 galaxies, the aperture matching scheme produced $NUV - r < 0$ in the spectroscopic aperture, these galaxies were also discarded. Moreover, we discard 22 galaxies with failed k-corrections and 721 with odd spectra where all fluxes were equal to zero. In combination, all these cuts yield a general sample of 228175 galaxies (note that the cuts are not mutually exclusive).

For most of the analysis, we use a subsample of 137994 galaxies with $z < 0.1$, as this ensures that the wavelength ranges covered by the GALEX filters do not deviate largely from their rest-frame values; we will refer to this subsample as our low- z sample.

Note that our sample is neither complete nor representative of the local galaxy population. Our goal was to select all galaxies for which GALEX photometry and SDSS spectra are available, which introduces a bias towards UV-bright sources. This bias can be verified

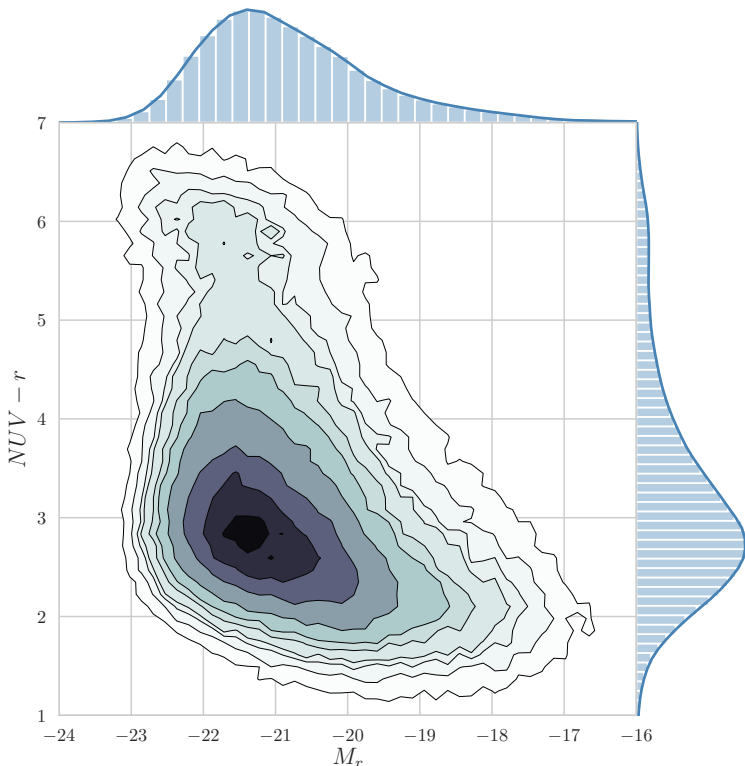


FIGURE 2.11: UV-Optical color-magnitude diagram for the general sample shown as a filled contour plot with marginal distributions. Lines plotted over the marginal histograms show a kernel density estimation.

in Figures 2.11 and 2.12, where we plot UV-Optical color-magnitude diagrams for our general and low- z samples. It is evident from the Figures, and specially from the marginal distributions of $NUV - r$, that our sample is depleted of red-sequence galaxies, as these are usually dimmer in the UV.

By comparing Figures 2.11 and 2.12 one can also notice that selecting galaxies with $z < 0.1$ preferentially discards galaxies at the bright end of the blue cloud. This happens due to the selection function of our data-sets, which determines the flux limit of sources that can be

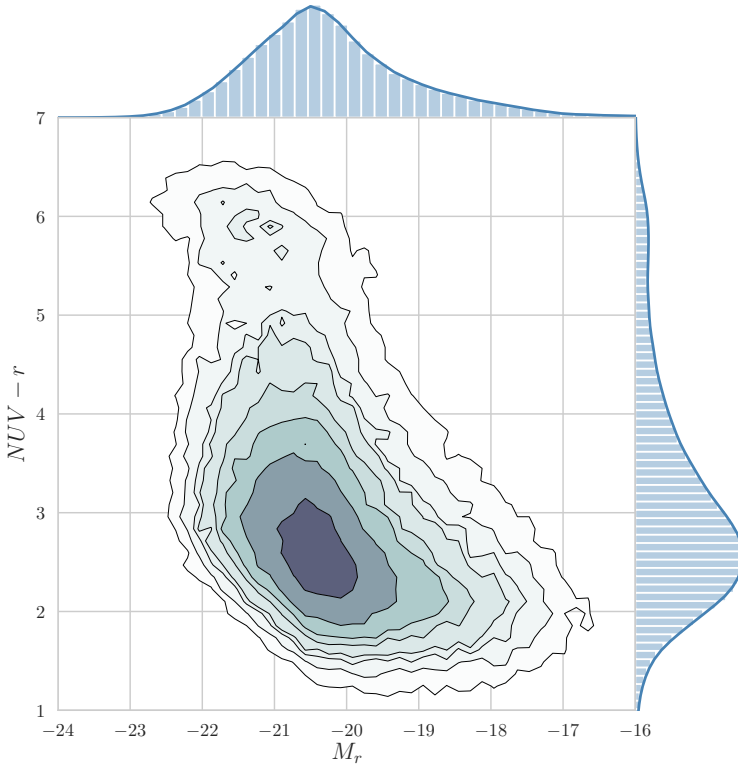


FIGURE 2.12: UV-Optical color-magnitude diagram for the low- z sample shown as a filled contour plot with marginal distributions. Lines plotted over the marginal histograms show a kernel density estimation.

detected at each redshift. For distant galaxies to be detected by both GALEX and SDSS, they have to be bright in both the optical and in the UV, introducing a bias towards massive spirals that is suppressed when selecting only $z < 0.1$ sources.

Is important to note that when our analysis calls for emission line measurements or morphological classification, our sample sizes are slightly smaller. The emission line measurements from Mateus et al. (2006) are available for 133294 galaxies in our low- z sample and morphological classification from Galaxy Zoo is available for 128891.

The complete data-set is available for 126036 galaxies.

Some other sub-samples are used for specific analysis throughout this work and will be introduced when needed.

Chapter 3

A new version of the STARLIGHT spectral synthesis code

“All models are wrong, but some of them are useful.”
— George Box

With the flood of new astronomical data that happened in the last decade, also came the demand for data analysis tools able to turn vast amounts of raw data into scientifically meaningful quantities.

In the extragalactic field, this demand led to the development of a variety of population synthesis tools, which aim to extract information encoded in the spectral energy distributions of galaxies by comparing them to stellar population models. One of the pioneering endeavors at this front is STARLIGHT, a Fortran 77 non-parametric spectral synthesis code built for the analysis of galaxy spectra, mainly in the optical. The code was originally presented in Cid Fernandes et al. (2005) and has a public version available at <http://www.starlight.ufsc.br> since the year 2007.

The landscape has continued to evolve, now reaching a point when data-sets are not only large, but also increasingly complex. An example is the widespread of IFU surveys such as CALIFA (Sánchez et al., 2012), MaNGA (Bundy et al., 2015) and SAMI (Allen et al., 2015), that open a new spatial dimension to the spectral analysis of galaxies. Another example, which is more directly related to the present work, is the rise in the popularity of panchromatic data-sets that provide galaxy data across the entire electromagnetic spectrum (e.g Brown et al., 2014; Driver et al., 2016). The main downside of

panchromatic data-sets is that they are mostly photometric, which imposes limitations to stellar population analysis.

The current landscape of extragalactic astrophysics requires methods that are able to combine data from different wavelengths, an approach taken in many modern applications of population synthesis (e.g da Cunha, Charlot & Elbaz, 2008; Leja et al., 2017). This is the motivation that led to the development of a new version of STARLIGHT that is able to simultaneously fit spectra and photometric fluxes. A combination that allows the exploration of photometric data outside the optical region while maintaining the detailed λ -by- λ information provided by spectra and critical for constraining non-parametric SFHs.

In this chapter, we will present this new version of STARLIGHT. An overview of the original code is presented in section 3.1, we then proceed to describe the inclusion of photometry in STARLIGHT in section 3.2. Section 3.3 takes a more practical approach, describing the usage of the new code and showing examples of fits. A manual of the new version of STARLIGHT is presented in Appendix C of this thesis.

3.1 The original STARLIGHT

The original STARLIGHT described in Cid Fernandes et al. (2005) remained as the foundation of the subsequent versions, including the one presented in this thesis. With that in mind, we will now take some time to review the aspects of STARLIGHT’s original version that are most relevant to this work.

3.1.1 Method

STARLIGHT fits an observed spectrum¹ O_λ by finding the model spectrum M_λ that minimizes the quantity

$$\chi^2 = \sum_{\lambda} w_{\lambda}^2 (O_{\lambda} - M_{\lambda})^2. \quad (3.1)$$

¹Broadly speaking, the code could be used to fit the spectrum of any astronomical object. However, in this work we will speak in the context of the spectral synthesis of galaxies, which is STARLIGHT’s main application.

where the inverse variance $w_\lambda = 1/\sigma_\lambda^2$ sets the weight of each flux based on its error σ_λ . Regions with bad pixels and/or emission lines are given $w_\lambda = 0$.

The model spectra M_λ are generated according to

$$M_\lambda = M_{\lambda_0} \left(\sum_{j=1}^{N_*} x_j b_{j,\lambda} \right) r_\lambda \otimes G(v_*, \sigma_*), \quad (3.2)$$

where M_{λ_0} is the flux at the normalization wavelength λ_0 , N_* is the number of base elements, x_j is the fraction of M_{λ_0} attributed to the j -th base component, $b_{j\lambda} = B_{j\lambda}/B_{j\lambda_0}$ are the base spectra normalized at λ_0 ,

$$r_\lambda = e^{-\tau_\lambda} = 10^{-0.4A_\lambda} \quad (3.3)$$

is the attenuation produced by a foreground dust screen of optical depth τ_λ and attenuation A_λ given by the product of V band attenuation (A_V) and an attenuation curve $q_\lambda = A_\lambda/A_V$. To account for stellar kinematics, the attenuated model spectra are convolved (\otimes is the convolution operator) with a Gaussian kernel $G(v_*, \sigma_*)$ of width σ_* (representing the stellar velocity dispersion) centered at v_* . A visual representation of equation 3.2 is shown in Figure 3.1.

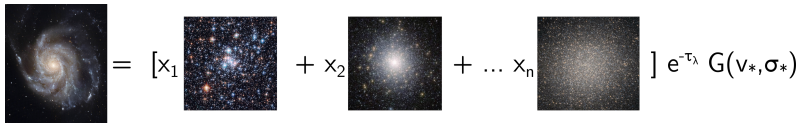


FIGURE 3.1: Illustration of STARLIGHT's fitting method. The image to the left represent an observed galaxy, other images represent the base components.

STARLIGHT's fitting procedure is based in a custom implementation of Markov Chain Monte Carlo (MCMC). The code is optimized to map the likelihood distribution and find the best global solution. Although at the end of the runs the code refits spectra with a reduced base that discards irrelevant components, no formal penalization scheme is applied to the χ^2 . These design choices allow STARLIGHT to capture very complex star-formation histories, at the expense of being unprotected against systematic effects.

3.1.2 Physical properties measured by STARLIGHT

In addition to the parameters fitted to obtain M_{λ} , STARLIGHT also returns star-formation histories and stellar masses. To obtain these quantities, the de-attenuated fluxes at the normalization wavelength

$$F_{\lambda_0,j}^0 = x_j F_{\lambda_0} 10^{0.4q_{\lambda_0} A_V} \quad (3.4)$$

are used to calculate the stellar mass each base component had at the time of formation

$$M_j^i = F_{\lambda_0,j}^0 4\pi D_L^2 \left(\frac{M}{L} \right)_j, \quad (3.5)$$

which have to be corrected by the mass lost to the interstellar medium (ISM) through winds and supernovae to obtain the current stellar masses M_j^c . These stellar masses can then be turned into mass fractions

$$\mu_j^i = \frac{M_j^i}{\sum M_j^i} \text{ and } \mu_j^c = \frac{M_j^c}{\sum M_j^c}. \quad (3.6)$$

Summing up the contribution of different metallicities to μ_j^i and plotting it against the age of each base component will give us the galaxy's star-formation history. Light-based descriptors of the star-formation histories are also widely used, these are based in the fraction of light at some wavelength which is associated with stellar populations of a given age.

Other galaxy properties can be calculated by reducing the dimensionality of the population vectors x_j and μ_j^c . Among these are luminosity and mass weighted mean stellar ages

$$\langle \log t_* \rangle_L = \sum_{j=1}^{N_*} x_j \log t_j \text{ and } \langle \log t_* \rangle_M = \sum_{j=1}^{N_*} \mu_j^c \log t_j, \quad (3.7)$$

as well as the luminosity and mass weighted mean stellar metallicities, calculated as

$$\langle Z_* \rangle_L = \sum_{j=1}^{N_*} x_j Z_j \text{ and } \langle Z_* \rangle_M = \sum_{j=1}^{N_*} \mu_j^c Z_j. \quad (3.8)$$

3.2 Including photometry in STARLIGHT

In this section, we will describe how STARLIGHT's method was modified to allow simultaneous spectroscopic and photometric fitting.

3.2.1 Calculating magnitudes from model spectra

Considering that the base spectra $B_{j\lambda}$ cover the wavelength range of a filter Y of transmission curve $T_{\lambda,Y}$, we can calculate the transmission average flux produced in this filter by a model spectrum M_λ as

$$\langle f_\lambda \rangle_Y = \frac{\int M_{\lambda(1+z)^{-1}}(1+z)T_{\lambda,Y}\lambda d\lambda}{\int T_{\lambda,Y}\lambda d\lambda} \quad (3.9)$$

where $T_{\lambda,Y}\lambda$ is the appropriate weighting for a photon-counting device² and $(1+z)$ is a cosmological correction that shifts M_λ to the observed frame.

The flux $\langle f_\lambda \rangle_Y$ can be used to calculate a magnitude m_Y . In our case, we will use magnitudes in the AB system (Oke & Gunn, 1983) which are characterized by a fixed zero point of 3631 Jy in any band. These are given by

$$\begin{aligned} m_Y &= -2.5 \log \frac{f_\nu}{3631 \text{Jy}} \\ &= -2.5 \log f_\nu + 8.9, \end{aligned} \quad (3.10)$$

or, for fluxes in cgs units of $\text{erg s}^{-1}\text{cm}^{-2}\text{Hz}^{-2}$:

$$m_Y = -2.5 \log f_\nu - 48.6. \quad (3.11)$$

In both of the above equations, f_ν is a flux per unit frequency, which differ from the flux per unit wavelength f_λ that we wish to calculate from M_λ . This difference between f_ν and f_λ may appear counter-intuitive, since fluxes should be the same regardless of being measured per frequency or per wavelength. The tricky bit is that the quantity measured by our detectors is neither f_ν nor f_λ but their integrals over some interval of frequency or wavelength, which are in fact the same.

²For an energy-counting device, the average flux in Y would simply be given by the average f_λ weighted by $T_{\lambda,Y}$.

The transmission averaged fluxes calculated from a f_ν spectrum are given by

$$\langle f_\nu \rangle_Y = \frac{\int f_\nu T_{\lambda,Y} \nu^{-1} d\nu}{\int T_{\lambda,Y} \nu^{-1} d\nu}. \quad (3.12)$$

Given that the integral of f_ν in some frequency interval is the same as the integral of f_λ in the corresponding wavelength interval, we have that

$$f_\nu d\nu = f_\lambda d\lambda, \quad (3.13)$$

which gives

$$f_\lambda = f_\nu \frac{d\nu}{d\lambda}. \quad (3.14)$$

Since $c = \lambda\nu$, we have

$$\frac{d\nu}{d\lambda} = -\frac{c}{\lambda^2}. \quad (3.15)$$

Combining with 3.14, it follows that

$$f_\lambda = -\frac{c}{\lambda^2} f_\nu, \quad (3.16)$$

which, combining with 3.13, gives the relation between the differentials

$$\frac{d\nu}{\nu} = -\frac{d\lambda}{\lambda}. \quad (3.17)$$

Plugging this relation into equation 3.12, we are able to obtain a flux per unit frequency f_ν from an f_λ spectrum:

$$\langle f_\nu \rangle_Y = \frac{\int f_\lambda T_{\lambda,Y} \lambda d\lambda}{c \int T_{\lambda,Y} \lambda^{-1} d\lambda}. \quad (3.18)$$

Finally, the AB magnitudes m_Y in a filter Y with transmission curve $T_{\lambda,Y}$ can be calculated from M_λ as

$$\begin{aligned} m_Y &= -2.5 \log \frac{\int M_{\lambda(1+z)^{-1}} (1+z) T_{\lambda,Y} \lambda d\lambda}{c \int T_{\lambda,Y} \lambda^{-1} d\lambda} - 48.6 \\ &= -2.5 \log \frac{\int M_{\lambda(1+z)^{-1}} (1+z) T_{\lambda,Y} \lambda d\lambda}{\int T_{\lambda,Y} \lambda^{-1} d\lambda} - 2.41 \end{aligned} \quad (3.19)$$

where c is the speed of light in $\text{\AA}/s$.

These magnitudes can be compared to the input data fed to STARLIGHT to find M_λ that best matches the observed photometry in filter Y . This depends on a complex comparison between spectroscopic and photometric figures of merit, which is the subject of our next section.

3.2.2 Combining photometric and spectroscopic figures of merit

We define the spectroscopic and photometric parts of the χ^2 as

$$\begin{aligned}\chi_{\text{SPEC}}^2 &= \sum_{\lambda} w_{\lambda}^2 (O_{\lambda} - M_{\lambda})^2 \\ \chi_{\text{PHO}}^2 &= \sum_{l=0}^{N_Y} \left(\frac{m_Y^{\text{obs}} - m_Y^{\text{mod}}}{\sigma_Y} \right)^2,\end{aligned}\quad (3.20)$$

where m_Y^{obs} and m_Y^{mod} are the observed and modeled AB magnitudes in filter Y , σ_Y are the errors in the magnitudes and N_Y is the number of photometric data-points. χ_{SPEC}^2 is the same as the χ^2 defined in equation 3.1 for purely spectral fits.

One could think about defining a total χ^2 as the simple sum of χ_{SPEC}^2 and χ_{PHO}^2 , however, in all practical applications, N_Y is much smaller than the number of spectroscopic data points N_{λ} – for instance, in the GALEX+SDSS analysis presented in the following chapters, $N_Y = 2$ and $N_{\lambda} \sim 4000$. In order to make this a fair fight and simultaneously minimize χ_{SPEC}^2 and χ_{PHO}^2 , this scale difference has to be circumvented in our definition of the total χ^2 .

To solve this issue and incorporate a variety of scaling philosophies, the code implements the equation

$$\chi_{\text{TOT}}^2 = S^{\gamma} \left[\chi_{\text{SPEC}}^2 + G_{\text{PHO}} \left(\frac{N_{\lambda}}{N_Y} \right)^{\alpha} \left(\frac{\chi_{\text{SPEC}}^2}{N_Y} \right)^{\beta} \chi_{\text{PHO}}^2 \right], \quad (3.21)$$

where G_{PHO} is a parameter that sets the relative weight of photometric and spectroscopic constraints. α and β are switches that can be set to 1 or 0, defining whether χ_{PHO}^2 is scaled according to the number

of spectroscopic data-points or to χ_{SPEC}^2 . γ is also a switch that turns on or off the global scale factor

$$S = \frac{N_\lambda + N_Y}{G_{\text{PHO}} N_\lambda^{\alpha+\beta} N_Y^{1-\alpha+\beta}}, \quad (3.22)$$

which aims on bringing χ_{TOT}^2 to the same order of magnitude as the number of data-points.

To minimize the frustration of the user, the interface of STARLIGHT hides equation 3.21 behind a set of three options:

1. WbN (Weight by number): sets $\alpha = 1$ and $\beta = 0$;
2. WbC (Weight by χ^2): sets $\alpha = 0$ and $\beta = 1$;
3. NoW (No weighting): sets $\alpha = 0$ and $\beta = 0$.

These codes and the value of γ are informed in STARLIGHT's grid file.

Is important to note that χ_{TOT}^2 will only be formal χ^2 when using the NoW option. In all other cases, the interpretability of χ_{TOT}^2 as the exponent of the likelihood function is lost.

3.2.3 Range fitting

STARLIGHT offers the possibility of treating the photometric data as upper or lower limits instead of values to be matched. Among other reasons, one might want to use this feature to deal with aperture differences between the spectroscopic and photometric data being fitted.

Range-fitting is implemented by replacing a conventional Gaussian likelihood function $e^{-\chi_Y^2/2}$ with a flat top Gaussian function where χ_Y^2 is given by

$$\chi_Y^2 = \begin{cases} \left(\frac{m_Y - m_Y^{\text{low}}}{\sigma_Y} \right)^2 & m_Y \leq m_Y^{\text{low}} \\ 0 & m_Y^{\text{low}} < m_Y < m_Y^{\text{upp}} \\ \left(\frac{m_Y - m_Y^{\text{upp}}}{\sigma_Y} \right)^2 & m_Y \geq m_Y^{\text{upp}}, \end{cases} \quad (3.23)$$

so that any value of m_Y within the $m_Y^{\text{low}} < m_Y < m_Y^{\text{upp}}$ range yields $\chi_Y^2 = 0$. Thus, all models leading to a Y -filter magnitude m_Y in

this interval are equally likely. Only models producing m_Y values outside this range are penalized with a lower likelihood (i.e., $\chi_Y^2 > 0$). Eq.3.23 reduces to a conventional

$$\chi_Y^2 = \left(\frac{m_Y - m_Y^{\text{obs}}}{\sigma_Y} \right)^2 \quad (3.24)$$

when $m_Y^{\text{low}} = m_Y^{\text{upp}} = m_Y^{\text{obs}}$, in which case STARLIGHT will try to match the observed magnitude m_Y^{obs} by decreasing the likelihood of models which predict m_Y too far (in units of σ_Y) from it.

Figure 3.2 shows the likelihood $e^{-\chi_Y^2/2}$ for 3 hypothetical situations: (a) $m_Y^{\text{low}} = m_Y^{\text{upp}} = m_Y^{\text{obs}} = 17$, a conventional Gaussian likelihood function; (b) $m_Y^{\text{upp}} = m_Y^{\text{obs}} = 17$ and $m_Y^{\text{low}} = -3$; and (c) $m_Y^{\text{upp}} = 17$, $m_Y^{\text{obs}} = m_Y^{\text{low}} = -3$. In all cases $\sigma_Y = 0.5$ mag was used. Figure 3.2a portrays the conventional fit situation, where we aim to match $m_Y^{\text{obs}} = 17 \pm 0.5$. Figure 3.2b corresponds to a case where we are confident (to within $\pm\sigma = \pm 0.5$ mag) that the magnitude in filter Y must be brighter than 17, so much so that we set m_Y^{upp} to a ridiculously bright -3 mag (off the plot's scale). This illustrates how to implement a lower-limit in the fits. To obtain a strict $m_Y > m_Y^{\text{obs}}$ limit it suffices to decrease σ_Y to a small value (say, 0.01 mag), effectively turning the likelihood curve to a Heaviside step function. Figure 3.2c illustrates a case where we are confident (again, to within ± 0.5 mag) that m_Y is in the 17–21 range. Naturally, the larger the range between m_Y^{low} and m_Y^{upp} the looser the constraints, but in some cases even a loose constraint can help (say, combining an optical spectrum with an upper limit to the UV flux).

3.3 Using STARLIGHT for simultaneous spectroscopic and photometric analysis

Having described the equations and astrophysical principles behind the new code, we will now turn to a more practical approach. This section is mostly aimed at people who already have some familiarity with STARLIGHT and are interested in using the code for simultaneous spectroscopic and photometric fitting. Moreover, we will also take this opportunity to provide a proof of concept for the new code. Since we are preaching to the converted here, we will allow ourselves to use a more technical language. For a thorough description of the

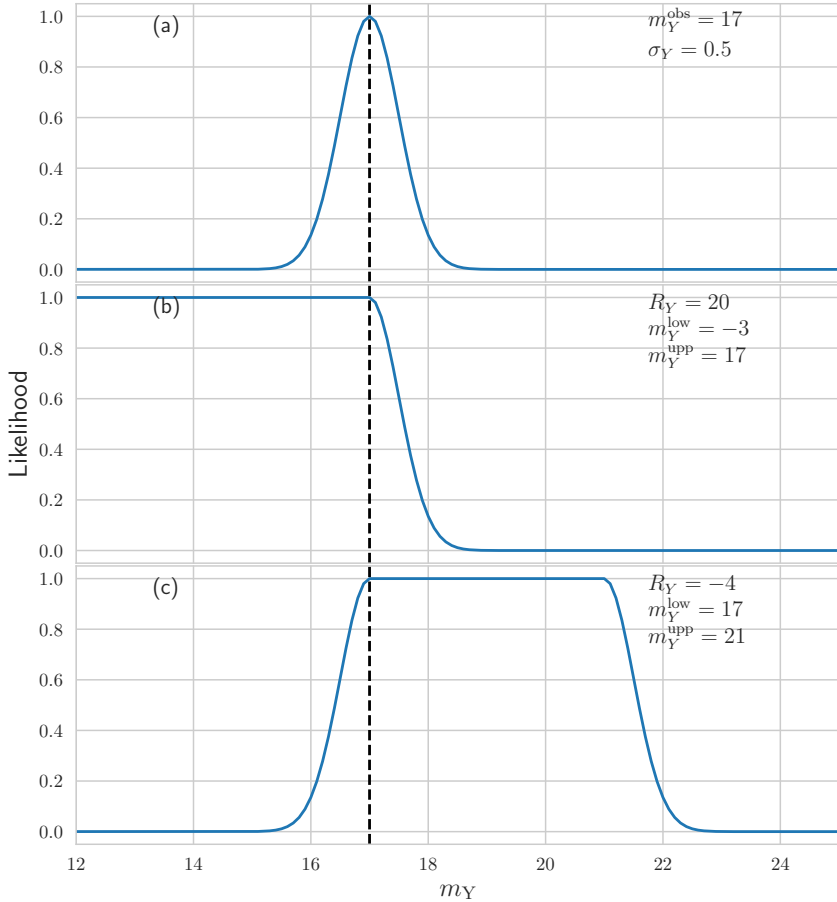


FIGURE 3.2: Likelihood functions for different values of the range parameter R_Y . Top panel shows a standard Gaussian likelihood function, middle panel shows a flat-top Gaussian used to fit observed magnitudes as lower limits, bottom panel shows a flat-top Gaussian that will give equal weight to any magnitude between m_Y^{low} and m_Y^{upp}

terminology used in this section, we refer to STARLIGHT's original manual available at <http://www.starlight.ufsc.br/downloads/>. For more details about how to use the code we refer to the manual of

this version, which is presented in Appendix C.

3.3.1 Basic example

To illustrate the usage of the code and provide a proof of concept, we will explore an example where we fit an SDSS spectrum below 5000 Å and use photometry from the *r* and *z* bands to constrain longer wavelengths. We do this by masking out all data above 5000 Å in the spectrum using the mask file. This way STARLIGHT will *predict* fluxes with wavelengths between 5000 and 9000 Å, which is the maximum wavelength taken into account by the fit (0lsyn_fin in STARLIGHT notation).

Some changes were made to the grid files (grid_file in the code's notation) with respect to the original STARLIGHT. The header of the grid_file used in the present example is shown below:

```

1 1 [n_fits]
2 ./bc2003/ [base_dir]
3 ./input/ [obs_dir]
4 ./masks/ [mask_dir]
5 ./photometry/ [pho_dir]
6 ./output/ [out_dir]
7 -958372728 [your phone number]
8 5350.0 [l1ow_SN]
9 5850.0 [lupp_SN]
10 3500.0 [0lsyn_ini]
11 9000.0 [0lsyn_fin]
12 1.0 [0dlsyn]
13 1.0 [fscale_chi2]
14 FIT [FIT/FXK]
15 1 [IsErrSpecAvailable]
16 1 [IsFlagSpecAvailable]
17 1.0e-17 [flux_unit]
18 0 0 1 WbN 0 [IsFIRcOn IsQHRcOn IsPH0cOn ESM & gamma]
```

If you are familiar with STARLIGHT, you probably noticed that everything was kept the same with except for the fifth line and the two last ones, which are highlighted in red. The fifth line indicates the directory `pho_dir` in which photometric data is stored. Line 17 sets the variable `flux_unit`, multiplying your input spectral fluxes by this constant converts them to units of $\text{erg s}^{-1}\text{cm}^{-2}\text{Å}^{-1}$.

The last line in the grid header contains switches that turn new features on or off. The first two switches are associated with features that are still under development and are not explored here. The third switch turns photometric constraints on or off. It can also be set to -1,

in which case photometric fluxes will be predicted from spectral fits. The other variables in the same line set the χ^2 scaling method and the value of γ (see section 3.2.2).

The second part of the `grid_file` is shown below, split in two due to lack of page space:

```

21 501-52235-368.spec 501-52235-368.pho 195.077 PMSv04.conf base_BC03
22 #spec_in          pho_in          lumdist arq_config arq_base

21 EL_mask.msk CCM 0.0 150 501-52235-368.out
22 arq_mask     ALO v0   vd   out_file

```

Once again, the new input info is shown in red. The second column lists the photometric input files (*.pho), which will be described soon and the third column corresponds to the luminosity distance (in Mpc) to the objects. Other entries in this grid file are as in the previous version. The first column list the input spectra, `PMSv04.conf` is the config file (`arq_conf`), `base_BC03` is a base file (`arq_base`), `EL_mask.msk` is a mask file (`arq_mask`) and `CAL` is an attenuation law.

As in previous versions, input spectra should be corrected for Galactic extinction and shifted to the rest-frame, the spectra are stored in ascii files containing two to four columns. The first two columns are mandatory and correspond to the wavelengths and fluxes, the remaining ones are optional and contain the observational errors and a flag to mask out bad pixels (STARLIGHT's sets $w_\lambda = 0$ where `flag>0`).

The first lines of photometric input file for our example (`501-52235-368.pho`) are shown bellow.

```

1 PHO
2 0.044      [PHO_Redshift]
3 2          [NPHO_Ys]
4 0.2       [PHO_GlobalChi2ScaleFactor]

```

These lines are a header containing the following information:

1. In the first line, the acronym `PHO` indicates that the file contains photometric information;
2. The second line indicates the galaxy's redshift (`PHO_Redshift` in the code's notation) used by STARLIGHT to shift base spectra to the galaxy's observed frame to compare model spectra with photometry;

3. The third line corresponds to the number of photometric filters to be considered in the fit;
4. The fourth line contains the variable `PH0_GlobalChi2ScaleFactor`, which corresponds to G_{PHO} in equation 3.21 and is used to give more or less weight to the photometric part of χ^2 ;

The following lines, containing photometric information about each of the filters, are shown below. Like before, we are splitting the lines in two due to lack of space:

```

5  r          r.dat          17.519         1.0
6  z          z.dat          16.794         1.0
7  #PH0_name PH0_Filter_file PH0_magY_TOT PH0_YFrac2Model

5  0.1        0.0            0.5
6  0.1        0.0            0.5
7  PH0_magYErr PH0_magYRange PH0_Chi2ScaleFactor
```

There is one line for each filter in the fit. Each line contains the following columns:

1. Name of the filter (`PH0_name`);
2. Name of the filter file, expected to be in the photometric directory (`PH0_Filter_file`);
3. AB apparent magnitude of the galaxy (`PH0_magY_TOT`);
4. The fraction of the flux to be considered by the code (`PH0_YFrac2Model`), which is likely to be deprecated soon;
5. Measurement errors of the magnitude (`PH0_magYErr`);
6. The range parameter (`PH0_magYRange`), useful to fiddle with the likelihood function (see section 3.2.3);
7. The fraction of the photometric χ^2 corresponding to the filter (`PH0_Chi2ScaleFactor`).

Masking the red part of the spectrum allows us to compare the results for the photometric+spectroscopic fit with the red part of the observed spectrum. This comparison is made in Figure 3.3, where we show the fit correspondent to the example input files described above. It is noticeable that the purely spectroscopic fit (shown in red) deviates from the red part of the spectrum. Including photometry

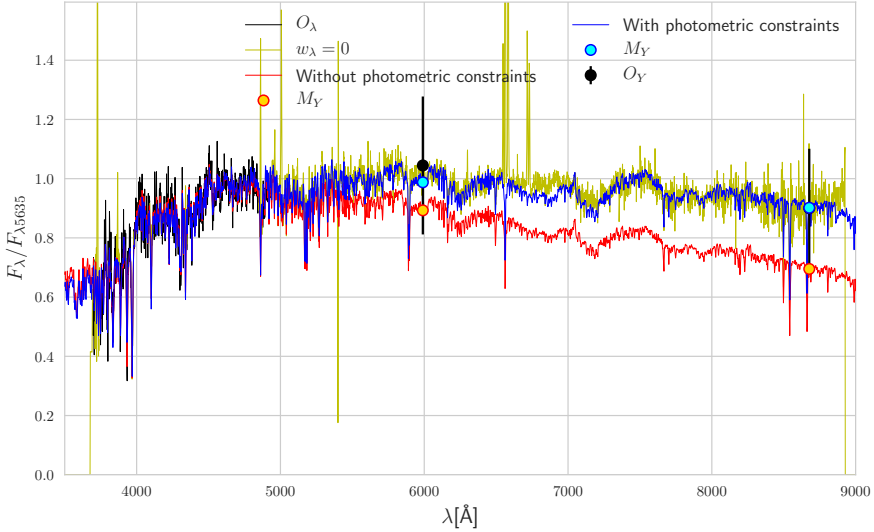


FIGURE 3.3: Example of simultaneous fitting of SDSS spectra up to 5000\AA and r and z photometric fluxes. The black line shows the observed spectrum with masked parts shown in yellow. The blue and red lines show fits with and without photometric constraints, respectively. Black points with error-bars show the observed photometry, cyan points are the model fluxes obtained in the fit with photometric constraints and orange points show fluxes estimated from the purely spectroscopic fit. All fluxes are normalized at $\lambda_0 = 5635$.

allows STARLIGHT to fit this part of spectrum remarkably well, even though λ -by- λ information is not provided.

Using optical photometry to complement spectra with narrow wavelength coverage is a promising application for STARLIGHT. For instance, some modern IFU spectrographs like MUSE miss the 4000 break, a key spectral feature for stellar population analysis that could be supplemented with photometry.

3.3.2 An example of UV-NIR synthesis

An important application of simultaneous spectroscopic and photometric fits is including UV and/or NIR data in the analysis. These

are regions of the electromagnetic spectrum where publicly available spectra of galaxies are not as widespread as in the optical, but that can provide important information on certain stellar populations. STARLIGHT's ability to produce such fits is showcased in Figure 3.4, where we plot a fit to the optical spectra NGC 0855 combined with GALEX *NUV* and *FUV*, SDSS *z* and 2MASS *J*, *H* and *K_s* photometry. The data was obtained from the spectral atlas of Brown et al. (2014). The photometric input file used in this fit is as follows:

```

1 PHO
2 0.00197 [PHO_Redshift]
3 6 [NPHO_Ys]
4 0.1 [PHO_GlobalChi2ScaleFactor]
5 FUV FUV.dat 15.85 1. 0.1 0.0
6 NUV NUV.dat 15.22 1. 0.1 0.0
7 z z.dat 11.89 1. 0.05 0.0
8 J J.dat 11.73 1. 0.05 0.0
9 H H.dat 11.59 1. 0.05 0.0
10 Ks Ks.dat 11.82 1. 0.05 0.0
11 #PHO_name PHO_Filter_file PHO_magY_TOT PHO_YFrac2Model PHO_magYErr PHO_magYRange

```

The purely optical fit in Figure 3.4 misses the UV and NIR data, as it lacks information on stellar populations that are most relevant at these wavelengths. The overestimation of UV fluxes is a long known systematic effect of STARLIGHT fits, and happens due to the lack of constraints on very young stellar populations. The effect on the NIR is not systematic, and is not statistically unusual for NIR fluxes to be correctly estimated from purely optical fits. Investigating stellar populations in the NIR is an interesting problem but beyond the scope of this thesis, which focuses in the UV.

3.3.3 Testing different χ^2 scaling methods

As explained in section 3.2.2, STARLIGHT offers a variety of χ^2 scaling methods. The difference between these methods, however, is more philosophical than practical, as they generally lead to similar results. Here we will illustrate the different methods by fitting the NGC 0855 data presented in the previous section using different combinations of technical parameters.

Figure 3.5 shows results with no weighting (NoW, top panel) and with weighting applied to the number of data points (WbN, second and third panels) and χ^2 (WbC, bottom panels), which are shown for two cases each ($\gamma = 0$ and $\gamma = 1$). Fits with no weighting are only marginally better in reproducing photometry than purely

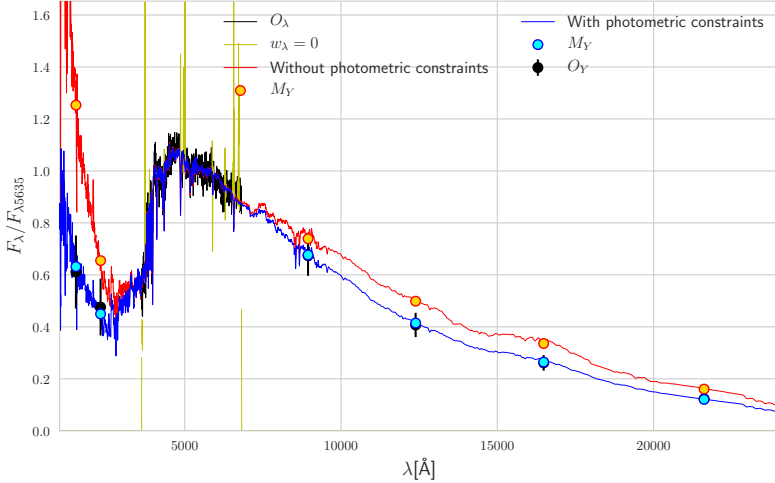


FIGURE 3.4: Simultaneous fit of optical spectra and UV+NIR photometry of NGC 0855. The black line shows the optical spectrum, with masked or flagged regions shown in yellow. Black points with error bars show (from left to right) GALEX NUV and FUV , SDSS z and 2MASS J , H and K_s photometric fluxes. Blue and red lines show fits with and without photometric constraints, respectively. Cyan points show photometric fluxes fitted in the combined spectroscopic and photometric analysis, while orange points show fluxes predicted in the purely spectroscopic fits. All fluxes are normalized at $\lambda_0 = 5635\text{\AA}$.

spectroscopic fits. That being said, the choice of weighting scheme is not very relevant to the quality of the fit, as all of them yield good results. The WbN method is slightly faster, specially with $\gamma = 0$, which makes this our favorite option.

With the exception of the first panel, results are shown for three values of G_{PHO} plotted in different colors. The green and magenta lines, showing $G_{\text{PHO}} = 1.0$ and $G_{\text{PHO}} = 0.01$ are barely visible in Figure 3.5, showing that the choice of G_{PHO} is irrelevant in this case. This happens because the NGC 0855 data used in the fit have low photometric errors and good aperture matching. In cases where spectra and photometry are not well matched or photometric errors are

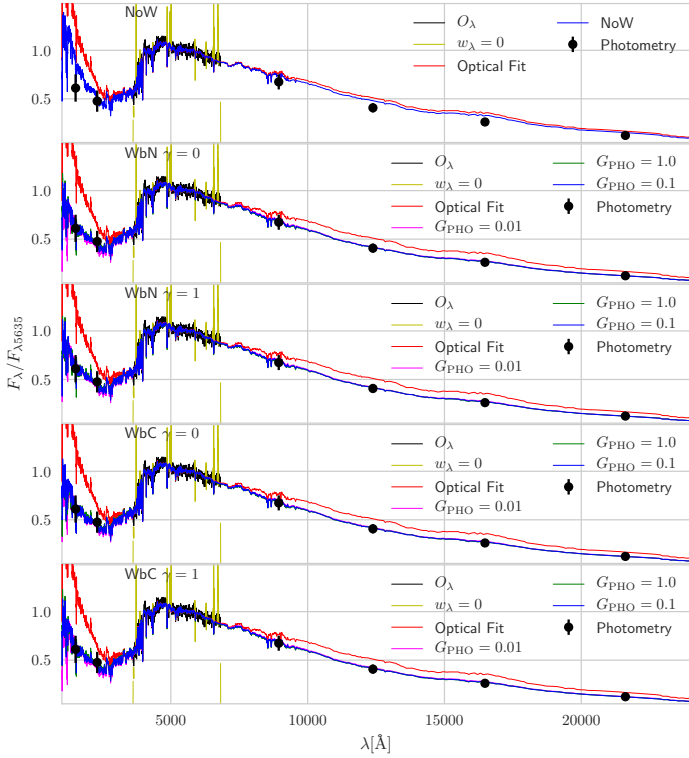


FIGURE 3.5: Simultaneous fit of optical spectra and UV+NIR photometry of NGC 0855 using different χ^2 scaling methods. From top to bottom, panels show fits with no weighting (NoW, first panel), weight by number of data-points with $\gamma = 0$ and $\gamma = 1$ (WbN, second and third panels) and weight by χ^2 with $\gamma = 0$ and $\gamma = 1$ (WbC, fourth and fifth panels). The black line shows the optical spectrum, with masked or flagged regions shown in yellow. Black points with error bars show (from left to right) GALEX *NUV* and *FUV*, SDSS *z* and 2MASS *J*, *H* and *K_s* photometric fluxes. A red line shows purely spectroscopic fit. With the exception of the top panel, fits with photometric constraints are shown for $G_{PHO} = 0.01$ (magenta lines), $G_{PHO} = 0.1$ (blue lines) and $G_{PHO} = 1$ (green lines).

large, varying G_{PHO} can be useful to choose between having a good spectroscopic fit that misses the photometry or fitting photometry at the expense of a bad spectroscopic fit. To explore this a bit further, we have re-fitted the NGC 0855 data with photometric errors multiplied by four, results are shown in Figure 3.6.

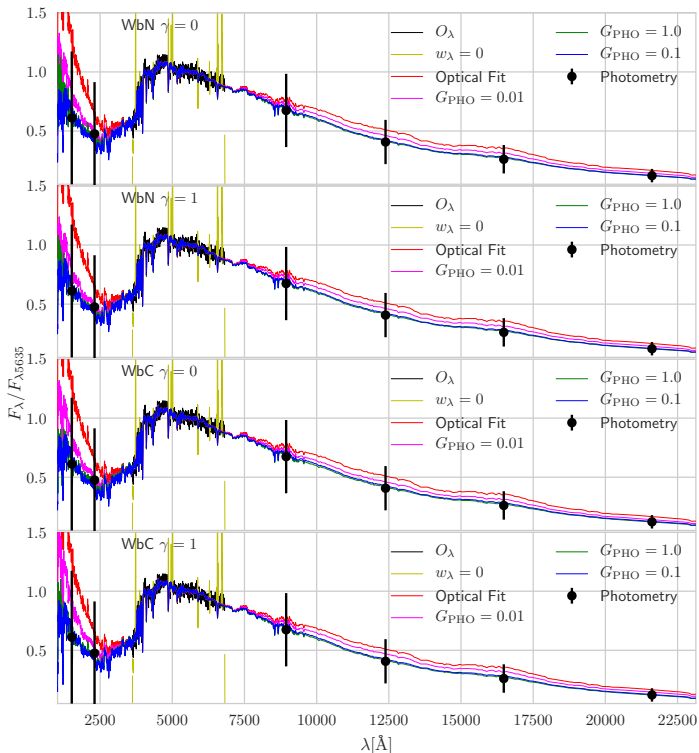


FIGURE 3.6: Same as Figure 3.5, but with quadruplicated error bars and without the top panel.

Although the fits in Figure 3.6 still look quite alike, it is now clear that there are three different lines in the plots. Specially, the magenta line clearly deviates from the fit, as the $G_{\text{PHO}} = 0.01$ value decreases the quality of the photometric fit. A mismatch between spectra and photometry would further increase the difference between fits with different G_{PHO} . That aside, Figure 3.6 confirms that the fits are not too dependent on the choice of χ^2 scaling method, as long as errors are not overwhelmingly big and the spectrophotometric

calibration is reliable. Still, it is recommended that the user tests different methods and choose the one that best matches their data-set and/or philosophical preference.

3.3.4 Range-fitting and upper or lower limits

Range fitting is controlled by the variable R_Y , (PHO_magYRange in the code's notation), which is set for each filter in the photometric input files.

As discussed in section 3.2.3, when range-fitting is applied, m_Y^{obs} do not represent values to be fitted, but one of the extremes of the top of a flat-top Gaussian likelihood function. When R_Y is positive, m_Y^{obs} is placed at the right boundary of the top of the Gaussian, when R_Y is negative, m_Y^{obs} is placed to the left (see Figure 3.2). In practice, this means that $R_Y > 0$ sets m_Y^{obs} as a lower flux limit, while $R_Y < 0$ sets m_Y^{obs} as an upper flux limit.

Since m_Y^{obs} is at the boundary of the top of the likelihood function, to fit a magnitude within a certain range, one has to inform a lower magnitude in the photometric input files. For instance, in order to match the m_Y^{obs} of NGC 0855 within ± 0.25 magnitudes, one has to set $m_Y^{\text{obs}} + 0.25$ in the photometric input and inform $R_Y = 0.5$, as in the example below.

```

1 PHO
2 0.00197 [PHO_Redshift]
3 6 [NPHO_Ys]
4 0.1 [PHO_GlobalChi2ScaleFactor]
5 FUV FUV.dat 16.1 1. 0.001 0.5
6 NUV NUV.dat 15.47 1. 0.001 0.5
7 z z.dat 12.14 1. 0.001 0.5
8 J J.dat 11.98 1. 0.001 0.5
9 H H.dat 11.84 1. 0.001 0.5
10 Ks Ks.dat 12.07 1. 0.001 0.5
11 #PHO_name PHO_Filter_file PHO_magY_TOT PHO_YFrac2Model PHO_magYErr PHO_magYRange

```

By setting $|R_Y|$ to an unrealistically large value, one would be fitting m_Y^{obs} as a global magnitude limit. An example of photometric input file that fits *NUV* and *FUV* fluxes as lower limits and *z*, *J*, *H* and *K_s* fluxes as upper limits for NGC 0855 is shown below:

```

1 PHO
2 0.00197 [PHO_Redshift]
3 6 [NPHO_Ys]
4 0.1 [PHO_GlobalChi2ScaleFactor]
5 FUV FUV.dat 15.85 1. 0.001 20.0

```

6	NUV	NUV.dat	15.22	1.	0.001	20.0	1.
7	z	z.dat	11.89	1.	0.001	-20.0	1.
8	J	J.dat	11.73	1.	0.001	-20.0	1.
9	H	H.dat	11.59	1.	0.001	-20.0	1.
10	Ks	Ks.dat	11.82	1.	0.001	-20.0	1.
11	#PHO_name	PHO_Filter_file	PHO_magY_TOT	PHO_YFrac2Model	PHO_magYErr	PHO_magYRange	PHO_Chi2

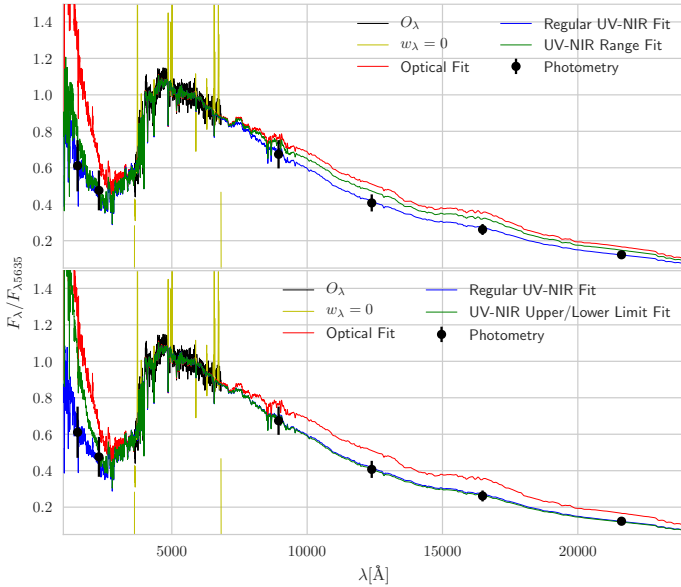


FIGURE 3.7: Simultaneous fit of optical spectra and UV+NIR photometry of NGC 0855 using range fitting and upper/lower limits. The black line shows the optical spectrum, with masked or flagged regions shown in yellow. Black points with error bars show (from left to right) GALEX *NUV* and *FUV*, SDSS *z* and 2MASS *J*, *H* and *K_s* photometric fluxes. Red lines shows the purely spectroscopic fit, blue lines show the standard photometric fit (weighting by number of data-points with $\gamma = 0$), green lines show fits giving equal weight in a $m_Y^{\text{obs}} \pm 0.25$ window (top panel) or fitting UV data as lower limits and NIR data as upper limits (bottom panel).

The results of both the examples above are plotted in Figure 3.7. At the top panel, constant weight is given to any value within ± 0.25

magnitudes of m_Y^{obs} . This brings the fits closer to what is obtained without photometric constraints. In the bottom panel, UV fluxes are viewed as lower limits, while other photometric points are treated as upper limits. Since the tendency of the optical fits in this galaxy is to overestimate all photometric fluxes, this setup overestimates the UV but is sufficient to constrain the NIR. This feature can be used when photometry is given in a different aperture than spectra and the user is unsure of how to match the data.

Now that we have described the new version of STARLIGHT and shown that it works, we will turn to the application of the code to GALEX and SDSS data.

Chapter 4

Spectral synthesis of GALEX and SDSS data with STARLIGHT

A core principle of STARLIGHT’s fitting philosophy is making as few assumptions as possible about the shape of the galaxy’s SFH. This makes the code good in picking up complex features in the SFH, but comes at a price. It cannot be stated enough that spectral synthesis is a highly degenerate problem that doesn’t have a unique solution. As a consequence, a code that lacks any form of penalization or smoothing for the SFH will be, by design, prone to overfitting.

This brings us to the original motivation behind this thesis: STARLIGHT fits to optical spectra tend to accommodate small contributions of young stellar populations that contribute little to the optical spectra of most galaxies but are dominant in the UV; which leads to an overshooting of UV fluxes. Including UV constraints in STARLIGHT analysis is therefore key for a better determination of galaxy properties. This was first done by López Fernández et al. (2016) for a combination of GALEX photometry and CALIFA integrated spectra, and is here extended to a much larger sample.

In this chapter, we will investigate how the addition of UV data affects STARLIGHT results for a sample of 137994 galaxies at $z < 0.1$. This is done by combining optical spectra from SDSS and UV photometry from GALEX, which are aperture-matched as described in section 2.2 chapter 2. A description of the setup used in this study is provided in section 4.1; changes in the spectral fits are reviewed in section 4.2. The effect of UV data in the measured physical properties is presented in the latter sections; sections 4.3 and 4.4 show changes

in star-formation histories and global properties, while section 4.5 takes a closer look at the effects of UV data in estimates of dust attenuation.

4.1 STARLIGHT setup

Spectral synthesis with STARLIGHT depends on a series of astrophysical ingredients and design choices. This section will briefly describe the pre-processing of data and our choices of ingredients and technical parameters.

4.1.1 Pre-processing data

Both optical spectra and UV photometry are corrected for Galactic extinction using the MW extinction law with $R_V = A_V/E(B - V) = 3.1$ as parameterized by Cardelli, Clayton & Mathis (1989). $E(B - V)$ values are obtained from the map by Schlegel, Finkbeiner & Davis (1998), considering the recalibration introduced in Schlafly & Finkbeiner (2011) that reduces the $E(B - V)$ by 14% due to a systematic effect.

The spectra are shifted to $z = 0$ by dividing wavelengths and multiplying fluxes by $(1 + z)$ and then re-sampled to 1\AA wavelength intervals. Bad pixels are flagged according to the flags provided by SDSS.

We note that the UV magnitudes used in the STARLIGHT fits are not k-corrected to rest-frame values. Instead, STARLIGHT uses the known redshift of the source to evaluate the predicted NUV and FUV magnitudes in the observed frame.

4.1.2 Stellar population base

The base of stellar population spectra is the main astrophysical ingredient involved in STARLIGHT analysis.

The base used in this work is built from SSP models from Charlot & Bruzual (in prep). This update of the classical Bruzual & Charlot (2003) models uses state of the art PARSEC isochrones (Bressan et al., 2012) and a series of spectral libraries, including MILES (Sánchez-Blázquez et al., 2006), IndoUS (Valdes et al., 2004) and Martins et al. (2005) in the optical, and a blend of models (Lanz & Hubeny, 2003a; Lanz & Hubeny, 2003b; Lanz & Hubeny, 2007; Rodríguez-Merino

et al., 2005; Rauch, 2003; Leitherer et al., 2010) and PoWR models (Sander, Hamann & Todt, 2012; Hamann, Gräfener & Liermann, 2006; Hainich et al., 2014; Hainich et al., 2015; Todt et al., 2015; Gräfener, Koesterke & Hamann, 2002; Hamann & Gräfener, 2003) in the UV. Models computed with a Chabrier (2003) IMF are adopted in this work.

After dividing the age range from $t = 1$ Myr to 14 Gyr onto 16 logarithmically spaced age bins, we use these SSP models to compute the spectra of CSPs resulting from periods of constant star formation rate (square bursts) at each of age bin according to

$$B_j(\lambda) = \int_{t_j}^{t_{j+1}} SSP(\lambda; t, Z) SFR(t, Z) dt, \quad (4.1)$$

where SFR is a constant whose value is adjusted to produce a total of $1 M_\odot$ over the $t_j \rightarrow t_{j+1}$ interval. The integration of $SSP(\lambda; t, Z)$ is carried out analytically using the original grid of SSP spectral models and interpolating them (linearly in $\log t$) between adjacent ages. The values of t_j are 1.00×10^6 , 1.81×10^6 , 3.29×10^6 , 5.98×10^6 , 1.08×10^7 , 1.97×10^7 , 3.58×10^7 , 6.51×10^7 , 1.18×10^8 , 2.14×10^8 , 3.90×10^8 , 7.08×10^8 , 1.28×10^9 , 2.33×10^9 , 4.24×10^9 , and 7.70×10^9 yr; with the last age bin going up to 1.4×10^9 yr. Seven values of metallicity are used: 0.0058, 0.029, 0.23, 0.47, 1.0, 1.76, and $3.52 Z_\odot$, ($Z_\odot = 0.017$ is the solar metallicity). Our final base is comprised of $16 \times 7 = 112$ CSPs. The resulting base spectra are plotted in Figures 4.1 (for the optical) and 4.2 (for the UV).

When using this CSP base, fewer base components are required to produce a good description of galaxy spectra. As a consequence, STARLIGHT computational times with CSPs are far shorter than with SSPs¹. A more physical reason to use CSPs is that galaxy spectra are generally measured in relatively large apertures (in kpc), so is plausible to assume that these include contributions of stars formed from multiple HII regions over different epochs. Under this interpretation, the square bursts of our CSP base provide a better set of priors than the instantaneous bursts assumed when using SSPs directly.

¹STARLIGHT computational times increase with the square of the number of base elements.

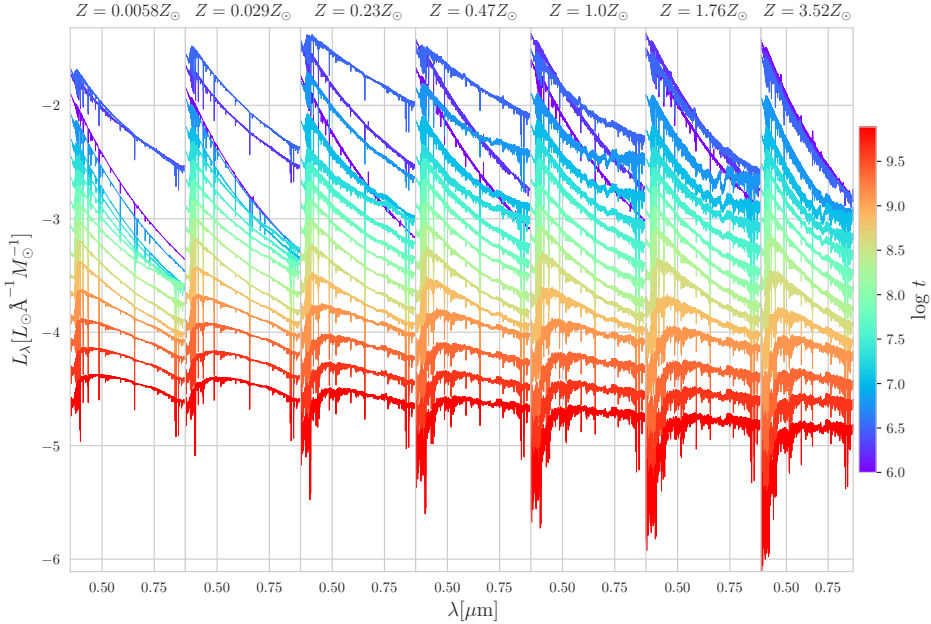


FIGURE 4.1: Optical spectra of base elements used in the synthesis. Each panel shows one of the metallicities included in the base, spectra are colored according to the log age at the younger boundary of the corresponding age bin (t_j in equation 4.1).

4.1.3 Dust attenuation model

The effects of dust attenuation are modeled as if produced by a single foreground dust screen that attenuates fluxes by a factor $e^{-\tau_\lambda}$, with τ_λ parameterized as the product of the optical depth in the V-band (τ_V) and a $q_\lambda \equiv \tau_\lambda / \tau_V$ attenuation or extinction curve. We remind the reader that, throughout this work, we adopt the standard definition of "extinction" as the scattering and absorption of photons out of the line of sight, while "attenuation" is defined as the combination of absorption and scattering in and out of the line of sight with local and global geometric effects.

We have performed spectral fits with two different recipes for q_λ : the MW law, as parameterized by Cardelli, Clayton & Mathis (1989) with $R_V = 3.1$ (CCM), and the Calzetti et al. (2000) law (CAL), modified in the $\lambda < 1846 \text{ \AA}$ range to smoothly turn into the curve derived

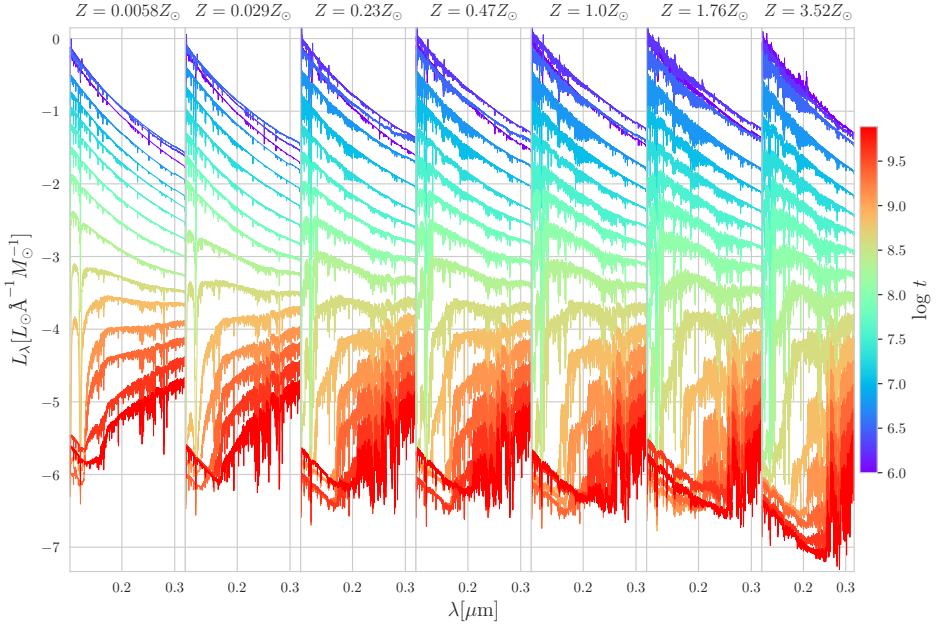


FIGURE 4.2: Same as Figure 4.1, but for UV wavelengths.

by Leitherer et al. (2002).² The most notable difference between these laws is the presence or absence of the so called "UV bump", or 2175 Å feature, a broad peak in q_λ at $\sim 2175 \pm 350$ Å (within the range of the *NUV* filter) first identified by Stecher (1965) in the MW. A more fundamental difference between them is that while CAL formally represents an attenuation law, CCM is originally an extinction curve, a crucial distinction when modeling the two processes (e.g Witt & Gordon 2000). In the context of this work, however, CCM is used to model attenuation, so the term "attenuation law" may sometimes loosely apply. These two laws are chosen because they are the most often used in STARLIGHT-based work, and also because they allow us to test how an UV bump affects the fitting of UV data. These characteristics suit our central goal, which is to showcase the potential of the combined analysis of optical spectra and UV photometry with STARLIGHT.

²This modification has only minor effects, restricted to the *FUV* band.

A comparison of results obtained with the two laws will be presented in the next chapter, but we anticipate that the best results for the general population of galaxies are obtained for the Calzetti law. Accordingly, all results presented up to section 5.3 assume this prescription.

4.1.4 Technical parameters

For the spectral part of the fits, we use a somewhat standard configuration of STARLIGHT. The normalization wavelength is set to $\lambda_0 = 5635\text{\AA}$ with a normalization window of $\pm 45\text{\AA}$. We use the SIGMA clipping method with a 4σ threshold, discarding points where the observed spectrum deviates from the model by more than 4 times the error. Stellar kinematics is fitted with initial parameters $v_0 = 0.0\text{km/s}$ and $\sigma_* = 150\text{km/s}$.

Photometry is fitted using the WbN scaling method with $\gamma = 0$ and $G_{\text{PHO}} = 0.1$ (see section 3.2.2). This set of parameters was chosen because it yielded good fits within reasonable computational time for a test sample of 5000 galaxies. Equal weights are given to both GALEX filters, although in practice the smaller errors of the *NUV* make it weight more than the *FUV* band. Range fitting is turned off.

4.2 Spectral fits and UV magnitudes

Figure 4.3 shows examples of spectra fitted with and without photometric constraints for three different galaxies, ordered from red (top) to blue (bottom) *NUV* – *r* colors. The observed SDSS spectra are shown in black, except for regions masked due to bad pixels or emission lines, which are shown in yellow. Red and blue lines show the optical and combined optical+UV fits, respectively. Observed UV fluxes are shown as black circles, while model values are plotted as orange circles for the optical-only fits and cyan for the optical+UV fits. All fluxes are relative to the flux at the normalization wavelength.

Figure 4.3 confirms the aforementioned systematic effect: Purely optical fits tend to predict UV fluxes much larger than the observed ones. This happens because optical-only fits can easily accommodate small contributions of very young stellar populations which hardly affect the optical fluxes, but become dominant at UV wavelengths. The addition of UV constraints allows STARLIGHT to successfully fit UV magnitudes with very little changes to the fitted optical spectra.

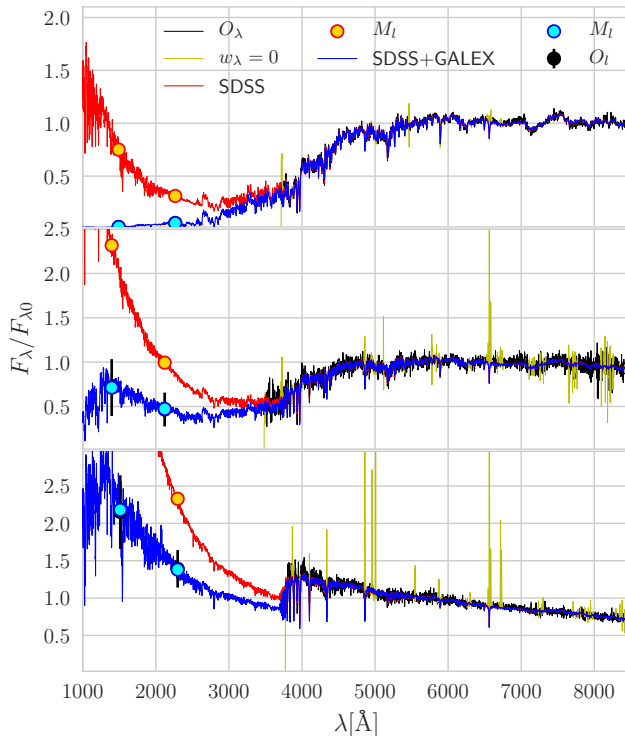


FIGURE 4.3: Examples of STARLIGHT fits for three galaxies in our sample. Black lines show optical spectra, with masked or flagged regions marked in green. Red lines show purely spectroscopic fits, while blue lines show combined UV + optical fits. Black circles with error bars mark the observed GALEX fluxes ($NUV_{1.5}$ and $FUV_{1.5}$, scaled to the SDSS aperture using the method described in Section 2.2), cyan circles are the fitted GALEX fluxes. Orange circles show UV fluxes predicted from purely optical fits. All fluxes are relative to the flux at 5635 \AA .

Also, since this effect involves only small fractions of stellar mass and optical light, no drastic change is observed in the measured star-formation histories, as will become clear in Figs. 4.5 and 4.6.

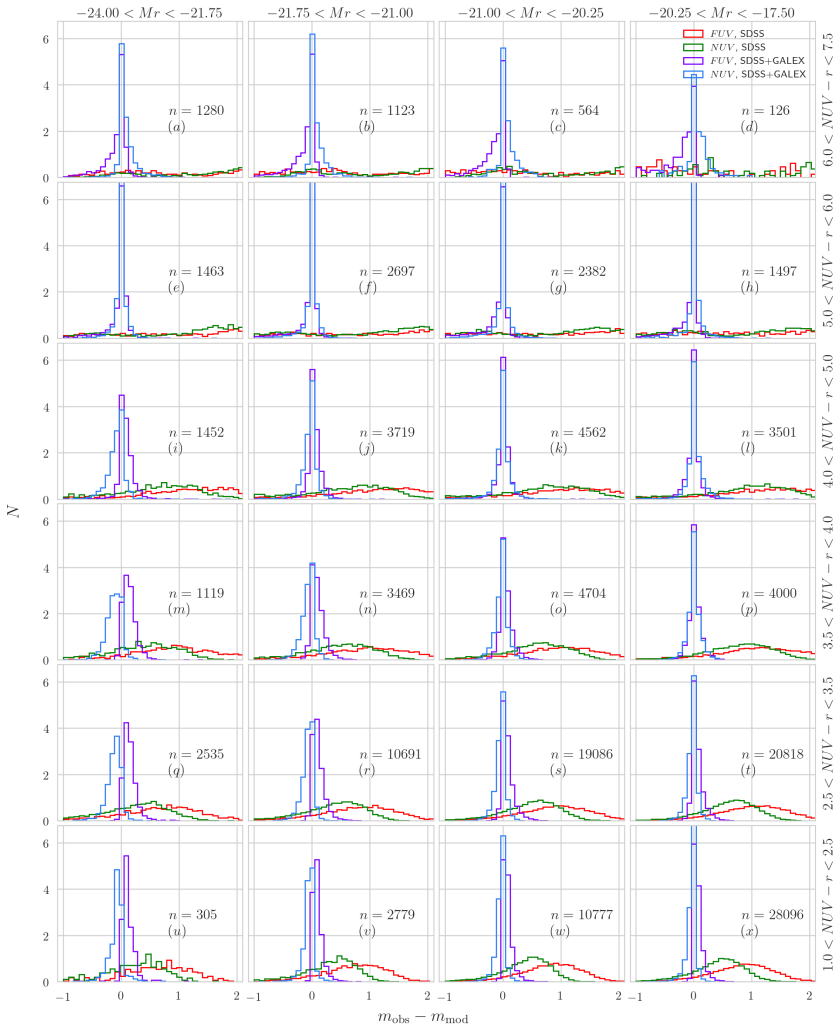


FIGURE 4.4: Histograms comparing differences between observed magnitudes and the values predicted from optical spectra (red lines for FUV , green lines for NUV) and fitted from GALEX photometry (purple lines for FUV , blue lines for NUV). Each panel corresponds to a color-magnitude bin. Histograms are normalized to have the same area.

This effect is further illustrated in Figure 4.4, where we plot histograms of the difference between the modeled and observed UV magnitudes in bins across the $NUV - r$ vs M_r color-magnitude diagram. In this diagram, and at the redshift limit of our sample, the blue cloud can be defined by the criterion of $NUV - r < 4$ and the red sequence by $NUV - r > 5$, while points in the $4 < NUV - r < 5$ range lie in the green valley (Salim, 2014).

Averaging through the whole sample, fits without photometric constraints overshoot UV magnitudes by 0.41 ± 0.91 magnitudes on NUV and 0.83 ± 1.32 on FUV , yielding values that are often brighter than the integrated UV magnitudes. This overestimation is systematic throughout all color-magnitude bins in Figure 4.4. When including UV constraints, the sample averaged magnitudes are very well matched, although Figure 4.4 reveals two caveats: (i) In the lower left of the Figure (mainly panels (m) and (q)) we see regions in color-magnitude space where NUV fluxes are slightly underestimated and FUV fluxes slightly overestimated, some of these objects have blue $NUV - r$ and relatively red $FUV - NUV$, a combination of colors that is sometimes hard to achieve and may indicate the limitations of our dust model; (ii) At the upper red-sequence (top panels), FUV are underestimated for galaxies with strong UV upturns, which happens because the strongest upturns in our stellar population models are at oldest populations, since our base is constructed from logarithmically spaced age bins and our oldest bin spans almost 4Gyr, the upturns from the oldest populations (13.5Gyr or older) are diluted. Albeit it is useful to keep these caveats in mind, they generally do not translate into problematic results in terms of physical properties.

4.3 Star Formation Histories

We now examine the changes in the derived SFHs generated by the inclusion of UV constraints in the analysis. Within STARLIGHT SFHs are described in terms of the light fraction population vector \vec{x} , which quantifies the contribution of different base components to the observed flux at a normalization wavelength. The mass fraction vector $\vec{\mu}$ is derived from \vec{x} and the light-to-mass ratios of the base populations.

4.3.1 The overall trend

Figure 4.5 shows the average \vec{x} and $\vec{\mu}$ vectors for all galaxies in our low z sample, obtained after collapsing the Z -axis (i.e., adding all components with same age but different metallicities). These distributions of mass and light with age are shown in both fractional (right panels) and cumulative forms (left).

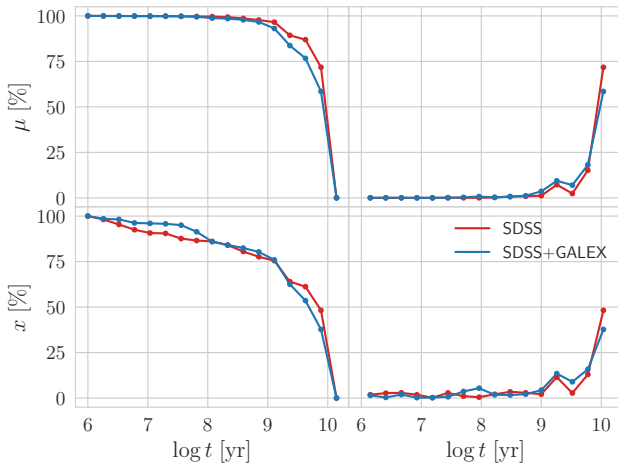


FIGURE 4.5: Average star formation histories calculated with and without photometric constraints. Top panels show cumulative (left) and non-cumulative (right) mass fractions as a function of age, while bottom panels show the corresponding curves in terms of light fractions at $\lambda_0 = 5635\text{\AA}$. Red lines show values for SDSS only STARLIGHT-fits and blue lines show values for SDSS+GALEX.

The addition of UV data shifts light fractions from the $< 10^7$ yr populations to slightly older ones, from 10^7 to 10^8 yr, as can be seen in the bottom panels of Figure 4.5. This is enough to prevent the overshooting of UV fluxes, but tends to produce a redder optical spectrum. To prevent this, STARLIGHT also removes contributions from the oldest stellar populations. The χ^2_{SPEC} values obtained with the addition of UV constraints are only marginally worse (by 3% on average) than those obtained with purely optical fits, confirming that the fitted optical spectra are kept essentially unchanged. When translating light fractions into mass fractions, the main difference

between the two types of fits lies in the older populations: Fits with UV constraints show a slower and smoother build-up of stellar mass at early epochs.

4.3.2 Star-formation histories in color-magnitude space

The sample averaged SFHs in Figure 4.5 mix very different kinds of galaxies. To get a sense of the diversity of SFHs in our sample and how they change with the addition of UV data, we calculated average light and mass fractions color-magnitude space. On the assumption that sources in a given locus of the CMD can be considered as a coeval population, these local averages are much less sensitive to sample selection effects. The results are plotted in Figure 4.6.

The largest changes in SFH occur for galaxies in the low-mass end of the blue cloud (bottom-right panels), where young stellar populations are more abundant and UV constraints are expected to play a larger role. The redistribution of $< 10^7$ and $> 10^9$ to 10^7 – 10^8 yr populations, which was the most noticeable change for the sample average, is very clear among these galaxies.

We also note that purely optical fits of red sequence galaxies (top panels) tend to wrongly identify very young populations ($t < 10$ Myr) at levels of $\sim 2\%$. These are the fake young bursts first identified by Ocvirk (2010) (see also Cid Fernandes & González Delgado 2010). The addition of UV data constrains these populations, thus averting the problem.

Overall, the differences between SFHs calculated with and without UV data become smaller with redder colors and increasing luminosity, i.e., as the contribution of old stars increase. For light fractions, our results are similar to the ones obtained by López Fernández et al. (2016). For mass fractions, however, there are differences. While López Fernández et al. (2016) finds faster rising cumulative $\mu(> t)$ curves for optical+UV fits than with purely optical ones in blue cloud galaxies, here we observe a trend in the opposite direction (as best seen in panel (w) of Figure 4.6). Besides the many differences in sample, data, aperture corrections and optical/UV weighing scheme, the current fits differ in the base models, which employ different isochrones and stellar libraries. We have verified that using base models compatible with those used by López Fernández et al. (2016) moves our $\mu(> t)$ curves closer to theirs. Limiting the optical fits to the same 3800–7000 Å range of their spectra further improves the agreement.

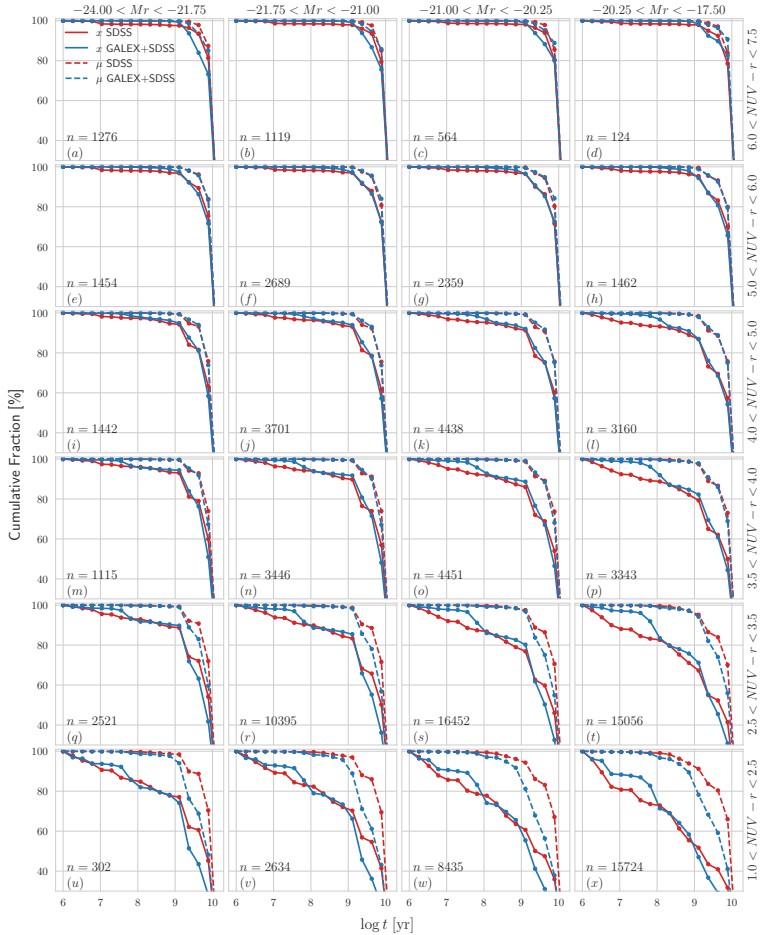


FIGURE 4.6: Average star-formation histories calculated with and without photometric UV constraints across the $NUV - r$ vs. M_r color-magnitude diagram. Solid lines show cumulative light fractions at $\lambda = 5635 \text{ \AA}$ while dashed lines show cumulative mass fractions. Red lines show results for pure SDSS fits and blue lines show results for combined GALEX+SDSS fits. Dots mark the edges of the CSP age bins. The number of galaxies in each bin (n) is indicated in the subplots.

4.4 Global properties

In addition to the population vectors discussed above, STARLIGHT also returns global properties such as mass and dust attenuation; other properties like mean stellar ages and metallicities can be calculated by reducing the dimensionality of the population vector. Figure 4.7 compares a series of these global properties derived with (y -axis) and without (x -axis) UV photometry. In order to highlight the general trends throughout the sample and give less weight to outliers, results are plotted as median curves with the region between 25 and 75% percentiles shaded in green. $\bar{\delta}$ and IQR values in each panel denote the median (bias) and interquartile region (scatter) of the difference between y and x values.

Panels (a) and (b) compare luminosity (at $\lambda = 5635\text{\AA}$) and mass weighted mean stellar ages, $\langle \log t \rangle_L$ and $\langle \log t \rangle_M$, respectively. In the case of $\langle \log t \rangle_L$ the bias is slightly positive ($\bar{\delta} = +0.04$ dex), and driven by the youngest systems, i.e., blue cloud galaxies, whose youngest populations shift from the $\log t = 6-7$ range to the next decade ($\log t = 7-8$) when UV constraints are used in the fits (see Figure 4.6). Mass weighted log ages (Figure 4.7b) are less sensitive to the recent SFH, thus spanning a much smaller range. Still, the negative bias of $\bar{\delta} = -0.04$ dex in $\langle \log t \rangle_M$ reflects how UV data leads STARLIGHT to bring down the contribution of the oldest stellar populations.

Panels (c) and (d) in Figure 4.7 show luminosity and mass weighted log metallicities, respectively. UV data makes the most metal-poor galaxies become slightly less so, although overall biases is zero for $\langle \log Z \rangle_L$ and negligible for $\langle \log Z \rangle_M$ ($\bar{\delta} = -0.01$ dex). López Fernández et al. (2016) find a larger negative bias in $\langle \log Z \rangle_M$, mostly due to late type, blue cloud galaxies, whose metallicities come out smaller in UV+optical fits. Again, this difference is due to differences in both data (mainly the spectral coverage in the optical) and ingredients in the analysis (base models). Repeating the analysis mimicking their setup we reproduce their results.

UV constraints do not affect the estimates of stellar masses, as seen in Figure 4.7(e). This is expected, given that we have seen that UV data mostly affects the youngest populations, which carry little mass. Somewhat more surprisingly, but in agreement with López Fernández et al. (2016), Figure 4.7(f) shows that, in general, optical and UV+optical fits produce similar estimates of the dust attenuation,

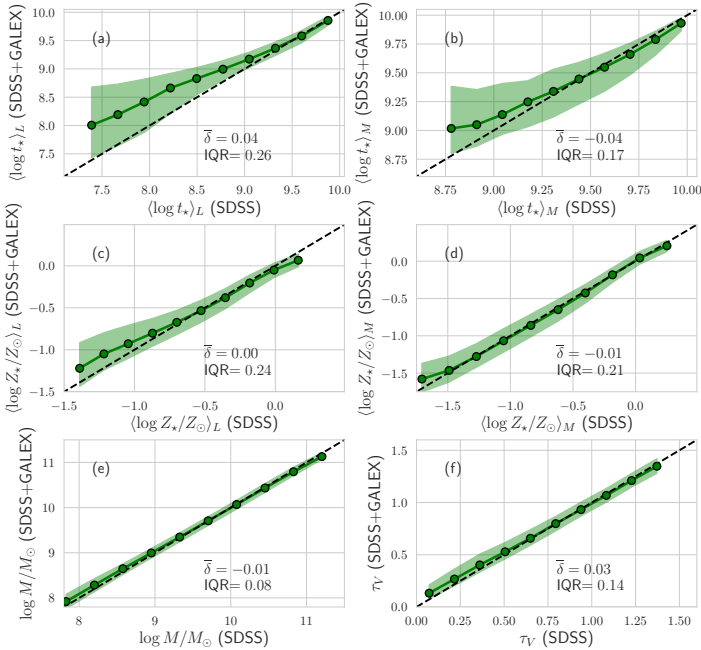


FIGURE 4.7: Comparison between galaxy properties derived with and without UV data. The y -axis corresponds to fits with UV constraints and the x -axis to fits to optical spectra, green lines show median curves with the center of each bin marked as a green dot with a black border. The region between 25 and 75% percentiles is shaded in green. Panels show mean stellar ages weighted by light (a) and mass (b), light (c) and mass (d) weighted mean stellar metallicities, stellar masses (e) and V-band dust optical depth (f). Dashed black lines show a $y = x$ relation. Median $y - x$ values ($\bar{\delta}$) and interquartile (IQR) regions are annotated on each panel.

here converted to dust optical depth τ_V . This counter-intuitive result will be dissected in the following section.

The median curves in Figure 4.7 highlight the general trends throughout the sample. As expected, there are points that fall out of this trend. This is the case for some galaxies with blue $NUV - r$ and

relatively red $FUV - NUV$, a combination of colors that is sometimes achieved by reddening very young populations. When this effect is in place, the addition of UV data makes galaxies significantly younger and more reddened, deviating from the relations shown in panels (a), (b) and (f) of Figure 4.7. This only happens for a small population of galaxies that bears no effect to the general trend, although this behavior is an interesting clue on galaxies that require two components of dust attenuation, which in principle could yield redder $FUV - NUV$, while having a smaller effect in $NUV - r$.

4.5 Effects on dust attenuation

As mentioned above, Figure 4.7f bears the unexpected result that no significant change in dust attenuation is found with the addition of UV constraints. While true for the general population of galaxies, there can be important changes in τ_V for galaxies dominated by young stars. This effect gets diluted in Figure 4.7, and its identification requires a more careful analysis.

A useful way to evaluate the sensitivity of our attenuation estimates to UV data is to investigate the relation between the far-UV attenuation (A_{FUV}) and the UV spectral slope (β , assuming $F_\lambda \propto \lambda^\beta$). This relation was originally found by Meurer, Heckman & Calzetti (1999) in a study of starburst galaxies³, and subsequently extended to larger and more diverse samples (Kong et al., 2004; Seibert et al., 2005; Buat et al., 2005; Burgarella, Buat & Iglesias-Páramo, 2005). A general conclusion from these studies is that the correlation between A_{FUV} and β found for starburst galaxies becomes much more scattered for more quiescent systems, indicating that the SFH plays an important role in the relation.

To build the relation from our data, we estimate the UV spectral slope from the $FUV - NUV$ color using $\beta_{GLX} = 2.286 (FUV - NUV) - 2.096$, as calibrated by Seibert et al. (2005). A_{FUV} is obtained from the Calzetti law, which gives $A_{FUV} = 2.53A_V$. In order to map the effects of the SFH we subdivide the sample into three bins in $\langle \log t_* \rangle_L$, the luminosity-weighted mean log age (evaluated at 5635 Å, as in Figure 4.7a).

The results of this analysis are shown in Figure 4.8, where A_{FUV} is plotted against β_{GLX} . The top panel shows the relations for A_{FUV}

³The relation also includes the ratio between far-infrared and UV luminosities (the IRX index), but this is not explored here.

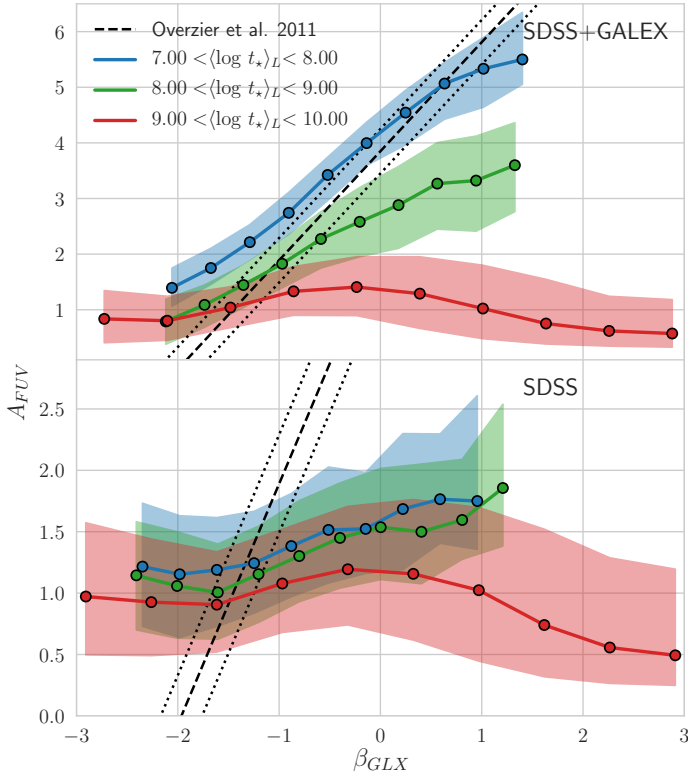


FIGURE 4.8: Relation between far-UV dust attenuation A_{FUV} UV power-law slope β for fits with (top) and without (bottom) UV data for three ranges of light-weighted mean stellar age $\langle \log t_* \rangle_L$. The relations are plotted as median curves with interquartile regions highlighted. Dotted and dashed lines represent the relation derived by Overzier et al. (2011).

obtained from SDSS+GALEX fits, while the bottom panel shows estimates of A_{FUV} derived from SDSS only. For comparison, we include the relation derived by Overzier et al. (2011): $A_{FUV} = 3.85 + 1.96\beta_{GLX} \pm 0.4$. In fits that include UV data, the relation is well reproduced in the younger age bin (analogous to starbursts),

with a smaller slope for intermediate $\langle \log t_* \rangle_L$ systems and no correlation for galaxies dominated by old stars. Overall this confirms the previous suggestions that the SFH has a major impact on the relation between A_{FUV} and β .

For SDSS-only fits, on the other hand, the relations are much weaker and more scattered, with no significant change in slope from the first to the second age bin. Note also that the values of A_{FUV} estimated from SDSS+GALEX fits for star-forming galaxies are compatible with the ones presented in the literature (eg. Meurer, Heckman & Calzetti 1999; Seibert et al. 2005; Overzier et al. 2011), while the values obtained from SDSS-only fits are underestimated.

Finally, a more technical but still important conclusion to be drawn from Figure 4.8 is that changes in stellar populations are not sufficient for STARLIGHT to reproduce the $FUV - NUV$ colors of galaxies with significant amounts of young stars. In these cases, an increase in dust attenuation is also required.

Chapter 5

Applications of the GALEX+SDSS Spectral Synthesis

Having compared properties derived with and without UV constraints, this section focuses on the results obtained with our combined UV + optical synthesis analysis. The goal here is to explore some of the learning possibilities offered by this combined approach.

The broad spectral range of these fits calls for an explicit assessment of the λ -dependence of luminosity-based descriptors of the SFH. This is the subject of section 5.1, where the cumulative light fraction SFHs across the CMD of Figure 4.6 are presented for a series of wavelengths from *FUV* to *z*. After that we address a series of unrelated astrophysical problems that benefit from our combined UV+optical analysis. Section 5.2 compares the SFHs of red-sequence ellipticals with (liney) and without (lineless) emission lines, in search for clues on why these otherwise similar galaxies differ in their emission line properties. Section 5.3 explores whether our UV+optical analysis can shed light on the issue of which attenuation law best describes dust attenuation in galaxies of different types. A preliminary study of the UV upturn in early-type galaxies is presented in section 5.4

5.1 Wavelength-dependent star formation histories

STARLIGHT-based studies make abundant use of the luminosity-weighted mean log age $\langle \log t \rangle_L$ and SFHs expressed in terms of the light fraction population vector \vec{x} (e.g. Cid Fernandes et al. 2005; Mateus et al. 2006; Asari et al. 2007; Cid Fernandes et al. 2013). Although mass-based descriptions of the SFH are more directly comparable to models, light-based descriptions bear a direct and much stronger relation to observed properties which form the basis of our empirical knowledge of galaxy evolution.

By their very definitions, STARLIGHT's light fractions and light-weighted mean stellar ages are λ -dependent. Chapter 4, for instance, presented results for $x(t)$ and $\langle \log t \rangle_L$ for $\lambda = 5635 \text{ \AA}$, an arbitrary wavelength chosen for no fundamental reason other than being in a relatively clean, feature-free window. The purpose of this section is to take advantage of this λ -dependence, examining stellar populations in the wavelength ranges in which they are most relevant. Particular attention is given to the GALEX bands, as they present clear descriptions of stellar populations that are easily overlooked (or even undetected) in the optical.

5.1.1 Spectral algebra: Converting $\vec{x}(\lambda_0)$ to $\vec{x}(\lambda)$

Consider a spectrum $L_\lambda = \sum L_{j,\lambda}$ built by superposing $j = 1 \dots N_\star$ components $L_{j,\lambda}$, and let $x_j(\lambda_0) = L_{j,\lambda_0} / L_{\lambda_0}$ be the fractional contribution of the j^{th} component to the total emission at λ_0 . Each $L_{j,\lambda}$ can be written as

$$L_{j,\lambda} = L_{j,\lambda_0} \left(\frac{L_{j,\lambda}}{L_{j,\lambda_0}} \right) = x_j(\lambda_0) L_{\lambda_0} \left(\frac{L_{j,\lambda}}{L_{j,\lambda_0}} \right) \quad (5.1)$$

where $x_j(\lambda_0) \equiv L_{\lambda_0} / L_{j,\lambda_0}$ quantifies the contribution of component j to the total emission at λ_0 . The term in between parentheses can be expressed in terms of ratio of the intrinsic (dust-free) luminosities, $b_{j,\lambda} \equiv L_{j,\lambda}^0 / L_{j,\lambda_0}^0$, and the ratio of attenuation factors at λ and λ_0 , so that

$$L_{j,\lambda} = x_j(\lambda_0) L_{\lambda_0} b_{j,\lambda} e^{-\tau_j(q_\lambda - q_{\lambda_0})} \quad (5.2)$$

where τ_j is the V-band effective optical depth of component j , and $q_\lambda \equiv \tau_\lambda/\tau_V$ is given by the reddening curve. In practice $\tau_j = \tau$ if only one attenuation is allowed for, as in the case in this paper. Notice also that $b_{j,\lambda}$ are just the base spectra normalized at λ_0 .

But $L_{j,\lambda}$ can also be equated to $x_j(\lambda)L_\lambda$, where L_λ is the total emission and $x_j(\lambda)$ is the fractional contribution of component j to this total spectrum at wavelength λ . Comparing these two expressions for $L_{j,\lambda}$ leads to the sought relation between $x_j(\lambda)$ and $x_j(\lambda_0)$:

$$x_j(\lambda) = \frac{x_j(\lambda_0) b_{j,\lambda}}{\sum_j x_j(\lambda_0) b_{j,\lambda}}, \quad (5.3)$$

which allows one to convert the light fraction population vector from a chosen normalization wavelength λ_0 to any other λ .

5.1.2 Wavelength-dependent SFHs in the CMD

With equation 5.3, we calculated light fractions for all GALEX and SDSS bands. Figure 5.1 shows the $x(> t, \lambda)$ cumulative light fractions as a function of age, as derived from our combined GALEX+SDSS fits. These λ -dependent descriptions of the SFH are broken into the same bins in the UV-optical CMD as in Figure 4.6. Colors code for the reference wavelength, as labeled in the top-left panel.

The $x(> t, \lambda)$ curves for the longer wavelengths like the r, i, and z bands rise faster for more massive galaxies (left panels) than for those of lower mass (right), revealing the usual downsizing pattern. Because of the small influence of young stars at these wavelengths these curves essentially reflect the mass growth curves previously shown in Figure 4.6. At UV wavelengths, on the other hand, the light is always dominated by $< 10^8$ yr populations, and the curves are similar for galaxies of different masses. Relevant changes in the *NUV* and *FUV* curves occur only in the vertical direction, with the proportion of 10^{6-7} to 10^{7-8} populations decreasing as *NUV* – *r* becomes redder.

Panels (i) to (l) show galaxies in the green valley, mostly populated by an intermediate population of recently quenched galaxies moving from the blue cloud to the red sequence. Accordingly, all $x(> t, \lambda)$ curves shift towards older ages. Unlike in the blue cloud, $> 10^8$ yr populations now contribute significantly even at UV wavelengths, particularly for the more massive galaxies.

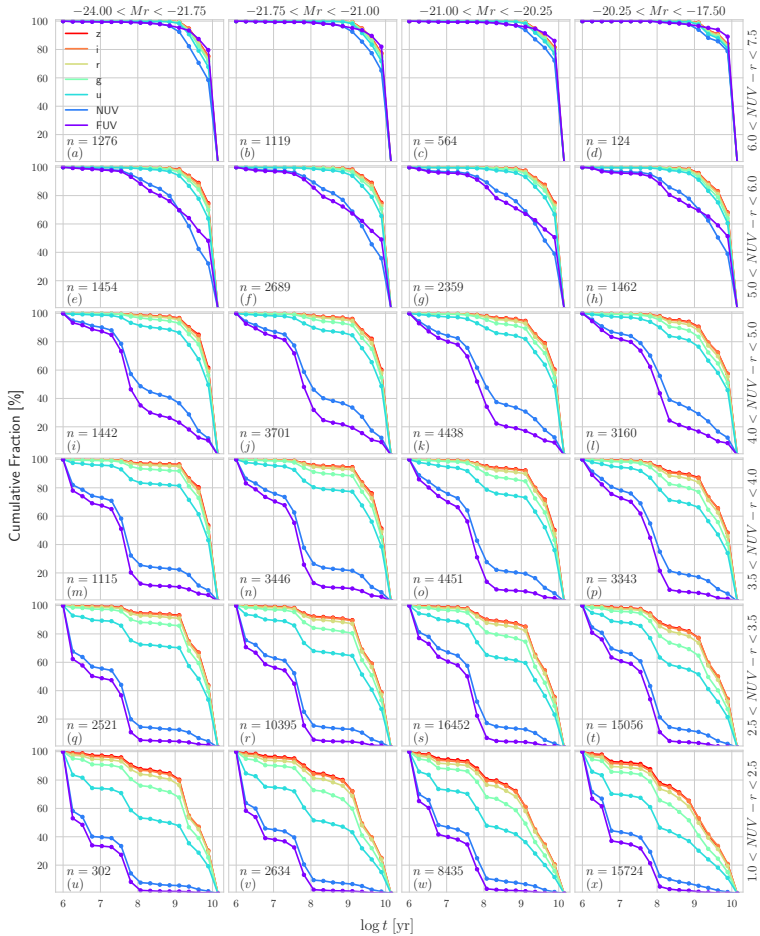


FIGURE 5.1: Average star formation histories for the same color-magnitude bins used on Fig 4.6, expressed as cumulative light fractions $x(> t, \lambda)$ in wavelengths corresponding to SDSS and GALEX bands. All curves correspond to results obtained in the combined GALEX+SDSS STARLIGHT fits.

Red sequence galaxies are shown in the top two rows of Figure 5.1. For galaxies in panels (e) to (h), intermediate age populations are still relevant, while galaxies in the upper red-sequence (top row,

panels a to d) are completely dominated by old stellar populations, even in the UV.

The evolutionary synthesis models used in this work become redder in $FUV - NUV$ up to stellar ages of 1 Gyr. After that the model spectra become bluer in the UV, and after about 4 Gyr the stellar populations emit more FUV per M_{\odot} than immediately younger populations. This results in a rise on the contribution of the oldest populations to FUV light, surpassing their contribution to the NUV . This tendency is connected to the UV upturn phenomenon, since at constant $NUV - r$ the contribution of old populations to FUV light correlates with $FUV - NUV$ color.

5.2 Liny and lineless retired galaxies

Up until now, we have used the UV-optical color-magnitude diagram as our guide to subdivide our sample into intelligible sub-classes. This diagram provides information on galaxy evolution and the bimodality of the local galaxy population. However, galaxies are complex systems, and no single diagram condenses all the information needed to describe them. Another popular way to divide the galaxy population is based on emission line diagrams. This type of classification separates galaxies with different sources of ionizing photons, an aspect that hasn't yet been touched in this work.

5.2.1 Wavelength-dependent SFHs in the WHAN diagram

A popular emission line based classification is the one based on the WHAN diagram, introduced by Cid Fernandes et al. (2011). This classification is based in the $[NII]\lambda 6584/H\alpha$ flux ratio and the $H\alpha$ equivalent width, given by

$$W_{H\alpha} = \int_{\lambda_1}^{\lambda_2} \left(1 - \frac{F_{\lambda,L}}{F_{\lambda,C}} \right) d\lambda, \quad (5.4)$$

where $F_{\lambda,L}$ and $F_{\lambda,C}$ are the fluxes per unit wavelength of the line and the continuum and λ_1 and λ_2 are arbitrary limits set to 6555\AA and 6575\AA , respectively.

The main advantage of the WHAN diagram over those based solely on line ratios (e.g. Baldwin, Phillips & Terlevich 1981) is

that it can identify retired galaxies (Stasińska et al., 2008; Stasińska et al., 2015), a class of galaxies that can be misclassified as AGN in other diagrams, even though their ionization field is dominated by H_OT Low Mass Evolved Stars (HOLMES) typical of old stellar populations. Retired galaxies are characterized by having $W_{\text{H}\alpha} < 3 \text{ \AA}$ and can be further subdivided into liny ($0.5 < W_{\text{H}\alpha} < 3 \text{ \AA}$) and lineless ($W_{\text{H}\alpha} < 0.5 \text{ \AA}$) systems, according to the presence or absence of emission lines. Other classes defined in the WHAN diagram are star-forming (SF; $\log[\text{NII}]\lambda 6584/\text{H}\alpha < -0.4$ and $W_{\text{H}\alpha} > 3 \text{ \AA}$), strong AGN (sAGN; $\log[\text{NII}]\lambda 6584/\text{H}\alpha > -0.4$ and $W_{\text{H}\alpha} < 6 \text{ \AA}$) and weak AGN (wAGN; $\log[\text{NII}]\lambda 6584/\text{H}\alpha > -0.4$ and $3 < W_{\text{H}\alpha} < 6 \text{ \AA}$)

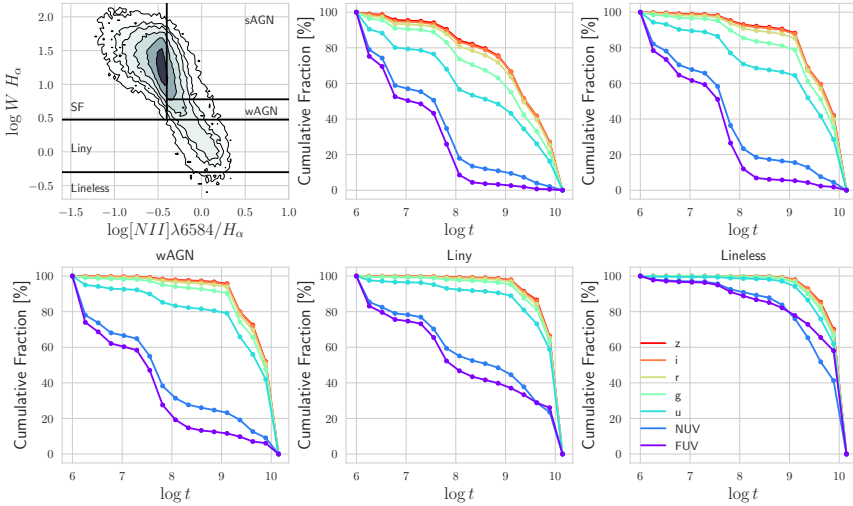


FIGURE 5.2: Wavelength dependent SFHs for galaxy classes defined in the WHAN diagram. Top left panel shows the WHAN diagram with the definition of the classes, other panels show λ -dependent SFHs for each of the five classes. Color codes are the same as in Fig 5.1.

The WHAN diagram for our sample is shown in Figure 5.2, with λ -dependent SFHs for each of the five classes. Although the UV population vectors highlight differences between all classes, most trends are as expected and can already be identified from optical bands: Star-forming galaxies are the youngest, followed by strong and weak AGN. However, the population vectors at UV wavelengths show

a distinction between the formation histories of liny and lineless retired galaxies that cannot be identified in the optical. This result will be discussed in the following subsection.

5.2.2 Differences between liny and lineless retired galaxies

The fact that some retired galaxies lack emission lines poses an interesting astrophysical problem, since the HOLMES in both subclasses produce ionizing photons enough to power line emission.

Through a pair-matching analysis, Herpich et al. (2018, hereafter H18) were able to identify very small but consistent differences between the two sub-classes of retired galaxies. Compared to lineless systems, liny ones tend to be brighter in the GALEX *NUV* and WISE *W3* bands, and have slightly smaller 4000 Å breaks. These results are indicative of differences in dust content and SFHs. These differences in SFH, however, are hard to measure directly in the optical.

As shown in Figure 5.2, the UV population vectors provide a clearer separation between the SFHs of liny and lineless retired galaxies. We will now take a closer look at the problem; to this end, we have refined our selection of retired galaxies: In addition to the $W_{\text{H}\alpha}$ criterion we also require galaxies to be classified as ellipticals by Galaxy Zoo. Out of the 16206 retired galaxies in this refined sample, 12% are lineless and the remaining are liny. We also divide the retired galaxy sample into four bins of stellar mass to control for downsizing effects.

Figure 5.3 shows mean cumulative light fraction curves for lineless (top panels) and liny (bottom panels) galaxies in the four mass ranges mentioned above. As in Figures 5.1 and 5.2, each panel shows the $x(> t)$ curves for seven wavelengths corresponding to the GALEX and SDSS filters. Variations in the curves from left to right panels reflect the well known downsizing pattern, with less massive galaxies having SFHs that are more extended in lookback time. The SFHs for the UV bands clearly show that liny galaxies experienced a more extended period of star-formation, a trend that is consistent in all mass ranges. The same signal is present in the $x(> t)$ curves for optical wavelengths, but at a much reduced amplitude.

Though populations of a few Myr may be present in low mass liny galaxies, the main difference is an excess of intermediate age populations ($\sim 0.1\text{--}1$ Gyr). This directly shows that the presence or absence of emission lines in retired galaxies is connected to slightly

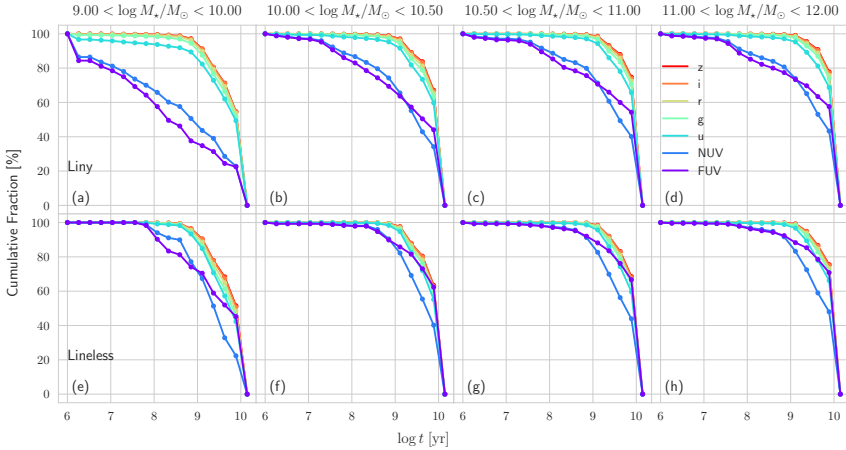


FIGURE 5.3: Wavelength dependent SFHs for liny (top row) and lineless (bottom row) retired galaxies divided into four mass ranges. Color codes are the same as in Fig 5.1.

different SFHs. H18 interprets this as due to an external reservoir of cold gas that is slowly accreted by liny galaxies, feeding a low level of star-formation over an extended period of time. In contrast, lineless systems exhausted their gas supply at an early epoch, leaving little or no gas to react to the ionizing radiation field produced by their HOLMES.

Another difference between these galaxy classes is the larger dust content in liny galaxies. The optical-only analysis on H18 is already capable of identifying higher τ_V values for liny galaxies at all mass ranges, a result that is confirmed here for both optical and UV+optical fits. Consistently with the H18 findings, we identify an average difference of $\Delta\tau_V = 0.15$ between liny and lineless galaxies.

5.3 Comparing results for different attenuation laws

Previous experiments with STARLIGHT found that spectral fits in the optical cannot distinguish among different choices of dust attenuation law. Asari et al. (2007), for instance, show that equally good fits are obtained with $q_\lambda = A_\lambda/A_V$ functions representative of the

Milky-Way, Magellanic Clouds, or starburst galaxies. This degeneracy is hardly surprising, given that the main differences between these alternative laws lies not in the optical, but in the UV.

One of the advantages of incorporating UV data in the STARLIGHT analysis is that it allows us to revisit this issue and investigate which dust attenuation law best fits the data. In this section we compare results obtained with the CAL and CCM laws, whose most notable difference is presence or absence of the UV bump at $\lambda \sim 2175 \text{ \AA}$. Given the overlap with the *NUV* filter, this feature is bound to affect our analysis. *FUV* fluxes are also affected by the choice of q_λ , given that the CCM law have a steeper far-UV slope, even though slopes in the optical are similar. Though the CAL and CCM laws do not span the wealth of dust attenuation effects studied in the literature (see Noll et al. 2009; Seon & Draine 2016; Salim, Boquien & Lee 2018; Narayanan et al. 2018), they serve as useful limits to investigate the effect of the bump. Moreover, they are both commonly used in STARLIGHT-based studies.

Qualitatively one expects fits using a CAL law to produce larger residuals in the UV than fits with a CCM law for galaxies with relevant UV bumps, and vice versa. It is therefore interesting to compare the UV residuals obtained with these two laws. To evaluate the quality of the fits in the UV let us use

$$\chi_{UV} = \sqrt{\frac{1}{2}\chi_{\text{PHO}}^2}, \quad (5.5)$$

which gives an average of the *NUV* and *FUV* reduced residuals.

For this analysis we will restrict the sample to galaxies with $NUV - r < 5$ that are classified as spirals by Galaxy Zoo. On the other hand we do allow systems beyond $z = 0.1$ in order to trace the effect of the *NUV* band moving out of the UV bump region as redshift increases. These cuts yield a sample of 81214 galaxies.

Figure 5.4 shows histograms of χ_{UV} for the CAL and CCM laws. The mean and rms values of χ_{UV} are 0.22 ± 0.26 for the CAL law and 0.41 ± 0.36 for CCM. The inset shows the histogram of $\Delta\chi_{UV} = \chi_{UV}^{\text{CAL}} - \chi_{UV}^{\text{CCM}}$. Over our whole sample $\Delta\chi_{UV}$ averages to -0.18 , showing that the CAL law is generally preferred over CCM.

We find that the main parameters controlling how worse the fits get with the CCM law are τ_V and redshift. Trends with mass and star-formation rate were also investigated, but we found no visible dependence of $\Delta\chi_{UV}$ with these parameters at fixed τ_V and redshift. In Figure 5.5, we plot median curves of $\Delta\chi_{UV}$ as a function of τ_V for

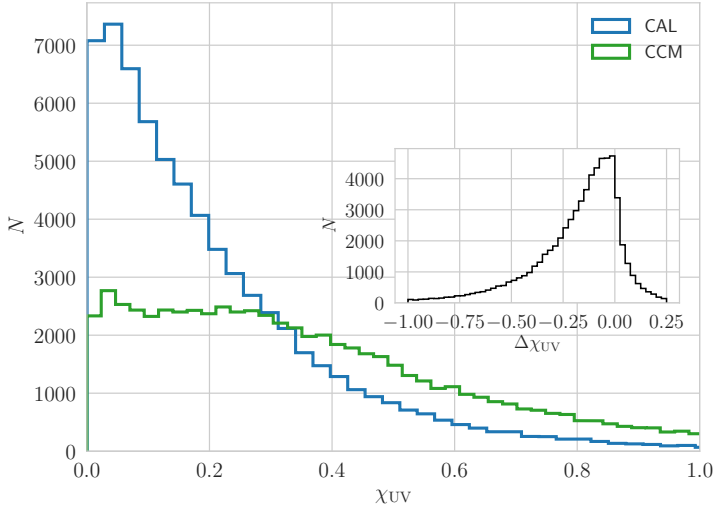


FIGURE 5.4: Histograms of χ_{UV} for the CAL attenuation (blue) and CCM extinction (green) laws. The inset shows the distribution of $\Delta\chi_{UV} = \chi_{UV}^{CAL} - \chi_{UV}^{CCM}$. Galaxies in these histograms are all Galaxy Zoo spirals with $NUV - r < 5$.

four different ranges in z . The τ_V values used in this plot are those derived from purely optical fits with a CAL attenuation law, which are independent from the UV. The plot shows that, in comparison with CCM, the CAL law yields progressively better fits of the GALEX photometry as τ_V increases. The systematic behavior shown in Figure 5.5 is expected to a certain degree, since the bump level is amplified as τ_V increases. Moreover, the quasi-universal relation between τ_V and the slope of the attenuation curve at any wavelength found by Chevillard et al. (2013) (and confirmed by Salim, Boquien & Lee 2018) also takes the results in this direction by favoring a steeper slope (MW-like) for low τ_V . The effects of redshift are also evident in this plot. At fixed τ_V , the $\Delta\chi_{UV}$ is largest (in modulus) at low redshift (blue curves in Figure 5.5). As redshift increases the CAL and CCM laws yield increasingly similar χ_{UV} . We interpret this as due to the gradual shifting of the UV bump away of the NUV band as redshift increases. To first order this makes the two laws similarly bump-less, although differences in far-UV slope between the two q_λ functions persist.

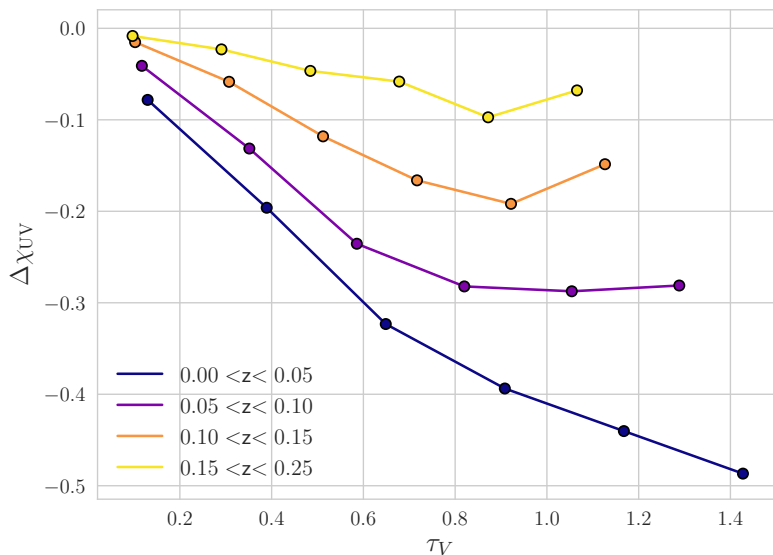


FIGURE 5.5: Median $\Delta\chi_{UV}$ plotted against dust optical depth τ_V in different bins of redshift. The center of the bins used to calculate the medians are indicated as points.

Overall, the results in Figure 5.5 indicate that the attenuation curves of the general population of spiral galaxies either lack the features that distinguish the MW extinction curve or exhibit them at a less significant level. This is compatible with other studies that generally find a small level of the bump both locally (Conroy, Schiminovich & Blanton, 2010; Wild et al., 2011; Salim, Boquien & Lee, 2018), and at higher redshift (Kriek & Conroy, 2013; Reddy et al., 2015). For instance, Buat et al. (2011) find an average bump amplitude of 35% the MW value for galaxies at $z > 1$. Similarly to our results, Battisti, Calzetti & Chary (2016) find that the population of local star-forming galaxies can be described by a CAL-like law, but small levels of the bump cannot be discarded. This is not indicative, however, that the dust grain population in the MW is somewhat unusual, as recent models show that a bumpless attenuation law can arise even when the underlying extinction curve is MW-like (Narayanan et al., 2018).

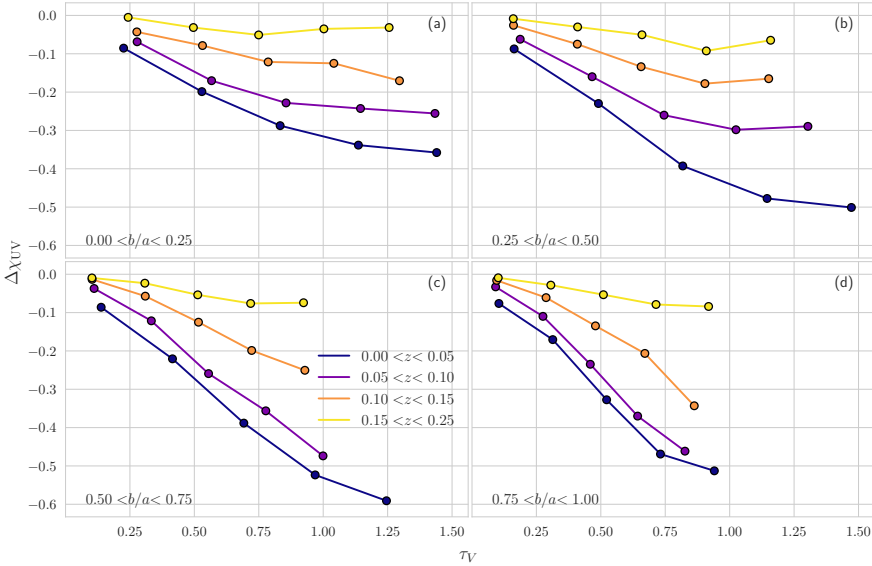


FIGURE 5.6: Median $\Delta\chi_{UV}$ plotted against dust optical depth τ_V in different bins of redshift in four ranges of inclination b/a . Edge-on galaxies are shown in the left and face-on galaxies in the right.

Identifying a population of galaxies with relevant UV-bumps in our data-set is not straightforward, since the relation of $\Delta\chi_{UV}$ with attenuation is so strong that it contaminates other correlations. For instance, a key parameter in this analysis is galaxy inclination, but, since b/a correlates strongly with attenuation, plotting it against $\Delta\chi_{UV}$ would only show the reverberation of the correlation of both variables with τ_V . An attempt to isolate the effects of galaxy inclination in the shape of the attenuation curve is shown in Figure 5.6, where we repeat Figure 5.5 splitting the sample in four ranges of b/a . Edge-on galaxies are shown on the top left and face-on ones on the bottom right. As in Figure 5.5, we are unable to identify a significant population of galaxies that is best fitted with the CCM law. That aside, a trend is clear in Figure 5.6: fits with the CCM law get worse with decreasing inclination (increasing b/a).

This goes in the direction of the results of Conroy, Schiminovich & Blanton (2010), although in that work it is found that a MW-like

extinction law is required to fit the UV spectral slope of highly inclined galaxies, while we find only that these are the galaxies where MW law works best. Even in these cases our results are better for the CAL law. The relation of $\Delta\chi_{UV}$ with inclination is consistent with the idea that the shape of the MW extinction curve in the UV is associated with diffuse dust (Wild et al., 2011), while the CAL law is best-suited for birth clouds. As galaxy inclination increases, the amount of dust from birth clouds in our line of sight stays constant, while the column of diffuse dust increases. In this interpretation, highly inclined galaxies should show attenuation curves with shapes closer to the MW extinction law, as seen in Figure 5.6. However, this result is not universal. For instance, the radiative transfer models of Pierini et al. (2004) show a decrease in the bump for edge-on galaxies.

Our analysis is sufficient to showcase the potential of combined SDSS+GALEX STARLIGHT fits in distinguishing between dust attenuation laws. A more thorough analysis, exploring laws with different slopes and bump strengths (e.g., Noll et al. 2009), as well as fits with a population-dependent dust attenuation (Charlot & Fall 2000) is deferred to a future study.

5.4 The UV upturn in early-type galaxies

Some early-type galaxies exhibit a phenomenon called "the UV upturn": a rise in the far UV flux with decreasing wavelength.

Figure 5.1 hints that some degree of UV upturn is common among early-type galaxies, given that old ($t > 10^9$) stellar populations emit more *FUV* than *NUV* per solar mass, which in turn results in blue *FUV* – *NUV* colors on optically red galaxies (see Figure 4.2). This rise on *FUV* contribution from old stellar populations is visible throughout the entire red sequence, consistently with what was recently found by Ali et al. (2018). Galaxies in the lower red-sequence ($5 < NUV - r < 6$), however, still retain enough younger (or not so old) stars to keep the upturn undetected. In the upper red-sequence the populations responsible for the upturn are dominant, producing bluer *FUV* – *NUV* colors. To investigate this further, we have selected a sample of UV upturn galaxies using the criteria from Yi et al. (2011): $NUV - r > 5.4$, $FUV - NUV < 0.9$ and $FUV - r < 6.6$. Furthermore, we also require galaxies to be classified as ellipticals by Galaxy Zoo, resulting in a sample of 526 UV upturn galaxies.

But before we take a closer look at the UV upturn, let us see if we can do a better job in fitting the FUV magnitudes of these galaxies. Our standard fits underestimate the FUV of some UV upturn galaxies, this has to do with the fact that the populations with stronger upturns are the very old ones, and their effect gets diluted when calculating the CSPs used as our STARLIGHT base. To mitigate this issue, we have built a base optimized for this type of object by splitting the oldest CSP bin of our standard base into five and allowing for an extra metallicity ($Z = 0.02$). We remind the reader that our models only include the upturn from post-AGB stars (central stars of planetary nebulae). In Figure 5.7 we check how this optimized base performs in comparison to our standard base by plotting histograms of

$$\chi_{FUV} = \sqrt{\left(\frac{FUV_{\text{obs}} - FUV_{\text{mod}}}{\sigma_{FUV}}\right)^2} \quad (5.6)$$

for both bases. Only our 526 UV upturn galaxies are included in the Figure. The optimized base fares significantly better, reproducing 62% of observed values within 0.25 magnitudes, against 42% for the standard base. However, a substantial amount of UV upturn galaxies is still not correctly modeled taking only post-AGBs into account, indicating that additional processes such as binary interactions may be required (e.g Hernández-Pérez & Bruzual, 2014).

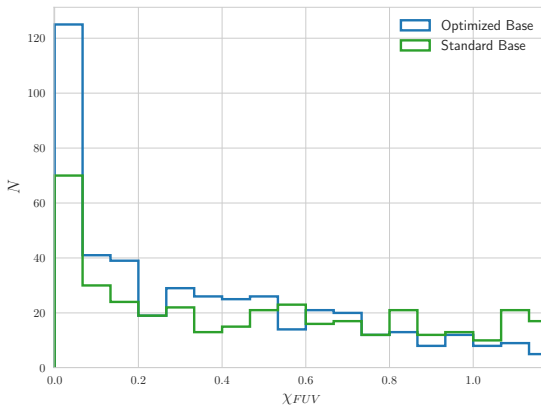


FIGURE 5.7: Histograms of χ_{FUV} of UV upturn galaxies for fits performed with our standard base (green) and for an optimized base (blue).

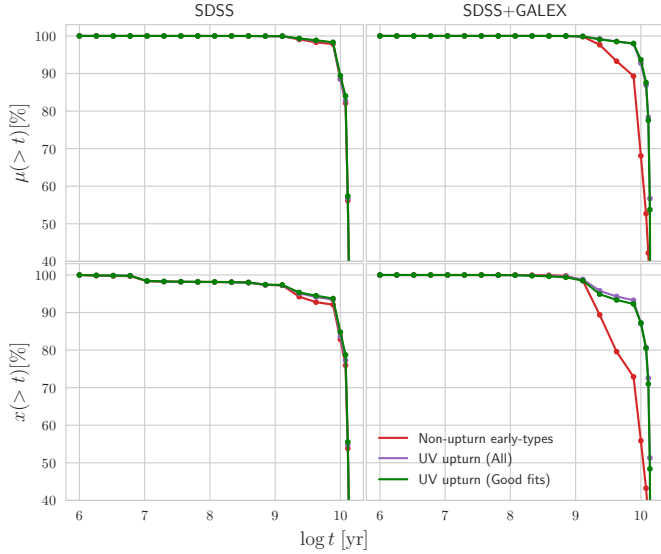


FIGURE 5.8: Average star-formation histories of UV upturn galaxies obtained with (right) and without (left) UV constraints. The average SFH for UV upturn galaxies for which $|FUV_{\text{obs}} - FUV_{\text{mod}}| < 0.25$ is plotted in green and the average for all UV upturn galaxies is plotted in purple. In red we plot the average SFH for red sequence galaxies without an UV upturn that are classified as ellipticals by Galaxy Zoo.

Star-formation histories of UV upturn galaxies obtained with the optimized base are plotted in Figure 5.8, a distinction is made between UV upturn galaxies for which $|FUV_{\text{obs}} - FUV_{\text{mod}}| < 0.25$ (green) and the complete sample of UV upturn galaxies (purple). SFHs in red show a population of early-types without UV upturn that are classified as ellipticals by Galaxy Zoo and have $NUV - r > 5$. Left panels show SFHs for optical-only fits, on which almost no difference is detected between UV upturn galaxies and other early types. On the right, we plot SFHs obtained with UV+Optical data, where we can clearly see that galaxies with the UV upturn present an excess of old stellar populations in comparison to other early-types. This result is not remarkable on itself, as it only reflects the fact that the stellar populations with the strongest upturns are the oldest ones. However, it showcases the potential of the UV upturn to provide

constraints to distinguish between very old stellar populations that are very similar in the optical.

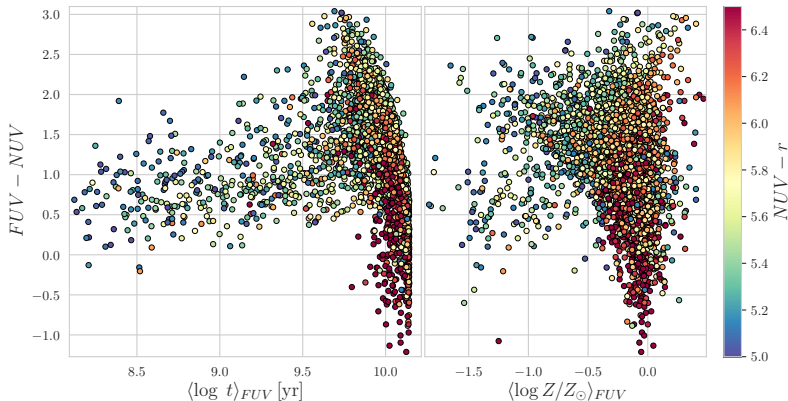


FIGURE 5.9: FUV averaged stellar ages ($\langle \log t_* \rangle_{FUV}$) and metallicities ($\langle \log Z_*/Z_\odot \rangle_{FUV}$) plotted against $FUV - NUV$ color. Points are colored by $NUV - r$.

It is also interesting to investigate what populations account for the UV emission throughout the red sequence in general, not only for UV upturn galaxies. For this, we introduce the FUV averaged stellar ages and metallicities defined as

$$\langle \log t_* \rangle_{FUV} = \sum_{j=1}^{N_*} x_j^{FUV} \log t_j \text{ and } \langle Z_* \rangle_{FUV} = \sum_{j=1}^{N_*} x_j^{FUV} Z_j. \quad (5.7)$$

which are analogous to STARLIGHT's mean light weighted ages, but using the FUV population vector to set the weights. These quantities measure the average age and metallicities of the populations responsible for FUV emission. In Figure 5.9 we plot $\langle \log t_* \rangle_{FUV}$ and $\langle \log Z_*/Z_\odot \rangle_{FUV}$ against $FUV - NUV$ for red sequence elliptical, coloring points according to $NUV - r$. For age (left panel), the distribution is somewhat bimodal. On the left of the plot are galaxies with relatively blue $FUV - NUV$ due to young stellar populations, these systems are more common in the lower red sequence, as evidenced by their $NUV - r$ values. More quiescent systems are on the right, with increasingly older $\langle \log t_* \rangle_{FUV}$ as $FUV - NUV$ becomes bluer.

As seen in other Figures UV upturn galaxies (bottom right of the plot) are more common among the upper red sequence. On the right hand side of the Figure, we see that populations of high metallicity are increasingly relevant for FUV emission as $FUV - NUV$ increases. Its also interesting to note that metal-poor populations are quite relevant for the FUV emission at the lower red sequence, in agreement to what is seen for $\langle \log t_* \rangle_{FUV}$.

Chapter 6

Final remarks

*“The philosopher
You know so much
About nothing at all”*
— Death, The Philosopher

This thesis has come to a somewhat anti-climatic ending: Although the combination of spectroscopic and photometric data in a nonparametric method represents an achievement in population synthesis, more work is needed to explore the full scientific potential of our method. In this final Chapter, we will summarize the contributions of this thesis to the field of galaxy spectral synthesis and point to scientific questions that can still be explored.

6.1 Conclusions

Our overall goal in this work was to perform the spectral synthesis of a combination of SDSS spectra and GALEX photometry. To this end, in Chapter 2, we have developed a method to estimate GALEX UV magnitudes in apertures consistent with SDSS spectra. Tests indicate that this method produces very little bias, but considerable scatter, making it suitable for statistical analysis of large data-sets, though not for individual sources. We have also shown that our method is compatible with the one from Battisti, Calzetti & Chary (2016).

We also improved upon the version of STARLIGHT used by López Fernández et al. (2016) (Chapter 3), introducing a new method for combining spectroscopic and photometric figures of merit. Other improvements on the code remain under the hood as we work towards a public distribution of this new version of STARLIGHT.

In Chapter 4, we used the new code to simultaneously analyze SDSS spectra and GALEX photometry, retrieving stellar population properties of 231643 galaxies. Our overall results agree with previous work based on CALIFA+GALEX data, with few exceptions introduced by differences in stellar population models and spectral coverage. As seen in Figure 4.3, with the addition of UV constraints STARLIGHT has to bring UV fluxes down without producing a redder optical spectrum. To achieve this, the code attributes larger light fractions to stellar populations with 10^7 to 10^8 yr, while cutting from the contribution of very young and very old stars to maintain optical colors.

As seen in Figure 4.7, this behavior produces slightly older mean stellar ages when weighted by light, and slightly younger when weighted in mass. We find a slight increase in metallicity in the most metal-poor systems and no change is observed in stellar mass. We also find an increase in dust attenuation, but restricted to a population of galaxies dominated by young stars (Figure 4.8).

After performing the synthesis and evaluating changes in physical properties, we proceed to explore a set of scientific questions that depend on ultraviolet information.

In section 4.5, we show that our results reproduce the $\beta \times A_{FUV}$ relation from Meurer, Heckman & Calzetti (1999) for galaxies dominated by young stars, which are comparable to the starburst galaxies in the original relation. A weaker trend is observed in galaxies with fewer young stars and no relation is observed for galaxies where stellar populations are mostly old. This relates the scatter in the $\beta \times A_{FUV}$ relation to a diversity of star-formation histories, as argued by Kong et al. (2004) and Grasha et al. (2013); although our work doesn't account for the effects of the variation in the shapes of attenuation laws, which is presented by Salim & Boquien (2019) as the main driver for the scatter in the relation.

In section 5.1, we calculated wavelength-dependent star formation histories in color-magnitude space. As expected, UV light fractions are good tracers of recent star formation in the blue cloud, while optical bands are mostly tracers of old stellar populations. We find a significant contribution of young stellar populations to the UV emission in the green valley and a small contribution in the faint end of the lower red-sequence. In the upper red-sequence, UV emission is dominated by the UV upturn phenomenon, which is also present to a smaller extent in the lower red-sequence. The ability of the code in distinguishing between different sources of UV emission in

early-type galaxies is remarkable, as evidenced by Figure 5.9.

We also identify that UV light fractions are able to distinguish the stellar populations of liny and lineless retired galaxies, classes whose small differences in SFH are barely noticeable in the optical. Our results confirm the ones from Herpich et al. (2018), indicating that liny retired galaxies have undergone a more extended period of star-formation.

In section 5.3, we showcase our ability to distinguish between attenuation laws of different shapes, while keeping a non-parametric analysis of stellar populations. Our results for the law of starburst galaxies of Calzetti et al. (2000) are systematically better than the ones for the MW law of Cardelli, Clayton & Mathis (1989), although the MW law fares better in highly inclined systems, which evidences the effect of star-dust geometry in the shape of attenuation laws, as discussed by Seon & Draine (2016) and Narayanan et al. (2018). A complete study on this topic, however, would have to include laws of different slopes and bump strengths (e.g Noll et al. 2009; Salim, Boquien & Lee 2018).

We find that our stellar population models are able to fit the *FUV* emission of UV upturn galaxies (as defined by Yi et al. 2011) within 0.25 magnitudes in 62% of cases. Since the UV upturn in our models comes solely from post-AGB stars, its likely that additional components such as binary stars are required to account for *FUV* emission in the remaining 38%. Despite this limitation, STARLIGHT is able to distinguish between galaxies where *FUV* emission is due old stars and systems with residual levels of recent star formation where *FUV* emission is due to young stellar populations.

6.2 Reveries about future work

Despite our contributions to the field of spectral synthesis, this work opens more issues than it closes. The full potential of the data-set provided by our analysis is beyond what is explored in this thesis, where we presented a limited amount of case-studies.

One of our main limitations is having a fixed attenuation law. Forcing the shape of the attenuation law may lead STARLIGHT to compensate the intrinsic curve by changing the stellar populations. The analysis of a grid of laws would allow a proper study of the shapes of attenuation curves in local galaxies, including effects such as the relation between τ_V and bump strength and its variation with

galaxy properties. Future studies may also include a two-component model for dust absorption, which would match well with a flexible attenuation curve. Such a thorough treatment of attenuation would allow us to disentangle the effects of dust and SFHs in the scatter of the Meurer, Heckman & Calzetti (1999) relation between β , IRX and A_{FUV} .

We have shown that the UV upturn phenomenon can serve as constraint on the early evolution of early-type galaxies, even with the limitations from our models. This could be combined with data on environment or kinematics on these galaxies to better understand their formation histories.

A promising application that hasn't been touched in this work is the combination of IFU spectra with photometry. In the case of the MUSE (Multi Unit Spectroscopic Explorer; Henault et al. 2003) spectrograph, photometry could provide measurements of the blue part of the stellar continuum, supplementing the main (perhaps the only) weakness of the instrument for local universe studies. Combining IFU data with high resolution photometry from the Hubble Space Telescope or the UV Imaging Telescope (Kumar et al., 2012) would allow for a spatially resolved version of the work presented in this thesis.

Moreover, the synthetic spectra obtained in our analysis provide a reliable set of stellar templates to measure photometric redshifts of galaxies at redshifts where the UV emission is shifted to the optical. This application is being pursued with data from the S-PLUS and J-PAS (Benitez et al., 2014) surveys. It should be noted, however, that this application depends on adding a nebular component to our synthetic spectra.

Appendix A

SQL query used for sample selection

This query was design to run in the GALEX CasJobs (<http://galex.stsci.edu/casjobs/>).

```

1  /* Run on MAST database (GALEX GR6/7 context) */
2
3  SELECT
4
5  /*    Identifiers and Basic Spectral Information:    */
6  ps.objid, ss.specObjID, ss.bestObjID, pg.objid as GALEXObjID,
7  x.SDSSobjid as matchID, ss.mjd, ss.plate, ss.fiberID, ps.ra as RA,
8  ps.dec as Dec, pg.ra as GALEXRA, pg.dec as GALEXDec, ss.z,
9  ss.legacy_target1 as spec_bitmask,
10
11 /*    Match Info    */
12 x.MultipleMatchCount, x.reverseMultipleMatchCount, x.distancerank,
13 x.dstArcSec as matchtdistance,
14
15 /*    Geometric Parameters(Optical):    */
16 ps.petroRad_u, ps.petroRad_g, ps.petroRad_r, ps.petroRad_i, ps.petroRad_z,
17 ps.petroRadErr_u, ps.petroRadErr_g, ps.petroRadErr_r, ps.petroRadErr_i,
18 ps.petroRadErr_z, ps.petroR50_u, ps.petroR50_g, ps.petroR50_r, ps.petroR50_i,
19 ps.petroR50_z, ps.petroR90_u, ps.petroR90_g, ps.petroR90_r, ps.petroR90_i,
20 ps.petroR90_z, ps.petroR50Err_u, ps.petroR50Err_g, ps.petroR50Err_r,
21 ps.petroR50Err_i, ps.petroR50Err_z, ps.petroR90Err_u, ps.petroR90Err_g,
22 ps.petroR90Err_r, ps.petroR90Err_i, ps.petroR90Err_z,
23
24 ps.deVAB_u, ps.deVAB_g, ps.deVAB_r, ps.deVAB_i, ps.deVAB_z, ps.deVABErr_u,
25 ps.deVABErr_g, ps.deVABErr_r, ps.deVABErr_i, ps.deVABErr_z,
26
27 /*    Fiber Magnitudes:    */
28 ps.fiberMag_u, ps.fiberMag_g, ps.fiberMag_r, ps.fiberMag_i, ps.fiberMag_z,
29 ps.fiberMagErr_u, ps.fiberMagErr_g, ps.fiberMagErr_r, ps.fiberMagErr_i,
30 ps.fiberMagErr_z,

```

```

31
32 /*      Petrosian Magnitudes:      */
33 ps.petroMag_u, ps.petroMag_g, ps.petroMag_r, ps.petroMag_i, ps.petroMag_z,
34 ps.petroMagErr_u, ps.petroMagErr_g, ps.petroMagErr_r, ps.petroMagErr_i,
35 ps.petroMagErr_z,
36
37 /*      Model Magnitudes (UV):      */
38 pg.NUV_MAG_AUTO, pg.FUV_MAG_AUTO, pg.NUV_MAGERR_AUTO, pg.FUV_MAGERR_AUTO,
39 pg.NUV_FLUX_AUTO, pg.FUV_FLUX_AUTO, pg.NUV_FLUXERR_AUTO, pg.FUV_FLUXERR_AUTO,
40
41 pg.nuv_mag, pg.fuv_mag, pg.nuv_magerr, pg.fuv_magerr,
42
43 /*      3 arcsec Aperture Magnitudes (UV):      */
44 pg.NUV_MAG_APER_1, pg.FUV_MAG_APER_1, pg.NUV_MAGERR_APER_1,
45 pg.FUV_MAGERR_APER_1, pg.NUV_FLUX_APER_1, pg.FUV_FLUX_APER_1,
46 pg.NUV_FLUXERR_APER_1, pg.FUV_FLUXERR_APER_1,
47
48
49 /*      4.6 arcsec Aperture Magnitudes (UV):      */
50 pg.NUV_MAG_APER_2, pg.FUV_MAG_APER_2, pg.NUV_MAGERR_APER_2,
51 pg.FUV_MAGERR_APER_2, pg.NUV_FLUX_APER_2, pg.FUV_FLUX_APER_2,
52 pg.NUV_FLUXERR_APER_2, pg.FUV_FLUXERR_APER_2,
53
54
55 /*      Geometric Parameters (UV):      */
56 pg.NUV_FLUX_RADIUS_2 as NUVR50, pg.NUV_FLUX_RADIUS_4 as NUVR90,
57 pg.FUV_FLUX_RADIUS_2 as FUVr50, pg.FUV_FLUX_RADIUS_4 as FUVr90
58
59 FROM SDSS_DR12..PhotoObj as ps
60
61 INTO mydb.phdata
62
63 /*      JOIN SDSS Spectra:      */
64 JOIN SDSS_DR12..SpecObj as ss ON ps.objid = ss.bestobjid
65
66 /*      JOIN GALEX Match Table:      */
67 JOIN xSDSSDR12 as x ON ps.objid = x.SDSSObjid
68
69 /*      JOIN GALEX Photometry Table:      */
70 JOIN PhotoObj AS pg ON x.objid = pg.objid
71
72 /*      Select only objects spectroscopically classified as galaxies; */
73 /*      Only the closest GALEX match to each SDSS source;          */
74 /*      Only objects detected in both GALEX bands;                  */
75 /*      And only objects in SDSS's main galaxy sample.              */
76 WHERE ss.class = 'GALAXY' AND
77        x.reversedistancerank = 1 AND
78        pg.band = 3 AND
79        ss.legacy_target1 & (64 | 128 | 256) > 0

```


Appendix B

**Article: Simultaneous
analysis of SDSS spectra
and GALEX photometry
with STARLIGHT: method
and early results**



Simultaneous analysis of SDSS spectra and *GALEX* photometry with STARLIGHT: method and early results

A. Werle[⊕],¹ R. Cid Fernandes,¹ N. Vale Asari,^{1,2†} G. Bruzual,³ S. Charlot,⁴
R. Gonzalez Delgado⁵ and F. R. Herpich[⊕],^{1,6}

¹Departamento de Física - CFM - Universidade Federal de Santa Catarina, PO Box 476, 88040-900 Florianópolis, SC, Brazil

²School of Physics and Astronomy, University of St Andrews, North Haugh, St Andrews KY16 9SS, UK

³Instituto de Radioastronomía y Astrofísica, Universidad Nacional Autónoma de México, Morelia, Michoacán, 58089 México

⁴Sorbonne Universités, UPMC-CNRS, UMR7095, Institut d'Astrophysique de Paris, F-75014 Paris, France

⁵Instituto de Astrofísica de Andalucía (CSIC), PO Box 3004, 18080 Granada, Spain

⁶Instituto de Astronomia, Geofísica e Ciências Atmosféricas, Universidade de São Paulo, R. do Matão 1226, 05508-090 São Paulo, Brazil

Accepted 2018 November 27. Received 2018 November 27; in original form 2018 September 3

ABSTRACT

We combine data from the Sloan Digital Sky Survey (SDSS) and the *Galaxy Evolution Explorer* (*GALEX*) to simultaneously analyse optical spectra and ultraviolet photometry of 231 643 galaxies with the STARLIGHT spectral synthesis code using state-of-the-art stellar population models. We present a new method to estimate *GALEX* photometry in the SDSS spectroscopic aperture, which proves quite reliable if applied to large samples. In agreement with previous experiments with CALIFA, we find that adding UV constraints leads to a moderate increase on the fraction of $\sim 10^7$ – 10^8 yr populations and a concomitant decrease of younger and older components, yielding slightly older luminosity-weighted mean stellar ages. These changes are most relevant in the low-mass end of the blue cloud. An increase in dust attenuation is observed for galaxies dominated by young stars. We investigate the contribution of different stellar populations to the fraction of light in *GALEX* and SDSS bands across the UV optical colour–magnitude diagram. As an example application, we use this λ dependence to highlight differences between retired galaxies with and without emission lines. In agreement with an independent study by Herpich et al., we find that the former shows an excess of intermediate-age populations when compared to the latter. Finally, we test the suitability of two different prescription for dust, finding that our data set is best-fitting using the attenuation law of starburst galaxies. However, results for the Milky Way extinction curve improve with decreasing τ_V , especially for edge-on galaxies.

Key words: galaxies: evolution – galaxies: stellar content – ultraviolet: galaxies.

1 INTRODUCTION

The spectral energy distribution (SED) of galaxies encodes properties such as star-formation histories (SFH), stellar masses, metallicities, and dust attenuation. Stellar population synthesis techniques aim to extract this information by comparing the SEDs of galaxies with models.

SED synthesis methods can be divided into two broad categories: parametric (Noll et al. 2009; Chevallard & Charlot 2016; Carnall et al. 2018) and non-parametric (or inverse) methods (Panter, Heavens & Jimenez 2003; Cid Fernandes et al. 2005; Ocvirk et al. 2006;

Tojeiro et al. 2007; Koleva et al. 2009; Cappellari 2017; Leja et al. 2017). The first compares galaxy spectra with a set of composite stellar population (CSP) models built by combining simple stellar population (SSPs) spectra according to prescribed star-formation and chemical enrichment histories. In contrast, the latter retrieves stellar population information without any assumptions about the functional form of the galaxy's SFH (see Walcher et al. 2011 and Conroy 2013 for complete reviews).

The main advantage of parametric models is that they require less detailed spectral information to constrain physical properties. This allows them to be applied to broad-band photometry, while the application of non-parametric population synthesis is usually restricted to λ -by- λ spectral fits of the stellar continuum (i.e. excluding nebular emission). For the same reason, certain galaxy properties such as abundance patterns and the contribution of binary stars to the SED

* E-mail: ariel@astro.ufsc.br

† Royal Society–Newton Advanced Fellowship

can currently only be investigated through parametric models. A particular asset of using broad-band photometry to measure galaxy properties is that large photometric data sets are publicly available across the entire electromagnetic spectrum, allowing for the analysis of panchromatic SEDs. Large data bases of galaxy spectra, on the other hand, are only available in the optical region.

To combine the best of both worlds, the STARLIGHT spectral synthesis code (Cid Fernandes et al. 2005) was updated to simultaneously account for spectral and photometric information, allowing the analysis of panchromatic data while maintaining the detailed spectral constraints necessary for a non-parametric fit. This method was first applied by López Fernández et al. (2016) to simultaneously fit integrated spectra from the CALIFA survey (Sánchez et al. 2012) and photometry from the *Galaxy Evolution Explorer* (GALEX, Martin et al. 2007). We note that while STARLIGHT is the first non-parametric code to include this feature, some parametric codes described in the literature also allow for the combination of spectra and photometry (e.g. BEAGLE, Chevallard & Charlot 2016, and BAGPIPES Carnall et al. 2018).

Several characteristics make the ultraviolet (UV) a natural choice for the expansion of the wavelength coverage of STARLIGHT fits. The main one is that this wavelength range provides key information about emission from OB stars, objects that dominate the UV emission in most galaxies even when they do not leave major footprints in the optical. Indeed, López Fernández et al. (2016) find that STARLIGHT fits to optical spectra alone tend to overestimate UV fluxes due to small (~ 2 per cent) fractions of optical light attributed to these young, hot stars. The UV also opens a window to other astrophysical problems, such as the UV upturn in elliptical galaxies and the shape of dust attenuation curves.

This work aims to extend the analysis of UV constraints with STARLIGHT to a combination of SDSS and GALEX data, taking advantage of a larger sample size. The paper is organized as follows: data sources and the procedure to match the data sets are described in Section 2. Novelty in the spectral synthesis method are presented in Section 3. Synthesis results are discussed in Section 4, with focus on the effect of UV data on the properties derived by STARLIGHT. Examples of applications of the data set to astrophysical problems are shown in Section 5. Finally, Section 6 summarizes our results. Throughout this work, we assume a standard Λ CDM cosmology with $\Omega_M = 0.3$, $\Omega_\Lambda = 0.7$, and $h = 0.7$.

2 DATA AND SAMPLE

2.1 Data sources and sample selection

The work presented in this paper is based primarily on optical spectra from SDSS DR8 (York et al. 2000; Aihara et al. 2011) and on UV photometry from GALEX GR6 (Martin et al. 2007), measured in two bands: *NUV* (effective wavelength $\lambda_{NUV}^{\text{eff}} = 2267$ Å) and *FUV* ($\lambda_{FUV}^{\text{eff}} = 1516$ Å).

Our general sample contains 231 643 galaxies from the SDSS main galaxy sample with photometry in both GALEX bands. The sample was selected from the GALEX CasJobs (<http://galex.stsc.iu.edu/casjobs/>) by matching the UV object closest to each of the SDSS sources within a 0.3 arcsec search radius. For most of the analysis, we use a sub-sample of 137 979 galaxies with $z < 0.1$, as this ensures that the wavelength ranges covered by the GALEX filters do not deviate largely from their rest-frame values; we will refer to this sub-sample as our low- z sample.

SDSS spectra and the *NUV* and *FUV* magnitudes from GALEX constitute the main observational data for our analysis, but we also

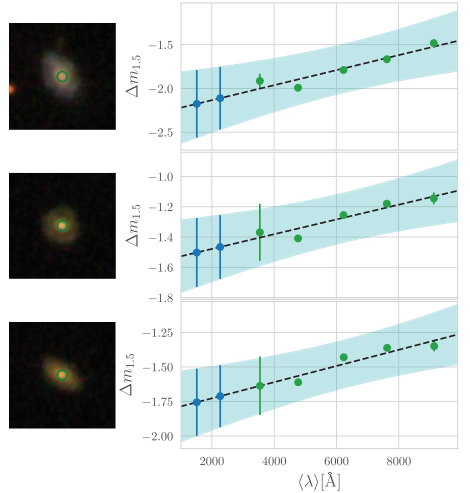


Figure 1. Examples of linear fits used to predict $\widehat{\Delta m}_{1.5}^{NUV}$ and $\widehat{\Delta m}_{1.5}^{FUV}$. Optical values of $\Delta m_{1.5}$ are plotted in green and the predicted values in blue. The best-fitting linear relation is shown as a dashed line. The cyan band shows a $\pm 1\sigma$ prediction band, used to estimate the uncertainties in $\widehat{\Delta m}_{1.5}^{NUV}$ and $\widehat{\Delta m}_{1.5}^{FUV}$. The estimated error bars are plotted in blue. An image of the corresponding galaxy is shown to the left of each fit, with the region covered by the SDSS fiber indicated by a green circle.

make use of SDSS *ugriz* photometry to estimate GALEX magnitudes in the SDSS spectroscopic aperture, as explained next.

2.2 Combining SDSS spectra and GALEX photometry

The main limitation to our analysis is the full width at half-maximum (FWHM) of the GALEX PSF (4.6 arcsec for *NUV* and 5.4 arcsec for *FUV*), which is larger than the aperture on which SDSS spectra are collected (1.5 arcsec in radius). Our strategy to circumvent this issue is to indirectly estimate the GALEX 1.5 arcsec magnitudes based on GALEX-integrated photometry and the difference between total (m_{tot}) and fibre ($m_{1.5}$) magnitudes $\Delta m_{1.5} \equiv m_{\text{tot}} - m_{1.5}$ in the SDSS *ugriz* bands.

The main factor that influences $\Delta m_{1.5}$ is the fraction of the galaxy's area sampled by the fibre; a secondary but important factor is that $\Delta m_{1.5}$ is larger in bluer filters, reflecting the difference in colour between the central regions of galaxies (bulges) and their integrated light. We also find that $\Delta m_{1.5}$ correlates weakly with galaxy morphology, and has no dependence on integrated colour and absolute magnitude, indicating that $\Delta m_{1.5}$ is not a strong function of galaxy type. Moreover, there is a tight correlation between $\Delta m_{1.5}$ on different SDSS filters, indicating that the values of $\Delta m_{1.5}$ in one band can be used to estimate $\Delta m_{1.5}$ in other wavelengths.

The relation of $\Delta m_{1.5}$ with the mean wavelength of the filters (λ) is shown in Fig. 1 for three example galaxies. This relation was used to predict values for $\Delta m_{1.5}$ in the ultraviolet by fitting a straight line to the *ugriz* measurements and extrapolating it to the GALEX bands (the dashed black lines). The lines were fitted using the BCES method (Akritas & Bershady 1996), as implemented in PYTHON

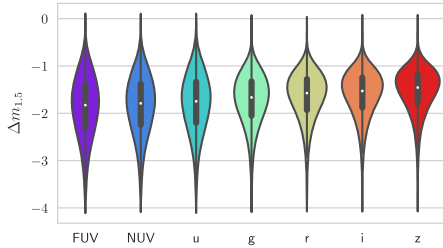


Figure 2. Violin plot of the distribution of $\Delta m_{1.5}$ in different bands. The distributions show measured values for SDSS and calculated values for *GALEX*. Box plots marking the medians and quartiles are shown inside each distribution.

by Nemmen et al. (2012). In this context, the offset of the fitted line acts as a first-order correction that is equal for all bands and accounts for the fraction of total light sampled by the spectroscopic fibre, while the slope accounts for the aforementioned difference between central and integrated colours.

The UV magnitudes in the SDSS spectroscopic aperture are thus estimated from

$$\begin{aligned} NUV_{1.5} &= NUV_{\text{tot}} - \widehat{\Delta m}_{1.5}^{NUV} \\ FUV_{1.5} &= FUV_{\text{tot}} - \widehat{\Delta m}_{1.5}^{FUV}, \end{aligned} \quad (1)$$

where $\widehat{\Delta m}_{1.5}^{NUV}$ and $\widehat{\Delta m}_{1.5}^{FUV}$ are the estimated corrections to the *NUV* and *FUV* bands. Notice that these corrections are estimated for each individual galaxy using its own *ugriz* data. In these expressions NUV_{tot} and FUV_{tot} are the values of `NUV_MAG_AUTO` and `FUV_MAG_AUTO` in the *GALEX* catalogue. The difference between Kron photometry from *GALEX* and petrosian photometry from SDSS is very small and is therefore neglected.

Uncertainties in $\widehat{\Delta m}_{1.5}^{NUV}$ and $\widehat{\Delta m}_{1.5}^{FUV}$ are derived from the $\pm 1\sigma$ prediction bands for the fitted lines, as indicated in Fig. 1. These aperture matching uncertainties are added in quadrature to the errors in NUV_{tot} and FUV_{tot} to obtain the error in $NUV_{1.5}$ and $FUV_{1.5}$.

The distributions of $\widehat{\Delta m}_{1.5}^{NUV}$ and $\widehat{\Delta m}_{1.5}^{FUV}$ are compared to the observed $\Delta m_{1.5}$ for the *ugriz* bands in the violin plot in Fig. 2. A box plot showing median and quartiles is plotted inside each distribution. The distribution of the calculated $\Delta m_{1.5}$ for *GALEX* is very similar to the *u*-band, and shifted to larger (more negative) values than for other bands.

The median aperture corrections for the sample are -1.79 mag for *NUV* and -1.82 for *FUV*, while the median errors are 0.28 and 0.31 mag, respectively. We note, however, that since our method is completely unsupervised, it is expected to produce outliers, in particular for galaxies in close pairs or with odd morphological features. Indeed, in some cases the method returns unphysical values such as $\Delta m_{1.5} > 0$ (0.08 per cent of the sample), as well as very high error estimates (larger than 1 mag in the *FUV* band for 0.07 per cent of the sample). Ultimately, the reliability of our method depends on the linearity of the $\Delta m_{1.5} \times (\lambda)$ relation. In cases where one or more bands deviate much from the linear trend the method is not reliable and will return high error estimates.

In order to test the reliability of our method, we use the *GALEX*–SDSS astrometry-matched radial profiles available in the NASA–Sloan Atlas (NSA, Blanton et al. 2011) to calculate the differences between the total magnitudes and that in an aperture of 6 arcsec in radius (Δm_6), where the image degradation caused by the *GALEX*

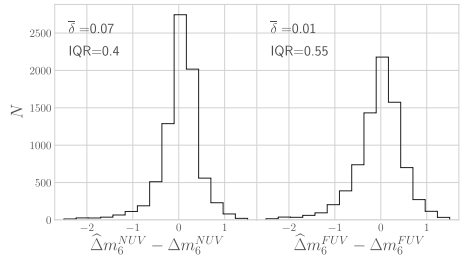


Figure 3. Comparison between predicted and measured values of Δm_6^{NUV} and Δm_6^{FUV} for a test sample of 6105 galaxies from the NASA–Sloan Atlas. Histograms show the differences between estimated and observed Δm_6 for *NUV* (left) and *FUV* (right) bands. Medians ($\bar{\delta}$) and interquartile regions (IQR) of the distributions are annotated in each panel.

PSF can be neglected. The idea behind this test is that $\Delta m_{1.5}$ can be thought of as the log of the ratio between total flux and the flux in the fibre, which is a relative quantity. Therefore, by choosing a larger aperture we can use nearby galaxies (with large projected radii) to mimic the distribution of $\Delta m_{1.5}$ in the general sample. With that in mind, we selected a test sample of 6105 galaxies with values of Δm_6 in the SDSS bands in the same range as the $\Delta m_{1.5}$ values for the general sample. Our method was then applied to estimate the values of Δm_6 for the test sample.

Results of this test are shown in the histograms of Fig. 3, where we plot the distributions of $\Delta m_6^{NUV} - \Delta m_6^{NUV}$ and $\Delta m_6^{FUV} - \Delta m_6^{FUV}$. The distributions are centred near zero, with medians of 0.07 mag for *NUV* and -0.01 for *FUV*. However, both distributions are quite wide, with interquartile regions of 0.4 on *NUV* and 0.55 on *FUV*. These statistics confirm that our estimates are good for large samples, although results for individual sources may not be reliable.

We also used the NSA to calculate Δm in an aperture of 2.25 arcsec in radius, which allows us to compare our aperture matching scheme to the one of Battisti, Calzetti & Chary (2016), that is calibrated in this aperture. This comparison is shown in Fig. 4. Magnitudes obtained with both methods are linearly correlated, although the method described here produces systematically dimmer magnitudes. Over the whole sample, the median difference between the methods is 0.19 magnitudes on *NUV* and 0.18 on *FUV*; the interquartile regions (IQR) are of 0.35 magnitudes on *NUV* and 0.56 on *FUV*, with a larger scatter for dimmer sources, specially in the *FUV* band. Considering that these two aperture matching schemes follow completely different routines and are even based on different data,¹ the agreement between the predicted magnitudes is reassuring for both methods.

Despite the wide distributions of $\widehat{\Delta m}_6^{NUV} - \Delta m_6^{NUV}$ and $\widehat{\Delta m}_6^{FUV} - \Delta m_6^{FUV}$, the predicted values are, on average, in very good agreement with the observed ones. This is sufficient for the purpose of this paper, since all our results will be averaged in relatively large samples. Nonetheless, in some cases this process can yield corrections that deviate from the distributions shown in Fig. 2. To circumvent this we remove galaxies with corrections larger than

¹The correction from Battisti et al. (2016) uses a convolution of the galaxy’s Sérsic profile in the *u* band with the *GALEX* PSF to calculate scale factors that are applied to the *GALEX* 1.5 arcsec photometry.

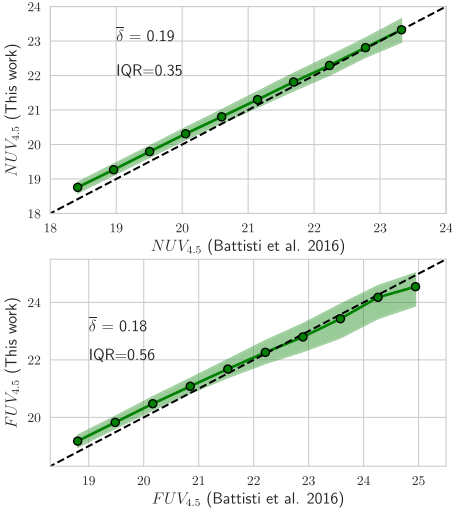


Figure 4. Comparison of UV magnitudes calculated by Battisti et al. (2016) with UV magnitudes calculated using the method of this paper for an aperture of radius 2.25 arcsec. The green lines show median curves with the region between 25 and 75 per cent percentiles shaded in green. Median $y - x$ ($\bar{\delta}$) values and interquartile regions (IQR) are annotated on each panel.

0 or smaller than -4 magnitudes in one of the GALEX bands, discarding 3300 galaxies (0.14 per cent of the sample).

2.3 Pre-processing steps

Besides the aperture matching correction explained above, the data undergo a few pre-processing steps before being fed to STARLIGHT.

From DR7 onwards, SDSS spectra are calibrated to match the flux of a point source within one FWHM of the point spread function (PSF), leading to fluxes typically 25 per cent smaller than their photometric counterparts for extended sources. Due to this offset, calculating NUV and FUV fluxes compatible with fibre photometry does not directly ensure compatibility with spectroscopic fluxes. We have thus rescaled the SDSS spectra to match the 3 arcsec photometry in the r band, as done in the MPA/JHU value added galaxy catalogue (www.mpa.mpa-garching.mpg.de/SDSS/DR7). Since the shape of the photometric SEDs is very similar to the shape of the spectra, this procedure ensures the compatibility of SDSS spectra with *ugriz* fibre photometry and, by extension, with the estimated $NUV_{1.5}$ and $FUV_{1.5}$ estimated fibre magnitudes.

Both the optical spectra and UV photometry are corrected for Galactic extinction using the Cardelli, Clayton & Mathis (1989) extinction law with $R_V = A_V/E(B - V) = 3.1$, and $E(B - V)$ values from Schlegel, Finkbeiner & Davis (1998) assuming the recalibration introduced in Schlafly & Finkbeiner (2011).

Finally, the spectra are shifted to $z = 0$ and re-sampled to 1 Å wavelength intervals. UV fluxes, however, are not k -corrected to rest-frame values. Instead, STARLIGHT uses the known redshift of the source to evaluate the predicted NUV and FUV magnitudes in the observed frame.

2.4 Ancillary data

The stellar population analysis presented in this work is based on the pre-processed SDSS spectra and GALEX magnitudes described in the previous sections. Even though no other data are required for this analysis, information on properties like emission lines and host morphology is key to the interpretation of the results. Following the statistical gist of this study, we will use such ancillary data to organize sources into different groups and examine the results in a comparative way. We use the Galaxy Zoo (Lintott et al. 2008) morphology to define sub-samples of ellipticals and spirals. Emission line fluxes used in Section 5.2 are drawn from Mateus et al. (2006).

The main method to group galaxies explored in this paper is the $NUV - r$ versus M_r colour–magnitude diagram (CMD). Unlike purely optical based CMDs, where the red sequence, blue cloud, and green valley populations exhibit substantial overlap, this UV-optical CMD clearly represents the bimodality of the local galaxy population, making it a valuable tool to examine trends for different galaxy types (Martin et al. 2007; Gonçalves et al. 2012; Salim 2014). To build this CMD we calculated absolute magnitudes, which are corrected for Galactic extinction and k -corrected to $z = 0$ using the KCORRECT code (Blanton & Roweis 2007). We note that this is the only use of k -correction in this paper.

3 SPECTRAL SYNTHESIS

3.1 Method

The version of STARLIGHT used in this paper introduces a few novelties with respect to López Fernández et al. (2016), the main change being the scheme for combining photometric and spectroscopic figures of merit.

The spectroscopic and photometric parts of the χ^2 are defined as

$$\chi_{\text{SPEC}}^2 = \sum_{\lambda} w_{\lambda}^2 (O_{\lambda} - M_{\lambda})^2$$

$$\chi_{\text{PHO}}^2 = \sum_{l=0}^{N_l} \left(\frac{m_l^{\text{obs}} - m_l^{\text{mod}}}{\sigma_l} \right)^2, \quad (2)$$

where O_{λ} and M_{λ} are the observed and model spectra, w_{λ} is the inverse error in O_{λ} (except in bad pixels and regions around emission lines, which are discarded from the fits by setting $w_{\lambda} = 0$), l is an index corresponding to each of the N_l photometric filters, m_l^{obs} and m_l^{mod} are the observed and modelled AB magnitudes in filter l and σ_l are the errors in the magnitudes. Model magnitudes are calculated by performing synthetic photometry in the model spectrum M_{λ} , after shifting it to the observed frame, ensuring consistency with the input apparent magnitudes m_l .

In all practical applications, N_l is much smaller than the number of spectroscopic data points N_{λ} – for instance, $N_l = 2$ and $N_{\lambda} \sim 4000$ in this paper. In order to simultaneously minimize χ_{SPEC}^2 and χ_{PHO}^2 , this scale difference has to be circumvented in our definition of the total χ^2 . Therefore, we define the total χ^2 as

$$\chi_{\text{TOT}}^2 = \chi_{\text{SPEC}}^2 + g_{\text{PHO}} \frac{N_{\lambda}}{N_l} \chi_{\text{PHO}}^2, \quad (3)$$

where g_{PHO} is a technical parameter that sets the relative weight of photometric and spectroscopic constraints.

López Fernández et al. (2016) did experiment with this recipe, but concluded that no scaling of χ_{PHO}^2 was necessary to adequately fit both their UV photometry and optical spectra. This is not, however, valid in general. In particular, the uncertainties in the spectroscopic

and photometric fluxes play a central role in defining the balance between χ^2_{SPEC} and χ^2_{PHO} . Optimal values of g_{PHO} are thus data set dependent.

For the combination of SDSS spectra and aperture-corrected *GALEX* photometry used in this paper, we find that g_{PHO} values of the order of 0.1 are necessary to adequately fit both the UV and optical data. So this is the value adopted throughout this work. Increasing g_{PHO} improves the fit of UV fluxes at the expense of degrading the quality of the fit of the optical spectrum (particularly in its blue end), and vice versa.

3.2 Stellar population base

Spectral synthesis with STARLIGHT depends on a few astrophysical ingredients, the main one being a base of stellar population spectra.

The base used in this paper is built from SSP models from Charlot & Bruzual (in preparation, CB18 hereafter), which includes considerable improvements upon the Bruzual & Charlot (2003) models. The CB18 models incorporate the PARSEC evolutionary tracks computed by Chen et al. (2015) for 16 values of the stellar metallicity ranging from $Z = 0$ to $Z = 0.06$. These tracks include the evolution of the most massive stars losing their hydrogen envelope through the Wolf–Rayet (WR) phase, and have been complemented with the work by Marigo et al. (2013) to follow the evolution of stars through the thermally pulsing asymptotic giant branch (TP-AGB) phase. A large number of empirical and theoretical stellar libraries is used to describe the spectrophotometric properties of the stars along these tracks. For the age and wavelength ranges of interest for this paper, the dominant stellar spectra come in the visible range from the MILES stellar library (Sánchez-Blázquez et al. 2006; Falcón-Barroso et al. 2011) and in the UV range from the theoretical libraries computed by Lanz & Hubeny (2003a,b, 2007), Leitherer et al. (2010), Martins et al. (2005), Rodríguez-Merino et al. (2005), Rauch (2003), and the high-resolution PoWR models (Gräfener, Koesterke & Hamann 2002; Hamann & Gräfener 2003; Hamann, Gräfener & Liermann 2006; Sander, Hamann & Todt 2012; Hainich et al. 2014, 2015; Todt et al. 2015) to describe stars in the WR phase. The effects of dust shells surrounding TP-AGB stars on their SED (Westera et al. 2002; Aringer et al. 2009; Rayner, Cushing & Vacca 2009) is treated as in González-Lópezzira et al. (2010). The CB18 models have been used, among others, by Gutkin, Charlot & Bruzual (2016), Wofford et al. (2016), Vidal-García et al. (2017), Fritz et al. (2017), Bitsakis et al. (2017). These models are available to the interested user upon request. A comparison between the new models and the ones from Bruzual & Charlot (2003) is made in appendix A of Vidal-García et al. (2017). A more detailed comparison will be provided by CB18.

We use these SSP models to compute the spectra of CSPs resulting from periods of constant star-formation rate. The age range from $t = 1$ Myr to 14 Gyr was divided into 16 logarithmically spaced age bins. We use seven values of metallicity between $Z = 0.0005$ and $3.5 Z_{\odot}$ ($Z_{\odot} = 0.017$), yielding a base of $16 \times 7 = 112$ CSPs.

3.3 Dust attenuation

The effects of dust attenuation² in this work are modelled as if produced by a single foreground screen that attenuates fluxes by a

factor $e^{-\tau_{\lambda}}$, with τ_{λ} parametrized as the product of the optical depth in the V-band (τ_V) and a $q_{\lambda} \equiv \tau_{\lambda}/\tau_V$ attenuation or extinction curve.

We have performed spectral fits with two different recipes for q_{λ} : the MW law, as parametrized by Cardelli et al. (1989) with $R_V = 3.1$ (CCM), and the Calzetti et al. (2000) law (CAL), modified in the $\lambda < 1846 \text{ \AA}$ range to smoothly turn into the curve derived by Leitherer et al. (2002).³ The most notable difference between these laws is the presence or absence of the so-called ‘UV bump’, a broad peak in q_{λ} around 2175 Å (Stecher 1965), within the range of the *NUV* filter. A more fundamental difference between them is that while CAL formally represents an attenuation law, CCM is originally an extinction curve, a crucial distinction when modelling the two processes (e.g. Witt & Gordon 2000). In the context of this work, however, CCM is used to model attenuation, so the term ‘attenuation law’ may loosely apply. These two laws are chosen because they are the most often used in STARLIGHT-based work, and also because they allow us to test how an UV bump affects the fitting of UV data. These characteristics suit our central goal, which is to showcase the potential of the combined analysis of optical spectra and UV photometry with STARLIGHT.

A comparison of results obtained with the two laws is presented in Section 5.3, but we anticipate that the best results for the general population of galaxies are obtained for the Calzetti law. Accordingly, all results presented up to Section 5.3 assume this prescription.

4 SYNTHESIS RESULTS

Having discussed the sample, how we handle the data, and the method of analysis, this section presents the results of the synthesis. Throughout this section the emphasis is on the comparison of results obtained from purely optical spectral fits to SDSS data with those obtained with the addition of *GALEX NUV* and *FUV* photometry.

4.1 Spectral fits and UV magnitudes

Fig. 5 shows examples of spectra fitted with and without photometric constraints for three different galaxies, ordered from red (top) to blue (bottom) *NUV* – *r* colours. The observed SDSS spectra are shown in black, except for regions masked because of bad pixels or emission lines, which are shown in yellow. The red and blue lines show the optical and combined optical + UV model fits, respectively. Observed UV fluxes are shown as black circles, while model values are plotted as orange circles for the optical-only fits and cyan for the optical + UV fits. All fluxes are relative to the flux at the normalization wavelength, set to $\lambda_0 = 5635 \text{ \AA}$.

Fig. 5 confirms the results of López Fernández et al. (2016), in that purely optical fits tend to predict UV fluxes much larger than the observed ones. This happens because, as will be discussed next, optical-only fits can easily accommodate small contributions of very young stellar populations that hardly affect the optical fluxes, but become dominant at UV wavelengths. The addition of UV constraints allows STARLIGHT to successfully fit UV magnitudes with very little changes to the fitted optical spectra. Also, since this effect involves only small fractions of stellar mass and optical light, no drastic change is observed in the measured SFHs, as will become clear in Figs 7 and 8.

²Throughout this paper, we adopt the standard definition of ‘extinction’ as the scattering and absorption of photons out of the line of sight, while

‘attenuation’ is defined as the combination of absorption and scattering in and out of the line of sight with local and global geometric effects.

³This modification has only minor effects, restricted to the *FUV* band.

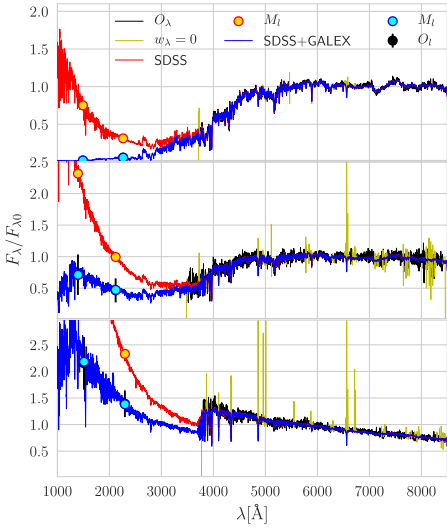


Figure 5. Examples of STARLIGHT fits for three galaxies in our sample. The black lines show optical spectra, with masked or flagged regions marked in yellow. The red lines show purely spectroscopic fits, while the blue lines show combined UV + optical fits. The black circles with error bars mark the observed GALEX fluxes ($NUV_{1.5}$ and $FUV_{1.5}$, scaled to the SDSS aperture using the method described in Section 2.2), the cyan circles are the fitted GALEX fluxes. The orange circles show UV fluxes predicted from purely optical fits. All fluxes are relative to the flux at 5635 Å.

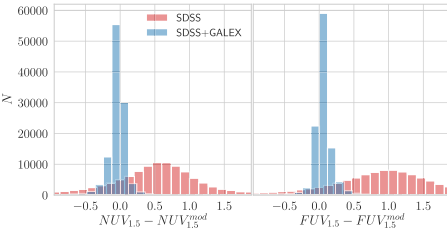


Figure 6. Histograms comparing differences between observed NUV (left) and FUV (right) magnitudes and the values predicted from optical spectra (red) and fitted from GALEX photometry (blue).

This effect is further illustrated in Fig. 6, where we plot histograms of the difference between the modelled and observed UV magnitudes for the full sample. For fits without photometric constraints, UV magnitudes are overshoot by 0.41 ± 0.91 magnitudes on NUV and 0.83 ± 1.32 on FUV , yielding values that are often brighter than the integrated UV magnitudes.

4.2 Star-formation histories

We now examine the changes in the derived SFHs generated by the inclusion of UV constraints in the analysis. Within STARLIGHT

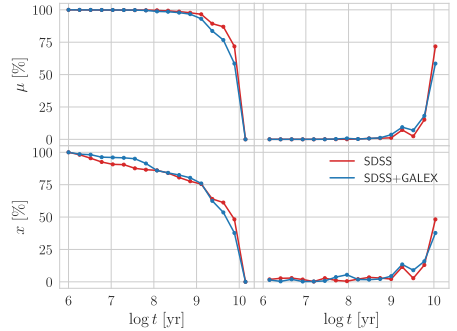


Figure 7. Average star formation histories calculated with and without photometric constraints. Top panels show cumulative (left) and non-cumulative (right) mass fractions as a function of age, while bottom panels show the corresponding curves in terms of light fractions at $\lambda_0 = 5635$ Å. The red lines show values for SDSS only STARLIGHT-fits and blue lines show values for SDSS + GALEX.

SFHs are described in terms of the light fraction population vector \vec{x} , which quantifies the contribution of different base components to the observed flux at a normalization wavelength. The mass fraction vector $\vec{\mu}$ is derived from \vec{x} and the light-to-mass ratios of the base populations.

Fig. 7 shows the average \vec{x} and $\vec{\mu}$ vectors for all galaxies in our low z sample, obtained after collapsing the Z -axis (i.e. adding all components with same age but different metallicities). These distributions of mass and light with age are shown in both fractional (right-hand panels) and cumulative forms (left).

The addition of UV data shifts light fractions from the $<10^7$ yr populations to slightly older ones, from 10^7 to 10^8 yr, as can be seen in the bottom panels of Fig. 7. This is enough to prevent the overshooting of UV fluxes, but tends to produce a redder optical spectrum. To prevent this, STARLIGHT also removes contributions from the oldest stellar populations. The χ^2_{SPEC} values obtained with the addition of UV constraints are only marginally worse (by 3 per cent on average) than those obtained with purely optical fits, confirming that the fitted optical spectra are kept essentially unchanged. When translating light fractions into mass fractions, the main difference between the two types of fits lies in the older populations: Fits with UV constraints show a slower and smoother build-up of stellar mass at early epochs.

The sample averaged SFHs in Fig. 7 mix very different kinds of galaxies, however. To get a sense of the diversity of SFHs in our sample and how they change with the addition of UV data, we calculated average light and mass fractions in bins across the $NUV - r$ versus M_r CMD. In this diagram, and at the redshift limit of our sample, the blue cloud can be defined by the criterion of $NUV - r < 4$ and the red sequence by $NUV - r > 5$, while points in the $4 < NUV - r < 5$ range lie in the green valley (Salim 2014). On the assumption that sources in a given locus of the CMD can be considered intrinsically similar, these local averages are much less sensitive to sample selection effects. The results are plotted in Fig. 8.

The largest changes in SFH occur for galaxies in the low-mass end of the blue cloud (bottom-right panels), where young stellar populations are more abundant and UV constraints are expected to

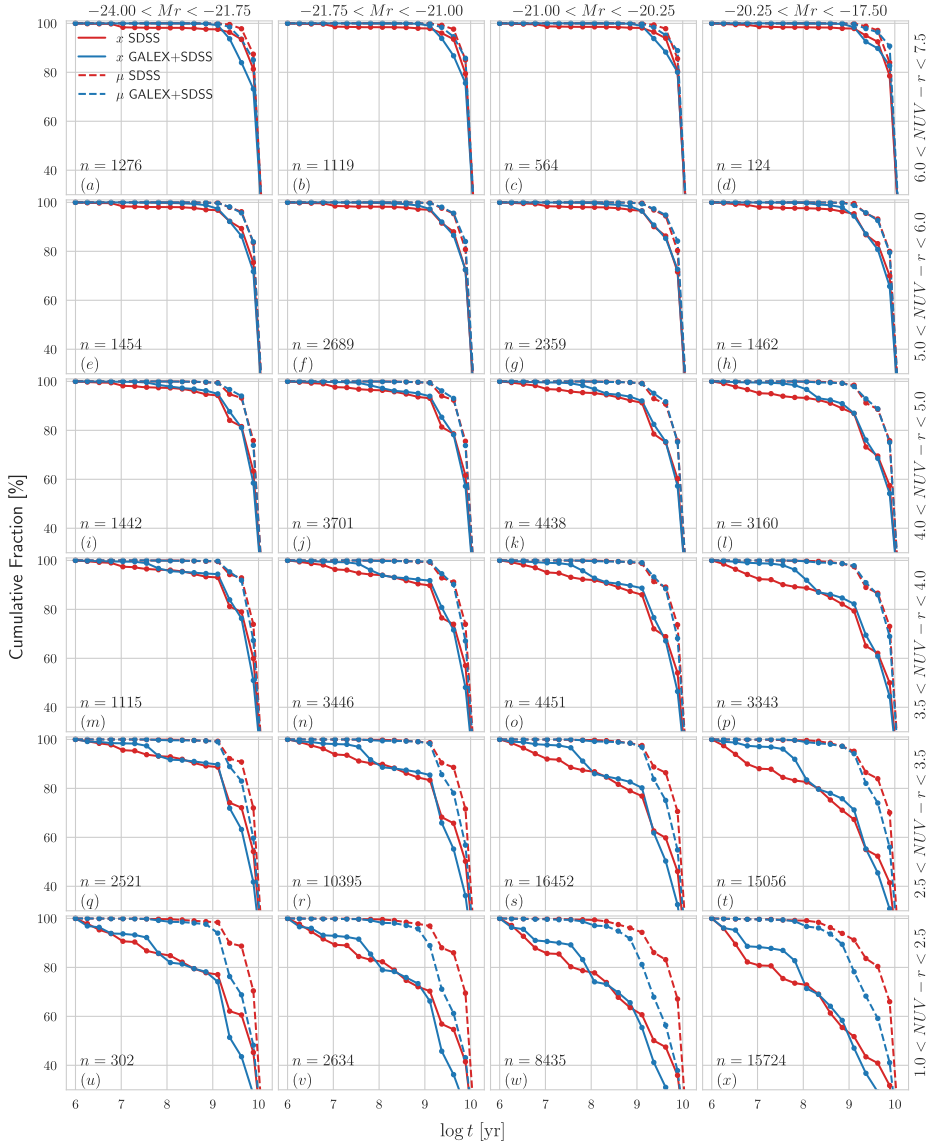


Figure 8. Average star-formation histories calculated with and without photometric UV constraints across the $NUV - r$ versus M_r colour-magnitude diagram. The solid lines show cumulative light fractions at $\lambda = 5635 \text{ \AA}$ while dashed lines show cumulative mass fractions. The red lines show results for pure SDSS fits and blue lines show results for combined *GALEX* + SDSS fits. The dots mark the edges of the CSP age bins. The number of galaxies in each bin (n) is indicated in the subplots.

play a larger role. The redistribution of $<10^7$ and $>10^9$ to 10^7 – 10^8 yr populations, which was the most noticeable change for the sample average, is very clear among these galaxies.

We also note that purely optical fits of red sequence galaxies (top panels) tend to wrongly identify very young populations ($t < 10$ Myr) at levels of the order of 2 per cent. These are the fake young bursts first identified by Ocivirk (2010; see also Cid Fernandes & González Delgado 2010). The addition of UV data constrains these populations, thus averting the problem.

Overall, the differences between SFHs calculated with and without UV data become smaller with redder colours and increasing luminosity, i.e. as the contribution of old stars increase. For light fractions, our results are similar to the ones obtained by López Fernández et al. (2016). For mass fractions, however, there are differences. While López Fernández et al. (2016) finds faster rising cumulative $\mu(> t)$ curves for optical + UV fits than with purely optical ones in blue cloud galaxies, here we observe a trend in the opposite direction (as best seen in panel w of Fig. 8). Besides the many differences in sample, data, aperture corrections, and optical/UV weighing scheme, the current fits differ in the base models, which employ different isochrones and stellar libraries. We have verified that using base models compatible with those used by López Fernández et al. (2016) moves our $\mu(> t)$ curves closer to theirs. Limiting the optical fits to the same 3800–7000 Å range of their spectra further improves the agreement.

4.3 Global properties

In addition to the population vectors discussed above, STARLIGHT also returns global properties such as mass and dust attenuation; other properties like mean stellar ages and metallicities can be calculated by reducing the dimensionality of the population vector. Fig. 9 compares a series of these global properties derived with (y -axis) and without (x -axis) UV photometry. In order to highlight the general trends throughout the sample and give less weight to outliers, results are plotted as median curves with the region between 25 and 75 per cent percentiles shaded in green. $\bar{\delta}$ and IQR values in each panel denote the median (bias) and interquartile region (scatter) of the difference between y and x values.

Panels (a) and (b) compare luminosity (at $\lambda = 5635$ Å) and mass-weighted mean stellar ages, $(\log t)_L$ and $(\log t)_M$, respectively. In the case of $(\log t)_L$ the bias is slightly positive ($\bar{\delta} = +0.04$ dex), and driven by the youngest systems, i.e. blue cloud galaxies, whose youngest populations shift from the $\log t = 6$ –7 range to the next decade ($\log t = 7$ –8) when UV constraints are used in the fits (see Fig. 8). Mass-weighted log ages (Fig. 9b) are less sensitive to the recent SFH, thus spanning a much smaller range. Still, the negative bias of $\bar{\delta} = -0.04$ dex in $(\log t)_M$ reflects how UV data leads STARLIGHT to bring down the contribution of the oldest stellar populations.

Panels (d) and (e) in Fig. 9 show luminosity and mass-weighted log metallicities, respectively. UV data makes the most metal-poor galaxies become slightly less so, although overall biases is zero for $(\log Z)_L$ and negligible for $(\log Z)_M$ ($\bar{\delta} = -0.01$ dex). López Fernández et al. (2016) find a larger negative bias in $(\log Z)_M$, mostly due to late-type, blue cloud galaxies, whose metallicities come out smaller in UV + optical fits. Again, this difference is due to differences in both data (mainly spectral coverage in the optical) and ingredients in the analysis (base models). Repeating the analysis mimicking their set-up we reproduce their results.

UV constraints do not affect the estimates of stellar masses, as seen in Fig. 9(c). This is expected, given that we have seen that UV data mostly affects the youngest populations, which carry little mass. Somewhat more surprisingly, but in agreement with López Fernández et al. (2016), Fig. 9(f) shows that, in general, optical and UV + optical fits produce similar estimates of the dust attenuation, here converted to dust optical depth τ_V . This counter-intuitive result will be dissected in the following section.

The median curves in Fig. 9 highlight the general trends throughout the sample. As expected, there are points that fall out of this trend. This is the case for some galaxies with blue $NUV - r$ and relatively red $FUV - NUV$, a combination of colours that is sometimes achieved by reddening very young populations. When this effect is in place, the addition of UV data makes galaxies significantly younger and more reddened, deviating from the relations shown in panels (a), (b), and (f) of Fig. 9. This only happens for a small population of galaxies that bears no effect to the general trend, although this behaviour is an interesting clue on galaxies that require two components of dust attenuation, which in principle could yield redder $FUV - NUV$, while having a smaller effect in $NUV - r$.

4.4 Effects on dust attenuation

As mentioned above, Fig. 9(f) bears the unexpected result that no significant change in dust attenuation is found with the addition of UV constraints. While true for the general population of galaxies, there can be important changes in τ_V for galaxies dominated by young stars. This effect gets diluted in Fig. 9, and its identification requires a more careful analysis.

A useful way to evaluate the sensitivity of our attenuation estimates to UV data is to investigate the relation between the far-UV attenuation (A_{FUV}) and the UV spectral slope (β , assuming $F_\lambda \propto \lambda^\beta$). This relation was originally found by Meurer, Heckman & Calzetti (1999) in a study of starburst galaxies,⁴ and subsequently extended to larger and more diverse samples (Kong et al. 2004; Buat et al. 2005; Burgarella, Buat & Iglesias-Páramo 2005; Seibert et al. 2005). A general conclusion from these studies is that the correlation between A_{FUV} and β found for starburst galaxies becomes much more scattered for more quiescent systems, indicating that the SFH plays an important role in the relation.

To build the relation from our data, we estimate the UV spectral slope from the $FUV - NUV$ colour using $\beta_{GLX} = 2.286(FUV - NUV) - 2.096$, as calibrated by Seibert et al. (2005). A_{FUV} is obtained from the Calzetti law, which gives $A_{FUV} = 2.53A_V$. In order to map the effects of the SFH we subdivide the sample into three bins in $(\log t_{*})_L$, the luminosity-weighted mean log age (evaluated at 5635 Å, as in Fig. 9a).

The results of this analysis are shown in Fig. 10, where A_{FUV} is plotted against β_{GLX} . The top panel shows the relations for A_{FUV} obtained from SDSS + GALEX fits, while the bottom panel shows estimates of A_{FUV} derived from SDSS only. For comparison, we include the relation derived by Overzier et al. (2011): $A_{FUV} = 3.85 + 1.96\beta_{GLX} \pm 0.4$. In fits that include UV data, the relation is well reproduced in the younger age bin (analogous to starbursts), with a smaller slope for intermediate $(\log t_{*})_L$ systems and no correlation for galaxies dominated by old stars. Overall this confirms the previous suggestions that the SFH has a major impact on the relation between A_{FUV} and β .

⁴The relation also includes the ratio between far-infrared and UV luminosities (the IRX index), but this is not explored here.

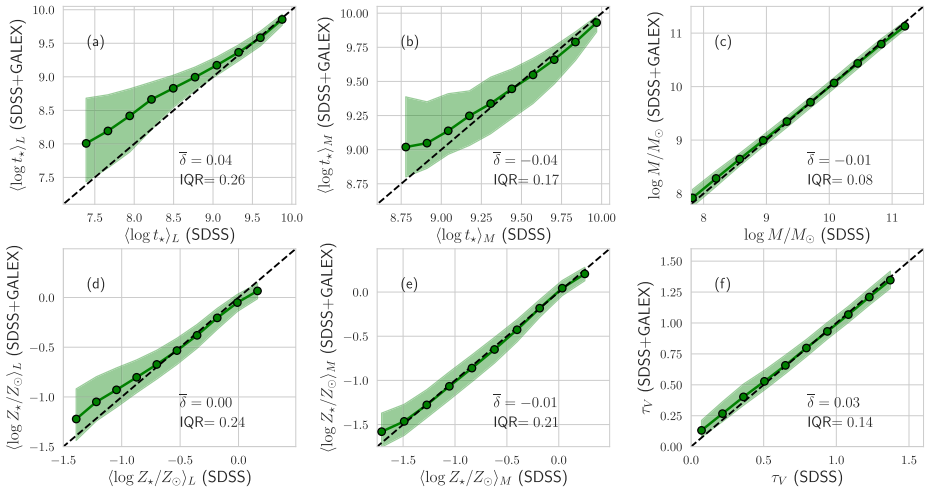


Figure 9. Comparison between galaxy properties derived with and without UV data. The y-axis corresponds to fits to UV constraints and the x-axis to fits to optical spectra; the green lines show median curves with the centre of each bin marked as a green dot with a black border. The region between 25 and 75 per cent percentiles is shaded in green. Panels show mean stellar ages weighted by light (a) and mass (b), stellar masses (c), light (d) and mass (e) weighted mean stellar metallicities and V-band dust optical depth (f). The dashed black lines show a $y = x$ relation. Median $y - x$ values ($\bar{\delta}$) and interquartile (IQR) regions are annotated on each panel.

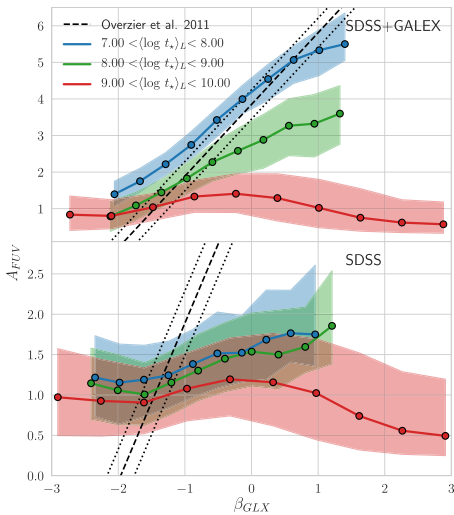


Figure 10. Relation between far-UV dust attenuation A_{FUV} UV power-law slope β for fits with (top) and without (bottom) UV data for three ranges of light-weighted mean stellar age $(\log t_*)_L$. The relations are plotted as median curves with interquartile regions highlighted. The dotted and dashed lines represent the relation derived by Overzier et al. (2011).

For SDSS-only fits, on the other hand, the relations are much weaker and more scattered, with no significant change in slope from the first to the second age bin. Note also that the values of A_{FUV} estimated from SDSS + GALEX fits for star-forming galaxies are compatible with the ones presented in the literature (e.g. Meurer et al. 1999; Seibert et al. 2005; Overzier et al. 2011), while the values obtained from SDSS-only fits are underestimated.

Finally, another important conclusion to be drawn from Fig. 10 is that changes in stellar populations are not sufficient for STARLIGHT to reproduce the $FUV - NUV$ colours of galaxies with significant amounts of young stars. In these cases, an increase in dust attenuation is also required.

5 APPLICATIONS

Having compared properties derived with and without UV constraints, this section focuses on the results obtained with our combined UV + optical synthesis analysis. The goal here is to explore some of the learning possibilities offered by this combined approach.

The broad spectral range of these fits calls for an explicit assessment of the λ -dependence of luminosity-based descriptors of the SFH. This is the subject of Section 5.1, where the cumulative light fraction SFHs across the CMD of Fig. 8 are presented for a series of wavelengths from FUV to z . After that we address two unrelated example issues that benefit from our combined UV + optical analysis. Section 5.2 compares the SFHs of red-sequence ellipticals with (liny) and without (lineless) emission lines, in search for clues on why these otherwise similar galaxies differ in their emission line properties. Finally, Section 5.3 explores whether our UV + optical

analysis can shed light on the issue of which attenuation law best describes dust attenuation in galaxies of different types.

5.1 Wavelength-dependent star formation histories

STARLIGHT-based studies make abundant use of the luminosity-weighted mean log age $(\log t)_L$ and SFHs expressed in terms of the light fraction population vector \vec{x} (e.g. Cid Fernandes et al. 2005; Mateus et al. 2006; Asari et al. 2007; Cid Fernandes et al. 2013). Although mass-based descriptions of the SFH are more directly comparable to models, light-based descriptions form a direct and much stronger relation to observed properties that form the basis of our empirical knowledge of galaxy evolution.

By their very definitions, STARLIGHT’s light fractions and light-weighted mean stellar ages are λ -dependent. Section 4, for instance, presented results for $x(t)$ and $(\log t)_L$ for $\lambda = 5635 \text{ \AA}$, an arbitrary wavelength chosen for no fundamental reason other than being in a relatively clean, feature-free window. The purpose of this section is to take advantage of this λ -dependence, examining stellar populations in the wavelength ranges in which they are most relevant. Particular attention is given to the *GALEX* bands, as they present clear descriptions of stellar populations that are easily overlooked (or even undetected) in the optical.

5.1.1 Spectral algebra: converting $\vec{x}(\lambda_0)$ to $\vec{x}(\lambda)$

Consider a spectrum $L_\lambda = \sum L_{j,\lambda}$ built by superposing $j = 1 \dots N_s$ components $L_{j,\lambda}$, and let $x_j(\lambda_0) = L_{j,\lambda_0}/L_{\lambda_0}$ be the fractional contribution of the j^{th} component to the total emission at λ_0 . Each $L_{j,\lambda}$ can be written as

$$L_{j,\lambda} = L_{j,\lambda_0} \left(\frac{L_{j,\lambda}}{L_{j,\lambda_0}} \right) = x_j(\lambda_0) L_{\lambda_0} \left(\frac{L_{j,\lambda}}{L_{j,\lambda_0}} \right), \quad (4)$$

where $x_j(\lambda) \equiv L_{j,\lambda}/L_{j,\lambda_0}$ quantifies the contribution of component j to the total emission at λ . The term in between parentheses can be expressed in terms of ratio of the intrinsic (dust-free) luminosities, $b_{j,\lambda} \equiv L_{j,\lambda}^0/L_{j,\lambda_0}^0$, and the ratio of attenuation factors at λ and λ_0 , so that

$$L_{j,\lambda} = x_j(\lambda_0) L_{\lambda_0} b_{j,\lambda} e^{-\tau_j(q_\lambda - q_{\lambda_0})}, \quad (5)$$

where τ_j is the V -band effective optical depth of component j , and $q_\lambda \equiv \tau_\lambda/\tau_V$ is given by the reddening curve. In practice $\tau_j = \tau$ if only one attenuation is allowed for, as in the case in this paper. Notice also that $b_{j,\lambda}$ are just the base spectra normalized at λ_0 .

But $L_{j,\lambda}$ can also be equated to $x_j(\lambda)L_\lambda$, where L_λ is the total emission and $x_j(\lambda)$ is the fractional contribution of component j to this total spectrum at wavelength λ . Comparing these two expressions for $L_{j,\lambda}$ leads to the sought relation between $x_j(\lambda)$ and $x_j(\lambda_0)$:

$$x_j(\lambda) = \frac{x_j(\lambda_0) b_{j,\lambda}}{\sum_j x_j(\lambda_0) b_{j,\lambda}}, \quad (6)$$

which allows one to convert the light fraction population vector from a chosen normalization wavelength λ_0 to any other λ .

5.1.2 Wavelength-dependent SFHs in the CMD

With equation (6), we calculated light fractions for all *GALEX* and SDSS bands. Fig. 11 shows the $x(> t, \lambda)$ cumulative light fractions as a function of age, as derived from our combined *GALEX* + SDSS fits. These λ -dependent descriptions of the SFH are broken into the

same bins in the UV-optical CMD as in Fig. 8. Colours code for the reference wavelength, as labelled in the top-left panel.

The $x(> t, \lambda)$ curves for the longer wavelengths like the r , i , and z bands rise faster for more massive galaxies (left-hand panels) than for those of lower mass (right), revealing the usual downsizing pattern. Because of the small influence of young stars at these wavelengths, these curves essentially reflect the mass growth curves previously shown in Fig. 8. At UV wavelengths, on the other hand, the light is always dominated by $<10^8$ yr populations, and the curves are similar for galaxies of different masses. Relevant changes in the *NUV* and *FUV* curves occur only in the vertical direction, with the proportion of 10^{6-7} to 10^{7-8} populations decreasing as $NUV - r$ becomes redder.

Panels (i) to (l) show galaxies in the green valley, mostly populated by an intermediate population of recently quenched galaxies moving from the blue cloud to the red sequence. Accordingly, all $x(> t, \lambda)$ curves shift towards largest ages. Unlike in the blue cloud, $>10^8$ yr populations now contribute significantly even at UV wavelengths, particularly for the more massive galaxies.

The red sequence galaxies are shown in the top two rows of Fig. 11. For galaxies in panels (e) to (h), intermediate-age populations are still relevant, while galaxies in the upper red-sequence (top row, panels a to d) are completely dominated by old stellar populations, even in the UV.

The evolutionary synthesis models used in this work become redder in $FUV - NUV$ up to stellar ages of 1 Gyr. After that the model spectra become bluer in the UV, and after about 4 Gyr the stellar populations emit more *FUV* per M_\odot than immediately younger populations. This results in a rise on the contribution of the oldest populations to *FUV* light, surpassing their contribution to the *NUV*. This tendency is connected to the UV upturn phenomenon, since at constant $NUV - r$ the contribution of old populations to *FUV* light correlates with $FUV - NUV$ colour.

5.2 Liny and lineless retired galaxies

Up until now, we have used the UV-optical CMD as our guide to subdivide our sample into intelligible sub-classes. This diagram provides information on galaxy evolution and the bimodality of the local galaxy population. However, galaxies are complex systems, and no single diagram condenses all the information needed to describe them. Another popular way to divide the galaxy population is based on emission line diagrams. This type of classification separates galaxies with different sources of ionizing photons, an aspect that has not yet been touched in this work.

A popular emission line based classification is the one based on the $[\text{N II}]\lambda 6584/\text{H}\alpha$ flux ratio and the $\text{H}\alpha$ equivalent width ($W_{\text{H}\alpha}$), the so-called WHAN diagram, introduced by Cid Fernandes et al. (2011). The main advantage of the WHAN diagram over those based solely on line ratios (e.g. Baldwin, Phillips & Terlevich 1981) is that it can identify retired galaxies (Stasińska et al. 2008, 2015). This diagram allows the identification of retired galaxies, characterized by having $W_{\text{H}\alpha} < 3 \text{ \AA}$. This class of galaxies can be misclassified as an active galactic nucleus in other diagrams, even though their ionization field is dominated by HoT Low Mass Evolved Stars (HOLMES) typical of old stellar populations.

Retired galaxies can be further sub-divided into liny ($0.5 < W_{\text{H}\alpha} < 3 \text{ \AA}$) and lineless ($W_{\text{H}\alpha} < 0.5 \text{ \AA}$) systems, according to the presence or absence of emission lines. The fact that some retired galaxies lack emission lines poses an interesting astrophysical problem, since the HOLMES in both sub-classes produce ionizing photons enough to power line emission. This problem is studied in detail by

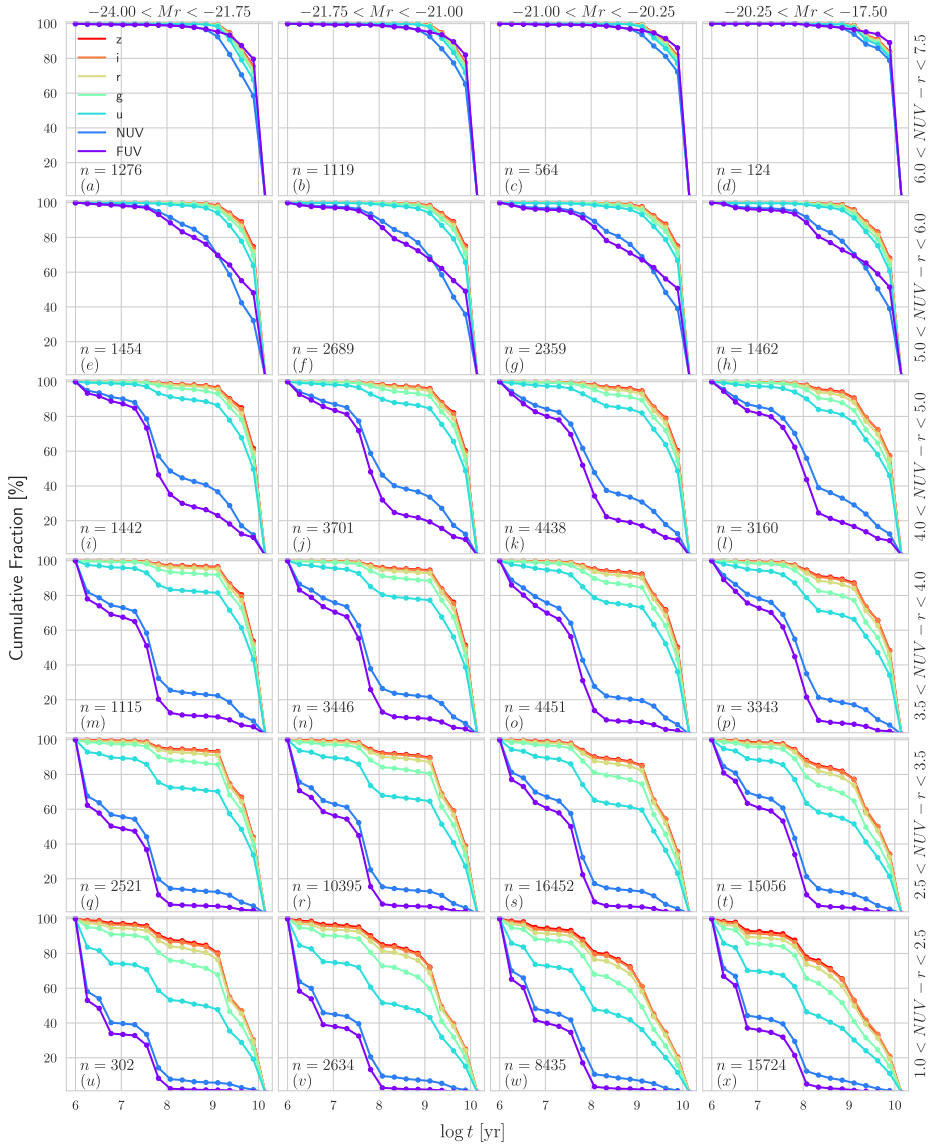


Figure 11. Average star formation histories for the same colour–magnitude bins used in Fig. 8, expressed as cumulative light fractions $x(> t, \lambda)$ in wavelengths corresponding to SDSS and GALEX bands. All curves correspond to results obtained in the combined GALEX + SDSS STARLIGHT fits.

Herpich et al. (2018, hereafter H18). The aim of this section is to complement their analysis using our UV-optical spectral synthesis.

Through a pair-matching analysis, H18 were able to identify very small but consistent differences between the two sub-classes of retired galaxies. Compared to lineless systems, liny ones tend to be brighter in the *GALEX NUV* and *WISE W3* bands, and have slightly smaller 4000 Å breaks. These results are indicative of differences in dust content and SFHs. These differences in SFH, however, are hard to measure directly in the optical.

We have used our combined *GALEX* + *SDSS* spectral analysis to address this issue in the hope that a wider wavelength range leads to a clearer separation between the SFHs of liny and lineless retired galaxies. To this end, we have culled a sample of retired galaxies out of our low- z sample. In addition to the $W_{H\alpha}$ selection we also require the galaxies to be classified as ellipticals by *Galaxy Zoo*. Out of the 16 206 retired galaxies in our sample, 12 per cent are lineless and the remaining are liny.

Fig. 12 shows mean cumulative light fraction curves for lineless (top panels) and liny (bottom panels) galaxies, split into four bins of stellar mass. As in Fig. 11, each panel shows the $x(> t)$ curves for seven wavelengths corresponding to the *GALEX* and *SDSS* filters. Variations in the curves from left-hand to right-hand panels reflect the well known downsizing pattern, with less massive galaxies having SFHs that are more extended in lookback time. The SFHs for the UV bands clearly show that liny galaxies experienced a more extended period of star formation, a trend that is consistent in all mass ranges. The same signal is present in the $x(> t)$ curves for optical wavelengths, but at a much reduced amplitude.

Though populations of a few Myr may be present in low-mass liny galaxies, the main difference is an excess of intermediate-age populations (~ 0.1 – 1 Gyr). This directly shows that the presence or absence of emission lines in retired galaxies is connected to slightly different SFHs. H18 interprets this as due to an external reservoir of cold gas that is slowly accreted by liny galaxies, feeding a low level of star-formation over an extended period of time. In contrast, lineless systems exhausted their gas supply at an early epoch, leaving little or no gas to react to the ionizing radiation field produced by their HOLMES.

Another difference between these galaxy classes is the larger dust content in liny galaxies. The optical-only analysis on H18 is already capable of identifying higher τ_V values for liny galaxies at all mass ranges, a result that is confirmed here for both optical and UV + optical fits. Consistently with the H18 findings, we identify an average difference of $\Delta\tau_V = 0.15$ between liny and lineless galaxies.

5.3 Comparing results for different attenuation laws

Previous experiments with STARLIGHT found that spectral fits in the optical cannot distinguish among different choices of dust attenuation law. Asari et al. (2007), for instance, show that equally good fits are obtained with $q_\lambda = A_\lambda/A_V$ functions representative of the Milky Way, Magellanic Clouds, or starburst galaxies. This degeneracy is hardly surprising, given that the main differences between these alternative laws lies not in the optical, but in the UV.

One of the advantages of incorporating UV data in the STARLIGHT analysis is that it allows us to revisit this issue and investigate which dust attenuation law best fits the data. In this section we compare results obtained with the CAL and CCM laws, whose most notable difference is presence or absence of the UV bump at $\lambda \sim 2175$ Å. Given the overlap with the *NUV* filter, this feature is bound to affect our analysis. *FUV* fluxes are also affected by the choice of q_λ , given

that the CCM law have a steeper far-UV slope, even though slopes in the optical are similar. Though the CAL and CCM laws do not span the wealth of dust attenuation effects studied in the literature (see Noll et al. 2009; Seon & Draine 2016; Narayanan et al. 2018; Salim, Boquien & Lee 2018), they serve as useful limits to investigate the effect of the bump. Moreover, they are both commonly used in STARLIGHT-based studies.

Qualitatively one expects fits using a CAL law to produce larger residuals in the UV than fits with a CCM law for galaxies with relevant UV bumps, and vice versa. It is therefore interesting to compare the UV residuals obtained with these two laws. To evaluate the quality of the fits in the UV let us use

$$\chi_{UV} = \sqrt{\frac{1}{2} \chi_{PHO}^2}, \quad (7)$$

which gives an average of the *NUV*- and *FUV*-reduced residuals.

For this analysis we will restrict the sample to galaxies with $NUV - r < 5$ that are classified as spirals by *Galaxy Zoo*. On the other hand we do allow systems beyond $z = 0.1$ in order to trace the effect of the *NUV* band moving out of the UV bump region as redshift increases. These cuts yield a sample of 81 214 galaxies.

Fig. 13 shows histograms of χ_{UV} for the CAL and CCM laws. The mean and rms values of χ_{UV} are 0.22 ± 0.26 for the CAL law and 0.41 ± 0.36 for CCM. The inset shows the histogram of $\Delta\chi_{UV} = \chi_{UV}^{CAL} - \chi_{UV}^{CCM}$. Over our whole sample $\Delta\chi_{UV}$ averages to -0.18 , showing that the CAL law is generally preferred over CCM.

We find that the main parameters controlling how worse the fits get with the CCM law are τ_V and redshift. Trends with mass and star-formation rate were also investigated, but we found no visible dependence of $\Delta\chi_{UV}$ with these parameters at fixed τ_V and redshift. In Fig. 14, we plot median curves of $\Delta\chi_{UV}$ as a function of τ_V for four different ranges in z . The τ_V values used in this plot are those derived from purely optical fits with a CAL attenuation law, which are independent from the UV. The plot shows that, in comparison with CCM, the CAL law yields progressively better fits of the *GALEX* photometry as τ_V increases. The systematic behaviour shown in Fig. 14 is expected to a certain degree, since the bump level is amplified as τ_V increases. Moreover, the quasi-universal relation between τ_V and the slope of the attenuation curve at any wavelength found by Chevallard et al. (2013) (and confirmed by Salim et al. 2018) also takes the results in this direction by favouring a steeper slope (MW-like) for low τ_V . The effects of redshift are also evident in this plot. At fixed τ_V , the $\Delta\chi_{UV}$ is largest (in modulus) at low redshift (the blue curves in Fig. 14). As redshift increases the CAL and CCM laws yield increasingly similar χ_{UV} . We interpret this as due to the gradual shifting of the UV bump away of the *NUV* band as redshift increases. To first order this makes the two laws similarly bump-less, although differences in far-UV slope between the two q_λ functions persist.

Overall, the results in Fig. 14 indicate that the attenuation curves of the general population of spiral galaxies either lack the features that distinguish the MW extinction curve or exhibit them at a less significant level. This is compatible with other studies that generally find a small level of the bump both locally (Conroy, Schiminovich & Blanton 2010; Wild et al. 2011; Salim et al. 2018), and at higher redshift (Kriek & Conroy 2013; Reddy et al. 2015). For instance, Buat et al. (2011) find an average bump amplitude of 35 per cent the MW value for galaxies at $z > 1$. Similar to our results, Battisti et al. (2016) find that the population of local star-forming galaxies can be described by a CAL-like law, but small levels of the bump cannot be discarded. This is not indicative, however, that the dust grain population in the MW is somewhat unusual, as recent models show

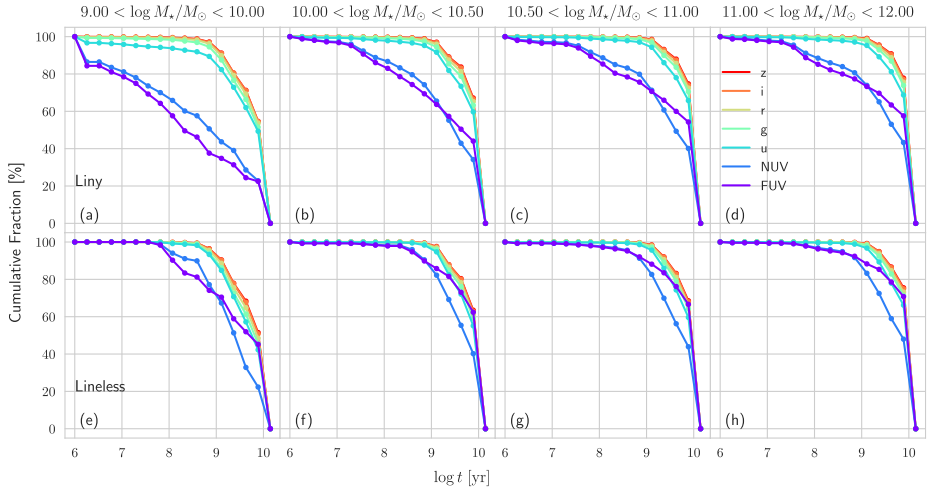


Figure 12. Wavelength-dependent SFHs for liny (top row) and lineless (bottom row) retired galaxies divided into four mass ranges. Colour codes are the same as in Fig. 11.

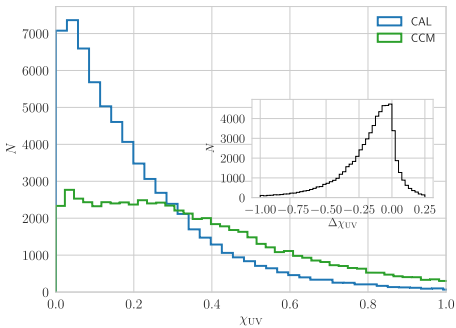


Figure 13. Histograms of χ_{UV} for the CAL attenuation (blue) and CCM extinction (green) laws. The inset shows the distribution of $\Delta\chi_{UV} = \chi_{UV}^{CAL} - \chi_{UV}^{CCM}$. Galaxies in these histograms are all Galaxy Zoo spirals with $NUV - r < 5$.

that a bumpless attenuation law can arise even when the underlying extinction curve is MW-like (Narayanan et al. 2018).

Identifying a population of galaxies with relevant UV-bumps in our data set is not straightforward, since the relation of $\Delta\chi_{UV}$ with attenuation is so strong that it contaminates other correlations. For instance, a key parameter in this analysis is galaxy inclination, but, since b/a correlates strongly with attenuation, plotting it against $\Delta\chi_{UV}$ would only show the reverberation of the correlation of both variables with τ_V . An attempt to isolate the effects of galaxy inclination in the shape of the attenuation curve is shown in Fig. 15, where we repeat Fig. 14 splitting the sample in four ranges of b/a .

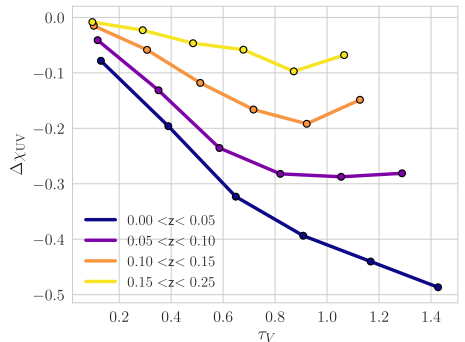


Figure 14. Median $\Delta\chi_{UV}$ plotted against dust optical depth τ_V in different bins of redshift. The centre of the bins used to calculate the medians are indicated as points.

Edge-on galaxies are shown on the left and face-on ones on the right. As in Fig. 14, we are unable to identify a significant population of galaxies that is best fitting with the CCM law. That aside, a trend is clear in Fig. 15: fits with the CCM law get worse with decreasing inclination (increasing b/a).

This goes in the direction of the results of Conroy et al. (2010), although in that work it is found that an MW-like extinction law is required to fit the UV spectral slope of highly inclined galaxies, while we find only that these are the galaxies where MW law works best. Even in these cases our results are better for the CAL law. The relation of $\Delta\chi_{UV}$ with inclination is consistent with the idea

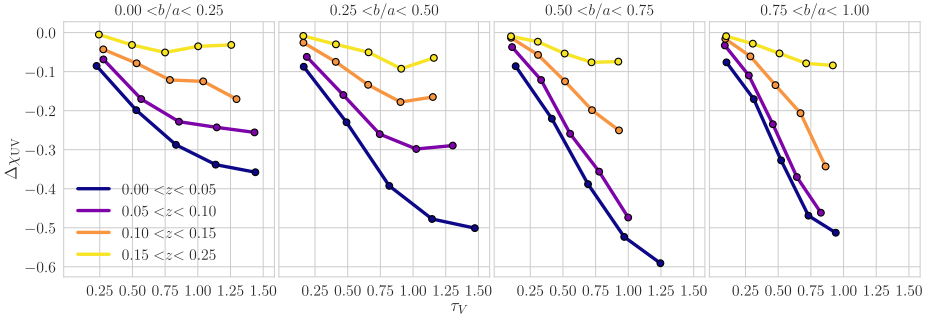


Figure 15. Median $\Delta\chi_{UV}$ plotted against dust optical depth τ_V in different bins of redshift in four ranges of inclination b/a . Edge-on galaxies are shown in the left and face-on galaxies in the right.

that the shape of the MW extinction curve in the UV is associated with diffuse dust (Wild et al. 2011), while the CAL law is best-suited for birth clouds. As galaxy inclination increases, the amount of dust from birth clouds in our line of sight stays constant, while the column of diffuse dust increases. In this interpretation, highly inclined galaxies should show attenuation curves with shapes closer to the MW extinction law, as seen in Fig. 15. However, this result is not universal. For instance, the radiative transfer models of Pierini et al. (2004) show a decrease in the bump for edge-on galaxies.

Our analysis is sufficient to showcase the potential of combined SDSS + GALEX STARLIGHT fits in distinguishing between dust attenuation laws. A more thorough analysis, exploring laws with different slopes and bump strengths (e.g. Noll et al. 2009), as well as fits with a population-dependent dust attenuation (Charlot & Fall 2000) is deferred to a future study.

6 SUMMARY

We have developed a method to estimate GALEX UV magnitudes in apertures consistent with SDSS spectra. Tests indicate that this method produces very little bias, but considerable scatter, making it suitable for statistical analysis of large data sets, though not for individual sources. We also improved upon the version of STARLIGHT used by López Fernández et al. (2016), introducing a new method for combining spectroscopic and photometric figures of merit. Other improvements on the code remain under the hood as we work towards a public distribution of this new version of STARLIGHT.

We use the new code to simultaneously analyse SDSS spectra and GALEX photometry, retrieving stellar population properties of 231 643 galaxies. Our overall results agree with previous work based on CALIFA + GALEX data, with few exceptions introduced by differences in stellar population models and spectral coverage. As seen in Fig. 5, with the addition of UV constraints STARLIGHT has to bring UV fluxes down without producing a redder optical spectrum. To achieve this, the code attributes larger light fractions to stellar populations with 10^7 – 10^8 yr, while cutting from the contribution of very young and very old stars to maintain optical colours. This behaviour produces slightly older mean stellar ages when weighted by light, and slightly younger when weighted in mass, as seen in Fig. 9. We also find an increase in dust attenuation for galaxies dominated by young stars (Fig. 10).

The panchromatic nature of our synthesis results was explored in Section 5.1 by calculating wavelength-dependent SFHs. As expected, UV light fractions are good tracers of recent star formation in the blue cloud, while optical bands are mostly tracers of old stellar populations. We also identify that UV light fractions are able to distinguish the stellar populations of liny and lineless retired galaxies, classes whose small differences in SFH are barely noticeable in the optical. In Section 5.3, we showcase our ability to distinguish between attenuation laws of different shapes, while keeping a non-parametric analysis of stellar populations. Our results for the law of starburst galaxies of Calzetti et al. (2000) are systematically better than the ones for the MW law of Cardelli et al. (1989). A complete study on this topic, however, would have to include laws of different slopes and bump strengths.

The methodology of this paper provides galaxy properties derived from non-parametric spectral synthesis applied to optical spectra and UV photometry, expanding on previous STARLIGHT-based studies. The full potential of the data set provided by our analysis is beyond what is explored in this paper, where we only presented short case studies. Future applications may include a study of the UV upturn in elliptical galaxies and a deeper analysis of the shape of dust attenuation curves, as well as the effects of binary stars and differential dust attenuation to the UV.

ACKNOWLEDGEMENTS

The authors thank the anonymous referee for the valuable comments about the paper and especially for inspiring us to write Section 4.4. AW would like to thank Andrew Battisti for the valuable discussions about GALEX + SDSS aperture matching schemes. This study was financed in part by the Coordenação de Aperfeiçoamento de Pessoal de Nível Superior – Brasil (CAPES) – Finance Code 001. AW, RCF, NVA, and FRH acknowledge the support from the CAPES CSF-PVE project 88881.068116/2014-01. NVA acknowledges support of the Royal Society and the Newton Fund via the award of a Royal Society–Newton Advanced Fellowship (grant NAF\R1\180403), and of Fundação de Amparo à Pesquisa e Inovação do Estado de Santa Catarina - FAPESC and Conselho Nacional de Desenvolvimento Científico e Tecnológico - CNPq. RGD thanks support from the Spanish Ministerio de Economía y Competitividad through the project AyA2016-77846-P. GB ac-

knowledges financial support through PAPIIT project IG100115 from DGAPA-UNAM. Funding for the SDSS and SDSS-II has been provided by the Alfred P. Sloan Foundation, the Participating Institutions, the National Science Foundation, the U.S. Department of Energy, the National Aeronautics and Space Administration, the Japanese Monbukagakusho, the Max Planck Society, and the Higher Education Funding Council for England. The SDSS Web Site is <http://www.sdss.org/>. The SDSS is managed by the Astrophysical Research Consortium for the Participating Institutions. The Participating Institutions are the American Museum of Natural History, Astrophysical Institute Potsdam, University of Basel, University of Cambridge, Case Western Reserve University, University of Chicago, Drexel University, Fermilab, the Institute for Advanced Study, the Japan Participation Group, Johns Hopkins University, the Joint Institute for Nuclear Astrophysics, the Kavli Institute for Particle Astrophysics and Cosmology, the Korean Scientist Group, the Chinese Academy of Sciences (LAMOST), Los Alamos National Laboratory, the Max-Planck-Institute for Astronomy (MPIA), the Max-Planck-Institute for Astrophysics (MPA), New Mexico State University, Ohio State University, University of Pittsburgh, University of Portsmouth, Princeton University, the United States Naval Observatory, and the University of Washington. This project made use of *GALEX* data and the Barbara A. Mikulski Archive for Space Telescopes.

REFERENCES

- Aihara H. et al., 2011, *ApJS*, 193, 29
- Akritas M. G., Bershadsky M. A., 1996, *AJ*, 112, 706
- Aringer B., Girardi L., Nowotny W., Marigo P., Lederer M. T., 2009, *A&A*, 503, 913
- Asari N. V., Cid Fernandes R., Stasińska G., Torres-Papaqui J. P., Mateus A., Sodré L., Schoenell W., Gomes J. M., 2007, *MNRAS*, 381, 263
- Baldwin J. A., Phillips M. M., Terlevich R., 1981, *PASP*, 93, 5
- Battisti A. J., Calzetti D., Chary R. R., 2016, *ApJ*, 818, 13
- Bitsakis T., Bonfimi P., González-Lópezlira R. A., Ramírez-Siordia V. H., Bruzual G., Charlot S., Maravelias G., Zaritsky D., 2017, *ApJ*, 845, 56
- Blanton M. R., Roweis S., 2007, *AJ*, 133, 734
- Blanton M. R., Kazin E., Muna D., Weaver B. A., Price-Whelan A., 2011, *AJ*, 142, 31
- Bruzual G., Charlot S., 2003, *MNRAS*, 344, 1000
- Buat V. et al., 2005, *ApJ*, 619, L51
- Buat V. et al., 2011, *A&A*, 533, A93
- Burgarella D., Buat V., Iglesias-Páramo J., 2005, *MNRAS*, 360, 1413
- Calzetti D., Armus L., Bohlin R. C., Kinney A. L., Koornneef J., Storchi-Bergmann T., 2000, *ApJ*, 533, 682
- Cappellari M., 2017, *MNRAS*, 466, 798
- Cardelli J. A., Clayton G. C., Mathis J. S., 1989, *ApJ*, 345, 245
- Carnall A. C., McLure R. J., Dunlop J. S., Davé R., 2018, *MNRAS*, 480, 4379
- Charlot S., Fall S. M., 2000, *ApJ*, 539, 718
- Chen Y., Bressan A., Girardi L., Marigo P., Kong X., Lanza A., 2015, *MNRAS*, 452, 1068
- Chevallard J., Charlot S., 2016, *MNRAS*, 462, 1415
- Chevallard J., Charlot S., Wandelt B., Will V., 2013, *MNRAS*, 432, 2061
- Cid Fernandes R., Mateus A., Sodré L., Stasińska G., Gomes J. M., 2005, *MNRAS*, 358, 363
- Cid Fernandes R., González Delgado R. M., 2010, *MNRAS*, 403, 780
- Cid Fernandes R., Stasińska G., Mateus A., Vale Asari N., 2011, *MNRAS*, 413, 1687
- Cid Fernandes R. et al., 2013, *A&A*, 557, A86
- Conroy C., 2013, *ARA&A*, 51, 393
- Conroy C., Schiminovich D., Blanton M. R., 2010, *ApJ*, 718, 184
- Falcón-Barroso J., Sánchez-Blázquez P., Vazdekis A., Ricciardelli E., Cardiel N., Cenarro A. J., Gorgas J., Peletier R. F., 2011, *A&A*, 532, A95
- Fritz J. et al., 2017, *ApJ*, 848, 132
- González-Lópezlira R. A., Bruzual-A. G., Charlot S., Ballesteros-Paredes J., Loinard L., 2010, *MNRAS*, 403, 1213
- Gonçalves T. S., Martín D. C., Menéndez-Delmestre K., Wyder T. K., Koekoemoer A., 2012, *ApJ*, 759, 67
- Gräferer G., Koesterke L., Hamann W. R., 2002, *A&A*, 387, 244
- Gutkin J., Charlot S., Bruzual G., 2016, *MNRAS*, 462, 1757
- Hainich R. et al., 2014, *A&A*, 565, A27
- Hainich R., Pasmann D., Todt H., Shenar T., Sander A., Hamann W. R., 2015, *A&A*, 581, A21
- Hamann W. R., Gräferer G., 2003, *A&A*, 410, 993
- Hamann W. R., Gräferer G., Liermann A., 2006, *A&A*, 457, 1015
- Herpich F., Stasińska G., Mateus A., Vale Asari N., Cid Fernandes R., 2018, *MNRAS*, 481, 1774(H18)
- Koleva M., Prugniel P., Bouchard A., Wu Y., 2009, *A&A*, 501, 1269
- Kong X., Charlot S., Brinchmann J., Fall S. M., 2004, *MNRAS*, 349, 769
- Kriek M., Conroy C., 2013, *ApJ*, 775, L16
- Lanz T., Hubeny I., 2003a, *ApJS*, 146, 417
- Lanz T., Hubeny I., 2003b, *ApJS*, 147, 225
- Lanz T., Hubeny I., 2007, *ApJS*, 169, 83
- Leitherer C., Li I. H., Calzetti D., Heckman T. M., 2002, *ApJS*, 140, 303
- Leitherer C., Ortiz Olávaro P. A., Bresolin F., Kudritzki R. P., Lo Faro B., Pauldrach A. W. A., Pettini M., Rix S. A., 2010, *ApJS*, 189, 309
- Leja J., Johnson B. D., Conroy C., van Dokkum P. G., Byler N., 2017, *ApJ*, 837, 170
- Lintott C. J. et al., 2008, *MNRAS*, 389, 1179
- López Fernández R. et al., 2016, *MNRAS*, 458, 184
- Marigo P., Bressan A., Nanni A., Girardi L., Pumo M. L., 2013, *MNRAS*, 434, 488
- Martins L. P., González Delgado R. M., Leitherer C., Cerviño M., Hauschildt P., 2005, *MNRAS*, 358, 49
- Martin D. C. et al., 2007, *ApJS*, 173, 342
- Mateus A., Sodré L., Cid Fernandes R., Stasińska G., Schoenell W., Gomes J. M., 2006, *MNRAS*, 370, 721
- Meurer G. R., Heckman T. M., Calzetti D., 1999, *ApJ*, 521, 64
- Narayanan D., Conroy C., Dave R., Johnson B., Popping G., 2018, preprint ([arXiv:1805.06905](https://arxiv.org/abs/1805.06905))
- Nemmen R. S., Georgantopoulos M., Guirice S., Meyer E. T., Gehrels N., Sambruna R. M., 2012, *Science*, 338, 1445
- Noll S., Burgarella D., Giovannoli E., Buat V., Marcellac D., Muñoz-Mateos J. C., 2009, *A&A*, 507, 1793
- Ocvirk P., 2010, *ApJ*, 709, 88
- Ocvirk P., Pichon C., Lançon A., Thiébaud E., 2006, *MNRAS*, 365, 74
- Overzier R. A. et al., 2011, *ApJ*, 726, L7
- Panther B., Heavens A. F., Jimenez R., 2003, *MNRAS*, 343, 1145
- Pierini D., Gordon K. D., Witt A. N., Madsen G. J., 2004, *ApJ*, 617, 1022
- Rauch T., 2003, *A&A*, 403, 709
- Vayner J. T., Cushing M. C., Vacca W. D., 2009, *ApJS*, 185, 289
- Reddy N. A. et al., 2015, *ApJ*, 806, 259
- Rodríguez-Merino L. H., Chavez M., Bertone E., Buzzoni A., 2005, *ApJ*, 626, 411
- Salim S., 2014, *Serb. Astron. J.*, 189, 1
- Salim S., Boquien M., Lee J. C., 2018, *ApJ*, 859, 11
- Sánchez-Blázquez P. et al., 2006, *MNRAS*, 371, 703
- Sánchez S. F. et al., 2012, *A&A*, 538, A8
- Sander A., Hamann W. R., Todt H., 2012, *A&A*, 540, A144
- Schlafly E. F., Finkbeiner D. P., 2011, *ApJ*, 737, 103
- Schlegel D. J., Finkbeiner D. P., Davis M., 1998, *ApJ*, 500, 525
- Seibert M. et al., 2005, *ApJ*, 619, L55
- Seon K. I., Draine B. T., 2016, *ApJ*, 833, 201
- Stasińska G. et al., 2008, *MNRAS*, 391, L29
- Stasińska G., Costa-Duarte M. V., Vale Asari N., Cid Fernandes R., Sodré L., 2015, *MNRAS*, 449, 559
- Stecher T. P., 1965, *ApJ*, 142, 1683

- Todt H., Sander A., Hainich R., Hamann W. R., Quade M., Shenar T., 2015, *A&A*, 579, A75
- Tojeiro R., Heavens A. F., Jimenez R., Panter B., 2007, *MNRAS*, 381, 1252
- Vidal-García A., Charlot S., Bruzual G., Hubeny I., 2017, *MNRAS*, 470, 3532
- Walcher J., Groves B., Budavári T., Dale D., 2011, *Ap&SS*, 331, 1
- Westera P., Lejeune T., Buser R., Cuisinier F., Bruzual G., 2002, *A&A*, 381, 524
- Wild V., Charlot S., Brinchmann J., Heckman T., Vince O., Pacifici C., Chevallard J., 2011, *MNRAS*, 417, 1760
- Witt A. N., Gordon K. D., 2000, *ApJ*, 528, 799
- Wofford A. et al., 2016, *MNRAS*, 457, 4296
- York D. G. et al., 2000, *AJ*, 120, 1579

This paper has been typeset from a \LaTeX file prepared by the author.

Appendix C

Manual of the Version of STARLIGHT Presented in this Thesis

Fitting spectra and photometry with the STARLIGHT spectral synthesis code

Ariel Werle & Roberto Cid Fernandes

May 5, 2019

Remember that cup of coffee you were drinking while reading STARLIGHT's original manual? It's time to grab another one.

This tutorial is intended for people who already have some experience with STARLIGHT and are interested in fitting spectra and photometry simultaneously.

Other new features of the code include FIR luminosity constraints, analysis of ionizing spectra using emission line fluxes and a more realistic treatment of dust. Most of these are still poorly tested and are therefore subjects for someone else's thesis.

Disclaimer: Before we get deeper into this, I should clarify that STARLIGHT is not built to fit photometric fluxes on their own. Instead, photometry is implemented to complement spectra in situations when your spectral wavelength coverage does not fully satisfy your needs.

Maintaining the "shoot first and ask questions later" philosophy of the original STARLIGHT manual, we will start with a little tutorial to give you a sense of how things work (sections 1 to 3). Only after that will we explain what STARLIGHT does and how it is done (section 5).

Contents

1	Downloading STARLIGHT	3
2	What's new	4
2.1	The updated grid files	4
2.2	The photometric input files	5
3	Running the code and looking at output	7
3.1	Running STARLIGHT	7
3.2	Output structure	7
3.3	Plotting output	11
4	Notes on input pre-processing	16
5	Implementation of photometric constraints within STARLIGHT	18
5.1	Calculating magnitudes from model spectra	18
5.2	Combining photometric and spectroscopic figures of merit	18
5.3	Photometric constraints as ranges	20
5.3.1	The math of range-fitting	20
5.3.2	How-to	21
5.3.3	Example	22

1 Downloading STARLIGHT

To get the new version of the code you can either clone our public repository using the command

```
git clone https://awerle@bitbucket.org/awerle/starlight_dev_public.git
```

or download the contents of the repository from https://bitbucket.org/awerle/starlight_dev_public/downloads/.

This will download everything you need to run your own fits: STARLIGHT's executable file (`starlight.exe`); a base of SSPs (`base_BC03_45`); a mask for emission lines; a configuration file (`PMSv04.conf`); a set of grid files (`grid_example*.in`) and the correspondent spectral and photometric input files for three example galaxies.

Note that this is still a development version of the code. Some changes may still be incorporated and some features may be deprecated until the final public release.

While you're at it, it wouldn't hurt to clone our `starlight_toolkit` repository, which contains python tools to read and plot STARLIGHT outputs, pre-process input spectra and perform other common tasks (still in early stages of development):

```
git clone https://github.com/arielwrl/starlight_toolkit.git
```

After cloning this second repository, you should add it to your PYTHONPATH. On Linux systems, adding this to your `.bashrc` should do the trick:

```
PYTHONPATH="${PYTHONPATH}:/path/to/directory/"  
export PYTHONPATH
```

Alternatively, if you are a Conda user, you can add the module with the following command:

```
conda-develop /path/to/directory/
```

To learn what to do once you've downloaded everything, proceed to the next section.

2 What's new

2.1 The updated grid files

This version introduces some changes to the grid files with respect to the original STARLIGHT. To illustrate the changes, let's take a look at the file `grid_example_PHO.in` in STARLIGHT's public repository. The file's header should look like this:

```
1 3 [n_fits]
2 ./bc2003/ [base_dir]
3 ./input/ [obs_dir]
4 ./masks/ [mask_dir]
5 ./photometry/ [pho_dir]
6 ./output/ [out_dir]
7 -958372728 [your phone number]
8 5350.0 [llow_SN]
9 5850.0 [lupp_SN]
10 3500.0 [Olsyn_ini]
11 9000.0 [Olsyn_fin]
12 1.0 [Odlsyn]
13 1.0 [fscale_chi2]
14 FIT [FIT/FXK]
15 1 [IsErrSpecAvailable]
16 1 [IsFlagSpecAvailable]
17 1.0e-17 [flux_unit]
18 0 0 1 WbN 0 [IsFIRcOn IsQHRcOn IsPHOcOn ESM & gamma]
```

If you are familiar with STARLIGHT, you probably noticed that everything was kept the same with except for the fifth line and the two last ones, which are highlighted in red. The fifth line indicates the directory `pho_dir` in which photometric data is stored. Line 17 sets the variable `flux_unit`: multiplying your input spectral fluxes by this constant converts them to units of $\text{erg s}^{-1}\text{cm}^{-2}\text{\AA}^{-1}$. Use `flux_unit = 1` if your fluxes are already in these units.

The last line in the grid header contains switches that turn new features on or off. The first two switches are associated with features that are still under development and are not explored here. The third switch turns photometric constraints on or off. It can also be set to -1, in which case photometric fluxes will be predicted from spectral fits. The other variables in the same line set the χ^2 scaling method and the value of γ , which will be explained later (section 5.2).

The second part of the `grid_file` is shown below. The file was split in two due to lack of space.

```
21 501-52235-368.spec 501-52235-368.pho 195.077 PMSv04.conf base_BC03 EL_mask_2.msk
22 2500-54178-58.spec 2500-54178-58.pho 145.723 PMSv04.conf base_BC03 EL_mask_2.msk
23 269-51910-497.spec 269-51910-497.pho 148.496 PMSv04.conf base_BC03 EL_mask_2.msk
24 #spec_in pho_in lumdist arq_config arq_base arq_mask
```

```

21 CAL 0.0 150 501-52235-368.out
22 CAL 0.0 150 2500-54178-58.out
23 CAL 0.0 150 269-51910-497.out
24 ALO v0 vd out_file

```

Once again, the new input info is shown in red. The second column lists the photometric input files (*.pho), which will be described soon, and the third column corresponds to the luminosity distance (in Mpc) to the objects.

If you want to use the current version of STARLIGHT but you don't have any photometric data, just set `IsPHOOn` to 0 and fill the second column with `no_data` or any other string.

This `grid_file` was built with data from the Sloan Digital Sky Survey. The idea of this example is to fit SDSS spectra below 5000 Å and use photometry from the *r* and *z* bands to constrain longer wavelengths. We do this by masking out all data in the spectra above 5000 Å using the mask file. This way STARLIGHT will *predict* fluxes with wavelengths between 5000 and 9000 Å, which is the maximum wavelength considered in the fit (`Ol1syn_fin` in STARLIGHT notation).

The mask file used in the example (`EL_mask_2.msk`) is printed below.

```

1 8
2 3710.0      3744.0      0.0 [OII] 3726+3729 emission line
3 3858.0      3880.0      0.0 [NeIII] 3869 emission line
4 3960.0      3980.0      0.0 Hepsilon 3970 emission line (over CaII H)
5 4092.0      4112.0      0.0 Hdelta 4102 emission line
6 4330.0      4350.0      0.0 Hgamma 4340 emission line
7 4848.0      4874.0      0.0 Hbeta 4861 emission line
8 4940.0      5028.0      0.0 [OIII] 4959 & 5007 emission lines
9 5000.0      9000.0      0.0 Masking out the red part of the spectrum

```

Other entries in this grid file are as in the previous version: `PMSv04.conf` is the config file (`arq_conf`), `base_BC03` is a base file (`arq_base`), `CAL` is an attenuation law, etc.

2.2 The photometric input files

The photometric input file for our first example (`501-52235-368.pho`) is shown below. The last line labels the columns and serves as a reminder of the order of the parameters for the user; it is not really necessary to run the code.

```

1 PHO
2 0.044      [PHO_Redshift]
3 2          [NPHO_Ys]
4 0.2       [PHO_GlobalChi2ScaleFactor]
5 r         r.dat      17.519      1.0      0.1      0.0      0.5
6 z         z.dat      16.794      1.0      0.1      0.0      0.5
7 #PHO_name PHO_Filter_file PHO_magY_TOT PHO_YFrac2Model PHO_magYErr PHO_magYRange PHO_Chi2ScaleFactor

```

This is what this file contains:

1. In the first line, you should type in the acronym PHO, to indicate that the file contains photometric information;
2. The second line indicates the galaxy's redshift (PHO_Redshift in the code's notation), used by STARLIGHT to shift base spectra to the galaxy's observed frame to compare model spectra with photometry. Use $z = 0$ if you are providing K-corrected photometry;
3. The third line corresponds to N_Y (NPHO_Ys), the number of photometric filters to be considered in the fit;
4. The fourth line contains the variable PHO_GlobalChi2ScaleFactor, used to give more or less weight to the photometric part of χ^2 . This variable will be further explored in section 5.2;
5. The next N_Y lines contain photometric information about each of the filters. These lines should have the following columns:
 - Name of the filter (PHO_name);
 - Name of the filter file, expected to be in the photometric directory (PHO_Filter_file);
 - AB apparent magnitude of the galaxy (PHO_magY_TOT);
 - The fraction of the flux to be considered by the code (PHO_YFrac2Model), which is likely to be deprecated soon;
 - Measurement errors of the magnitude (PHO_magYErr);
 - The range parameter (PHO_magYRange), useful to fiddle with the likelihood function (see section 5.3);
 - The fraction of the photometric χ^2 corresponding to the filter (PHO_Chi2ScaleFactor).

The filter files (PHO_Filter_file) should contain two columns: the first should be the wavelength in angstroms and the second should be the filter's transmission for a **photon counting device**. See files `r.dat` and `z.dat` for examples corresponding to SDSS r and z filters.

3 Running the code and looking at output

3.1 Running STARLIGHT

Now that you know what's new, go ahead and run the example you downloaded:

```
./starlight.exe < grid_example_PH0.in
```

This should fit the SDSS spectra up till 5000 Å and use photometry from r and z bands to constrain longer wavelengths. The fits will probably run fast, as the base `base_BC03_45` contains only 45 components¹. In case you want to run this as fast as possible you can execute the command more than once. Each process will run in a different node in your CPU and will fit a different entry from the grid file.

For comparison, let's run two more tests:

1. Turn photometric analysis off by replacing the 1 in the `[IsPH0c0n]` option of `grid_example_PH0.in` with a 0, change the name of the output files and run the code again. This will fit the spectra up till 5000 Å and try to predict the red part of the spectra without the aid of photometry. We suggest renaming output files from `*_PH0.out` to `*_spec_masked.out`, as this will maintain compatibility with the rest of this tutorial, but this decision is up to you;
2. Leave photometric constraints turned off and use the mask file `EL_mask.msk`, which will mask emission lines in the optical region. This will run a traditional STARLIGHT fit, fitting the whole optical spectrum with no photometric constraints. We chose to name the output files of this test `*_spec.out`.

We suggest that you play around with `grid_example_PH0.in` and make the necessary changes yourself, but in case you are in a hurry, we have prepared the files `grid_example_spec_masked.in` (for test 1) and `grid_example_spec.in` (for test 2), which will run the additional tests.

In the following subsections you will learn how the photometric output is organized and compare fits with and without photometry.

3.2 Output structure

Take a long, deep breath; this section will be a tough one.

The photometric output is stored at the end of the output file, and will be explored in the following paragraphs using `501-52235-368_PH0.out` (the output for the first galaxy in our grid file `grid_PH0.in`) as an example.

Starting at line 5770 of `501-52235-368_PH0.out`, you have:

```
5770 #####
5771 ## PH0c-FIT RELATED OUTPUT ##
```

¹The speed of STARLIGHT goes roughly with the second power of the number of base elements.

```

5772 #####
5773
5774 ## PH0: Input info
5775 501-52235-368.pho [arq_ETCinfo]
5776 195.0770 [LumDist (Mpc)]
5777 0.044068 [PH0_redshift]
5778 0.2000 [PH0_GlobalChi2ScaleFactor]
5779 2 [NPH0_Ys = number of PH0-bands included in fit]
5780
5781 #name/code filter_file magY_TOT YFrac2Model ErrMagY RangeMagY Chi2ScaleFactor magY_obs magY_low magY_upper
5782 r r.dat 17.5191 1.0000 0.1000 0.0000 0.1000 17.5191 17.5191 17.5191
5783 z z.dat 16.7947 1.0000 0.1000 0.0000 0.1000 16.7947 16.7947 16.7947

```

First there is some input info, which is basically what you've put in the photometric input file. Then there is some information from the grid file: the photometric input file name, the luminosity distance, redshift, χ^2 scale factor, and number of photometric filters. The last two lines in the table above repeat the input photometric data and add two new columns at the end: the new entries `magY_low` and `magY_upper` are the lower and upper limits for the magnitudes calculated from the range parameter (see section 5.3).

After this block you will see some information about the spectroscopic and photometric parts of the χ^2 (more on this in section 5.2):

```

5785 ## PH0: Results for best model
5786 3.1164 96.8836 [%-chi2: PH0/TOT & Opt/TOT]
5787 1.21272E+01 3.77014E+02 3.89141E+02 [chi2_PHO chi2_Opt chi2_TOT]

```

Note that this part of the output, and also the following ones, will probably be a bit different in your test. This is expected, as `STARLIGHT` will not always return the exact same results if you run it on different machines.

Following the information about χ^2 , you will find the main part of the photometric output, the fitted magnitudes and fluxes. This output section is organized in a table where each line corresponds to a different filter. There are 13 columns containing the following information:

1. Index of the filter;
2. Filter's name;
3. The transmission weighted mean λ , defined as

$$\langle \lambda \rangle_Y = \frac{\int T_{\lambda,Y} \lambda d\lambda}{\int \lambda d\lambda}; \quad (1)$$

where Y denotes a filter index ($Y = 1$ for r and 2 for z in our example).

4. The filter's pivot wavelength, used to convert AB magnitudes to flux and defined as

$$\lambda_Y^{\text{piv}} = \sqrt{\frac{\int T_{\lambda,Y} \lambda d\lambda}{\int T_{\lambda,Y} \lambda^{-1} d\lambda}}; \quad (2)$$

5. Standard deviation of the filter transmission curve;
6. A_λ/A_V at $\langle\lambda\rangle_V$;
7. Observed magnitude;
8. Fitted magnitude;
9. Observed flux in units of $\text{erg s}^{-1}\text{cm}^{-2}\text{\AA}^{-1}$ (converted from the observed magnitude);
10. Fitted flux in units of $\text{erg s}^{-1}\text{cm}^{-2}\text{\AA}^{-1}$ (converted from the fitted magnitude);
11. χ^2 of the filter;
12. χ^2 of the filter divided by the spectroscopic χ^2 ;
13. χ^2 of the filter divided by the total χ^2 .

There are too many columns to fit on this page, so I will break the example in two. The first 10 columns on 501-52235-368_PH0.out look like this:

5789	#	name/code	MeanLamb	PivotLamb	StdDevLamb	q_MeanLamb	magY_obs	magY_obs	fY_obs	fY_mod
5790	1	r	6186.20	6176.57	343.83	0.8765	17.5191	17.5758	2.800E-16	2.657E-16
5791	2	z	8961.48	8946.70	525.46	0.4822	16.7947	16.7968	2.601E-16	2.596E-16

The 3 following columns, carrying information about the χ^2 , look like this:

5789	chi2_Y	chi2_Y/chi2_Opt	chi2_Y/chi2_TOT
5790	1.2111E+01	3.2123E-02	3.1122E-02
5791	1.6536E-02	4.3860E-05	4.2493E-05

Next you will see the following table:

5793	#	j	age_j (yr)	Z_j	exAV?	x_j (%)	AV_tot	% - Y:	1	2
5794	1	1	1.000000E+06	0.00400	0	12.2545	0.6500		2.8	0.9
5795	2	3	3.160000E+06	0.00400	0	14.5252	0.6500		4.4	2.0
5796	3	5	5.010000E+06	0.00400	0	0.0576	0.6500		0.0	0.0
5797	4	1	1.000000E+07	0.00400	0	0.0000	0.6500		0.0	0.0
5798	5	2	2.512000E+07	0.00400	0	0.0000	0.6500		0.0	0.0
5799	6	4	4.000000E+07	0.00400	0	0.0000	0.6500		0.0	0.0
5800	7	1	1.015200E+08	0.00400	0	0.0000	0.6500		0.0	0.0
5801	8	2	2.861200E+08	0.00400	0	0.0000	0.6500		0.0	0.0
5802	9	6	6.405400E+08	0.00400	0	0.0000	0.6500		0.0	0.0
5803	10	9	9.047900E+08	0.00400	0	0.0000	0.6500		0.0	0.0
5804	11	1	1.434000E+09	0.00400	0	0.0000	0.6500		0.0	0.0
5805	12	2	2.500000E+09	0.00400	0	0.0000	0.6500		0.0	0.0
5806	13	5	5.000000E+09	0.00400	0	0.0000	0.6500		0.0	0.0
5807	14	1	1.100000E+10	0.00400	0	18.2779	0.6500		23.9	24.7
5808	15	1	1.300000E+10	0.00400	0	26.2476	0.6500		34.6	36.0

5809	16	1.000000E+06	0.02000	0	0.0000	0.6500	0.0	0.0
5810	17	3.160000E+06	0.02000	0	0.0000	0.6500	0.0	0.0
5811	18	5.010000E+06	0.02000	0	0.0000	0.6500	0.0	0.0
5812	19	1.000000E+07	0.02000	0	0.0000	0.6500	0.0	0.0
5813	20	2.512000E+07	0.02000	0	0.0000	0.6500	0.0	0.0
5814	21	4.000000E+07	0.02000	0	0.0000	0.6500	0.0	0.0
5815	22	1.015200E+08	0.02000	0	0.0000	0.6500	0.0	0.0
5816	23	2.861200E+08	0.02000	0	0.0000	0.6500	0.0	0.0
5817	24	6.405400E+08	0.02000	0	0.0000	0.6500	0.0	0.0
5818	25	9.047900E+08	0.02000	0	0.0000	0.6500	0.0	0.0
5819	26	1.434000E+09	0.02000	0	0.0000	0.6500	0.0	0.0
5820	27	2.500000E+09	0.02000	0	0.0123	0.6500	0.0	0.0
5821	28	5.000000E+09	0.02000	0	0.0000	0.6500	0.0	0.0
5822	29	1.100000E+10	0.02000	0	0.0000	0.6500	0.0	0.0
5823	30	1.300000E+10	0.02000	0	0.0000	0.6500	0.0	0.0
5824	31	1.000000E+06	0.05000	0	0.0000	0.6500	0.0	0.0
5825	32	3.160000E+06	0.05000	0	0.0000	0.6500	0.0	0.0
5826	33	5.010000E+06	0.05000	0	0.0000	0.6500	0.0	0.0
5827	34	1.000000E+07	0.05000	0	0.0000	0.6500	0.0	0.0
5828	35	2.512000E+07	0.05000	0	0.0000	0.6500	0.0	0.0
5829	36	4.000000E+07	0.05000	0	0.0000	0.6500	0.0	0.0
5830	37	1.015200E+08	0.05000	0	0.0000	0.6500	0.0	0.0
5831	38	2.861200E+08	0.05000	0	0.0000	0.6500	0.0	0.0
5832	39	6.405400E+08	0.05000	0	14.5291	0.6500	10.8	9.1
5833	40	9.047900E+08	0.05000	0	10.0714	0.6500	10.0	9.1
5834	41	1.434000E+09	0.05000	0	0.0000	0.6500	0.0	0.0
5835	42	2.500000E+09	0.05000	0	0.0000	0.6500	0.0	0.0
5836	43	5.000000E+09	0.05000	0	5.3408	0.6500	9.6	12.8
5837	44	1.100000E+10	0.05000	0	1.7708	0.6500	3.8	5.4
5838	45	1.300000E+10	0.05000	0	0.0000	0.6500	0.0	0.0

This part of the output shows the contribution of each base element to the flux in each of the filters, the columns containing the following:

1. Index j of each base element;
2. Age age_j of base element j ;
3. Metallicity Z_j of base element j ;
4. The population vector \vec{x} ;
5. Extinction AV_{tot} ;
6. The next N_Y columns show the fraction of the flux on each of the N_Y filters associated the j th base element; these columns are organized by the filter index.

In our case, index 1 corresponds to r and index 2 corresponds to z .

3.3 Plotting output

We will now explore our output file using the `starlight_toolkit` package. The package is compatible with python 3, and is still under development.

To start, you should navigate to your output directory and run python (or ipython) from there. Once you've done that, import the following:

```
import matplotlib.pyplot as plt
from starlight_toolkit.output import read_output_file
from starlight_toolkit.plotting import plot_spec
from starlight_toolkit.plotting import plot_spec_simple
# For cosmetic purpose:
import seaborn as sns
sns.set_style('whitegrid')
```

The function `read_output_file` will organize STARLIGHT's output in a python dictionary. Let's take a look at how this works, start by reading an output file and printing out the keys of the dictionary:

```
out = read_output_file('501-52235-368_spec_masked.out')
out.keys()
```

This will return the following:

```
['PHO',
 'spectra',
 'keywords',
 'population']
```

The photometric information is stored in the 'PHO' key, observed and synthetic spectra are in the 'spectra' key, the population vectors are under 'population' and other results and information about the fit are stored under 'keywords'.

Now let's plot some fits. To build up to a climax, let's start by plotting the fit without photometric constraints.

```
#Run output plotter (syn_color control's the color of
#the synthetic fluxes, default value is 'blue'):
plot_spec(out='501-52235-368_spec_masked.out', plot_PHO=False)
#Create legend and show plot:
plt.legend(ncol=2, frameon=False, fontsize=8)
plt.ylim(0, 1.7)
plt.show()
```

This will hopefully produce something similar to figure 1, where our fit without photometric constraints is plotted in red. The parts of the spectrum considered in the fit are plotted in black and the parts of the spectrum that were masked, flagged points are shown in green, masked points in yellow. Clipped points would be plotted as purple x's if there were any. If you don't like the colors, feel free to customize them by changing the values of `syn_color` (for the synthetic spectrum), `obs_color` (for the observed spectrum), `mask_color` (for masked points) and `flag_color` (for flagged points). Note that all spectroscopic fluxes north of 5000 Å are plotted in yellow, as they were masked in `mask_EL_2.msk`. The argument `plot_PHO` is set to `False` because we don't want to plot the estimated photometry right now.

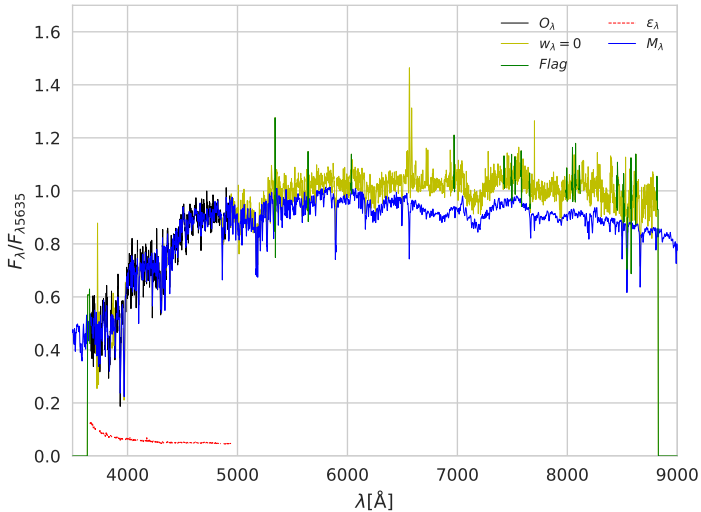


Figure 1

Fig. 1 is an expected tragedy. STARLIGHT is only looking at the blue end of the spectrum and is thus getting the red part of the spectrum completely wrong. Let's see if we can fix this problem with photometry:

```
#Create figure with axis:
fig, axis = plt.subplots()
```

```

#Plot the fit without photometry. The argument
#syn_label controls the synthetic spectrum's legend.
#Note that you may have to change the name of the
#output file.
plot_spec_simple(out='501-52235-368_spec_masked.out', ax=axis
, syn_color='r', PHO_color='orange'
, syn_label='Without photometric constraints')

#Plot fit with photometric constraints, plot_obs=False
#prevents the function to plot the observed spectrum twice.
#Here we will use the default blue color for the synthetic
#spectrum.
plot_spec_simple(out='501-52235-368_PHO.out', ax=axis
, plot_obs=False, syn_label='With photometric constraints')

#Create legend and show plot:
plt.legend(ncol=2, frameon=False, fontsize=8)
plt.ylim(0, 1.7)
plt.show()

```

This should create Fig. 2, where the fits with (blue) and without (red) photometric constraints are compared. For this comparison we used the `plot_spec_simple`, which plots masked, clipped and flagged points all in yellow. This helps when overplotting different fits.

The result shown in Fig. 2 looks great! When we are just considering the blue part of the spectrum, we can reasonably fit the red part by adding photometric constraints. To see how close the fit with photometric constraints is to a complete λ by λ fit, let's plot all 3 synthetic spectra for this galaxy:

```

#Create figure with axis:
fig, axis = plt.subplots()

#Plot the fit without photometry:
plot_spec_simple(out='501-52235-368_spec_masked.out', ax=axis
, syn_color='r', PHO_color='orange'
, syn_label='Without photometric constraints')

#Plot fit with photometric constraints:
plot_spec_simple(out='501-52235-368_PHO.out', ax=axis
, plot_obs=False, syn_label='With photometric constraints')

#Plot complete spectroscopic fit:

```

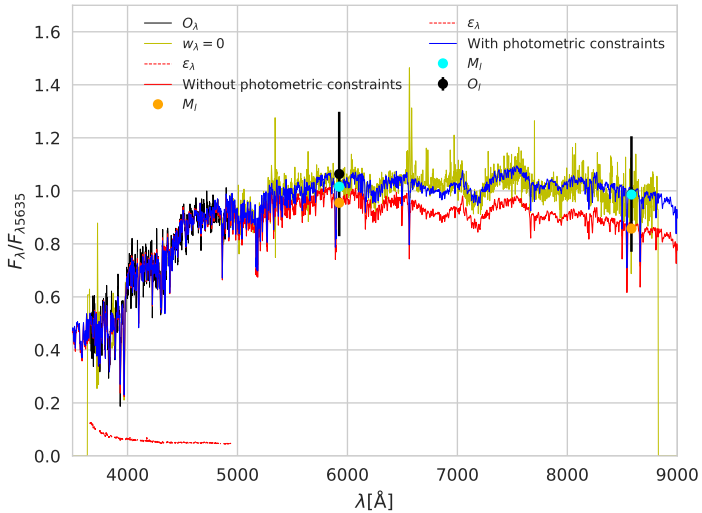



Figure 2

```
plot_spec_simple(out='501-52235-368_spec.out', ax=axis
, plot_obs=False, syn_color='g', plot_PH0=False
, syn_label='$\lambda$ by $\lambda$ fit')
```

```
#Create legend and show plot:
plt.legend(ncol=2, frameon=False, fontsize=8)
plt.ylim(0, 1.7)
plt.show()
```

The fit with photometry in Fig. 3 is so close to the λ by λ fit that is hard to distinguish the blue line from the green one. Although this example was not cherry-picked, we should say that this does not always work so remarkably well, but it usually does a good job.

You should be good to go with what we covered up until now, but we recommend having a sneak peek in the next section, where we make some remarks about how to

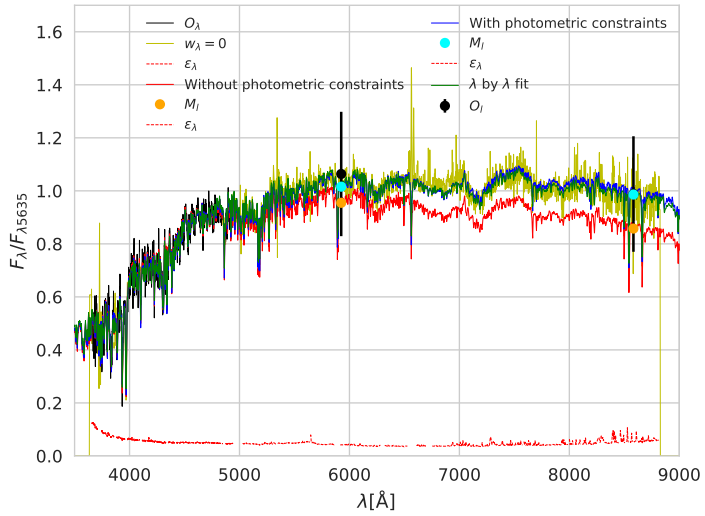


Figure 3

pre-process the input data. If you want to learn about the inner workings of STARLIGHT, section 5 will also be useful.

4 Notes on input pre-processing

This is where things start to get tricky: in order for STARLIGHT to properly account for spectra and photometry, the user has to make sure that both measurements are consistent with each other.

The first possible problem regarding compatibility between spectra and photometry is the flux calibration of the spectra. For example, SDSS spectra are calibrated to match the flux of a point source within one FWHM of the PSF. This leads to a discrepancy between spectra and photometry for extended sources. Fluxes calculated from spectra are, on average, 25% smaller than their photometric equivalents. To deal with this offset, the authors of the MPA/JHU value added galaxy catalog propose matching the synthetic photometry to the observed photometry in the r band. This correction is sufficient because the shape of the photometric SEDs is very similar to the shape of the spectra.

To calculate synthetic fluxes from spectra in a given flux, one should calculate the average spectral flux weighted by the filter’s transmission curve. This is given by

$$\langle f_\lambda \rangle_Y = \frac{\int f_\lambda T_{\lambda,Y} \lambda d\lambda}{\int T_{\lambda,Y} \lambda d\lambda}, \quad (3)$$

where $T_{\lambda,Y}$ denotes the transmission curve of the filter Y , the $T_{\lambda,Y} \lambda$ weighting assumes that the transmission curve is given for a photon counting device.

After calculating this average flux, you should make sure it is compatible with the photometric flux in the same filter. If not, we suggest you apply a correction to the spectra to match it to the photometry².

Other possible source of problems are cosmological corrections. STARLIGHT is built to work with rest-frame spectra and observed frame photometry, to compare the two, STARLIGHT will shift the model spectra to the observed frame and divide the spectral fluxes by $(1+z)$. If your cosmological corrections are incompatible with this process, you will get wrong results.

To summarize, the recipe for pre-processing input is this:

1. Make sure that your **observed frame spectra** matches the observed photometric fluxes in a reference filter of your preference; if it doesn’t, apply the necessary corrections;
2. Correct spectra and photometry for MW extinction (this is the only correction applied to the photometry);

²Or the opposite, if you trust your spectra.

3. Convert your spectra to the rest frame using the following:

$$\begin{aligned}\lambda^{\text{rest}} &= \frac{\lambda^{\text{obs}}}{(1+z)} \\ f_{\lambda}^{\text{rest}} &= (1+z)f_{\lambda}^{\text{obs}};\end{aligned}\tag{4}$$

4. Re-sample spectra to equal intervals of λ .

Note that the order of the steps matters! If, for instance, you decide to re-sample your spectra in the observed frame, dividing λ by $(1+z)$ will ruin the re-sampling.

5 Implementation of photometric constraints within STARLIGHT

5.1 Calculating magnitudes from model spectra

To compare base spectra with the input magnitudes, STARLIGHT will start by calculating synthetic magnitudes from your base spectra.

Providing that the spectra $B_{j\lambda}$ from the SSP base cover the whole region of a filter Y of transmission curve $T_{\lambda,Y}$, we may calculate the average flux in this filter as

$$\langle f_{\lambda} \rangle_Y = \frac{\int M_{\lambda(1+z)^{-1}}(1+z)T_{\lambda,Y}\lambda d\lambda}{\int T_{\lambda,Y}\lambda d\lambda}, \quad (5)$$

where M_{λ} is the good and old model spectrum. The factors of $(1+z)$ shift the model spectra to the observed frame, as we want to compare this to observed magnitudes.

After a couple of unit conversions, we can convert the fluxes to magnitudes using

$$m_Y = -2.5 \log \frac{\int M_{\lambda(1+z)^{-1}}(1+z)T_{\lambda,Y}\lambda d\lambda}{\int T_{\lambda,Y}\lambda^{-1} d\lambda} - 2.41, \quad (6)$$

which is the equation implemented in the code.

The magnitudes m_Y are compared to input magnitudes to find the modeled spectrum M_{λ} that best describes spectra and photometry simultaneously. In the next subsection, you will learn how input magnitudes are compared to model magnitudes, and how photometric and spectroscopic constraints are combined.

5.2 Combining photometric and spectroscopic figures of merit

To simultaneously fit spectra and photometry, the traditional χ^2 minimization scheme of STARLIGHT was redefined. The spectroscopic part³ of the χ^2 remains the same and is defined as

$$\chi_{SPEC}^2 = \sum_{\lambda} w_{\lambda}^2 (O_{\lambda} - M_{\lambda})^2. \quad (7)$$

In addition to the spectroscopic χ^2 , we now also have a photometric one:

$$\chi_{PHO}^2 = \sum_{l=1}^{N_l} \left(\frac{m_Y^{obs} - m_Y}{\sigma_Y} \right)^2. \quad (8)$$

Combining these quantities is a tricky business. One may think of using

$$\chi_{TOT}^2 = \chi_{SPEC}^2 + \chi_{PHO}^2 \quad (9)$$

³Although we are using the notation χ_{SPEC}^2 in the text, for historical reasons the variable is called `chi2_0pt` in the code.

as a definition of total χ^2 , which seems like a consistent solution. The problem with this definition is that spectra have a lot of data points, yielding a typical χ_{SPEC}^2 of the order of 1000. In contrast, we usually deal with a handful of photometric data points. Because of this, χ_{SPEC}^2 contributes with a much larger portion of the total χ^2 . To promote a fair fight, we have to give more weight to χ_{PHO}^2 , but there are lots of ways to tackle this issue. To allow for a variety of fitting philosophies, we choose to define our total χ^2 as

$$\chi_{TOT}^2 = S^\gamma \left[\chi_{SPEC}^2 + G_{PHO} \left(\frac{N_\lambda}{N_Y} \right)^\alpha \left(\frac{\chi_{SPEC}^2}{N_Y} \right)^\beta \chi_{PHO}^2 \right]. \quad (10)$$

Don't panic! Let me explain what each of these factors mean: G_{PHO} is a parameter that sets the relative weight of photometric and spectroscopic constraints, it is presented as PHO_GlobalChi2ScaleFactor in the code. α and β are switches that can be set to 1 or 0, defining whether χ_{PHO}^2 is scaled according to the number of spectroscopic data-points or to χ_{SPEC}^2 . γ is also a switch that turns on or off the global scale factor

$$S = \frac{N_\lambda + N_Y}{G_{PHO} N_\lambda^{\alpha+\beta} N_Y^{1-\alpha+\beta}}, \quad (11)$$

which aims on bringing χ_{TOT}^2 to the same order of magnitude as the number of data-points.

To minimize the frustration of the user, the interface of STARLIGHT hides equation 10 behind a set of three options:

1. wBn (Weight by number): sets $\alpha = 1$ and $\beta = 0$;
2. wBc (Weight by χ^2): sets $\alpha = 0$ and $\beta = 1$;
3. NoW (No weighting): sets $\alpha = 0$ and $\beta = 0$.

These codes and the value of γ are informed in the last line of STARLIGHT's grid file, this is why you may feel like you seen them before.

Is important to note that χ_{TOT}^2 will only be formal χ^2 when using the NoW option. In all other cases, the interpretability of χ_{TOT}^2 as the exponent of the likelihood function is lost.

Is hard to define a straightforward way to decide what values of PHO_GlobalChi2ScaleFactor (G_{PHO} in equation 10) to use, and this is why we leave it for the user to decide. We can, however, establish some guidelines: the conundrum involved in setting this parameter is that, although photometric input has fewer points, these points correspond to a large range in wavelength. The user could think of the wavelength range defined by the photometric filters as a proxy to choose a G_{PHO} value; for instance, if the wavelength range

represented by the photometry is a third of the spectral range, 0.3 would be a sensible value for G_{PHO} . Unfortunately, this philosophy doesn't hold up for values of G_{PHO} larger than 0.5 or so, as these large values of G_{PHO} prevent STARLIGHT from properly fitting some spectral features. It be noted that this logic only holds up if photometric errors are well estimated, which is not always the case.

5.3 Photometric constraints as ranges

STARLIGHT offers the possibility of treating the photometric data as upper or lower limits instead of values to be matched. Among other reasons, one might want to use this feature to deal with aperture differences between the spectroscopic and photometric data being fitted.

5.3.1 The math of range-fitting

Range-fitting is implemented by replacing a conventional Gaussian likelihood function $e^{-\chi_Y^2/2}$ with a flat top Gaussian function where χ_Y^2 is given by

$$\chi_Y^2 = \begin{cases} \left(\frac{m_Y - m_Y^{\text{low}}}{\sigma_Y}\right)^2 & m_Y \leq m_Y^{\text{low}} \\ 0 & m_Y^{\text{low}} < m_Y < m_Y^{\text{upp}} \\ \left(\frac{m_Y - m_Y^{\text{upp}}}{\sigma_Y}\right)^2 & m_Y \geq m_Y^{\text{upp}}, \end{cases} \quad (12)$$

so that any value of m_Y within the $m_Y^{\text{low}} < m_Y < m_Y^{\text{upp}}$ range yields $\chi_Y^2 = 0$. Thus, all models leading to a Y -filter magnitude m_Y in this interval are equally likely. Only models producing m_Y values outside this range are penalized with a lower likelihood (i.e., $\chi_Y^2 > 0$). Eq.12 reduces to a conventional

$$\chi_Y^2 = \left(\frac{m_Y - m_Y^{\text{obs}}}{\sigma_Y}\right)^2 \quad (13)$$

when $m_Y^{\text{low}} = m_Y^{\text{upp}} = m_Y^{\text{obs}}$, in which case STARLIGHT will try to match the observed magnitude m_Y^{obs} by decreasing the likelihood of models which predict m_Y too far (in units of σ_Y) from it.

Figure 4 shows the likelihood $e^{-\chi_Y^2/2}$ for 3 hypothetical situations: (a) $m_Y^{\text{low}} = m_Y^{\text{upp}} = m_Y^{\text{obs}} = 17$, a conventional Gaussian likelihood function; (b) $m_Y^{\text{upp}} = m_Y^{\text{obs}} = 17$ and $m_Y^{\text{low}} = -3$; and (c) $m_Y^{\text{upp}} = 17$, $m_Y^{\text{obs}} = m_Y^{\text{low}} = -3$. In all cases $\sigma_Y = 0.5$ mag was used. Figure 4a portrays the conventional fit situation, where we aim to match $m_Y^{\text{obs}} = 17 \pm 0.5$. Figure 4b corresponds to a case where we are confident (to within $\pm\sigma = \pm 0.5$ mag) that the magnitude in filter Y must be brighter than 17, so much so that we set m_Y^{upp} to a ridiculously bright -3 mag (off the plot's scale). This illustrates how to implement a lower-limit in the fits. To obtain a strict $m_Y > m_Y^{\text{obs}}$ limit it suffices to decrease σ_Y to

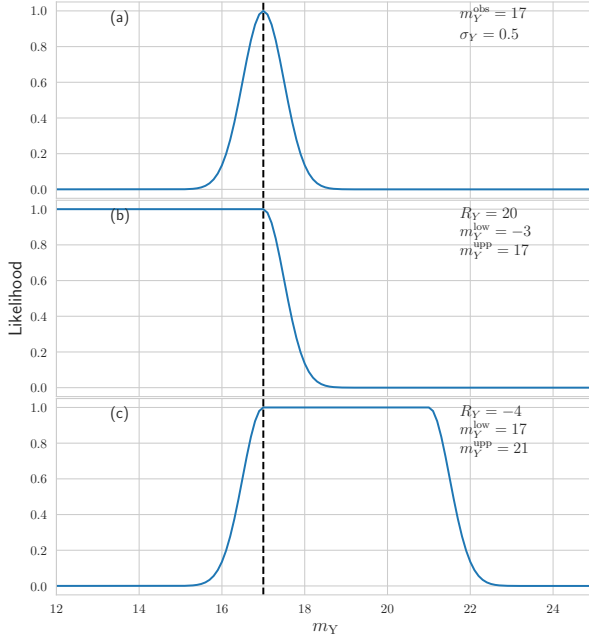


Figure 4: Likelihood functions for different values of the range parameter R_Y . Top panel shows a standard Gaussian likelihood function, middle panel shows a flat-top Gaussian used to fit observed magnitudes as lower limits, bottom panel shows a flat-top Gaussian that will give equal weight to any magnitude between m_Y^{low} and m_Y^{upp}

a small value (say, 0.01 mag), effectively turning the likelihood curve to a Heaviside step function. Figure 4c illustrates a case where we are confident (again, to within ± 0.5 mag) that m_Y is in the 17–21 range. Naturally, the larger the range between m_Y^{low} and m_Y^{upp} the looser the constraints, but in some cases even a loose constraint can help (say, combining an optical spectrum with an upper limit to the UV flux).

5.3.2 How-to

The whole range-fitting scheme is controlled by R_Y , a variable set by the PH0_magYRange entry, the 6th column in the photometric input files. Lower and upper limits m_Y^{low} and m_Y^{upp} are set in one of two ways, depending on the signal of Range_Y. When R_Y is

positive, m_Y^{obs} is placed at the right boundary of the top of the Gaussian, when R_Y is negative, m_Y^{obs} is placed to the left (see figure 4). In practice, this means that $R_Y > 0$ sets m_Y^{obs} as a lower flux limit, while $R_Y < 0$ sets m_Y^{obs} as an upper flux limit.

Since m_Y^{obs} is at the boundary of the top of the likelihood function, to fit a magnitude within a certain range, one has to inform a lower magnitude in the photometric input files. For instance, in order to match the m_Y^{obs} of NGC 0855 within ± 0.25 magnitudes, one has to set $m_Y^{\text{obs}} + 0.25$ in the photometric input and inform $R_Y = 0.5$, as in the example below.

If none of this interests you then just set `PHO_magYRange = 0` and the code will perform a conventional fit, penalizing with $\chi_Y^2 > 0$ any model which produces $m_Y \neq m_Y^{\text{obs}}$ (eq. 13).

5.3.3 Example

In the example fit `501-52235-368.pho` given in section 2.2 one has `PHO_magYRange = 0` for both r and z filters, so that `STARLIGHT` performs a conventional fit of the corresponding magnitudes. Here is an alternative photometric input file where the r and z -band photometry are used as upper flux-limits (hence lower limits to the magnitude) of the same galaxy:

```

1 PHO
2 0.044
3 2
4 0.2
5 r      r.dat      17.519      1.0      0.01      -20.0      0.5
6 z      z.dat      16.794      1.0      0.01      -20.0      0.5
7 #PHO_name PHO_Filter_file PHO_magY_TOT PHO_YFrac2Model PHO_magYErr PHO_magYRange PHO_Chi2ScaleFactor
```

By setting `PHO_magYRange = -20` we will allow any solution producing $m_r^{\text{low}} = 17.519 < m_r < 37.519 = m_r^{\text{upp}}$ and $m_z^{\text{low}} = 16.794 < m_z < 36.794 = m_z^{\text{upp}}$. Note that in practice these upper limits mean infinitely faint. We have also changed `PHO_magYErr` to 0.01 to use the observed magnitudes as hard lower limits (as opposed to a soft/smooth limit obtained with larger errors).

Bibliography

- Aihara, H. et al. (Apr. 2011). “The Eighth Data Release of the Sloan Digital Sky Survey: First Data from SDSS-III”. In: *ApJS* 193, 29, p. 29. DOI: [10.1088/0067-0049/193/2/29](https://doi.org/10.1088/0067-0049/193/2/29). arXiv: [1101.1559](https://arxiv.org/abs/1101.1559) [astro-ph.IM].
- Akritas, M. G. & M. A. Bershady (Oct. 1996). “Linear Regression for Astronomical Data with Measurement Errors and Intrinsic Scatter”. In: *ApJ* 470, p. 706. DOI: [10.1086/177901](https://doi.org/10.1086/177901). eprint: [astro-ph/9605002](https://arxiv.org/abs/astro-ph/9605002).
- Ali, S. S., M. N. Bremer, S. Phillipps & R. De Propris (May 2018). “UV SEDs of early-type cluster galaxies: a new look at the UV upturn”. In: *MNRAS* 476, pp. 1010–1020. DOI: [10.1093/mnras/sty227](https://doi.org/10.1093/mnras/sty227). arXiv: [1801.09688](https://arxiv.org/abs/1801.09688) [astro-ph.GA].
- Allen, J. T. et al. (Jan. 2015). “The SAMI Galaxy Survey: Early Data Release”. In: *MNRAS* 446, pp. 1567–1583. DOI: [10.1093/mnras/stu2057](https://doi.org/10.1093/mnras/stu2057). arXiv: [1407.6068](https://arxiv.org/abs/1407.6068).
- Alongi, M. et al. (Mar. 1993). “Evolutionary sequences of stellar models with semiconvection and convective overshoot. I - $Z = 0.008$ ”. In: *A&AS* 97, pp. 851–871.
- Aringer, B., L. Girardi, W. Nowotny, P. Marigo & M. T. Lederer (Sept. 2009). “Synthetic photometry for carbon rich giants. I. Hydrostatic dust-free models”. In: *A&A* 503, pp. 913–928. DOI: [10.1051/0004-6361/200911703](https://doi.org/10.1051/0004-6361/200911703). arXiv: [0905.4415](https://arxiv.org/abs/0905.4415) [astro-ph.SR].
- Asari, N. V. et al. (Oct. 2007). “The history of star-forming galaxies in the Sloan Digital Sky Survey”. In: *MNRAS* 381, pp. 263–279. DOI: [10.1111/j.1365-2966.2007.12255.x](https://doi.org/10.1111/j.1365-2966.2007.12255.x). arXiv: [0707.3578](https://arxiv.org/abs/0707.3578).
- Baldry, I. K., M. L. Balogh, R. Bower, K. Glazebrook & R. C. Nichol (Dec. 2004). “Color bimodality: Implications for galaxy evolution”. In: *The New Cosmology: Conference on Strings and Cosmology*. Ed. by Roland E. Allen, Dimitri V. Nanopoulos & Christopher N. Pope. Vol. 743. American Institute of Physics Conference Series, pp. 106–119. DOI: [10.1063/1.1848322](https://doi.org/10.1063/1.1848322). arXiv: [astro-ph/0410603](https://arxiv.org/abs/astro-ph/0410603) [astro-ph].

- Baldwin, J. A., M. M. Phillips & R. Terlevich (Feb. 1981). "Classification parameters for the emission-line spectra of extragalactic objects". In: *PASP* 93, pp. 5–19. DOI: [10.1086/130766](https://doi.org/10.1086/130766).
- Barnes, J. E. & L. E. Hernquist (Apr. 1991). "Fueling starburst galaxies with gas-rich mergers". In: *ApJ* 370, pp. L65–L68. DOI: [10.1086/185978](https://doi.org/10.1086/185978).
- Battisti, A. J., D. Calzetti & R.-R. Chary (Feb. 2016). "Characterizing Dust Attenuation in Local Star-forming Galaxies: UV and Optical Reddening". In: *ApJ* 818, 13, p. 13. DOI: [10.3847/0004-637X/818/1/13](https://doi.org/10.3847/0004-637X/818/1/13). arXiv: [1601.00208](https://arxiv.org/abs/1601.00208).
- (Dec. 2017). "Characterizing Dust Attenuation in Local Star-forming Galaxies: Inclination Effects and the 2175 Å Feature". In: *ApJ* 851, 90, p. 90. DOI: [10.3847/1538-4357/aa9a43](https://doi.org/10.3847/1538-4357/aa9a43). arXiv: [1711.04814](https://arxiv.org/abs/1711.04814).
- Bell, E. F. et al. (June 2004). "Nearly 5000 Distant Early-Type Galaxies in COMBO-17: A Red Sequence and Its Evolution since $z \sim 1$ ". In: *ApJ* 608, pp. 752–767. DOI: [10.1086/420778](https://doi.org/10.1086/420778). eprint: [astro-ph/0303394](https://arxiv.org/abs/astro-ph/0303394).
- Benitez, N. et al. (Mar. 2014). "J-PAS: The Javalambre-Physics of the Accelerated Universe Astrophysical Survey". In: *ArXiv e-prints*. arXiv: [1403.5237](https://arxiv.org/abs/1403.5237) [[astro-ph](https://arxiv.org/abs/astro-ph).CO].
- Bertin, E. & S. Arnouts (June 1996). "SExtractor: Software for source extraction." In: *A&AS* 117, pp. 393–404. DOI: [10.1051/aas:1996164](https://doi.org/10.1051/aas:1996164).
- Bertola, F. & M. Capaccioli (Sept. 1975). "Dynamics of early type galaxies. I - The rotation curve of the elliptical galaxy NGC 4697". In: *ApJ* 200, pp. 439–445. DOI: [10.1086/153808](https://doi.org/10.1086/153808).
- Bica, E. & D. Alloin (Aug. 1987). "Analysis of absorption-line spectra in a sample of 164 galactic nuclei". In: *A&AS* 70, pp. 281–301.
- Binney, J. (May 1978). "On the rotation of elliptical galaxies". In: *MNRAS* 183, pp. 501–514. DOI: [10.1093/mnras/183.3.501](https://doi.org/10.1093/mnras/183.3.501).
- Blanton, M. R. & S. Roweis (Feb. 2007). "K-Corrections and Filter Transformations in the Ultraviolet, Optical, and Near-Infrared". In: *AJ* 133, pp. 734–754. DOI: [10.1086/510127](https://doi.org/10.1086/510127). eprint: [astro-ph/0606170](https://arxiv.org/abs/astro-ph/0606170).
- Blanton, M. R., E. Kazin, D. Muna, B. A. Weaver & A. Price-Whelan (July 2011). "Improved Background Subtraction for the Sloan Digital Sky Survey Images". In: *AJ* 142, 31, p. 31. DOI: [10.1088/0004-6256/142/1/31](https://doi.org/10.1088/0004-6256/142/1/31). arXiv: [1105.1960](https://arxiv.org/abs/1105.1960) [[astro-ph](https://arxiv.org/abs/astro-ph).IM].
- Bluck, A. F. L. et al. (Mar. 2012). "The Structures and Total (Minor + Major) Merger Histories of Massive Galaxies up to $z \sim 3$ in the HST GOODS NICMOS Survey: A Possible Solution to the Size

- Evolution Problem". In: *ApJ* 747, 34, p. 34. DOI: [10.1088/0004-637X/747/1/34](https://doi.org/10.1088/0004-637X/747/1/34). arXiv: [1111.5662](https://arxiv.org/abs/1111.5662).
- Boquien, M. et al. (Mar. 2012). "The IRX- β relation on subgalactic scales in star-forming galaxies of the Herschel Reference Survey". In: *A&A* 539, A145, A145. DOI: [10.1051/0004-6361/201118624](https://doi.org/10.1051/0004-6361/201118624). arXiv: [1201.2405](https://arxiv.org/abs/1201.2405).
- Boquien, M. et al. (Nov. 2018). "CIGALE: a python Code Investigating GALaxy Emission". In: *arXiv e-prints*, arXiv:1811.03094, arXiv:1811.03094. arXiv: [1811.03094](https://arxiv.org/abs/1811.03094) [[astro-ph.GA](https://arxiv.org/archive/astro)].
- Brammer, G. B., P. G. van Dokkum & P. Coppi (Oct. 2008). "EAZY: A Fast, Public Photometric Redshift Code". In: *ApJ* 686, pp. 1503–1513. DOI: [10.1086/591786](https://doi.org/10.1086/591786). arXiv: [0807.1533](https://arxiv.org/abs/0807.1533).
- Bressan, A., F. Fagotto, G. Bertelli & C. Chiosi (Sept. 1993). "Evolutionary sequences of stellar models with new radiative opacities. II - $Z = 0.02$ ". In: *A&AS* 100, pp. 647–664.
- Bressan, A. et al. (Nov. 2012). "PARSEC: stellar tracks and isochrones with the PADova and TRIeste Stellar Evolution Code". In: *MNRAS* 427, pp. 127–145. DOI: [10.1111/j.1365-2966.2012.21948.x](https://doi.org/10.1111/j.1365-2966.2012.21948.x). arXiv: [1208.4498](https://arxiv.org/abs/1208.4498) [[astro-ph.SR](https://arxiv.org/archive/astro)].
- Brinchmann, J. et al. (July 2004). "The physical properties of star-forming galaxies in the low-redshift Universe". In: *MNRAS* 351, pp. 1151–1179. DOI: [10.1111/j.1365-2966.2004.07881.x](https://doi.org/10.1111/j.1365-2966.2004.07881.x). arXiv: [astro-ph/0311060](https://arxiv.org/abs/astro-ph/0311060) [[astro-ph](https://arxiv.org/archive/astro)].
- Brown, M. J. I. et al. (June 2014). "An Atlas of Galaxy Spectral Energy Distributions from the Ultraviolet to the Mid-infrared". In: *ApJS* 212, 18, p. 18. DOI: [10.1088/0067-0049/212/2/18](https://doi.org/10.1088/0067-0049/212/2/18). arXiv: [1312.3029](https://arxiv.org/abs/1312.3029).
- Brown, Michael J. I. et al. (2017). "Calibration of Ultraviolet, Mid-infrared, and Radio Star Formation Rate Indicators". In: *The Astrophysical Journal* 847.2, p. 136. DOI: [10.3847/1538-4357/aa8ad2](https://doi.org/10.3847/1538-4357/aa8ad2). URL: <https://doi.org/10.3847/2F1538-4357%2Faa8ad2>.
- Bruzual, G. & S. Charlot (Oct. 2003). "Stellar population synthesis at the resolution of 2003". In: *MNRAS* 344, pp. 1000–1028. DOI: [10.1046/j.1365-8711.2003.06897.x](https://doi.org/10.1046/j.1365-8711.2003.06897.x). eprint: [astro-ph/0309134](https://arxiv.org/abs/astro-ph/0309134).
- Buat, V. et al. (Jan. 2005). "Dust Attenuation in the Nearby Universe: A Comparison between Galaxies Selected in the Ultraviolet and in the Far-Infrared". In: *ApJ* 619, pp. L51–L54. DOI: [10.1086/423241](https://doi.org/10.1086/423241). eprint: [astro-ph/0411343](https://arxiv.org/abs/astro-ph/0411343).
- Buat, V. et al. (Sept. 2011). "GOODS-Herschel: evidence of a UV extinction bump in galaxies at $z>1$ ". In: *A&A* 533, A93, A93. DOI: [10.1051/0004-6361/201117264](https://doi.org/10.1051/0004-6361/201117264). arXiv: [1107.1049](https://arxiv.org/abs/1107.1049).

- Bundy, K. et al. (Jan. 2015). "Overview of the SDSS-IV MaNGA Survey: Mapping nearby Galaxies at Apache Point Observatory". In: *ApJ* 798, 7, p. 7. DOI: [10.1088/0004-637X/798/1/7](https://doi.org/10.1088/0004-637X/798/1/7). arXiv: [1412.1482](https://arxiv.org/abs/1412.1482).
- Burgarella, D., V. Buat & J. Iglesias-Páramo (July 2005). "Star formation and dust attenuation properties in galaxies from a statistical ultraviolet-to-far-infrared analysis". In: *MNRAS* 360, pp. 1413–1425. DOI: [10.1111/j.1365-2966.2005.09131.x](https://doi.org/10.1111/j.1365-2966.2005.09131.x). eprint: [astro-ph/0504434](https://arxiv.org/abs/astro-ph/0504434).
- Calzetti, D., A. L. Kinney & T. Storchi-Bergmann (July 1994). "Dust extinction of the stellar continua in starburst galaxies: The ultraviolet and optical extinction law". In: *ApJ* 429, pp. 582–601. DOI: [10.1086/174346](https://doi.org/10.1086/174346).
- Calzetti, D., L. Armus, R. C. Bohlin, A. L. Kinney, J. Koornneef & T. Storchi-Bergmann (Apr. 2000). "The Dust Content and Opacity of Actively Star-forming Galaxies". In: *ApJ* 533, pp. 682–695. DOI: [10.1086/308692](https://doi.org/10.1086/308692). eprint: [astro-ph/9911459](https://arxiv.org/abs/astro-ph/9911459).
- Cappellari, M. (2017). "Improving the full spectrum fitting method: accurate convolution with Gauss-Hermite functions". In: *MNRAS* 466, pp. 798–811. DOI: [10.1093/mnras/stw3020](https://doi.org/10.1093/mnras/stw3020). eprint: [1607.08538](https://arxiv.org/abs/1607.08538).
- Cappellari, M. et al. (Sept. 2011). "The ATLAS^{3D} project - VII. A new look at the morphology of nearby galaxies: the kinematic morphology-density relation". In: *MNRAS* 416, pp. 1680–1696. DOI: [10.1111/j.1365-2966.2011.18600.x](https://doi.org/10.1111/j.1365-2966.2011.18600.x). arXiv: [1104.3545](https://arxiv.org/abs/1104.3545) [[astro-ph](https://arxiv.org/abs/astro-ph).C0].
- Cappellari, Michele et al. (Apr. 2012). "Systematic variation of the stellar initial mass function in early-type galaxies". In: *Nature* 484, pp. 485–488. DOI: [10.1038/nature10972](https://doi.org/10.1038/nature10972). arXiv: [1202.3308](https://arxiv.org/abs/1202.3308) [[astro-ph](https://arxiv.org/abs/astro-ph).C0].
- Cardelli, J. A., G. C. Clayton & J. S. Mathis (Oct. 1989). "The relationship between infrared, optical, and ultraviolet extinction". In: *ApJ* 345, pp. 245–256. DOI: [10.1086/167900](https://doi.org/10.1086/167900).
- Carnall, A. C., R. J. McLure, J. S. Dunlop & R. Davé (Aug. 2018). "Inferring the star-formation histories of massive quiescent galaxies with BAGPIPES: Evidence for multiple quenching mechanisms". In: *MNRAS*. DOI: [10.1093/mnras/sty2169](https://doi.org/10.1093/mnras/sty2169). arXiv: [1712.04452](https://arxiv.org/abs/1712.04452).
- Chabrier, G. (July 2003). "Galactic Stellar and Substellar Initial Mass Function". In: *PASP* 115, pp. 763–795. DOI: [10.1086/376392](https://doi.org/10.1086/376392). eprint: [astro-ph/0304382](https://arxiv.org/abs/astro-ph/0304382).

- Charlot, S. & S. M. Fall (Aug. 2000). “A Simple Model for the Absorption of Starlight by Dust in Galaxies”. In: *ApJ* 539, pp. 718–731. DOI: [10.1086/309250](https://doi.org/10.1086/309250). eprint: [astro-ph/0003128](https://arxiv.org/abs/astro-ph/0003128).
- Chen, Y., A. Bressan, L. Girardi, P. Marigo, X. Kong & A. Lanza (Sept. 2015). “PARSEC evolutionary tracks of massive stars up to $350 M_{\odot}$ at metallicities $0.0001 \leq Z \leq 0.04$ ”. In: *MNRAS* 452, pp. 1068–1080. DOI: [10.1093/mnras/stv1281](https://doi.org/10.1093/mnras/stv1281). arXiv: [1506.01681](https://arxiv.org/abs/1506.01681) [[astro-ph.SR](https://arxiv.org/abs/1506.01681)].
- Chevallard, J. & S. Charlot (Oct. 2016). “Modelling and interpreting spectral energy distributions of galaxies with BEAGLE”. In: *MNRAS* 462, pp. 1415–1443. DOI: [10.1093/mnras/stw1756](https://doi.org/10.1093/mnras/stw1756). arXiv: [1603.03037](https://arxiv.org/abs/1603.03037).
- Chevallard, J., S. Charlot, B. Wandelt & V. Wild (July 2013). “Insights into the content and spatial distribution of dust from the integrated spectral properties of galaxies”. In: *MNRAS* 432, pp. 2061–2091. DOI: [10.1093/mnras/stt523](https://doi.org/10.1093/mnras/stt523). arXiv: [1303.6631](https://arxiv.org/abs/1303.6631).
- Choi, Jieun, Charlie Conroy & Nell Byler (Apr. 2017). “The Evolution and Properties of Rotating Massive Star Populations”. In: *ApJ* 838, 159, p. 159. DOI: [10.3847/1538-4357/aa679f](https://doi.org/10.3847/1538-4357/aa679f). arXiv: [1702.04722](https://arxiv.org/abs/1702.04722) [[astro-ph.SR](https://arxiv.org/abs/1702.04722)].
- Cid Fernandes, R. & R. M. González Delgado (Apr. 2010). “Testing spectral models for stellar populations with star clusters - I. Methodology”. In: *MNRAS* 403, pp. 780–796. DOI: [10.1111/j.1365-2966.2009.16153.x](https://doi.org/10.1111/j.1365-2966.2009.16153.x). arXiv: [0912.0410](https://arxiv.org/abs/0912.0410).
- Cid Fernandes, R., A. Mateus, L. Sodré, G. Stasińska & J. M. Gomes (Apr. 2005). “Semi-empirical analysis of Sloan Digital Sky Survey galaxies - I. Spectral synthesis method”. In: *MNRAS* 358, pp. 363–378. DOI: [10.1111/j.1365-2966.2005.08752.x](https://doi.org/10.1111/j.1365-2966.2005.08752.x). eprint: [astro-ph/0412481](https://arxiv.org/abs/astro-ph/0412481).
- Cid Fernandes, R., G. Stasińska, A. Mateus & N. Vale Asari (May 2011). “A comprehensive classification of galaxies in the Sloan Digital Sky Survey: how to tell true from fake AGN?” In: *MNRAS* 413, pp. 1687–1699. DOI: [10.1111/j.1365-2966.2011.18244.x](https://doi.org/10.1111/j.1365-2966.2011.18244.x). arXiv: [1012.4426](https://arxiv.org/abs/1012.4426).
- Cid Fernandes, R. et al. (Sept. 2013). “Resolving galaxies in time and space. I. Applying STARLIGHT to CALIFA datacubes”. In: *A&A* 557, A86, A86. DOI: [10.1051/0004-6361/201220616](https://doi.org/10.1051/0004-6361/201220616). arXiv: [1304.5788](https://arxiv.org/abs/1304.5788).
- Cid Fernandes, R. et al. (Jan. 2014). “Resolving galaxies in time and space. II. Uncertainties in the spectral synthesis of datacubes”. In:

- A&A* 561, A130, A130. DOI: [10.1051/0004-6361/201321692](https://doi.org/10.1051/0004-6361/201321692). arXiv: [1307.0562](https://arxiv.org/abs/1307.0562).
- Cid Fernandes, Roberto (Jan. 2007). "Paleontology of Galaxies: Recovering the Star Formation & Chemical Enrichment Histories from Galaxy Spectra". In: *arXiv e-prints*, astro-ph/0701902, astro-ph/0701902. arXiv: [astro-ph/0701902](https://arxiv.org/abs/astro-ph/0701902) [[astro-ph](https://arxiv.org/abs/astro-ph)].
- Cirasuolo, M. et al. (Sept. 2007). "The evolution of the near-infrared galaxy luminosity function and colour bimodality up to $z \sim 2$ from the UKIDSS Ultra Deep Survey Early Data Release". In: *MNRAS* 380, pp. 585–595. DOI: [10.1111/j.1365-2966.2007.12038.x](https://doi.org/10.1111/j.1365-2966.2007.12038.x). eprint: [astro-ph/0609287](https://arxiv.org/abs/astro-ph/0609287).
- Code, A. D. & G. A. Welch (Feb. 1979). "Ultraviolet photometry from the Orbiting Astronomical Observatory. XXVI - Energy distributions of seven early-type galaxies and the central bulge of M31". In: *ApJ* 228, pp. 95–104. DOI: [10.1086/156825](https://doi.org/10.1086/156825).
- Conroy, C. (Aug. 2013). "Modeling the Panchromatic Spectral Energy Distributions of Galaxies". In: *ARA&A* 51, pp. 393–455. DOI: [10.1146/annurev-astro-082812-141017](https://doi.org/10.1146/annurev-astro-082812-141017). arXiv: [1301.7095](https://arxiv.org/abs/1301.7095).
- Conroy, C., D. Schiminovich & M. R. Blanton (July 2010). "Dust Attenuation in Disk-dominated Galaxies: Evidence for the 2175 Å Dust Feature". In: *ApJ* 718, pp. 184–198. DOI: [10.1088/0004-637X/718/1/184](https://doi.org/10.1088/0004-637X/718/1/184). arXiv: [1003.2202](https://arxiv.org/abs/1003.2202).
- Conroy, Charlie & Pieter G. van Dokkum (2012). "THE STELLAR INITIAL MASS FUNCTION IN EARLY-TYPE GALAXIES FROM ABSORPTION LINE SPECTROSCOPY. II. RESULTS". In: *The Astrophysical Journal* 760.1, p. 71. DOI: [10.1088/0004-637x/760/1/71](https://doi.org/10.1088/0004-637x/760/1/71). URL: <https://doi.org/10.1088/0004-637x/760/1/71>.
- Conselice, C. J., M. A. Bershadsky, M. Dickinson & C. Papovich (Sept. 2003). "A Direct Measurement of Major Galaxy Mergers at $z < 3$ ". In: *AJ* 126, pp. 1183–1207. DOI: [10.1086/377318](https://doi.org/10.1086/377318). eprint: [astro-ph/0306106](https://arxiv.org/abs/astro-ph/0306106).
- da Cunha, E., S. Charlot & D. Elbaz (Aug. 2008). "A simple model to interpret the ultraviolet, optical and infrared emission from galaxies". In: *MNRAS* 388, pp. 1595–1617. DOI: [10.1111/j.1365-2966.2008.13535.x](https://doi.org/10.1111/j.1365-2966.2008.13535.x). arXiv: [0806.1020](https://arxiv.org/abs/0806.1020).
- de Vaucouleurs, G. (Jan. 1948). "Recherches sur les Nebuleuses Extragalactiques". In: *Annales d'Astrophysique* 11, p. 247.
- Djorgovski, S. & M. Davis (Feb. 1987). "Fundamental properties of elliptical galaxies". In: *ApJ* 313, pp. 59–68. DOI: [10.1086/164948](https://doi.org/10.1086/164948).

- Dokkum, Pieter G. van & Charlie Conroy (2012). "THE STELLAR INITIAL MASS FUNCTION IN EARLY-TYPE GALAXIES FROM ABSORPTION LINE SPECTROSCOPY. I. DATA AND EMPIRICAL TRENDS". In: *The Astrophysical Journal* 760.1, p. 70. DOI: [10.1088/0004-637x/760/1/70](https://doi.org/10.1088/0004-637x/760/1/70). URL: <https://doi.org/10.1088/0004-637x/760/1/70>.
- Draine, B. T. (2003). "Interstellar Dust Grains". In: *ARA&A* 41, pp. 241–289. DOI: [10.1146/annurev.astro.41.011802.094840](https://doi.org/10.1146/annurev.astro.41.011802.094840). eprint: [astro-ph/0304489](https://arxiv.org/abs/astro-ph/0304489).
- Dressler, A. (Mar. 1980). "Galaxy morphology in rich clusters - Implications for the formation and evolution of galaxies". In: *ApJ* 236, pp. 351–365. DOI: [10.1086/157753](https://doi.org/10.1086/157753).
- Driver, S. P. et al. (Feb. 2016). "Galaxy And Mass Assembly (GAMA): Panchromatic Data Release (far-UV-far-IR) and the low-z energy budget". In: *MNRAS* 455, pp. 3911–3942. DOI: [10.1093/mnras/stv2505](https://doi.org/10.1093/mnras/stv2505). arXiv: [1508.02076](https://arxiv.org/abs/1508.02076).
- Eldridge, J. J. & E. R. Stanway (Jan. 2012). "The effect of stellar evolution uncertainties on the rest-frame ultraviolet stellar lines of C IV and He II in high-redshift Lyman-break galaxies". In: *MNRAS* 419, pp. 479–489. DOI: [10.1111/j.1365-2966.2011.19713.x](https://doi.org/10.1111/j.1365-2966.2011.19713.x). arXiv: [1109.0288](https://arxiv.org/abs/1109.0288).
- Emsellem, Eric et al. (Aug. 2007). "The SAURON project - IX. A kinematic classification for early-type galaxies". In: *MNRAS* 379, pp. 401–417. DOI: [10.1111/j.1365-2966.2007.11752.x](https://doi.org/10.1111/j.1365-2966.2007.11752.x). arXiv: [astro-ph/0703531](https://arxiv.org/abs/astro-ph/0703531) [[astro-ph](https://arxiv.org/abs/astro-ph)].
- Faber, S. M. (Sept. 1972). "Quadratic programming applied to the problem of galaxy population synthesis." In: *A&A* 20, pp. 361–374.
- Faber, S. M. & R. E. Jackson (Mar. 1976). "Velocity dispersions and mass-to-light ratios for elliptical galaxies". In: *ApJ* 204, pp. 668–683. DOI: [10.1086/154215](https://doi.org/10.1086/154215).
- Ferreras, I. et al. (2013). "Systematic variation of the stellar initial mass function with velocity dispersion in early-type galaxies." In: *MNRAS* 429, pp. L15–L19. DOI: [10.1093/mnrasl/sls014](https://doi.org/10.1093/mnrasl/sls014). arXiv: [1206.1594](https://arxiv.org/abs/1206.1594) [[astro-ph](https://arxiv.org/abs/astro-ph).[C0](https://arxiv.org/abs/astro-ph)].
- Folkes, S. et al. (Sept. 1999). "The 2dF Galaxy Redshift Survey: spectral types and luminosity functions". In: *MNRAS* 308, pp. 459–472. DOI: [10.1046/j.1365-8711.1999.02721.x](https://doi.org/10.1046/j.1365-8711.1999.02721.x). eprint: [astro-ph/9903456](https://arxiv.org/abs/astro-ph/9903456).
- Fukugita, M., T. Ichikawa, J. E. Gunn, M. Doi, K. Shimasaku & D. P. Schneider (Apr. 1996). "The Sloan Digital Sky Survey Photometric System". In: *AJ* 111, p. 1748. DOI: [10.1086/117915](https://doi.org/10.1086/117915).

- Gavazzi, G., A. Zaccardo, G. Sanvito, A. Boselli & C. Bonfanti (Apr. 2004). "Spectrophotometry of galaxies in the Virgo cluster. II. The data". In: *A&A* 417, pp. 499–514. DOI: [10.1051/0004-6361:20034105](https://doi.org/10.1051/0004-6361:20034105). eprint: [astro-ph/0401636](https://arxiv.org/abs/astro-ph/0401636).
- Girardi, L., A. Bressan, G. Bertelli & C. Chiosi (Feb. 2000). "Evolutionary tracks and isochrones for low- and intermediate-mass stars: From 0.15 to 7 M_{sun} , and from $Z=0.0004$ to 0.03". In: *A&AS* 141, pp. 371–383. DOI: [10.1051/aas:2000126](https://doi.org/10.1051/aas:2000126). eprint: [astro-ph/9910164](https://arxiv.org/abs/astro-ph/9910164).
- Gonçalves, T. S., D. C. Martin, K. Menéndez-Delmestre, T. K. Wyder & A. Koekemoer (Nov. 2012). "Quenching Star Formation at Intermediate Redshifts: Downsizing of the Mass Flux Density in the Green Valley". In: *ApJ* 759, 67, p. 67. DOI: [10.1088/0004-637X/759/1/67](https://doi.org/10.1088/0004-637X/759/1/67). arXiv: [1209.4084](https://arxiv.org/abs/1209.4084).
- González-Lópezlira, R. A., G. Bruzual-A., S. Charlot, J. Ballesteros-Paredes & L. Loinard (Apr. 2010). "Tracers of stellar mass loss - I. Optical and near-IR colours and surface brightness fluctuations". In: *MNRAS* 403, pp. 1213–1238. DOI: [10.1111/j.1365-2966.2009.16205.x](https://doi.org/10.1111/j.1365-2966.2009.16205.x). arXiv: [0908.4133](https://arxiv.org/abs/0908.4133).
- Gordon, K. D., G. C. Clayton, K. A. Misselt, A. U. Landolt & M. J. Wolff (Sept. 2003). "A Quantitative Comparison of the Small Magellanic Cloud, Large Magellanic Cloud, and Milky Way Ultraviolet to Near-Infrared Extinction Curves". In: *ApJ* 594, pp. 279–293. DOI: [10.1086/376774](https://doi.org/10.1086/376774). eprint: [astro-ph/0305257](https://arxiv.org/abs/astro-ph/0305257).
- Gräfener, G., L. Koesterke & W.-R. Hamann (May 2002). "Line-blanketed model atmospheres for WR stars". In: *A&A* 387, pp. 244–257. DOI: [10.1051/0004-6361:20020269](https://doi.org/10.1051/0004-6361:20020269).
- Grasha, Kathryn, Daniela Calzetti, Jennifer E. Andrews, Janice C. Lee & Daniel A. Dale (2013). "The Nature of the Second Parameter in the I R_X - β Relation for Local Galaxies". In: *ApJ* 773, 174, p. 174. DOI: [10.1088/0004-637X/773/2/174](https://doi.org/10.1088/0004-637X/773/2/174). arXiv: [1307.1680](https://arxiv.org/abs/1307.1680) [[astro-ph.GA](https://arxiv.org/abs/astro-ph.GA)].
- Hainich, R. et al. (May 2014). "The Wolf-Rayet stars in the Large Magellanic Cloud. A comprehensive analysis of the WN class". In: *A&A* 565, A27, A27. DOI: [10.1051/0004-6361/201322696](https://doi.org/10.1051/0004-6361/201322696). arXiv: [1401.5474](https://arxiv.org/abs/1401.5474) [[astro-ph.SR](https://arxiv.org/abs/astro-ph.SR)].
- Hainich, R., D. Pasemann, H. Todt, T. Shenar, A. Sander & W.-R. Hamann (Sept. 2015). "Wolf-Rayet stars in the Small Magellanic Cloud. I. Analysis of the single WN stars". In: *A&A* 581, A21, A21. DOI: [10.1051/0004-6361/201526241](https://doi.org/10.1051/0004-6361/201526241). arXiv: [1507.04000](https://arxiv.org/abs/1507.04000) [[astro-ph.SR](https://arxiv.org/abs/astro-ph.SR)].

- Hamann, W.-R. & G. Gräfener (Nov. 2003). “A temperature correction method for expanding atmospheres”. In: *A&A* 410, pp. 993–1000. DOI: [10.1051/0004-6361:20031308](https://doi.org/10.1051/0004-6361:20031308).
- Hamann, W.-R., G. Gräfener & A. Liermann (Oct. 2006). “The Galactic WN stars. Spectral analyses with line-blanketed model atmospheres versus stellar evolution models with and without rotation”. In: *A&A* 457, pp. 1015–1031. DOI: [10.1051/0004-6361:20065052](https://doi.org/10.1051/0004-6361:20065052). eprint: [astro-ph/0608078](https://arxiv.org/abs/astro-ph/0608078).
- Han, Z., Ph. Podsiadlowski & A. E. Lynas-Gray (Sept. 2007). “A binary model for the UV-upturn of elliptical galaxies”. In: *Monthly Notices of the Royal Astronomical Society* 380.3, pp. 1098–1118. ISSN: 0035-8711. DOI: [10.1111/j.1365-2966.2007.12151.x](https://doi.org/10.1111/j.1365-2966.2007.12151.x). eprint: <http://oup.prod.sis.lan/mnras/article-pdf/380/3/1098/2801247/mnras0380-1098.pdf>. URL: <https://dx.doi.org/10.1111/j.1365-2966.2007.12151.x>.
- Heavens, A. F., R. Jimenez & O. Lahav (Oct. 2000). “Massive lossless data compression and multiple parameter estimation from galaxy spectra”. In: *MNRAS* 317, pp. 965–972. DOI: [10.1046/j.1365-8711.2000.03692.x](https://doi.org/10.1046/j.1365-8711.2000.03692.x). eprint: [astro-ph/9911102](https://arxiv.org/abs/astro-ph/9911102).
- Heckman, T. M. (July 1980). “An optical and radio survey of the nuclei of bright galaxies - Activity in normal galactic nuclei”. In: *A&A* 87, pp. 152–164.
- Heckman, T. M. & P. N. Best (Aug. 2014). “The Coevolution of Galaxies and Supermassive Black Holes: Insights from Surveys of the Contemporary Universe”. In: *ARA&A* 52, pp. 589–660. DOI: [10.1146/annurev-astro-081913-035722](https://doi.org/10.1146/annurev-astro-081913-035722). arXiv: [1403.4620](https://arxiv.org/abs/1403.4620).
- Henault, F. et al. (Mar. 2003). “MUSE: a second-generation integral-field spectrograph for the VLT”. In: *Instrument Design and Performance for Optical/Infrared Ground-based Telescopes*. Ed. by M. Iye & A. F. M. Moorwood. Vol. 4841. Proc. SPIE, pp. 1096–1107. DOI: [10.1117/12.462334](https://doi.org/10.1117/12.462334).
- Hernández-Pérez, F. & G. Bruzual (May 2013). “Revisiting binary stars in population synthesis models”. In: *MNRAS* 431, pp. 2612–2621. DOI: [10.1093/mnras/stt368](https://doi.org/10.1093/mnras/stt368). arXiv: [1302.6623](https://arxiv.org/abs/1302.6623).
- Hernández-Pérez, Fabiola & Gustavo Bruzual (Nov. 2014). “Binary stars and the UVX in early-type galaxies”. In: *MNRAS* 444, pp. 2571–2579. DOI: [10.1093/mnras/stu1627](https://doi.org/10.1093/mnras/stu1627). arXiv: [1408.3426](https://arxiv.org/abs/1408.3426) [[astro-ph](https://arxiv.org/abs/astro-ph)].
- Herpich, F., G. Stasińska, A. Mateus, N. Vale Asari & R. Cid Fernandes (Dec. 2018). “Why do many early-type galaxies lack emission lines? I. Fossil clues”. In: *MNRAS* 481, pp. 1774–1785. DOI: [10.1093/mnras/sty2391](https://doi.org/10.1093/mnras/sty2391). arXiv: [1808.10405](https://arxiv.org/abs/1808.10405).

- Hetherington, N. S. (Apr. 1970). "The Shapley-Curtis Debate". In: *Leaflet of the Astronomical Society of the Pacific* 10, pp. 313–320.
- Hopkins, P. F., T. J. Cox, J. D. Younger & L. Hernquist (Feb. 2009). "How do Disks Survive Mergers?" In: *ApJ* 691, pp. 1168–1201. DOI: [10.1088/0004-637X/691/2/1168](https://doi.org/10.1088/0004-637X/691/2/1168). arXiv: [0806.1739](https://arxiv.org/abs/0806.1739).
- Hubble, E. (Mar. 1929). "A Relation between Distance and Radial Velocity among Extra-Galactic Nebulae". In: *Proceedings of the National Academy of Science* 15, pp. 168–173. DOI: [10.1073/pnas.15.3.168](https://doi.org/10.1073/pnas.15.3.168).
- Hubble, E. P. (May 1925). "Cepheids in spiral nebulae". In: *The Observatory* 48, pp. 139–142.
- (Dec. 1926). "Extragalactic nebulae." In: *ApJ* 64. DOI: [10.1086/143018](https://doi.org/10.1086/143018).
- (1936). *Realm of the Nebulae*.
- Illingworth, G. (Dec. 1977). "Rotation in 13 elliptical galaxies". In: *ApJ* 218, pp. L43–L47. DOI: [10.1086/182572](https://doi.org/10.1086/182572).
- Jeong, H. et al. (Oct. 2009). "The SAURON project - XIII. SAURON-GALEX study of early-type galaxies: the ultraviolet colour-magnitude relations and Fundamental Planes". In: *MNRAS* 398, pp. 2028–2048. DOI: [10.1111/j.1365-2966.2009.15238.x](https://doi.org/10.1111/j.1365-2966.2009.15238.x). arXiv: [0906.3318](https://arxiv.org/abs/0906.3318).
- Jogee, S. et al. (Oct. 2008). "Frequency and Impact of Galaxy Mergers and Interactions over the Last 7 Gyr". In: *Formation and Evolution of Galaxy Disks*. Ed. by J. G. Funes & E. M. Corsini. Vol. 396. Astronomical Society of the Pacific Conference Series, p. 337. arXiv: [0802.3901](https://arxiv.org/abs/0802.3901).
- Kaviraj, S., J. E. G. Devriendt, I. Ferreras & S. K. Yi (June 2005). "The elliptical galaxy colour-magnitude relation as a discriminant between the monolithic and merger paradigms". In: *MNRAS* 360, pp. 60–68. DOI: [10.1111/j.1365-2966.2005.08883.x](https://doi.org/10.1111/j.1365-2966.2005.08883.x). eprint: [astro-ph/0401126](https://arxiv.org/abs/astro-ph/0401126).
- Kaviraj, S. et al. (Dec. 2007). "UV-Optical Colors As Probes of Early-Type Galaxy Evolution". In: *ApJS* 173, pp. 619–642. DOI: [10.1086/516633](https://doi.org/10.1086/516633). eprint: [astro-ph/0601029](https://arxiv.org/abs/astro-ph/0601029).
- Kennicutt Robert C., Jr. (Apr. 1992). "A Spectrophotometric Atlas of Galaxies". In: *The Astrophysical Journal Supplement Series* 79, p. 255. DOI: [10.1086/191653](https://doi.org/10.1086/191653).
- Kennicutt Jr., R. C. (Sept. 1989). "The star formation law in galactic disks". In: *ApJ* 344, pp. 685–703. DOI: [10.1086/167834](https://doi.org/10.1086/167834).
- (1998). "Star Formation in Galaxies Along the Hubble Sequence". In: *ARA&A* 36, pp. 189–232. DOI: [10.1146/annurev.astro.36.1.189](https://doi.org/10.1146/annurev.astro.36.1.189). eprint: [astro-ph/9807187](https://arxiv.org/abs/astro-ph/9807187).

- Kennicutt, Robert C. & Neal J. Evans (Sept. 2012). "Star Formation in the Milky Way and Nearby Galaxies". In: *Annual Review of Astronomy and Astrophysics* 50, pp. 531–608. DOI: [10.1146/annurev-astro-081811-125610](https://doi.org/10.1146/annurev-astro-081811-125610). arXiv: [1204.3552](https://arxiv.org/abs/1204.3552) [astro-ph.GA].
- Kinney, Anne L., Daniela Calzetti, Eduardo Bica & Thaisa Storchi-Bergmann (July 1994). "The Reddening Law outside the Local Group Galaxies: The Case of NGC 7552 and NGC 5236". In: *ApJ* 429, p. 172. DOI: [10.1086/174309](https://doi.org/10.1086/174309).
- Koleva, M., P. Prugniel, A. Bouchard & Y. Wu (July 2009). "ULySS: a full spectrum fitting package". In: *A&A* 501, pp. 1269–1279. DOI: [10.1051/0004-6361/200811467](https://doi.org/10.1051/0004-6361/200811467). arXiv: [0903.2979](https://arxiv.org/abs/0903.2979) [astro-ph.IM].
- Kong, X., S. Charlot, J. Brinchmann & S. M. Fall (Apr. 2004). "Star formation history and dust content of galaxies drawn from ultraviolet surveys". In: *MNRAS* 349, pp. 769–778. DOI: [10.1111/j.1365-2966.2004.07556.x](https://doi.org/10.1111/j.1365-2966.2004.07556.x). eprint: [astro-ph/0312474](https://arxiv.org/abs/astro-ph/0312474).
- Kormendy, J. & G. Illingworth (May 1982). "Rotation of the bulge components of disk galaxies". In: *ApJ* 256, pp. 460–480. DOI: [10.1086/159923](https://doi.org/10.1086/159923).
- Kriek, M. & C. Conroy (Sept. 2013). "The Dust Attenuation Law in Distant Galaxies: Evidence for Variation with Spectral Type". In: *ApJ* 775, L16, p. L16. DOI: [10.1088/2041-8205/775/1/L16](https://doi.org/10.1088/2041-8205/775/1/L16). arXiv: [1308.1099](https://arxiv.org/abs/1308.1099).
- Kriek, Mariska et al. (Oct. 2010). "The Spectral Energy Distribution of Post-starburst Galaxies in the NEWFIRM Medium-band Survey: A Low Contribution from TP-AGB Stars". In: *ApJ* 722, pp. L64–L69. DOI: [10.1088/2041-8205/722/1/L64](https://doi.org/10.1088/2041-8205/722/1/L64). arXiv: [1008.4357](https://arxiv.org/abs/1008.4357) [astro-ph.CO].
- Kroupa, P. (Apr. 2001). "On the variation of the initial mass function". In: *MNRAS* 322, pp. 231–246. DOI: [10.1046/j.1365-8711.2001.04022.x](https://doi.org/10.1046/j.1365-8711.2001.04022.x). eprint: [astro-ph/0009005](https://arxiv.org/abs/astro-ph/0009005).
- Kroupa, P., C. A. Tout & G. Gilmore (June 1993). "The distribution of low-mass stars in the Galactic disc". In: *MNRAS* 262, pp. 545–587. DOI: [10.1093/mnras/262.3.545](https://doi.org/10.1093/mnras/262.3.545).
- Krumholz, M. R., A. Dekel & C. F. McKee (Jan. 2012). "A Universal, Local Star Formation Law in Galactic Clouds, nearby Galaxies, High-redshift Disks, and Starbursts". In: *ApJ* 745, 69, p. 69. DOI: [10.1088/0004-637X/745/1/69](https://doi.org/10.1088/0004-637X/745/1/69). arXiv: [1109.4150](https://arxiv.org/abs/1109.4150).
- Kumar, Amit et al. (2012). "Ultra Violet Imaging Telescope (UVIT) on ASTROSAT". In: *Space Telescopes and Instrumentation 2012:*

- Ultraviolet to Gamma Ray*. Vol. 8443. Society of Photo-Optical Instrumentation Engineers (SPIE) Conference Series, 84431N. DOI: [10.1117/12.924507](https://doi.org/10.1117/12.924507). arXiv: [1208.4670](https://arxiv.org/abs/1208.4670) [[astro-ph.IM](#)].
- La Barbera, F. et al. (2013). "SPIDER VIII - constraints on the stellar initial mass function of early-type galaxies from a variety of spectral features". In: *MNRAS* 433.4, pp. 3017–3047. DOI: [10.1093/mnras/stt943](https://doi.org/10.1093/mnras/stt943). arXiv: [1305.2273](https://arxiv.org/abs/1305.2273) [[astro-ph.CO](#)].
- Lacey, C. G. et al. (Nov. 2016). "A unified multiwavelength model of galaxy formation". In: *MNRAS* 462, pp. 3854–3911. DOI: [10.1093/mnras/stw1888](https://doi.org/10.1093/mnras/stw1888). arXiv: [1509.08473](https://arxiv.org/abs/1509.08473).
- Lanz, T. & I. Hubeny (June 2003a). "A Grid of Non-LTE Line-blanketed Model Atmospheres of O-Type Stars". In: *ApJS* 146, pp. 417–441. DOI: [10.1086/374373](https://doi.org/10.1086/374373). eprint: [astro-ph/0210157](https://arxiv.org/abs/astro-ph/0210157).
- (July 2003b). "Erratum: "A Grid of Non-LTE Line-blanketed Model Atmospheres of O-Type Stars"". In: *ApJS* 147, pp. 225–225. DOI: [10.1086/377130](https://doi.org/10.1086/377130).
- (Mar. 2007). "A Grid of NLTE Line-blanketed Model Atmospheres of Early B-Type Stars". In: *ApJS* 169, pp. 83–104. DOI: [10.1086/511270](https://doi.org/10.1086/511270). eprint: [astro-ph/0611891](https://arxiv.org/abs/astro-ph/0611891).
- Larson, R. B. (Mar. 1974). "Dynamical models for the formation and evolution of spherical galaxies". In: *MNRAS* 166, pp. 585–616. DOI: [10.1093/mnras/166.3.585](https://doi.org/10.1093/mnras/166.3.585).
- Le Borgne, J.-F. et al. (May 2003). "STELIB: A library of stellar spectra at $R \sim 2000$ ". In: *A&A* 402, pp. 433–442. DOI: [10.1051/0004-6361:20030243](https://doi.org/10.1051/0004-6361:20030243). eprint: [astro-ph/0302334](https://arxiv.org/abs/astro-ph/0302334).
- Leavitt, H. S. & E. C. Pickering (Mar. 1912). "Periods of 25 Variable Stars in the Small Magellanic Cloud." In: *Harvard College Observatory Circular* 173, pp. 1–3.
- Leitherer, C. et al. (Aug. 2010). "A Library of Theoretical Ultraviolet Spectra of Massive, Hot Stars for Evolutionary Synthesis". In: *ApJS* 189, pp. 309–335. DOI: [10.1088/0067-0049/189/2/309](https://doi.org/10.1088/0067-0049/189/2/309). arXiv: [1006.5624](https://arxiv.org/abs/1006.5624) [[astro-ph.SR](#)].
- Leitherer, Claus, I-Hui Li, Daniela Calzetti & Timothy M. Heckman (2002). "Global Far-Ultraviolet (912-1800 Å) Properties of Star-forming Galaxies". In: *The Astrophysical Journal Supplement Series* 140.2, p. 303. URL: <http://stacks.iop.org/0067-0049/140/i=2/a=303>.
- Leja, J., B. D. Johnson, C. Conroy, P. G. van Dokkum & N. Byler (Mar. 2017). "Deriving Physical Properties from Broadband Photometry with Prospector: Description of the Model and a Demonstration

- of its Accuracy Using 129 Galaxies in the Local Universe". In: *ApJ* 837, 170, p. 170. DOI: [10.3847/1538-4357/aa5ffe](https://doi.org/10.3847/1538-4357/aa5ffe). arXiv: [1609.09073](https://arxiv.org/abs/1609.09073).
- Lemaître, G. (1927). "Un Univers homogène de masse constante et de rayon croissant rendant compte de la vitesse radiale des nébuleuses extra-galactiques". In: *Annales de la Société Scientifique de Bruxelles* 47, pp. 49–59.
- Lintott, C. J. et al. (Sept. 2008). "Galaxy Zoo: morphologies derived from visual inspection of galaxies from the Sloan Digital Sky Survey". In: *MNRAS* 389, pp. 1179–1189. DOI: [10.1111/j.1365-2966.2008.13689.x](https://doi.org/10.1111/j.1365-2966.2008.13689.x). arXiv: [0804.4483](https://arxiv.org/abs/0804.4483).
- López Fernández, R. et al. (May 2016). "Simultaneous spectroscopic and photometric analysis of galaxies with STARLIGHT: CALIFA+GALEX". In: *MNRAS* 458, pp. 184–199. DOI: [10.1093/mnras/stw260](https://doi.org/10.1093/mnras/stw260). arXiv: [1602.01123](https://arxiv.org/abs/1602.01123).
- Lotz, J. M. et al. (Jan. 2008). "The Evolution of Galaxy Mergers and Morphology at $z < 1.2$ in the Extended Groth Strip". In: *ApJ* 672, pp. 177–197. DOI: [10.1086/523659](https://doi.org/10.1086/523659). eprint: [astro-ph/0602088](https://arxiv.org/abs/astro-ph/0602088).
- Lotz, J. M. et al. (Dec. 2011). "The Major and Minor Galaxy Merger Rates at $z < 1.5$ ". In: *ApJ* 742, 103, p. 103. DOI: [10.1088/0004-637X/742/2/103](https://doi.org/10.1088/0004-637X/742/2/103). arXiv: [1108.2508](https://arxiv.org/abs/1108.2508) [[astro-ph](https://arxiv.org/abs/astro-ph).C0].
- Madau, P. & M. Dickinson (Aug. 2014). "Cosmic Star-Formation History". In: *ARA&A* 52, pp. 415–486. DOI: [10.1146/annurev-astro-081811-125615](https://doi.org/10.1146/annurev-astro-081811-125615). arXiv: [1403.0007](https://arxiv.org/abs/1403.0007).
- Maraston, C. et al. (Nov. 2006). "Evidence for TP-AGB Stars in High-Redshift Galaxies, and Their Effect on Deriving Stellar Population Parameters". In: *ApJ* 652, pp. 85–96. DOI: [10.1086/508143](https://doi.org/10.1086/508143). arXiv: [astro-ph/0604530](https://arxiv.org/abs/astro-ph/0604530) [[astro-ph](https://arxiv.org/abs/astro-ph)].
- Maraston, Claudia (Sept. 2005). "Evolutionary population synthesis: models, analysis of the ingredients and application to high- z galaxies". In: *MNRAS* 362, pp. 799–825. DOI: [10.1111/j.1365-2966.2005.09270.x](https://doi.org/10.1111/j.1365-2966.2005.09270.x). arXiv: [astro-ph/0410207](https://arxiv.org/abs/astro-ph/0410207) [[astro-ph](https://arxiv.org/abs/astro-ph)].
- Marigo, P., A. Bressan, A. Nanni, L. Girardi & M. L. Pumo (Sept. 2013). "Evolution of thermally pulsing asymptotic giant branch stars - I. The COLIBRI code". In: *MNRAS* 434, pp. 488–526. DOI: [10.1093/mnras/stt1034](https://doi.org/10.1093/mnras/stt1034). arXiv: [1305.4485](https://arxiv.org/abs/1305.4485) [[astro-ph](https://arxiv.org/abs/astro-ph).SR].
- Marigo, P. et al. (Jan. 2017). "A New Generation of PARSEC-COLIBRI Stellar Isochrones Including the TP-AGB Phase". In: *ApJ* 835, 77, p. 77. DOI: [10.3847/1538-4357/835/1/77](https://doi.org/10.3847/1538-4357/835/1/77). arXiv: [1701.08510](https://arxiv.org/abs/1701.08510) [[astro-ph](https://arxiv.org/abs/astro-ph).SR].

- Martin, D. C. et al. (Jan. 2005). "The Galaxy Evolution Explorer: A Space Ultraviolet Survey Mission". In: *ApJ* 619, pp. L1–L6. DOI: [10.1086/426387](https://doi.org/10.1086/426387). eprint: [astro-ph/0411302](https://arxiv.org/abs/astro-ph/0411302).
- Martin, D. C. et al. (Dec. 2007). "The UV-Optical Galaxy Color-Magnitude Diagram. III. Constraints on Evolution from the Blue to the Red Sequence". In: *ApJS* 173, pp. 342–356. DOI: [10.1086/516639](https://doi.org/10.1086/516639). eprint: [astro-ph/0703281](https://arxiv.org/abs/astro-ph/0703281).
- Martins, L. P., R. M. González Delgado, C. Leitherer, M. Cerviño & P. Hauschildt (Mar. 2005). "A high-resolution stellar library for evolutionary population synthesis". In: *MNRAS* 358, pp. 49–65. DOI: [10.1111/j.1365-2966.2005.08703.x](https://doi.org/10.1111/j.1365-2966.2005.08703.x). eprint: [astro-ph/0501225](https://arxiv.org/abs/astro-ph/0501225).
- Mateus, A., L. Sodr e, R. Cid Fernandes, G. Stasińska, W. Schoenell & J. M. Gomes (Aug. 2006). "Semi-empirical analysis of Sloan Digital Sky Survey galaxies - II. The bimodality of the galaxy population revisited". In: *MNRAS* 370, pp. 721–737. DOI: [10.1111/j.1365-2966.2006.10565.x](https://doi.org/10.1111/j.1365-2966.2006.10565.x). eprint: [astro-ph/0511578](https://arxiv.org/abs/astro-ph/0511578).
- Mateus, A., L. Sodr e, R. Cid Fernandes & G. Stasińska (Feb. 2007). "Semi-empirical analysis of Sloan Digital Sky Survey galaxies - IV. A nature via nurture scenario for galaxy evolution". In: *MNRAS* 374, pp. 1457–1472. DOI: [10.1111/j.1365-2966.2006.11290.x](https://doi.org/10.1111/j.1365-2966.2006.11290.x). eprint: [astro-ph/0604063](https://arxiv.org/abs/astro-ph/0604063).
- Meurer, G. R., T. M. Heckman & D. Calzetti (Aug. 1999). "Dust Absorption and the Ultraviolet Luminosity Density at $z \sim 3$ as Calibrated by Local Starburst Galaxies". In: *ApJ* 521, pp. 64–80. DOI: [10.1086/307523](https://doi.org/10.1086/307523). eprint: [astro-ph/9903054](https://arxiv.org/abs/astro-ph/9903054).
- Montes, Mireia & Ignacio Trujillo (Jan. 2019). "Intracluster light: a luminous tracer for dark matter in clusters of galaxies". In: *MNRAS* 482, pp. 2838–2851. DOI: [10.1093/mnras/sty2858](https://doi.org/10.1093/mnras/sty2858). arXiv: [1807.11488](https://arxiv.org/abs/1807.11488) [[astro-ph](https://arxiv.org/abs/astro-ph). GA].
- Morgan, W. W. (Dec. 1956). "The Integrated Spectral Types of Globular Clusters". In: *PASP* 68, p. 509. DOI: [10.1086/126988](https://doi.org/10.1086/126988).
- Moustakas, J., R. C. Kennicutt Jr., C. A. Tremonti, D. A. Dale, J.-D. T. Smith & D. Calzetti (Oct. 2010). "Optical Spectroscopy and Nebular Oxygen Abundances of the Spitzer/SINGS Galaxies". In: *ApJS* 190, pp. 233–266. DOI: [10.1088/0067-0049/190/2/233](https://doi.org/10.1088/0067-0049/190/2/233). arXiv: [1007.4547](https://arxiv.org/abs/1007.4547).
- Moustakas, John & Jr. Robert C. Kennicutt (2006). "Integrated Nebular Abundances of Disk Galaxies". In: *The Astrophysical Journal* 651.1, pp. 155–166. DOI: [10.1086/507570](https://doi.org/10.1086/507570). URL: <https://doi.org/10.1086%2F507570>.

- Narayanan, D., C. Conroy, R. Dave, B. Johnson & G. Popping (May 2018). "A Theory for the Variation of Dust Attenuation Laws in Galaxies". In: *ArXiv e-prints*. arXiv: [1805.06905](https://arxiv.org/abs/1805.06905).
- Negroponte, J. & S. D. M. White (Dec. 1983). "Simulations of mergers between disc-halo galaxies". In: *MNRAS* 205, pp. 1009–1029. DOI: [10.1093/mnras/205.4.1009](https://doi.org/10.1093/mnras/205.4.1009).
- Nemmen, R. S., M. Georganopoulos, S. Guiriec, E. T. Meyer, N. Gehrels & R. M. Sambruna (Dec. 2012). "A Universal Scaling for the Energetics of Relativistic Jets from Black Hole Systems". In: *Science* 338, p. 1445. DOI: [10.1126/science.1227416](https://doi.org/10.1126/science.1227416). arXiv: [1212.3343](https://arxiv.org/abs/1212.3343) [[astro-ph.HE](#)].
- Netzer, H. (Aug. 2015). "Revisiting the Unified Model of Active Galactic Nuclei". In: *ARA&A* 53, pp. 365–408. DOI: [10.1146/annurev-astro-082214-122302](https://doi.org/10.1146/annurev-astro-082214-122302). arXiv: [1505.00811](https://arxiv.org/abs/1505.00811).
- Noll, S., D. Burgarella, E. Giovannoli, V. Buat, D. Marcillac & J. C. Muñoz-Mateos (Dec. 2009). "Analysis of galaxy spectral energy distributions from far-UV to far-IR with CIGALE: studying a SINGS test sample". In: *A&A* 507, pp. 1793–1813. DOI: [10.1051/0004-6361/200912497](https://doi.org/10.1051/0004-6361/200912497). arXiv: [0909.5439](https://arxiv.org/abs/0909.5439).
- Ocvirk, P. (Jan. 2010). "Fake Star Formation Bursts: Blue Horizontal Branch Stars Masquerade as Young Massive Stars in Optical Integrated Light Spectroscopy". In: *ApJ* 709, pp. 88–96. DOI: [10.1088/0004-637X/709/1/88](https://doi.org/10.1088/0004-637X/709/1/88). arXiv: [0911.3156](https://arxiv.org/abs/0911.3156).
- Ocvirk, P., C. Pichon, A. Lançon & E. Thiébaud (Jan. 2006). "STECKMAP: STEllar Content and Kinematics from high resolution galactic spectra via Maximum A Posteriori". In: *MNRAS* 365, pp. 74–84. DOI: [10.1111/j.1365-2966.2005.09323.x](https://doi.org/10.1111/j.1365-2966.2005.09323.x). eprint: [astro-ph/0507002](https://arxiv.org/abs/astro-ph/0507002).
- Oke, J. B. & J. E. Gunn (Mar. 1983). "Secondary standard stars for absolute spectrophotometry". In: *ApJ* 266, pp. 713–717. DOI: [10.1086/160817](https://doi.org/10.1086/160817).
- Overzier, Roderik A. et al. (Jan. 2011). "Dust Attenuation in UV-selected Starbursts at High Redshift and Their Local Counterparts: Implications for the Cosmic Star Formation Rate Density". In: *ApJ* 726, L7, p. L7. DOI: [10.1088/2041-8205/726/1/L7](https://doi.org/10.1088/2041-8205/726/1/L7). arXiv: [1011.6098](https://arxiv.org/abs/1011.6098) [[astro-ph.CO](#)].
- Panther, B., A. F. Heavens & R. Jimenez (Aug. 2003). "Star formation and metallicity history of the SDSS galaxy survey: unlocking the fossil record". In: *MNRAS* 343, pp. 1145–1154. DOI: [10.1046/j.1365-8711.2003.06722.x](https://doi.org/10.1046/j.1365-8711.2003.06722.x). eprint: [astro-ph/0211546](https://arxiv.org/abs/astro-ph/0211546).
- Peacock, John A. et al. (Mar. 2001). "A measurement of the cosmological mass density from clustering in the 2dF Galaxy Redshift

- Survey". In: *Nature* 410, pp. 169–173. arXiv: [astro-ph/0103143](#) [[astro-ph](#)].
- Peng, Y., R. Maiolino & R. Cochrane (May 2015). "Strangulation as the primary mechanism for shutting down star formation in galaxies". In: *Nature* 521, pp. 192–195. DOI: [10.1038/nature14439](#). arXiv: [1505.03143](#).
- Peng, Y.-j. et al. (Sept. 2010). "Mass and Environment as Drivers of Galaxy Evolution in SDSS and zCOSMOS and the Origin of the Schechter Function". In: *ApJ* 721, pp. 193–221. DOI: [10.1088/0004-637X/721/1/193](#). arXiv: [1003.4747](#) [[astro-ph.CO](#)].
- Penoyre, Zephyr, Benjamin P. Moster, Debora Sijacki & Shy Genel (July 2017). "The origin and evolution of fast and slow rotators in the Illustris simulation". In: *MNRAS* 468, pp. 3883–3906. DOI: [10.1093/mnras/stx762](#). arXiv: [1703.00545](#) [[astro-ph.GA](#)].
- Petrosian, V. (Oct. 1976). "Surface brightness and evolution of galaxies". In: *ApJ* 209, pp. L1–L5. DOI: [10.1086/182253](#).
- Pierini, D., K. D. Gordon, A. N. Witt & G. J. Madsen (Dec. 2004). "Dust Attenuation in Late-Type Galaxies. I. Effects on Bulge and Disk Components". In: *ApJ* 617, pp. 1022–1046. DOI: [10.1086/425651](#). eprint: [astro-ph/0409183](#).
- Rauch, T. (May 2003). "A grid of synthetic ionizing spectra for very hot compact stars from NLTE model atmospheres". In: *A&A* 403, pp. 709–714. DOI: [10.1051/0004-6361:20030412](#). eprint: [astro-ph/0303464](#).
- Rayner, J. T., M. C. Cushing & W. D. Vacca (Dec. 2009). "The Infrared Telescope Facility (IRTF) Spectral Library: Cool Stars". In: *ApJS* 185, pp. 289–432. DOI: [10.1088/0067-0049/185/2/289](#). arXiv: [0909.0818](#) [[astro-ph.SR](#)].
- Reddy, N. A. et al. (June 2015). "The MOSDEF Survey: Measurements of Balmer Decrements and the Dust Attenuation Curve at Redshifts $z \sim 1.4$ – 2.6 ". In: *ApJ* 806, 259, p. 259. DOI: [10.1088/0004-637X/806/2/259](#). arXiv: [1504.02782](#).
- Rodríguez-Merino, L. H., M. Chavez, E. Bertone & A. Buzzoni (June 2005). "UVBLUE: A New High-Resolution Theoretical Library of Ultraviolet Stellar Spectra". In: *ApJ* 626, pp. 411–424. DOI: [10.1086/429858](#). eprint: [astro-ph/0504307](#).
- Rowlands, K. et al. (Jan. 2018). "Galaxy And Mass Assembly (GAMA): The mechanisms for quiescent galaxy formation at $z < 1$ ". In: *MNRAS* 473, pp. 1168–1185. DOI: [10.1093/mnras/stx1903](#). arXiv: [1707.07989](#).

- Rubin, V. C. & W. K. Ford Jr. (Feb. 1970). "Rotation of the Andromeda Nebula from a Spectroscopic Survey of Emission Regions". In: *ApJ* 159, p. 379. DOI: [10.1086/150317](https://doi.org/10.1086/150317).
- Salim, S. (Dec. 2014). "Green Valley Galaxies". In: *Serbian Astronomical Journal* 189, pp. 1–14. DOI: [10.2298/SAJ1489001S](https://doi.org/10.2298/SAJ1489001S). arXiv: [1501.01963](https://arxiv.org/abs/1501.01963).
- Salim, Samir & Médéric Boquien (2019). "Diversity of Galaxy Dust Attenuation Curves Drives the Scatter in the IR X- β Relation". In: *ApJ* 872, 23, p. 23. DOI: [10.3847/1538-4357/aaf88a](https://doi.org/10.3847/1538-4357/aaf88a). arXiv: [1812.05606](https://arxiv.org/abs/1812.05606) [[astro-ph.GA](#)].
- Salim, Samir, Médéric Boquien & Janice Lee (Apr. 2018). "Dust Attenuation Curves in the Local Universe: Demographics and New Laws for Star-forming Galaxies and High-redshift Analogs". In: *The Astrophysical Journal* 859.
- Salpeter, E. E. (Jan. 1955). "The Luminosity Function and Stellar Evolution." In: *ApJ* 121, p. 161. DOI: [10.1086/145971](https://doi.org/10.1086/145971).
- Sánchez, S. F. et al. (Feb. 2012). "CALIFA, the Calar Alto Legacy Integral Field Area survey. I. Survey presentation". In: *A&A* 538, A8, A8. DOI: [10.1051/0004-6361/201117353](https://doi.org/10.1051/0004-6361/201117353). arXiv: [1111.0962](https://arxiv.org/abs/1111.0962).
- Sánchez, S. F. et al. (Apr. 2016). "Pipe3D, a pipeline to analyze Integral Field Spectroscopy Data: I. New fitting philosophy of FIT3D". In: *Rev. Mexicana Astron. Astrofis.* 52, pp. 21–53. arXiv: [1509.08552](https://arxiv.org/abs/1509.08552) [[astro-ph.IM](#)].
- Sánchez-Blázquez, P. et al. (Sept. 2006). "Medium-resolution Isaac Newton Telescope library of empirical spectra". In: *MNRAS* 371, pp. 703–718. DOI: [10.1111/j.1365-2966.2006.10699.x](https://doi.org/10.1111/j.1365-2966.2006.10699.x). eprint: [astro-ph/0607009](https://arxiv.org/abs/astro-ph/0607009).
- Sander, A., W.-R. Hamann & H. Todt (Apr. 2012). "The Galactic WC stars. Stellar parameters from spectral analyses indicate a new evolutionary sequence". In: *A&A* 540, A144, A144. DOI: [10.1051/0004-6361/201117830](https://doi.org/10.1051/0004-6361/201117830). arXiv: [1201.6354](https://arxiv.org/abs/1201.6354) [[astro-ph.SR](#)].
- Schlafly, E. F. & D. P. Finkbeiner (Aug. 2011). "Measuring Reddening with Sloan Digital Sky Survey Stellar Spectra and Recalibrating SFD". In: *ApJ* 737, 103, p. 103. DOI: [10.1088/0004-637X/737/2/103](https://doi.org/10.1088/0004-637X/737/2/103). arXiv: [1012.4804](https://arxiv.org/abs/1012.4804) [[astro-ph.GA](#)].
- Schlegel, D. J., D. P. Finkbeiner & M. Davis (June 1998). "Maps of Dust Infrared Emission for Use in Estimation of Reddening and Cosmic Microwave Background Radiation Foregrounds". In: *ApJ* 500, pp. 525–553. DOI: [10.1086/305772](https://doi.org/10.1086/305772). eprint: [astro-ph/9710327](https://arxiv.org/abs/astro-ph/9710327).
- Schmidt, M. (Mar. 1959). "The Rate of Star Formation." In: *ApJ* 129, p. 243. DOI: [10.1086/146614](https://doi.org/10.1086/146614).

- Seibert, M. et al. (Jan. 2005). "Testing the Empirical Relation between Ultraviolet Color and Attenuation of Galaxies". In: *ApJ* 619, pp. L55–L58. DOI: [10.1086/427843](https://doi.org/10.1086/427843).
- Seon, K.-I. & B. T. Draine (Dec. 2016). "Radiative Transfer Model of Dust Attenuation Curves in Clumpy, Galactic Environments". In: *ApJ* 833, 201, p. 201. DOI: [10.3847/1538-4357/833/2/201](https://doi.org/10.3847/1538-4357/833/2/201). arXiv: [1606.02030](https://arxiv.org/abs/1606.02030).
- Sérsic, J. L. (1963). "Influence of the atmospheric and instrumental dispersion on the brightness distribution in a galaxy". In: *Boletín de la Asociación Argentina de Astronomía La Plata Argentina* 6, p. 41.
- Silk, J. & M. J. Rees (Mar. 1998). "Quasars and galaxy formation". In: *A&A* 331, pp. L1–L4. eprint: [astro-ph/9801013](https://arxiv.org/abs/astro-ph/9801013).
- Skrutskie, M. F. et al. (Feb. 2006). "The Two Micron All Sky Survey (2MASS)". In: *AJ* 131, pp. 1163–1183. DOI: [10.1086/498708](https://doi.org/10.1086/498708).
- Slipher, V. M. (Jan. 1915). "Spectrographic Observations of Nebulae". In: *Popular Astronomy* 23, pp. 21–24.
- Springel, V. et al. (June 2005). "Simulations of the formation, evolution and clustering of galaxies and quasars". In: *Nature* 435, pp. 629–636. DOI: [10.1038/nature03597](https://doi.org/10.1038/nature03597). eprint: [astro-ph/0504097](https://arxiv.org/abs/astro-ph/0504097).
- Stasińska, G. et al. (Nov. 2008). "Can retired galaxies mimic active galaxies? Clues from the Sloan Digital Sky Survey". In: *MNRAS* 391, pp. L29–L33. DOI: [10.1111/j.1745-3933.2008.00550.x](https://doi.org/10.1111/j.1745-3933.2008.00550.x). arXiv: [0809.1341](https://arxiv.org/abs/0809.1341).
- Stasińska, G., M. V. Costa-Duarte, N. Vale Asari, R. Cid Fernandes & L. Sodré (May 2015). "Retired galaxies: not to be forgotten in the quest of the star formation - AGN connection". In: *MNRAS* 449, pp. 559–573. DOI: [10.1093/mnras/stv078](https://doi.org/10.1093/mnras/stv078). arXiv: [1501.03812](https://arxiv.org/abs/1501.03812) [[astro-ph.GA](https://arxiv.org/abs/astro-ph.GA)].
- Stecher, T. P. (Nov. 1965). "Interstellar Extinction in the Ultraviolet". In: *ApJ* 142, p. 1683. DOI: [10.1086/148462](https://doi.org/10.1086/148462).
- Taylor, Edward N. et al. (Dec. 2011). "Galaxy And Mass Assembly (GAMA): stellar mass estimates". In: *MNRAS* 418, pp. 1587–1620. DOI: [10.1111/j.1365-2966.2011.19536.x](https://doi.org/10.1111/j.1365-2966.2011.19536.x). arXiv: [1108.0635](https://arxiv.org/abs/1108.0635) [[astro-ph.CO](https://arxiv.org/abs/astro-ph.CO)].
- Tinsley, B. M. (Feb. 1968). "Evolution of the Stars and Gas in Galaxies". In: *ApJ* 151, p. 547. DOI: [10.1086/149455](https://doi.org/10.1086/149455).
- Todt, H., A. Sander, R. Hainich, W.-R. Hamann, M. Quade & T. Shenar (July 2015). "Potsdam Wolf-Rayet model atmosphere grids for WN stars". In: *A&A* 579, A75, A75. DOI: [10.1051/0004-6361/201526253](https://doi.org/10.1051/0004-6361/201526253).

- Tojeiro, R., A. F. Heavens, R. Jimenez & B. Panter (Nov. 2007). “Recovering galaxy star formation and metallicity histories from spectra using VESPA”. In: *MNRAS* 381, pp. 1252–1266. DOI: [10.1111/j.1365-2966.2007.12323.x](https://doi.org/10.1111/j.1365-2966.2007.12323.x). arXiv: [0704.0941](https://arxiv.org/abs/0704.0941).
- Toomre, A. & J. Toomre (Dec. 1972). “Galactic Bridges and Tails”. In: *ApJ* 178, pp. 623–666. DOI: [10.1086/151823](https://doi.org/10.1086/151823).
- Treu, T., M. W. Auger, L. V. E. Koopmans, R. Gavazzi, P. J. Marshall & A. S. Bolton (Feb. 2010). “The Initial Mass Function of Early-Type Galaxies”. In: *ApJ* 709, pp. 1195–1202. DOI: [10.1088/0004-637X/709/2/1195](https://doi.org/10.1088/0004-637X/709/2/1195). arXiv: [0911.3392](https://arxiv.org/abs/0911.3392).
- Trussler, James et al. (Nov. 2018). “Starvation as the primary quenching mechanism in galaxies”. In: *arXiv e-prints*, arXiv:1811.09283, arXiv:1811.09283. arXiv: [1811.09283](https://arxiv.org/abs/1811.09283) [[astro-ph.GA](#)].
- Tully, R. B. & J. R. Fisher (Feb. 1977). “A new method of determining distances to galaxies”. In: *A&A* 54, pp. 661–673.
- Valdes, F., R. Gupta, J. A. Rose, H. P. Singh & D. J. Bell (June 2004). “The Indo-US Library of Coudé Feed Stellar Spectra”. In: *ApJS* 152, pp. 251–259. DOI: [10.1086/386343](https://doi.org/10.1086/386343). eprint: [astro-ph/0402435](https://arxiv.org/abs/astro-ph/0402435).
- Vazdekis, A. et al. (June 2010). “Evolutionary stellar population synthesis with MILES - I. The base models and a new line index system”. In: *MNRAS* 404, pp. 1639–1671. DOI: [10.1111/j.1365-2966.2010.16407.x](https://doi.org/10.1111/j.1365-2966.2010.16407.x). arXiv: [1004.4439](https://arxiv.org/abs/1004.4439) [[astro-ph.CO](#)].
- Vazdekis, A. et al. (May 2015). “Evolutionary stellar population synthesis with MILES - II. Scaled-solar and α -enhanced models”. In: *MNRAS* 449, pp. 1177–1214. DOI: [10.1093/mnras/stv151](https://doi.org/10.1093/mnras/stv151). arXiv: [1504.08032](https://arxiv.org/abs/1504.08032).
- Vazdekis, A., M. Koleva, E. Ricciardelli, B. Röck & J. Falcón-Barroso (Dec. 2016). “UV-extended E-MILES stellar population models: young components in massive early-type galaxies”. In: *MNRAS* 463, pp. 3409–3436. DOI: [10.1093/mnras/stw2231](https://doi.org/10.1093/mnras/stw2231). arXiv: [1612.01187](https://arxiv.org/abs/1612.01187).
- Vogelsberger, M. et al. (May 2014). “Properties of galaxies reproduced by a hydrodynamic simulation”. In: *Nature* 509, pp. 177–182. DOI: [10.1038/nature13316](https://doi.org/10.1038/nature13316). arXiv: [1405.1418](https://arxiv.org/abs/1405.1418).
- Walcher, J., B. Groves, T. Budavári & D. Dale (Jan. 2011). “Fitting the integrated spectral energy distributions of galaxies”. In: *Ap&SS* 331, pp. 1–52. DOI: [10.1007/s10509-010-0458-z](https://doi.org/10.1007/s10509-010-0458-z). arXiv: [1008.0395](https://arxiv.org/abs/1008.0395).
- Werle, A. et al. (Feb. 2019). “Simultaneous analysis of SDSS spectra and GALEX photometry with STARLIGHT: method and early results”. In: *MNRAS* 483, pp. 2382–2397. DOI: [10.1093/mnras/sty3264](https://doi.org/10.1093/mnras/sty3264). arXiv: [1811.11255](https://arxiv.org/abs/1811.11255) [[astro-ph.GA](#)].

- Westera, P., T. Lejeune, R. Buser, F. Cuisinier & G. Bruzual (Jan. 2002). "A standard stellar library for evolutionary synthesis. III. Metallicity calibration". In: *A&A* 381, pp. 524–538. DOI: [10.1051/0004-6361:20011493](https://doi.org/10.1051/0004-6361:20011493). eprint: [astro-ph/0110559](https://arxiv.org/abs/astro-ph/0110559).
- Wild, V. et al. (Nov. 2011). "Empirical determination of the shape of dust attenuation curves in star-forming galaxies". In: *MNRAS* 417, pp. 1760–1786. DOI: [10.1111/j.1365-2966.2011.19367.x](https://doi.org/10.1111/j.1365-2966.2011.19367.x). arXiv: [1106.1646](https://arxiv.org/abs/1106.1646).
- Wild, V. et al. (Nov. 2016). "The evolution of post-starburst galaxies from $z=2$ to 0.5". In: *MNRAS* 463, pp. 832–844. DOI: [10.1093/mnras/stw1996](https://doi.org/10.1093/mnras/stw1996). arXiv: [1608.00588](https://arxiv.org/abs/1608.00588).
- Williams, R. J., R. F. Quadri, M. Franx, P. van Dokkum & I. Labbé (Feb. 2009). "Detection of Quiescent Galaxies in a Bicolor Sequence from $Z = 0-2$ ". In: *ApJ* 691, pp. 1879–1895. DOI: [10.1088/0004-637X/691/2/1879](https://doi.org/10.1088/0004-637X/691/2/1879). arXiv: [0806.0625](https://arxiv.org/abs/0806.0625).
- Witt, A. N. & K. D. Gordon (Jan. 2000). "Multiple Scattering in Clumpy Media. II. Galactic Environments". In: *ApJ* 528, pp. 799–816. DOI: [10.1086/308197](https://doi.org/10.1086/308197). eprint: [astro-ph/9907342](https://arxiv.org/abs/astro-ph/9907342).
- Wood, D. B. (July 1966). "Multicolor Photoelectric Photometry of Galaxies". In: *ApJ* 145, p. 36. DOI: [10.1086/148737](https://doi.org/10.1086/148737).
- Worthey, G., S. M. Faber, J. J. Gonzalez & D. Burstein (Oct. 1994). "Old stellar populations. 5: Absorption feature indices for the complete LICK/IDS sample of stars". In: *ApJS* 94, pp. 687–722. DOI: [10.1086/192087](https://doi.org/10.1086/192087).
- Wu, Po-Feng et al. (2018). "Fast and Slow Paths to Quiescence: Ages and Sizes of 400 Quiescent Galaxies from the LEGA-C Survey". In: *The Astrophysical Journal* 868.1, p. 37. DOI: [10.3847/1538-4357/aae822](https://doi.org/10.3847/1538-4357/aae822). URL: <https://doi.org/10.3847/1538-4357/aae822>.
- Wyder, T. K. et al. (Dec. 2007). "The UV-Optical Galaxy Color-Magnitude Diagram. I. Basic Properties". In: *ApJS* 173, pp. 293–314. DOI: [10.1086/521402](https://doi.org/10.1086/521402). arXiv: [0706.3938](https://arxiv.org/abs/0706.3938).
- Yi, S. K. (2008). "The Current Understanding on the UV Upturn". In: *Hot Subdwarf Stars and Related Objects*. Ed. by U. Heber, C. S. Jeffery & R. Napiwotzki. Vol. 392. Astronomical Society of the Pacific Conference Series, p. 3. arXiv: [0808.0254](https://arxiv.org/abs/0808.0254).
- Yi, S. K. et al. (Jan. 2005). "Galaxy Evolution Explorer Ultraviolet Color-Magnitude Relations and Evidence of Recent Star Formation in Early-Type Galaxies". In: *ApJ* 619, pp. L111–L114. DOI: [10.1086/422811](https://doi.org/10.1086/422811). eprint: [astro-ph/0411327](https://arxiv.org/abs/astro-ph/0411327).
- Yi, S. K., J. Lee, Y.-K. Sheen, H. Jeong, H. Suh & K. Oh (Aug. 2011). "The Ultraviolet Upturn in Elliptical Galaxies and Environmental

- Effects". In: *ApJS* 195, 22, p. 22. DOI: [10.1088/0067-0049/195/2/22](https://doi.org/10.1088/0067-0049/195/2/22). arXiv: [1107.0005](https://arxiv.org/abs/1107.0005).
- Yi, Suhyoung, Pierre Demarque & Jr. Oemler Augustus (Sept. 1997). "On the Origin of the UV Upturn in Elliptical Galaxies. I. Sensitivity of UV Population Synthesis to Various Input Parameters". In: *ApJ* 486, pp. 201–229. DOI: [10.1086/304498](https://doi.org/10.1086/304498). arXiv: [astro-ph/9705173](https://arxiv.org/abs/astro-ph/9705173) [[astro-ph](https://arxiv.org/abs/astro-ph)].
- York, D. G. et al. (Sept. 2000). "The Sloan Digital Sky Survey: Technical Summary". In: *AJ* 120, pp. 1579–1587. DOI: [10.1086/301513](https://doi.org/10.1086/301513). eprint: [astro-ph/0006396](https://arxiv.org/abs/astro-ph/0006396).
- Zibetti, Stefano, Anna Gallazzi, Daniele Pierini & Anna Pasquali (2013). "Near-infrared spectroscopy of post-starburst galaxies: a limited impact of TP-AGB stars on galaxy spectral energy distributions". In: 1497, pp. 1479–1497. DOI: [10.1093/mnras/sts126](https://doi.org/10.1093/mnras/sts126).
- Zwicky, F. (1933). "Die Rotverschiebung von extragalaktischen Nebeln". In: *Helvetica Physica Acta* 6, pp. 110–127.